

**UC Davis**

**UC Davis Electronic Theses and Dissertations**

**Title**

Mechanisms of Meiotic Spindle Initiation in *Caenorhabditis elegans* Oocytes

**Permalink**

<https://escholarship.org/uc/item/34x339vd>

**Author**

GONG, TING

**Publication Date**

2023

Peer reviewed|Thesis/dissertation

Mechanisms of Meiotic Spindle Initiation in *Caenorhabditis elegans* Oocytes

By

TING GONG  
DISSERTATION

Submitted in partial satisfaction of the requirements for the degree of

DOCTOR OF PHILOSOPHY

in

Biochemistry, Molecular, Cellular and Developmental Biology

in the

OFFICE OF GRADUATE STUDIES

of the

UNIVERSITY OF CALIFORNIA

DAVIS

Approved:

---

Francis McNally, Chair

---

JoAnne Engebrecht

---

Richard J. McKenney

Committee in Charge

2023

# Acknowledgements

First, I would like to express my sincere gratitude to my Ph. D advisor Dr. Francis McNally. I am grateful for the opportunity to pursue my research interest in the lab. For me, Frank is a model scientist with enormous enthusiasm for research and high work ethics. He is also a great mentor dedicated to graduate and undergraduate training. I am truly grateful for the professional, caring and fun lab environment he has established. It makes my graduate experience one of the most memorable pieces of my life.

I would also like to thank the members of my thesis committee, Dr. Joanne Engebrecht and Dr. Richard McKenney for the support and guidance in the last five years.

I also would like to thank the amazing scientists and faculties in the MCB department for invaluable feedback during seminar discussions. I appreciate the opportunity to participate in seminars and journal clubs for amazing scientific training.

In addition to scientific conversations, I would also like to thank BMCDB graduate group mentor Dr. Enoch Baldwin and my academic advisor Dr. Qizhi Gong for guiding me through first-year lab rotation, switching labs and all the way to get my doctorate degree. It was a tough time for me to study abroad -time studying abroad, but they made this transition so much easier, and I am so lucky to have them to be my mentors. I am grateful for everyone in McNally Lab, Rose Lab, and BMCDB graduate group for support, friendship and companion during pandemic and post pandemic days. It has been a long and rough journey, but I am so thankful to have been surrounded by the most kind and supportive people.

Finally, I am grateful to my family and friends for their love and support. I especially thank my parents for their encouragement to pursue my interest although they do not understand what I am studying. I would like to thank all my friends in Davis for making Davis a home for me in the US.

# Abstract

Microtubule-based spindle formation is essential to faithful chromosome segregation during cell division. In many animal species, the oocyte meiotic spindle forms without centrosomes (the major microtubule organizing centers), unlike most mitotic cells. Even in mitotic cells, centrosomes are sometimes dispensable for bipolar spindle formation, indicating a redundant pathway initiating spindle assembly. In this study, we examined meiotic spindle assembly in *C. elegans* oocytes. We have demonstrated: First, metaphase I spindle formation is Ran-GEF and Ran-GAP independent in meiotic embryos. Second, free tubulin, also called soluble tubulin, concentrates in the nuclear volume during Germinal Vesicle Breakdown (GVBD) as well as in the spindle region during metaphase I and metaphase II. We then showed that the concentration of free tubulin at metaphase II spindle region is enclosed by dense ER sheets which exclude cytoplasmic organelles including mitochondria and yolk granules from the meiotic spindle. Similar observations are also shown in early mitotic cells. Together, this suggests free tubulin concentrating in the nuclear region might be a common mechanism promoting spindle formation through volume exclusion in both meiotic and early mitotic embryos in *C. elegans*. Moreover, the movement of molecules during GVBD depends on the size and the charge of the molecules.

## Table of Contents

<b>Title Page</b> .....	<b>i</b>
<b>Acknowledgements</b> .....	<b>ii</b>
<b>Abstract</b> .....	<b>iv</b>
<b>Chapter 1</b> .....	<b>1</b>
Introduction.....	2
Results.....	8
Discussion and future directions.....	18
Materials and Methods.....	21
References.....	23
Figures.....	31
Figure Legends .....	40
<b>Chapter 2</b> .....	<b>47</b>
<i>Caenorhabditis elegans</i> spermatocytes can segregate achiasmate homologous chromosomes apart at higher than random frequency during meiosis I. ....	47
<b>Chapter 3</b> .....	<b>60</b>
Evidence for anaphase pulling forces during <i>C. elegans</i> meiosis.....	60
<b>Chapter 4</b> .....	<b>85</b>
Paternal mitochondria from an <i>rmd-2</i> , <i>rmd-3</i> , <i>rmd-6</i> triple mutant are properly positioned in the <i>C.</i> <i>elegans</i> zygote. ....	85
<b>Chapter 5</b> .....	<b>88</b>
Cohesin is required for meiotic spindle assembly independent of its role in cohesion in <i>C. elegans</i> . .....	88

# Chapter 1

My research interests lie in the meiotic division in both males and females. My major project is trying to understand the mechanism of acentrosomal spindle assembly in *C. elegans* oocytes, which will be covered in Chapter 1. This is collaborative work with many members in McNally lab: I performed most of the experiments. Dr. Francis McNally conceived this project and helped with designing experiments. Siri Konanoor helped a lot with generating worm strains, worm crosses, live imaging data acquisition and data analysis. Cynthia Bailey, Alma Peraza, Elizabeth Beath and Shuyan Qiu kindly shared their live-imaging data of VIT-2, ER, COX-4, and PLIN-1 (Figure 5). Stefanie Redemann from the University of Virginia provided original electron tomograph data of meiotic spindles. And Karen McNally generously contributed her time to this project during her retirement. She reconstituted these meiotic spindles, performed quantification and figure making (Fig 6).

My research project for my qualifying exam, which is to understand the difference of meiosis in oocytes and male spermatocytes in response to crossover failure, is covered in Chapter 2.

I have also worked with other members in the lab and participated in their research projects, the findings of which are demonstrated as separate chapters (Chapter 3, 4 and 5).

## Introduction

Errors in chromosome segregation result in chromosome aneuploidy, a leading cause of pregnancy loss, embryonic lethality, and congenital defects if they occur during meiosis and cancer if they occur during mitosis (Nasmyth, 2002). Faithful chromosome segregation in most eukaryotes relies on the bipolar spindle segregating chromosomes into daughter cells. The bipolar spindle is a highly elaborate structure composed of thousands of microtubules, whose organization and stability are dynamically regulated to ensure proper chromosome attachment, alignment and segregation (Bennabi et al., 2016; Kline-Smith and Walczak, 2004; Mullen et al., 2019).

In most mitotic cells, centrosomes at the two spindle poles act as major microtubule organization centers (MTOCs), in which spindle assembly factors (SAFs) are recruited to nucleate spindle microtubules (Petry, 2016; Prosser and Pelletier, 2017). Each centrosome contains a pair of centrioles and surrounding pericentriolar material (PCM) proteins (Bornens, 2012; Hinchcliffe, 2014; Kellogg et al., 2003; Sanchez and Feldman, 2017; Wang et al., 2014). However, mitotic cells lacking centrosomes can sometimes still assemble bipolar spindles, indicating the existence of additional pathways in spindle formation (Conduit et al., 2015; Khodjakov et al., 2000; Prosser and Pelletier, 2017). Moreover, centrosomes gradually degenerate during oogenesis, and female meiotic spindles in many animal species form without centrosomes (Dumont and Desai, 2012; Gruss, 2018; Heald et al., 1997; Mikeladze-Dvali et al., 2012; Schuh and Ellenberg, 2007). It is well-known that human oocytes, especially from individuals with advanced maternal ages or in vitro fertilizations (IVF) are highly prone to meiotic spindle formation



errors, resulting in pregnancy loss and aneuploid embryos (Angell, 1991; Fair and Lonergan, 2023; Thomas et al., 2021).

Many redundant pathways have been proposed to replace centrosomes and nucleate microtubules for spindle formation in different organisms (Li et al., 2006; Schuh and Ellenberg, 2007; Wu et al., 2022). In mouse oocytes, multiple de novo MTOCs originate from cytoplasmic microtubules prior to GVBD, which later increase largely in number and cluster into multipolar spindle. These MTOCs are enriched in PCM proteins, referred as non-centrosomal MTOCs (ncMTOCs) (Schuh and Ellenberg, 2007). Recently, MTOC-like structures have been shown in human oocytes, driven by microtubule associated protein TACC3 (Wu et al., 2022). No ncMTOCs have been reported in *Drosophila* oocytes and *C. elegans* oocytes.

Studies using *Xenopus* egg extracts suggest that spindle bipolarity is an intrinsic nature of the chromosomes and the cytoplasm where microtubules are self-assembled into a bipolar spindle in centrosome-independent manner, driven by microtubule sorting proteins (Heald et al., 1996). However, the mechanism of spindle microtubule nucleation without centrosomes is not fully understood.

Three molecular mechanisms have been proposed for microtubules nucleation around chromosomes in spindle regions lacking centrosomes: Ran-GTP pathway, Chromosome Passenger Complex (CPC) pathway and Augmin pathway. These mechanisms have been nicely summarized in (Bennabi et al., 2016).

The small GTPase Ran has been demonstrated to play a critical role in spindle formation in addition to its role in nuclear transport (Carazo-Salas et al., 1999; Drutovic et al., 2020;

Hetzer et al., 2002; Kalab et al., 1999). Ran exists in its inactive GDP bound form (Ran-GDP) and active GTP bound form (Ran-GTP). Ran in its active GTP-bound form can release inactive SAFs from binding with Importins, thereby turning them (e.g., TPX2) into an active state and nucleating microtubules for spindle formation. Addition of constitutively active Ran-GTP in *Xenopus* egg extracts induces spindle formation in the absence of Ran. However, manipulating levels of Ran-GTP in mouse or *X. laevis* oocytes did not inhibit assembly of functional meiosis I spindles, indicating a centriole and Ran-GTP independent spindle assembly pathway in vertebrate oocytes (Dumont et al., 2007). The Ran-GTP and Ran-GDP cycle is regulated by the Ran Guanine Exchange Factor (Ran-GEF) RCC1, the Ran GTPase-Activating Protein (Ran-GAP) and Ran Binding Protein (Ran-BP). The Ran GEF, RCC1, which creates Ran-GTP by promoting exchange of GTP for GDP, is localized in interphase nuclei and on condensed chromatin from prometaphase through anaphase during mitosis in cultured human cells (Moore et al., 2002; Ohtsubo et al., 1989), cultured rodent cells (Li et al., 2003), and *Xenopus* sperm chromatin incubated in M-phase *Xenopus* egg extract (Bilbao-Cortés et al., 2002; Li et al., 2003). The amount of RCC1 associated with mitotic chromatin peaks at the metaphase-anaphase transition in cycling *Xenopus* egg extracts (Arnaoutov and Dasso, 2003), indicating RCC1 might play a role primarily in anaphase. In cultured human cells, metaphase phosphorylation of RCC1 causes it to turnover on chromatin more rapidly than when dephosphorylated during anaphase (Hutchins et al., 2004), suggesting that the activity of RCC1 can be tuned through its phosphorylation. Chromatin-bound RCC1 forms a transient complex with Ran during mitosis (Bilbao-Cortés et al., 2002; Li et al., 2003). RCC1 may bind chromatin through direct binding to histones (Nemergut et al., 2001),

however, it is distributed throughout mitotic cytoplasm in *Drosophila* embryos (Frasch, 1991).

RCC1 linked to beads is sufficient to drive bipolar spindle assembly in *Xenopus* egg extracts (Halpin et al., 2011). Depletion of Ran-GTP in *Drosophila* and *C. elegans* delays but do not abolish meiotic spindle formation (Cesario and McKim, 2011; Chuang et al., 2020).

The CPC is composed of Aurora B/C kinase, the inner centromeric protein (INCENP), Survivin, and Borealin, which target it to chromatin. The chromosome-associated CPC is required for bipolar spindle assembly during *C. elegans* oocyte meiosis (Divekar et al., 2021) although a cloud of disorganized microtubules is still nucleated near chromosomes. The Augmin complex recruits  $\gamma$ -tubulin and nucleates new microtubules on the sides of preexisting microtubules (Colombié et al., 2013; Goshima et al., 2008; Lawo et al., 2009; Petry et al., 2011; Sánchez-Huertas and Lüders, 2015; Uehara et al., 2009).

A less-studied pathway that may promote spindle assembly in the vicinity of chromosomes is the concentration of  $\alpha/\beta$ -tubulin dimers in the nuclear volume at Nuclear Envelope Breakdown (NEBD). Unpolymerized tubulin, monitored in cells treated with microtubule-depolymerizing drugs, is excluded from nuclei during interphase. During NEBD, rather than equilibrating to equal concentrations in the cytoplasm and nucleus, tubulin dimers have been reported to concentrate in the nuclear volume in *Drosophila* mitotic embryos (~ 1.6-fold, Yao et al., 2012), *C. elegans* mitotic embryos (~ 2-fold, Hayashi et al., 2012), *Drosophila* S2 cells (~ 1.5-fold, Schweizer et al., 2015) and *Drosophila* neuroblasts (Métivier et al., 2021). The concentration of tubulin dimer

independently of microtubule polymerization has been proposed to be related to binding to spindle matrix, the mechanisms of which remain controversial. Interestingly, non-proteinaceous molecules like dextran (a polysaccharide) can also concentrate in the nuclear region, raising the question whether binding to a spindle matrix is necessary or not. Depletion of Ran by RNAi affects this concentration and causes spindle defects in *C. elegans* mitotic embryos (Hayashi et al., 2012) and *Drosophila* neuroblasts (Métivier et al., 2021). It is unclear whether the concentration of tubulin may be a component of the Ran pathway, or the defects observed might be the indirect result of altering the kinetics of nuclear import/export long before mitosis.

In the *C. elegans* female gonad, the microtubules in the -1 oocyte (most mature oocyte) remain cytoplasmic prior to germinal vesicle breakdown (GVBD). As the -1 oocyte matures, its nucleus moves away from the center, approaching the future anterior cortex. Upon fertilization at the future posterior end by the sperm, the -1 oocyte is ovulated into the spermatheca. At the same time, the nuclear envelope of the -1 oocyte is permeabilized (Germinal Vesicle breakdown; GVBD), and a dense microtubule cloud forms around chromosomes as spindle assembly initiates (Kim et al., 2013).

*C. elegans* female meiosis is unique in a few different ways. First, no distinct MTOCs or PCM protein enrichment have been observed in mature oocytes (unpublished data in McNally Lab). Second, RNAi knockdown of *C. elegans* Ran RAN-1 decreases spindle microtubule levels but does not block meiotic spindle formation (Chuang et al., 2020). Third, depletion of *C. elegans*  $\gamma$ -tubulin (seeds for templated microtubule nucleation) TBG-1 by RNAi also leads to spindle microtubule loss but does not prevent meiotic division. Although oocytes depleted of  $\gamma$ -tubulin and katanin (microtubule severing

protein) by RNAi failed to form any microtubule asters (McNally et al., 2006). Lastly, most SAFs remain cytoplasmic prior to GVBD (McNally et al., 2022). This suggests there might be a novel mechanism underlying the microtubule nucleation and spindle assembly without centrosomes in *C. elegans* oocytes. The mechanisms observed in *C. elegans* may indicate a universal pathway that exists as a redundant pathway in other systems, as we have mentioned earlier. Understanding this mechanism has significant implications for fertility and the development of healthy embryos, as it reveals factors that can induce spindle assembly errors. These factors can be potential therapeutic targets to improve the efficacy of IVF.

## Results

### **Ran-2 and Ran-3 are weakly associated with chromosomes during meiotic spindle assembly in *C. elegans* oocytes.**

A previous study depleting Ran in *C. elegans* by *ran-1* (*C. elegans* homolog of human RCC1) RNAi showed female meiotic spindles still formed although with a reduced density of microtubules (Chuang et al., 2020). As RAN-1 may not have been fully depleted by RNAi, we created conditional knockdown worm strains of Ran-GEF and Ran-GAP by Auxin Induced Degradation (AID) system to further determine whether acentrosomal spindle formation is Ran-dependent (Zhang et al., 2015). We added sequences of AID and Halo tag to endogenous *ran-2* (Ran-GAP in *C. elegans*) and *ran-3* (Ran-GEF in *C. elegans*). Worms were sterile after depleting RAN-2 or RAN-3 through AID, indicating RAN-3 or RAN-2 depletion leads to germline defects (Fig 1B). Previous depletion of RAN-3 or RAN-2 by RNAi caused >90% embryonic lethality but did not affect brood size (Askjaer et al., 2002). This suggests that depletion of RAN-2 or RAN-3 through the AID system might result in more complete depletion than RNAi.

It has been proposed that chromosome associated RCC1(Ran-GEF) establishes a Ran-GTP gradient in the vicinity and promotes spindle assembly by recruiting active SAFs in the proximity of chromosomes in mitosis. The localization and function of Ran-GEF or Ran-GAP in meiosis has not been determined in vivo. To establish a Ran-GTP gradient, Ran-GAP remains mostly cytoplasmic while chromosome bound/associated Ran-GEF releases inactive SAFs from binding with importins (Fig 1A). Consistent with these ideas, we observed RAN-3::AID::HALO in the nucleoplasm and predominantly associated with chromosomes before GVBD. After GVBD, Ran-3 diffused from the

nucleus and only faintly associated with chromosomes at metaphase I and II. In contrast, RAN-3 strongly localized to chromosomes at anaphase I and anaphase II (Fig 1C). RAN-2::AID::HALO was strongly associated with the nuclear envelope before GVBD. Later, Ran-2 faintly labeled metaphase I and metaphase II spindles. At anaphase, Ran-2 localized to the spindle midzone, and its intensity increased as anaphase progressed, and it strongly associated with inner side of separating chromosomes (Fig 1D). These results suggest that Ran-3 and Ran-2 might function primarily at anaphase.

**Ran-GEF and Ran-GAP are required for meiotic chromosome segregation but not metaphase I spindle formation.**

Previous studies suggest Ran regulators are also involved in nuclear transport, defects in which usually leads to small and leaky nuclei. By treating the worms with auxin for a brief period, we sought to only evaluate the function of RAN-3 and RAN-2 on meiotic spindle formation without disrupting meiotic prophase and nuclear transport.

When treated with Auxin for 4hrs, expression of Halo-AID-RAN-3 in the nucleoplasm and chromosomes in diakinesis oocytes was significantly reduced (Fig 2A-B). At 6hr auxin treatment, the expression level was comparable to control oocytes with no Halo expression. Moreover, -1 oocytes treated with auxin for 4hrs were slightly smaller, and compartmentalization of nucleus is compromised: microtubules were less excluded from the nucleus. Worms treated with auxin for extended periods (36hrs) have even smaller nuclei and worse compartmentalization (Fig S1A-C), suggesting Ran-3 might be required for nuclear transport in diakinesis oocytes.

Similarly, expression of Halo-AID-RAN-2 in the cytoplasm and nuclear envelope in diakinesis oocytes was significantly reduced when treated with 4hr or 6hr auxin (Fig 2B). At 6hr auxin treatment, the expression level was comparable to control oocytes with no Halo expression. The sizes of oocytes treated with 4hr and 6hr auxin was normal, and their nuclei were not leaky compared to controls (Fig S1B-C). RAN-2::AID::HALO oocytes treated with auxin for extended periods were not examined as nucleus in the oocytes are severely disorganized.

Consistent with the localization of Ran-3 and Ran-2, loss of Ran-3 or Ran-2 when treated with 4hrs or 6hrs auxin did not abolish bipolar spindle formation at metaphase I, although significantly more oocytes were arrested at anaphase I than in control worms without AID insertion or without auxin treatment (Fig 2E-F).

Attempt to make Ran-1(RAN in *C. elegans*) depletion strain was made but no successful edit was obtained, possibly because modification of *ran-1* leads to lethality.

### **Free tubulin is concentrated in the nuclear volume at GVBD.**

At the onset of mitosis in *C. elegans* and *Drosophila*, soluble tubulin concentrates in the nuclear/spindle volume relative to the surrounding cytoplasm (Hayashi et al., 2012; Métivier et al., 2021; Schweizer et al., 2015; Yao et al., 2012). Since microtubule polymerization is concentration dependent, this concentration might facilitate spindle formation in the vicinity of chromosomes in meiotic oocytes. In DMSO-treated control -1 oocytes, NeonGreen::TBB-2 ( $\beta$ -tubulin) labelled microtubules in the cytoplasm and was excluded from the nucleus (Fig 3A, 3B). Upon fenestration of the nuclear envelope (GVBD: germinal vesical breakdown), indicated by leakage of non-chromosomal



mCherry::histone out of the nucleus, NeonGreen::TBB-2 fluorescence increased within the nuclear volume in 10/10 time-lapse sequences (Fig. 3B) as previously described (McNally et al., 2006; Mullen and Wignall, 2017). Tubulin fluorescence then transformed into a “microtubule cage” (Mullen and Wignall, 2017) and eventually a bipolar spindle in 10 out of 10 time-lapse sequences. Surprisingly, in oocytes treated with nocodazole to depolymerize microtubules, tubulin was diffused in the cytoplasm prior to GVBD (Fig. 3C), and still concentrated in the nuclear volume during and after GVBD (Fig 3C; Fig. 3D, 3E). Simple diffusion from the cytoplasm into the nuclear volume should result in equal fluorescence intensities of NeonGreen::tubulin in the nucleus and cytoplasm but fluorescence instead increased in the nuclear volume to 1.2-fold greater than the cytoplasm (Fig. 3E). After ovulation, chromosomes in nocodazole-treated zygotes were dispersed and loosely wrapped by sparse short microtubules. No spindle formation or chromosome separation was observed before pronucleus formation in 12 out of 12 time-lapse sequences.

Similar results in previous studies of mitosis led to the interpretation that alpha/beta tubulin dimers concentrate in the nuclear volume of unperturbed cells during spindle assembly. However, it is possible that nocodazole does not completely block microtubule polymerization and the fluorescence accumulating in the nuclear volume of nocodazole-treated oocytes represents accumulation of short microtubules. It is also possible that this phenomenon is induced by nocodazole and does not occur in unperturbed cells.

**Accumulation of tetrameric GFP and un-polymerizable tubulin in the “nuclear volume” at GVBD.**

Previous investigators suggested that tubulin dimers concentrate either by binding to something in the nuclear volume (Hayashi et al., 2012; Métivier et al., 2021) or by being excluded by cytoplasmic organelles that are kept out of the spindle volume by the ER envelope that still envelopes the spindle after nuclear envelope breakdown (Schweizer et al., 2015; Fig. 4A). We analyzed the behavior of two fluorescent probes designed to address three major issues: 1. Incomplete depolymerization by nocodazole; 2. Concentration of alpha/beta dimers in the absence of nocodazole; 3. Specific binding of tubulin to a nuclear binding site vs volume exclusion by cytoplasmic organelles. GFP::GCN4-pLI is a tetramerized GFP designed to have a native molecular weight similar to an alpha/beta tubulin dimer, but which should not bind to any tubulin-specific binding sites in the nuclear volume (Mittl et al., 2000; Fig. 4B). GFP::TBA-2(T349E) is an alpha tubulin mutant that can dimerize with beta tubulin, cannot polymerize (Johnson et al., 2011; Fig. 4C), and should bind any specific tubulin binding sites in the nuclear volume. Both GFP::GCN4-pLi (Fig. 4B) and GFP::tba-2(T349E) (Fig. 4C) concentrated in the nuclear volume at GVBD in the absence of nocodazole. These results 1. Suggested that the concentration of GFP::tubulin in nocodazole was not due to incomplete depolymerization; 2. That tubulin dimers concentrate in the nuclear volume during unperturbed spindle assembly; and 3. That binding to a tubulin-specific binding site in the nuclear volume is not required for concentration.

Because GFP::GCN4-pLI and GFP::tba-2(T349E) could be tracked in the absence of nocodazole, we could examine their behavior during normal meiotic divisions. Chromosome segregation was normal in GFP::tba-2(T349E) oocytes and GFP::GCN4-pLi oocytes (12/12 and 10/10 filmed respectively) suggesting that expression of GFP::tba-

2(T349E) or GFP::*GCN4*-pLi did not severely disturb normal spindle function. Interestingly, their concentration at GVBD lasted through Metaphase I but diffused to a 1:1 spindle: cytoplasm ratio at Anaphase I, followed by re-accumulation at metaphase II and dispersion at Anaphase II (Fig 4B, 4C, 4D). This is very interesting as the nuclear envelope does not re-form prior to Metaphase II, raising the question of what delimits the concentration at Metaphase II and how this happens. Our results suggest that alpha/beta tubulin dimers are concentrated in the nuclear region to a critical concentration that allows timely and proper meiotic spindle formation.

### **The ER instead of the nuclear envelope delimits the accumulation of free tubulin during meiosis and early mitosis.**

The fact that tubulin-sized molecules concentrate in the nuclear volume draws our attention to the nucleo-cytoplasmic environment in the oocytes that might favor the accumulation of the free tubulin during GVBD, metaphase I and metaphase II. The nuclear envelope, a double-membrane barrier, separates nucleoplasm from cytoplasm. It allows small molecules to freely diffuse in and out through nuclear pores, while excluding larger molecules unless through active nucleo-cytoplasmic transport. Although the process of GVBD is diverse in different species, it usually starts with the disassembly of nuclear pore complexes (NPCs) allowing for the influx of molecules up to 70 kDa, then the fenestration of membrane allows for the influx of 500 kDa Dextran, followed by the complete rupture of nucleus membrane leading to the mixing of nucleoplasm and cytoplasm (Wesolowska et al., 2020). To understand where the free tubulin is concentrated, we first tracked nuclear proteins and nuclear Lamin, which might persist or re-organize in *C. elegans* meiotic embryos after GVBD (Fig 5A). GFP::*NPP-6*, a nuclear

pore protein of the Y complex (Galy et al., 2003), disappeared from the nuclear envelope after GVBD and did not re-locate to the nuclear membrane until the pronuclear formation (Fig 5B). Although it persisted in the cytoplasm at pre-metaphase I and localized on chromosomes through meiosis (Fig 5B), it differs from where free tubulin concentrated (Fig 4C, 4E). Similarly, GFP::LMN-1, the *C. elegans* nuclear Lamin (Galy et al., 2003), disappeared at GVBD, and only re-appeared after anaphase II (Fig 5C). These suggest that the nucleus disassembles before metaphase I and does not reform before Metaphase II.

On the other hand, ER is continuous with the outer nuclear membrane (Fig 5A), and it has been shown to remain throughout meiosis although undergoing dramatic morphological changes in *C. elegans* oocytes (Kimura et al., 2017). Indeed, ER forms a ring around the nucleus in the -1 oocyte, then ruffles around spindle microtubules upon GVBD (Fig 5D). After GVBD, ER wraps around meiotic spindles at metaphase I and metaphase II, with strong clustering at two spindle poles. Cytoplasmic ER at metaphase stage demonstrated a typical sheet structure. At anaphase I and II, ER dispersed to a tubular structure (Fig 5D). Also, the dramatic morphological change of ER coincides with the concentration and dispersion of GFP::GCN4-pLI during meiosis (Video 1, available upon request).

It has been shown that free tubulin in spindle region during early mitosis is 2 times as concentrated as in cytoplasm. We wondered if this also pairs with ER changes. Similarly, dense ER sheets delimit the concentration of GFP::GCN4-pLI at Metaphase and disperse when GFP::GCN4-pLI diffuse at Anaphase during the first and second mitosis (Video 2, available upon request). This suggests the concentration of free tubulin

enclosed by ER may be a prevalent mechanism to promote spindle formation in both meiosis and mitosis.

**ER sheets between the metaphase meiotic spindle and cytoplasm form a barrier to vesicles and mitochondria, but not to ribosomes.**

It is often stated that cytoplasm is like busy streets full of organelles, cytoskeleton, and protein synthesis machinery, mainly ribosomes. This cytoplasmic environment accelerates or slows down certain cellular processes by attuning molecular concentrations or molecular movements. *C. elegans* ooplasm is filled with yolk granules, lipid droplets, and mitochondria and others (Chen et al., 2020). GFP::VIT-2 encodes *C. elegans* yolk proteins Vitellogenin YP170B (Depina et al., 2011). GFP::VIT-2 is highly expressed in meiotic embryo but is excluded from the meiotic spindle by the ER. The exclusion is slightly alleviated during anaphase I and II when ER disperses (Fig 5D). The exclusion of yolk proteins from the meiotic spindle is stereotypical in meiotic embryos although the functional significance remains unclear. Similarly, GFP tagged mitochondrial inner membrane protein COX-4 (GFP::COX-4) are also highly expressed and excluded from the meiotic spindle (Fig 5E; Raiders et al., 2018). PLIN-1 labelled liquid droplets tagged with GFP (GFP::PLIN-1) are also highly expressed in oocytes (Fig 5F; Na et al., 2015).

In meiotic embryos reconstituted from electron tomographs, the sheet-like ER at metaphase and tubular-like ER at anaphase are beautifully revealed (Fig 6A-D, Video 3, 4, available upon request). At metaphase II, vesicles and mitochondria are excluded from the chromosomes by dense ER sheets (Fig 6A-B, Video 3). At anaphase I, vesicles and mitochondria are no longer excluded by dispersed tubular-like ER, invading anaphase

spindle region (Fig 6C-D, Video 4). Interestingly, ribosomes, also abundant in cytoplasm, are roughly equally distributed in the spindle region and the cytoplasm at metaphase I and metaphase II, suggesting ER sheets between metaphase spindle and the cytoplasm only excludes vesicles and mitochondria but not ribosomes (Fig 6E). This is consistent with GFP tagged ribosomes subunit rpl-29 (GFP::RPL-29) evening between the nucleus and the cytoplasm upon ovulation in 9/9 time-lapse sequences (Fig 6F).

### **The concentration of molecules during GVBD is size dependent.**

In immature starfish oocytes, fluorescent dextrans of 25 kDa or larger are excluded from the nucleus (Lénárt et al., 2003), similar to our results with GFP::tubulin, GFP::GCN4pLI and GFP::TBA-2(T349E), presumably because they are too large to diffuse freely through NPCs. In contrast, 10 kDa fluorescent dextrans accumulated in the nucleus of immature starfish oocytes at a concentration twice that of the cytoplasm (Lénárt et al., 2003). It was suggested that this is because the small dextrans diffuse freely through NPCs and because yolk granules occupy 50% of the cytoplasmic volume thus driving apparent concentration of small dextrans in the nucleus (Lénárt et al., 2003). We found that a 36 kDa monomeric GFP concentrated in *C. elegans* oocyte nuclei before GVBD (Fig. 7A, B) to a concentration twice that of the cytoplasm (Fig. 7D), like 10 kDa dextrans in starfish oocytes. To rule out the possibility that this might be mediated by a cryptic NLS on GFP, we expressed a 34 kDa monomeric HALO tag in the *C. elegans* germline, which also concentrated to a 2-fold higher concentration in the nucleus relative to the cytoplasm in diakinesis oocytes prior to GVBD (Fig 7C-E).

These results suggested that the same mechanisms driving concentration of larger proteins during GVBD might be responsible for the concentration of smaller proteins after

GVBD. However, monomeric HALO tag did not stay concentrated after GVBD and instead diffused to a 1:1 fluorescence ratio inside and outside the spindle envelope (Fig. 7E-F). The monomeric HALO tag did not grossly perturb meiotic progression (Fig. 5E) in 12/12 time-lapse sequences. These results suggested that there might be a size-dependence for concentration of proteins in the nuclear volume during meiotic spindle assembly.

### **Molecule movement during GVBD is charge dependent.**

Although the tubulin-sized molecules that concentrated in the nuclear volume at GVBD are larger than the smaller HALO tag that quickly dispersed to a 1:1 ratio between nuclear and cytoplasmic volumes at GVBD, these proteins also differ in net charge (Fig. 7A), with the concentrating proteins more negative than the dispersing protein. One possibility is that electrostatic interactions of molecules with different local environments in the nucleus vs the cytoplasm might drive accumulation in the nuclear volume. To test this, we added arginines to tetrameric GFP to either neutralize net charge or add a net positive charge to GFP::GCN4-pLI. Similar to tetrameric GFP, GFP::GCN4-pLI with neutral or positive charges were excluded from the nucleus before GVBD (Fig 8A-D; -10 min). GFP::GCN4-pLI (neutral charge) remained excluded from the nuclear volume at GVBD for a longer period of time after histone leakage out of the nucleus than negatively charged GFP::GCN4-pLI and exhibited only a slight accumulation in the nuclear volume (~7min after GVBD onset) (Fig 8A, 8C), a significant delay compared to GFP::GCN4-pLI with negative charges (~2min after GVBD onset, Fig 4C). GFP::GCN4-pLI (positive charge) remained excluded from the nuclear volume for an even longer period after GVBD (Fig 8B, 8D). This result suggested that proteins with negative charge concentrate in the nuclear volume at GVBD whereas proteins with neutral or positive charges do not.

## Discussion and future directions

Our data suggests that the ran pathway is dispensable for spindle formation but is essential for chromosome segregation during meiosis. Free tubulin concentrated in the nuclear volume during and after GVBD in *C. elegans* oocytes treated with nocodazole recapitulating what has been reported in *C. elegans* mitotic cells and *Drosophila* S2 cells (Baumgart et al., 2019; Hayashi et al., 2012; Schweizer et al., 2015). The concentration of tubulin-sized molecules: tetrameric GFP and un-polymerizable tubulin in the nuclear volume further confirms that it is polymerization independent.

Furthermore, tetrameric GFP and un-polymerizable tubulin concentrated in metaphase II spindle region when nuclear pore protein NPP-6 and nuclear lamina are absent. We have shown that this concentration is instead enclosed by dense ER sheets, which later disperse at anaphase when tetrameric GFP evens out.

The *C. elegans* ooplasm is populated with yolk granules, lipid droplets, mitochondria, ribosomes, and others. During metaphase, they are excluded from the meiotic spindle by ER sheets. It is not clear why the ER morphology changes dramatically and periodically from metaphase to anaphase, but in addition to protein production, we think that ER might function as a selective barrier, preventing cytoplasmic organelles from perturbing metaphase spindle formation. However, tubulin dimers, at this stage, are free to travel through the barrier of ER. Without membrane organelles, the nucleus volume provides more available space for tubulin, thus driving the concentration of tubulin in the nuclear volume, referred as “volume exclusion model” by previous studies (Schweizer et al., 2015). If this volume exclusion model by ER is true, disrupting ER during GVBD or metaphase might lead to defects in spindle formation and chromosome segregation. We



are currently working on disrupting ER by knocking down ATX-2 via Auxin-Induced-Degradation and testing whether it will affect concentration of tetrameric GFP. ATX-2 is the *C. elegans* ortholog of human Ataxin-2, related to the late-onset neurodegenerative disease Spinocerebellar ataxia type-2 (SCA2). Loss of ATX-2 in *C. elegans* results in collapse of ER in the germline (Ciosk et al., 2004; del Castillo et al., 2022). It is unclear whether the ER sheets around the metaphase spindle and exclusion of cytoplasm organelles will be abolished in ATX-2 mutant. Another way to disrupt ER is by laser-blazing the ER around the forming spindle. Problems that might come with this are: 1) laser operation during ovulation can be challenging; 2) the oocyte might arrest after laser ablation.

It is interesting whether the same mechanism exists in aged oocytes or oocytes used for IVF where ER stress is present. Understanding the mechanisms of how ER affects spindle formation could provide insights on drug development to reduce meiotic errors and increase success rate in assisted reproduction (Schwarz and Blower, 2015).

In the volume exclusion model, the size of the molecules is the key. With the barrier of nuclear envelope before GVBD, monomeric GFP or HALO tag without NLS are not excluded from the nucleus possibly because they are small enough to diffuse through the nuclear pores. It is surprising why they even out instead of concentrating more as tubulin does after GVBD. One explanation is that after GVBD, volume exclusion affects molecules with various sizes differently. While the nuclear volume grants more available space to tubulin-sized molecules, it makes no difference to smaller molecules like monomeric Halo Tag. We also tried to make ribosome-sized molecules, which will tell us

how volume exclusion would affect bigger molecules. However, it is not evenly distributed in the oocyte cytoplasm as other probes we have showed in this study.

Although the tubulin-sized molecules exhibit higher fluorescence intensity in the nuclear volume, it does not necessarily mean it has higher concentration in the nuclear volume than in the cytoplasm. Despite this, the crowded cytoplasm environment might be unfavorable for microtubule polymerization by promoting microtubule catastrophe while the nuclear volume with more open space has less restrictions for microtubule polymerization and spindle formation, even when the concentration of tubulin is same inside and out of the nuclear volume.

Finally, we have shown that concentration of free tubulin is not just size-dependent. Tetrameric GFP with negative charge are more concentrated than tetrameric GFP with positive charge or neutral charge during GVBD. It remains unclear why negatively charged molecules are favored to get in. The cytoplasmic faces of cytoplasmic organelles are thought to be negatively charged due to phosphoinositides and phosphatidylserine (PtdSer). A recent study mapping the electrostatic profile of cellular membranes suggests that plasma membrane, ER, mitochondria, Golgi are all negatively charged in HeLa cells (Eisenberg et al., 2021; average surface potential ranging from -14mV to -35mV). The negatively charged lipid heads will have counterions neutralizing these charges. However, it is possible the negative surface charge of cellular membranes in oocytes like ER, mitochondria might act like cation exchange chromatography beads, causing transient binding of counterions such as tetrameric GFP with positive charges, restraining them from getting into the nuclear volume. It will be interesting to determine whether monomeric Halo tag with positive charge will still concentrate in the immature oocytes.

## Materials and Methods

### C. *elegans* strains and maintenance

Worms used in this study were maintained under standard laboratory conditions. The strains used in this study and their sources are listed below:

Strain name	Genotype	Source
FM917	<i>fxls1</i> [ <i>pie-1p::TIR1::mRuby</i> , <i>l:2851009</i> ] I; <i>ltls37</i> [ <i>pAA64</i> ; <i>pie-1p::mCh::his-58 + unc-119(+)</i> ]; <i>ruls57</i> [ <i>pie-1p::GFP::tubulin + unc-119(+)</i> ] V	This study
FM1054	<i>fxls1</i> [ <i>pie-1p::TIR1::mRuby</i> , <i>l:2851009</i> ] I; <i>ran-3</i> ( <i>syb7781</i> [ <i>ran-3-3xGAS-AID-3xGAS-HALO</i> ]) II; <i>ltls37</i> [ <i>pAA64</i> ; <i>pie-1p::mCh::his-58 + unc-119(+)</i> ]; <i>ruls57</i> [ <i>pie-1p::GFP::tubulin + unc-119(+)</i> ] V	This study
FM1056	<i>fxls1</i> [ <i>pie-1p::TIR1::mRuby</i> , <i>l:2851009</i> ] I; <i>ran-2</i> ( <i>syb7819</i> [ <i>ran-2-3xGAS-AID-3xGAS-HALO</i> ]) III; <i>ltls37</i> [ <i>pAA64</i> ; <i>pie-1p::mCh::his-58 + unc-119(+)</i> ]; <i>ruls57</i> [ <i>pie-1p::GFP::tubulin + unc-119(+)</i> ] V	This study
FM971	[ <i>GFP(SMU)-GCN4-pLi</i> ] II; <i>ltls37</i> [ <i>pAA64</i> ; <i>pie-1p::mCh::his-58 + unc-119(+)</i> ]; <i>him-8</i> ( <i>e1489</i> )	This study
FM1011	[ <i>GFP(SMU)::tba-2(T349E)</i> ] II <i>ltls37</i> [ <i>pAA64</i> ; <i>pie-1p::mCh::his-58 + unc-119(+)</i> ]; <i>him-8</i> ( <i>e1489</i> )	This study
FM628	<i>unc-119</i> ( <i>ed3</i> ) III; <i>ItSi464</i> [ <i>pNH103</i> ; <i>Pmex-5::npp6::GFP::tbb-2 3'UTR</i> ; <i>cbunc-119(+)</i> ] I; <i>ltls37</i> [ <i>pAA64</i> ; <i>pie-1::mCherry::his-58</i> ; <i>unc-119 (+)</i> ] IV	A gift from Oegema- Desai Lab
BN359	<i>ima-2(ok256)</i> I/hT2[ <i>bli-4</i> ( <i>e937</i> ) <i>let-?</i> ( <i>q782</i> ) <i>qls48</i> ] (I,III); <i>qals3502</i> [ <i>pie-1p::YFP::lmn-1 + pie-1p::CFP::H2B +</i> <i>unc-119(+)</i> ]	CGC
FM991	<i>wjls76</i> [ <i>Cn_unc-119(+)</i> ; <i>pie-1p::mKate2::tba-2</i> ]; <i>vit-2</i> ( <i>crg9070</i> [ <i>vit-2::gfp</i> ]) X; <i>egxSi126</i> [ <i>mex-5p::hsp-3(aa 1-19)::halotag::HDEL::pie-1 3'UTR+ unc-119(+)</i> ] I. "	This study
FM691	<i>cox-4</i> ( <i>zu476</i> [ <i>cox-4::eGFP::3xFLAG</i> ]) I; <i>wjls76</i> [ <i>Cn_unc-119(+)</i> ; <i>pie-1p::mKate2::tba-2</i> ]	This study
FM1077	<i>hj178</i> [ <i>plin-1a/c::GFP_TEV_3xFLAG</i> ] I; <i>ltls44</i> <i>pAA173</i> ; [ <i>pie-1p-mCh::PH(PLC1delta 1) + unc-119(+)</i> ]V; <i>vit-2</i> ( <i>syb5705</i> [ <i>halo-tag</i> ])X (A); <i>wjls76</i> [ <i>Cn_unc-119(+)</i> ; <i>pie-1p::mKate2::tba-2</i> ]"	This study
CZ18550	<i>juSi123</i> [ <i>rpl-29::GFP</i> ] II; <i>rpl-29</i> ( <i>tm3555</i> ) IV	CGC

FM1103	<i>[halo(smu)] II;</i> <i>ruls57 [pie-1p::GFP::tubulin + unc-119(+)] V</i> <i>itls37 [pie-1p::mCh::H2B::pie-1 3'UTR + unc-119(+)]</i> <i>IV"</i>	This study
FM1168	<i>[plus7-GFP(SMU)::GCn4-pLI] II;</i> <i>itls37[pAA64; pie-1::mCherry::his-58; unc-119 (+)] IV</i>	Neutral Charge; this study
FM1169	<i>[plus21-GFP(SMU)::GCn4-pLI] II;</i> <i>itls37[pAA64; pie-1::mCherry::his-58; unc-119 (+)] IV</i>	Positive Charge; this study

### ***Drug treatment***

For nocodazole treatment, 5mg/ml stock nocodazole solution (Sigma-Aldrich, St. Louis, MO, dissolved in 100% DMSO) was diluted into tricaine/tetramisole anesthetics to 5ug/ml just before adding to worms for live imaging. 100% DMSO without nocodazole were diluted in the same way for control treatment.

### ***Live imaging and Statistical Analysis***

Worms were anesthetized with tricaine/tetramisole as described (Kirby et al. 1990; McCarter et al. 1999) and gently mounted between a coverslip and a thin 2% agarose pad on a slide. All live imaging were captured with a Solamere Spinning Disk Confocal equipped with a Yokogawa CSU10, Hamamatsu Orca FLASH 4.0 cMOS and an Olympus 100x 1.35 oil objective. For measuring fluorescence intensity or nucleus sizes (in Fig 2A-C; Fig 7B-C; Fig S1A), z-stack images were taken in 1-micron step size to capture the center of nucleus for measurements. For time-lapse movies of GVBD and meiosis, images were captured every 30s. The fluorescence intensity in the background (where there was no worm) were subtracted before the fluorescence in the nucleus or cytoplasm before quantification.

## References

- Angell RR. 1991. Predivision in human oocytes at meiosis I: a mechanism for trisomy formation in man. *Hum Genet* **86**:383–387. doi:10.1007/BF00201839
- Askjaer P, Galy V, Hannak E, Mattaj IW. 2002. Ran GTPase cycle and importins alpha and beta are essential for spindle formation and nuclear envelope assembly in living *Caenorhabditis elegans* embryos. *Mol Biol Cell* **13**:4355–4370. doi:10.1091/MBC.E02-06-0346
- Baumgart J, Kirchner M, Redemann S, Bond A, Woodruff J, Verbavatz J-M, Jülicher F, Müller-Reichert T, Hyman AA, Brugués J. 2019. Soluble tubulin is significantly enriched at mitotic centrosomes. *J Cell Biol* **218**:3977–3985. doi:10.1083/jcb.201902069
- Bennabi I, Terret ME, Verlhac MH. 2016. Meiotic spindle assembly and chromosome segregation in oocytes. *J Cell Biol* **215**:611–619. doi:10.1083/JCB.201607062
- Bornens M. 2012. The centrosome in cells and organisms. *Science (80- )* **335**:422–426. doi:10.1126/SCIENCE.1209037
- Carazo-Salas RE, Guarguaglini G, Gruss OJ, Segref A, Karsenti E, Mattaj LW. 1999. Generation of GTP-bound Ran by RCC1 is required for chromatin-induced mitotic spindle formation. *Nat 1999 4006740* **400**:178–181. doi:10.1038/22133
- Cesario J, McKim KS. 2011. RanGTP is required for meiotic spindle organization and the initiation of embryonic development in *Drosophila*. *J Cell Sci* **124**:3797–3810. doi:10.1242/JCS.084855
- Chen WW, Lemieux GA, Camp CH, Chang TC, Ashrafi K, Cicerone MT. 2020. Spectroscopic coherent Raman imaging of *Caenorhabditis elegans* reveals lipid

- particle diversity. *Nat Chem Biol* **16**:1087. doi:10.1038/S41589-020-0565-2
- Chuang CH, Schlientz AJ, Yang J, Bowerman B. 2020. Microtubule assembly and pole coalescence: Early steps in *Caenorhabditis elegans* oocyte meiosis I spindle assembly. *Biol Open* **9**. doi:10.1242/BIO.052308
- Ciosk R, DePalma M, Priess JR. 2004. ATX-2, the *C. elegans* ortholog of ataxin 2, functions in translational regulation in the germline. *Development* **131**:4831–4841. doi:10.1242/DEV.01352
- Colombié N, Głuszek AA, Meireles AM, Ohkura H. 2013. Meiosis-Specific Stable Binding of Augmin to Acentrosomal Spindle Poles Promotes Biased Microtubule Assembly in Oocytes. *PLOS Genet* **9**:e1003562. doi:10.1371/JOURNAL.PGEN.1003562
- Conduit PT, Wainman A, Raff JW. 2015. Centrosome function and assembly in animal cells. *Nat Rev Mol Cell Biol* **16**:611–624. doi:10.1038/nrm4062
- del Castillo U, Norkett R, Lu W, Serpinskaya A, Gelfand VI. 2022. Ataxin-2 is essential for cytoskeletal dynamics and neurodevelopment in *Drosophila*. *iScience* **25**. doi:10.1016/J.ISCI.2021.103536
- Depina AS, Iser WB, Park SS, Maudsley S, Wilson MA, Wolkow CA. 2011. Regulation of *Caenorhabditis elegans* vitellogenesis by DAF-2/IIS through separable transcriptional and posttranscriptional mechanisms. *BMC Physiol* **11**:1–12. doi:10.1186/1472-6793-11-11
- Drutovic D, Duan X, Li R, Kalab P, Solc P. 2020. RanGTP and importin  $\beta$  regulate meiosis I spindle assembly and function in mouse oocytes. *EMBO J* **39**:e101689. doi:10.15252/EMBJ.2019101689
- Dumont J, Desai A. 2012. Acentrosomal spindle assembly and chromosome segregation

- during oocyte meiosis. *Trends Cell Biol* **22**:241–249. doi:10.1016/j.tcb.2012.02.007
- Eisenberg S, Haimov E, Walpole GFW, Plumb J, Kozlov MM, Grinstein S. 2021. Mapping the electrostatic profiles of cellular membranes. *Mol Biol Cell* **32**:301–310. doi:10.1091/MBC.E19-08-0436
- Fair T, Lonergan P. 2023. The oocyte: the key player in the success of assisted reproduction technologies. *Reprod Fertil Dev*. doi:10.1071/RD23164
- Galy V, Mattaj IW, Askjaer P. 2003. Caenorhabditis elegans Nucleoporins Nup93 and Nup205 Determine the Limit of Nuclear Pore Complex Size Exclusion In Vivo. *Mol Biol Cell* **14**:5104. doi:10.1091/MBC.E03-04-0237
- Goshima G, Mayer M, Zhang N, Stuurman N, Vale RD. 2008. Augmin: A protein complex required for centrosome-independent microtubule generation within the spindle. *J Cell Biol* **181**:421–429. doi:10.1083/JCB.200711053
- Gruss OJ. 2018. Animal Female Meiosis: The Challenges of Eliminating Centrosomes. *Cells* 2018, Vol 7, Page 73 **7**:73. doi:10.3390/CELLS7070073
- Hayashi H, Kimura K, Kimura A. 2012. Localized accumulation of tubulin during semi-open mitosis in the Caenorhabditis elegans embryo. *Mol Biol Cell* **23**:1688–1699. doi:10.1091/MBC.E11-09-0815
- Heald R, Tournebize R, Habermann A, Karsenti E, Hyman A. 1997. Spindle Assembly in Xenopus Egg Extracts: Respective Roles of Centrosomes and Microtubule Self-Organization. *J Cell Biol* **138**:615–628. doi:10.1083/JCB.138.3.615
- Hetzer M, Gruss OJ, Mattaj IW. 2002. The Ran GTPase as a marker of chromosome position in spindle formation and nuclear envelope assembly. *Nat Cell Biol* 2002 **4**:E177–E184. doi:10.1038/ncb0702-e177

- Hinchcliffe EH. 2014. Centrosomes and the Art of Mitotic Spindle Maintenance. *Int Rev Cell Mol Biol* **313**:179–217. doi:10.1016/B978-0-12-800177-6.00006-2
- Johnson V, Ayaz P, Huddleston P, Rice LM. 2011. Design, Overexpression, and Purification of Polymerization-Blocked Yeast  $\alpha\beta$ -Tubulin Mutants. *Biochemistry* **50**:8636–8644. doi:10.1021/BI2005174
- Kalab P, Pu RT, Dasso M. 1999. The Ran GTPase regulates mitotic spindle assembly. *Curr Biol* **9**:481–484. doi:10.1016/S0960-9822(99)80213-9
- Kellogg DR, Moritz M, Alberts BM. 2003. THE CENTROSOME AND CELLULAR ORGANIZATION. <https://doi.org/10.1146/annurev.bi63070194003231> **63**:639–674. doi:10.1146/ANNUREV.BI.63.070194.003231
- Khodjakov A, Cole RW, Oakley BR, Rieder CL. 2000. Centrosome-independent mitotic spindle formation in vertebrates. *Curr Biol* **10**:59–67. doi:10.1016/S0960-9822(99)00276-6
- Kim S, Spike C, Greenstein D. 2013. Control of Oocyte Growth and Meiotic Maturation in *C. elegans*. *Adv Exp Med Biol* **757**:277–320. doi:10.1007/978-1-4614-4015-4\_10
- Kimura K, Mamane A, Sasaki T, Sato K, Takagi J, Niwayama R, Hufnagel L, Shimamoto Y, Joanny JF, Uchida S, Kimura A. 2017. Endoplasmic-reticulum-mediated microtubule alignment governs cytoplasmic streaming. *Nat Cell Biol* **2017** **19**:399–406. doi:10.1038/ncb3490
- Kline-Smith SL, Walczak CE. 2004. Mitotic Spindle Assembly and Chromosome Segregation: Refocusing on Microtubule Dynamics. *Mol Cell* **15**:317–327. doi:10.1016/J.MOLCEL.2004.07.012
- Lawo S, Bashkurov M, Mullin M, Ferreria MG, Kittler R, Habermann B, Tagliaferro A,



- Poser I, Hutchins JRA, Hegemann B, Pinchev D, Buchholz F, Peters JM, Hyman AA, Gingras AC, Pelletier L. 2009. HAUS, the 8-subunit human Augmin complex, regulates centrosome and spindle integrity. *Curr Biol* **19**:816–826. doi:10.1016/J.CUB.2009.04.033
- Lénárt P, Rabut G, Daigle N, Hand AR, Terasaki M, Ellenberg J. 2003. Nuclear envelope breakdown in starfish oocytes proceeds by partial NPC disassembly followed by a rapidly spreading fenestration of nuclear membranes. *J Cell Biol* **160**:1055–1068. doi:10.1083/jcb.200211076
- Li X, Qin Y, Wilsher S, Allen WR. 2006. Centrosome changes during meiosis in horse oocytes and first embryonic cell cycle organization following parthenogenesis, fertilization and nuclear transfer. *Reproduction* **131**:661–667. doi:10.1530/REP.1.00795
- McNally K, Audhya A, Oegema K, McNally FJ. 2006. Katanin controls mitotic and meiotic spindle length. *J Cell Biol* **175**:881–891. doi:10.1083/jcb.200608117
- McNally KP, Beath EA, Danlasky BM, Barroso C, Gong T, Li W, Martinez-Perez E, McNally FJ. 2022. Cohesin is required for meiotic spindle assembly independent of its role in cohesion in *C. elegans*. *PLOS Genet* **18**:e1010136. doi:10.1371/JOURNAL.PGEN.1010136
- Métivier M, Gallaud E, Thomas A, Pascal A, Gagné JP, Poirier GG, Chrétien D, Gibeaux R, Richard-Parpaillon L, Benaud C, Giet R. 2021. Drosophila Tubulin-Specific Chaperone E Recruits Tubulin around Chromatin to Promote Mitotic Spindle Assembly. *Curr Biol* **31**:684-695.e6. doi:10.1016/J.CUB.2020.11.009
- Mikeladze-Dvali T, von Tobel L, Strnad P, Knott G, Leonhardt H, Schermelleh L, Gönczy

- P. 2012. Analysis of centriole elimination during *C. elegans* oogenesis. *Development* **139**:1670–1679. doi:10.1242/DEV.075440
- Mittl PRE, Deillon C, Sargent D, Liu N, Klauser S, Thomas RM, Gutte B, Grütter MG. 2000. The retro-GCN4 leucine zipper sequence forms a stable three-dimensional structure. *Proc Natl Acad Sci U S A* **97**:2562–2566. doi:10.1073/PNAS.97.6.2562
- Mullen TJ, Davis-Roca AC, Wignall SM. 2019. Spindle assembly and chromosome dynamics during oocyte meiosis. *Curr Opin Cell Biol* **60**:53–59. doi:10.1016/J.CEB.2019.03.014
- Mullen TJ, Wignall SM. 2017. Interplay between microtubule bundling and sorting factors ensures acentriolar spindle stability during *C. elegans* oocyte meiosis. *PLoS Genet* **13**. doi:10.1371/journal.pgen.1006986
- Na H, Zhang P, Chen Y, Zhu X, Liu Yi, Liu Yangli, Xie K, Xu N, Yang F, Yu Y, Cichello S, Mak HY, Wang MC, Zhang H, Liu P. 2015. Identification of lipid droplet structure-like/resident proteins in *Caenorhabditis elegans*. *Biochim Biophys Acta - Mol Cell Res* **1853**:2481–2491. doi:10.1016/J.BBAMCR.2015.05.020
- Nasmyth K. 2002. Segregating sister genomes: The molecular biology of chromosome separation. *Science (80- )* **297**:559–565. doi:10.1126/science.1074757
- Petry S. 2016. Mechanisms of Mitotic Spindle Assembly. <https://doi.org/10.1146/annurev-biochem-060815-014528> **85**:659–683. doi:10.1146/ANNUREV-BIOCHEM-060815-014528
- Petry S, Pugieux C, Nédélec FJ, Vale RD. 2011. Augmin promotes meiotic spindle formation and bipolarity in *Xenopus* egg extracts. *Proc Natl Acad Sci U S A* **108**:14473–14478. doi:10.1073/PNAS.1110412108

- Prosser SL, Pelletier L. 2017. Mitotic spindle assembly in animal cells: a fine balancing act. *Nat Rev Mol Cell Biol* 2017 183 **18**:187–201. doi:10.1038/nrm.2016.162
- Raiders SA, Eastwood MD, Bacher M, Priess JR. 2018. Binucleate germ cells in *Caenorhabditis elegans* are removed by physiological apoptosis. *PLoS Genet* **14**. doi:10.1371/JOURNAL.PGEN.1007417
- Sánchez-Huertas C, Lüders J. 2015. The Augmin Connection in the Geometry of Microtubule Networks. *Curr Biol* **25**:R294–R299. doi:10.1016/J.CUB.2015.02.006
- Sanchez AD, Feldman JL. 2017. Microtubule-organizing centers: from the centrosome to non-centrosomal sites. *Curr Opin Cell Biol* **44**:93–101. doi:10.1016/J.CEB.2016.09.003
- Schuh M, Ellenberg J. 2007. Self-Organization of MTOCs Replaces Centrosome Function during Acentrosomal Spindle Assembly in Live Mouse Oocytes. *Cell* **130**:484–498. doi:10.1016/J.CELL.2007.06.025
- Schwarz DS, Blower MD. 2015. The endoplasmic reticulum: structure, function and response to cellular signaling. *Cell Mol Life Sci* 2015 731 **73**:79–94. doi:10.1007/S00018-015-2052-6
- Schweizer N, Pawar N, Weiss M, Maiato H. 2015. An organelle-exclusion envelope assists mitosis and underlies distinct molecular crowding in the spindle region. *J Cell Biol* **210**:695–704. doi:10.1083/jcb.201506107
- Thomas C, Cavazza T, Schuh M. 2021. Aneuploidy in human eggs: contributions of the meiotic spindle. *Biochem Soc Trans* **49**:107–118. doi:10.1042/BST20200043
- Uehara R, Nozawa RS, Tomioka A, Petry S, Vale RD, Obuse C, Goshima G. 2009. The augmin complex plays a critical role in spindle microtubule generation for mitotic

- progression and cytokinesis in human cells. *Proc Natl Acad Sci U S A* **106**:6998–7003. doi:10.1073/PNAS.0901587106
- Wang G, Jiang Q, Zhang C. 2014. The role of mitotic kinases in coupling the centrosome cycle with the assembly of the mitotic spindle. *J Cell Sci* **127**:4111–4122. doi:10.1242/JCS.151753
- Wesolowska N, Avilov I, Machado P, Geiss C, Kondo H, Mori M, Lénárt P. 2020. Actin assembly ruptures the nuclear envelope by prying the lamina away from nuclear pores and nuclear membranes in starfish oocytes. *Elife* **9**. doi:10.7554/eLife.49774
- Wu T, Dong J, Fu J, Kuang Y, Chen B, Gu H, Luo Y, Gu R, Zhang M, Li W, Dong X, Sun X, Sang Q, Wang L. 2022. The mechanism of acentrosomal spindle assembly in human oocytes. *Science (80- )* **378**. doi:10.1126/SCIENCE.ABQ7361
- Yao C, Rath U, Maiato H, Sharp D, Girton J, Johansen KM, Johansen J. 2012. A nuclear-derived proteinaceous matrix embeds the microtubule spindle apparatus during mitosis. *Mol Biol Cell* **23**:3532–3541. doi:10.1091/MBC.E12-06-0429
- Zhang L, Ward JD, Cheng Z, Dernburg AF. 2015. The auxin-inducible degradation (AID) system enables versatile conditional protein depletion in *C. elegans*. *Dev* **142**:4374–4384. doi:10.1242/DEV.129635

## Figures

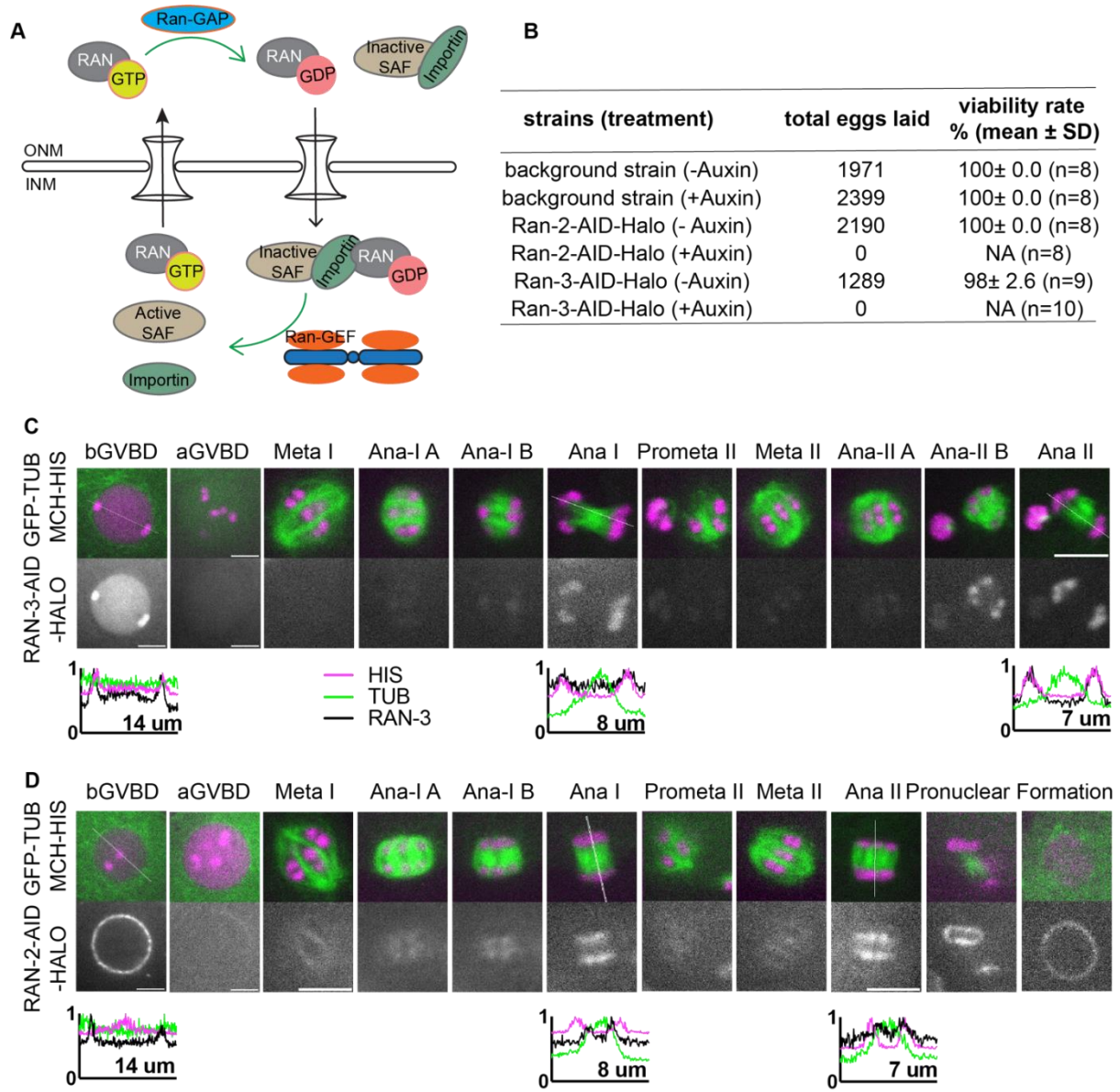


Fig 1. RAN-3 and RAN-2 in meiotic embryos/RAN-3 and RAN-2 associate with chromosomes during meiotic cell division.

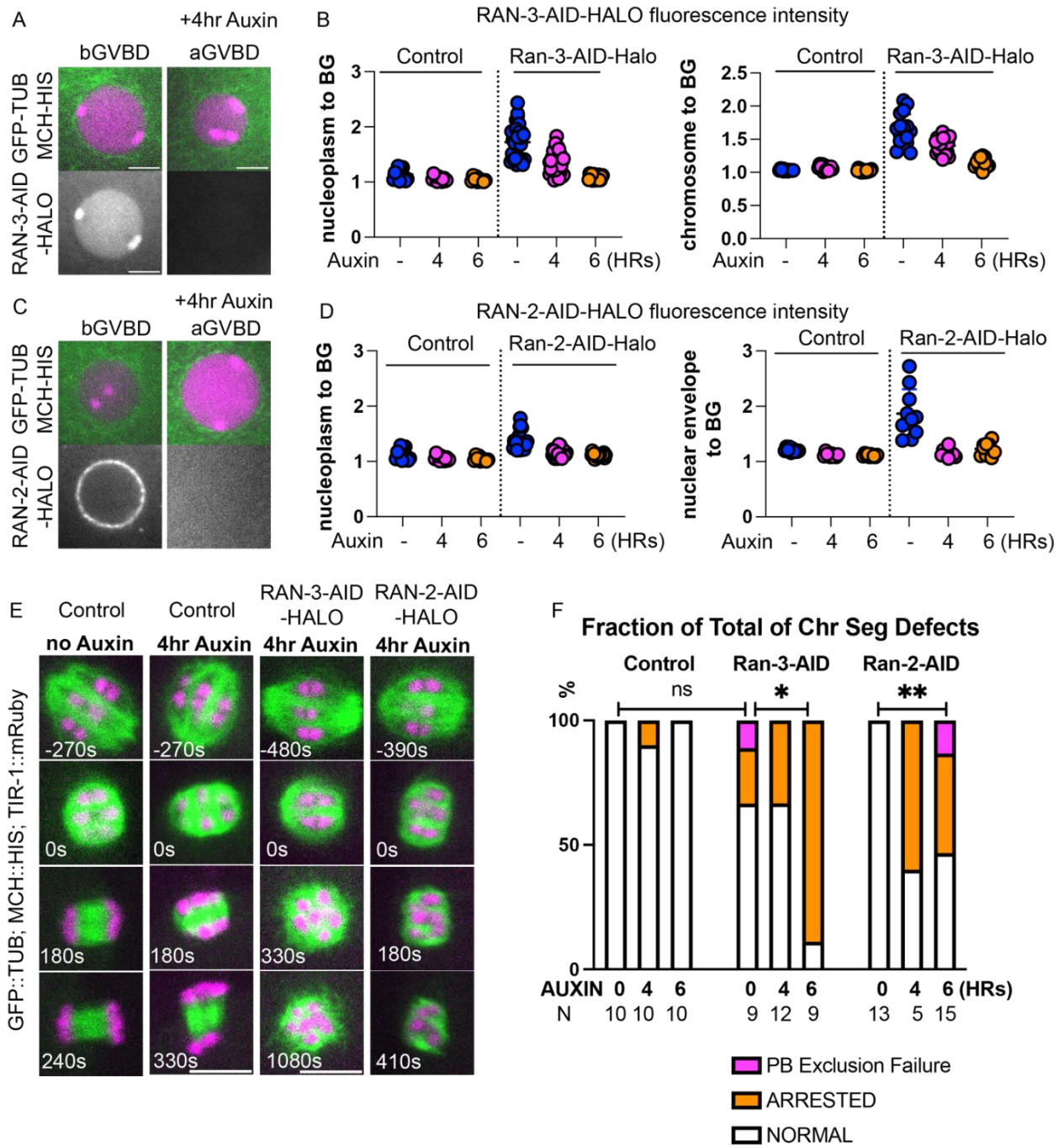


Fig 2. Ran-GEF and Ran-GAP are required for meiotic chromosome segregation but not for meiotic spindle initiation.

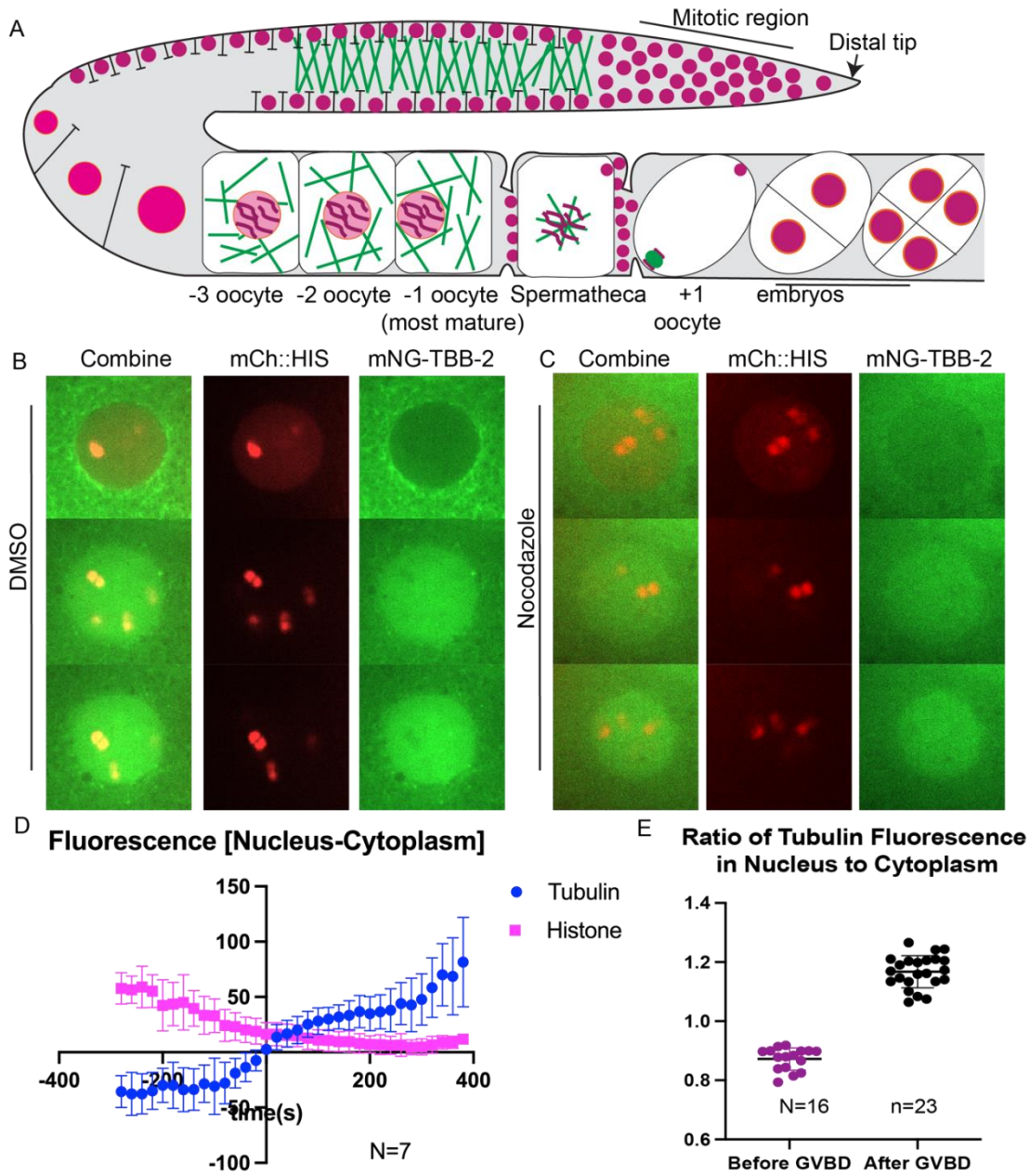


Fig 3. Ran-GEF and Ran-GAP are required for meiotic chromosome segregation but not metaphase I spindle formation.

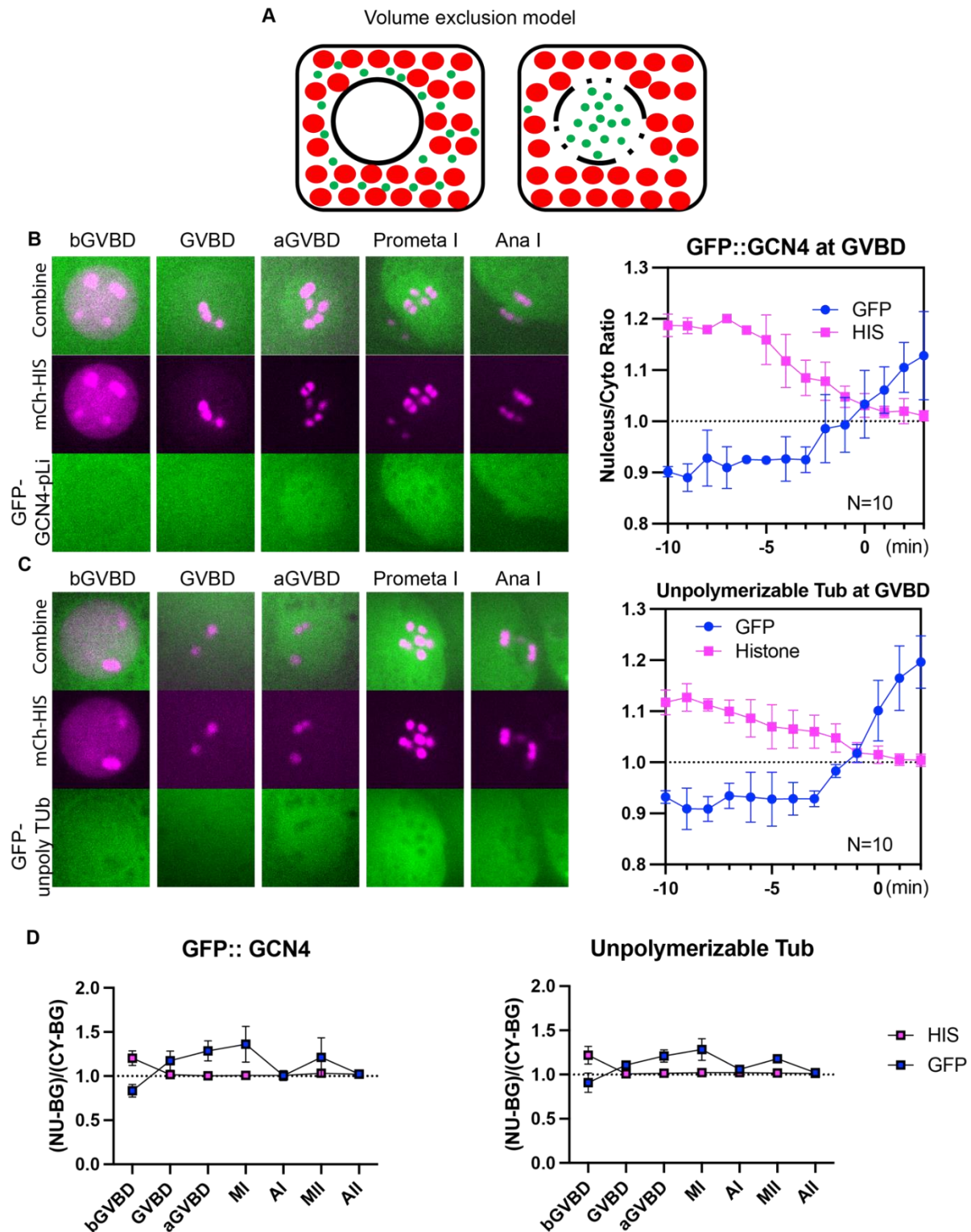


Fig 4. Free tubulin is concentrated in the nuclear volume at GVBD.



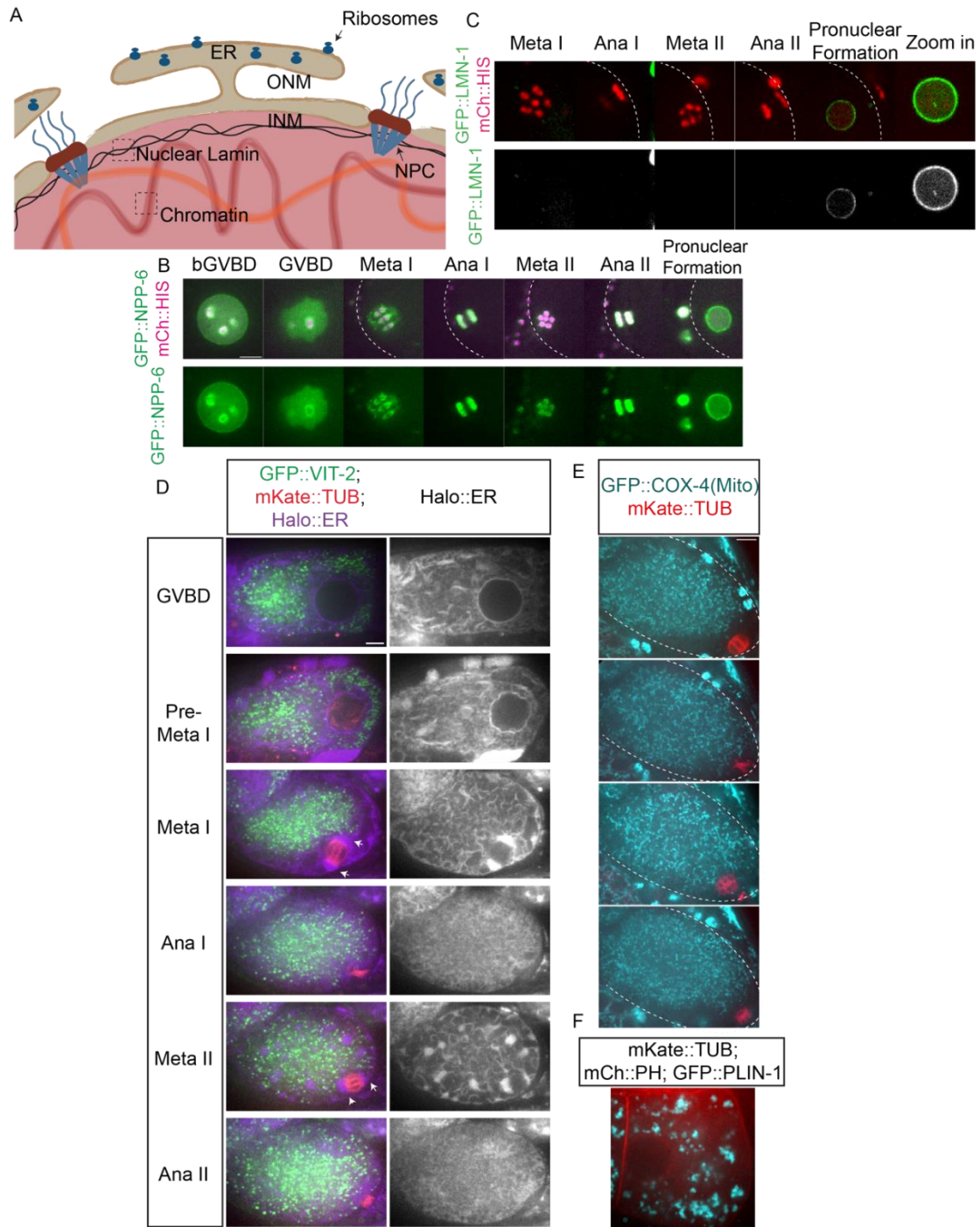


Fig 5. The ER instead of the nuclear envelope delimits the accumulation of free tubulin during meiosis and early mitosis.

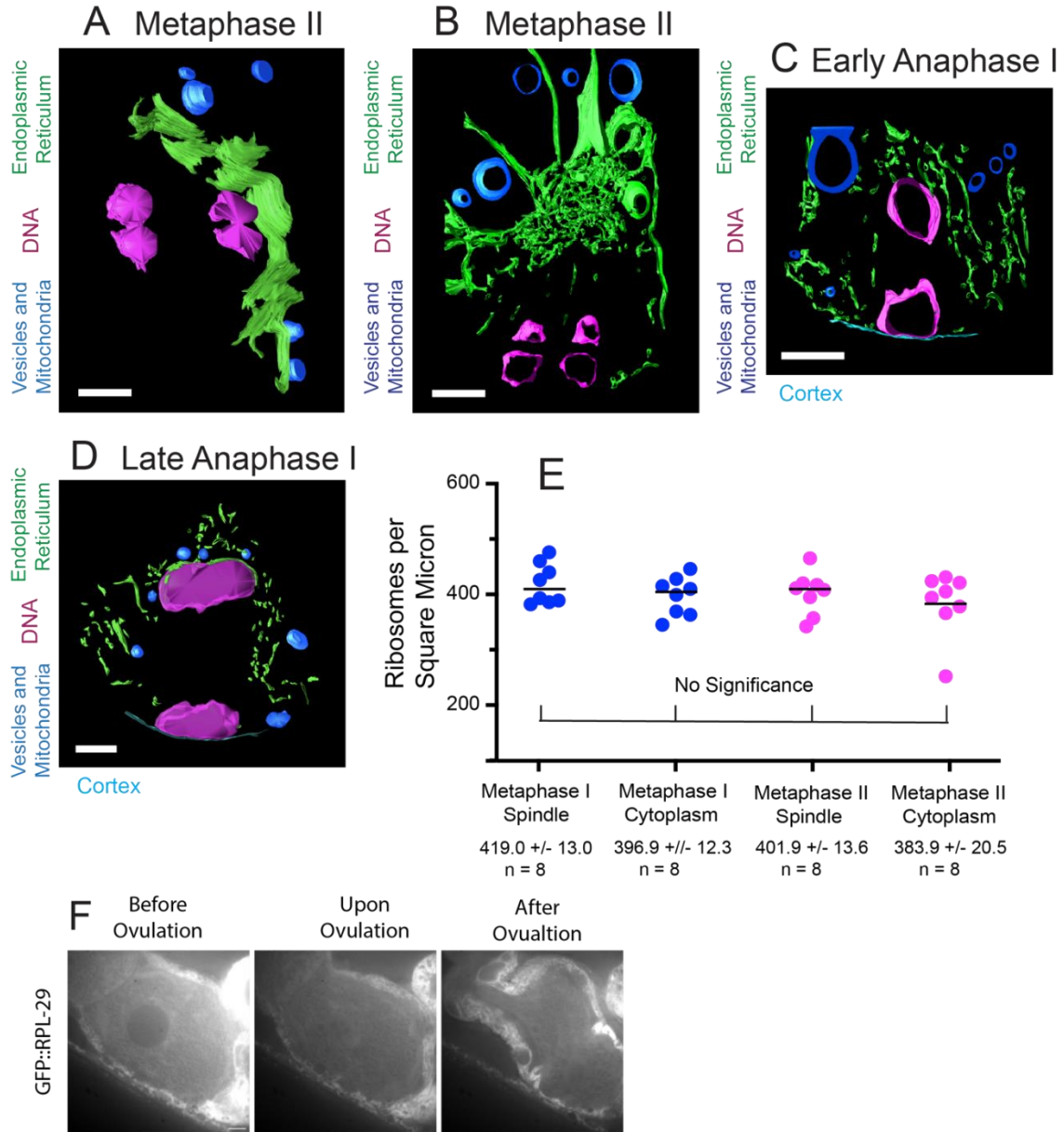


Figure 6. ER sheets between the metaphase meiotic spindle and cytoplasm form a barrier to vesicles and mitochondria, but not to ribosomes.

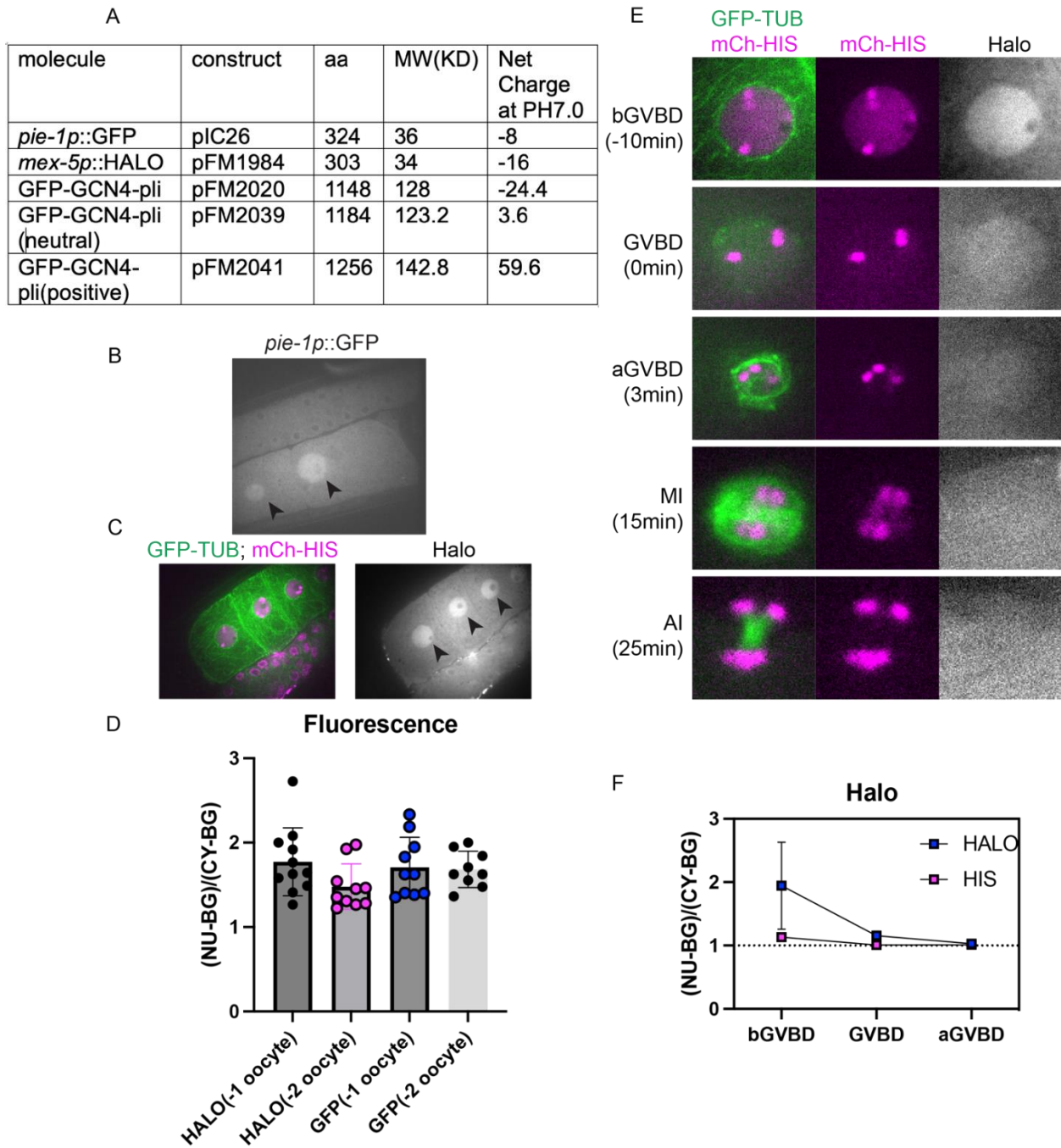


Fig 7. The concentration of molecules during GVBD is size dependent.

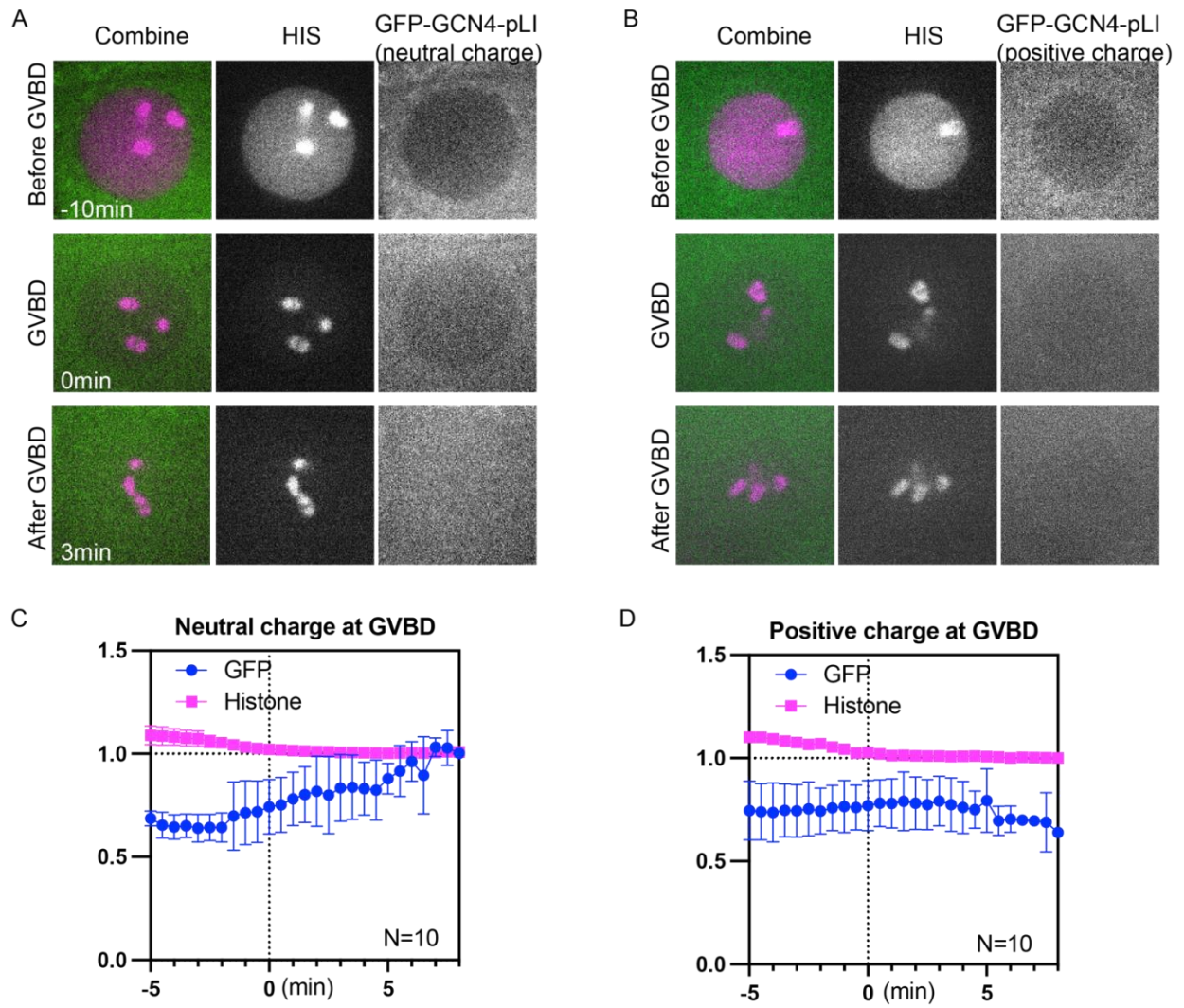


Fig 8. Molecule movement during GVBD is charge dependent.

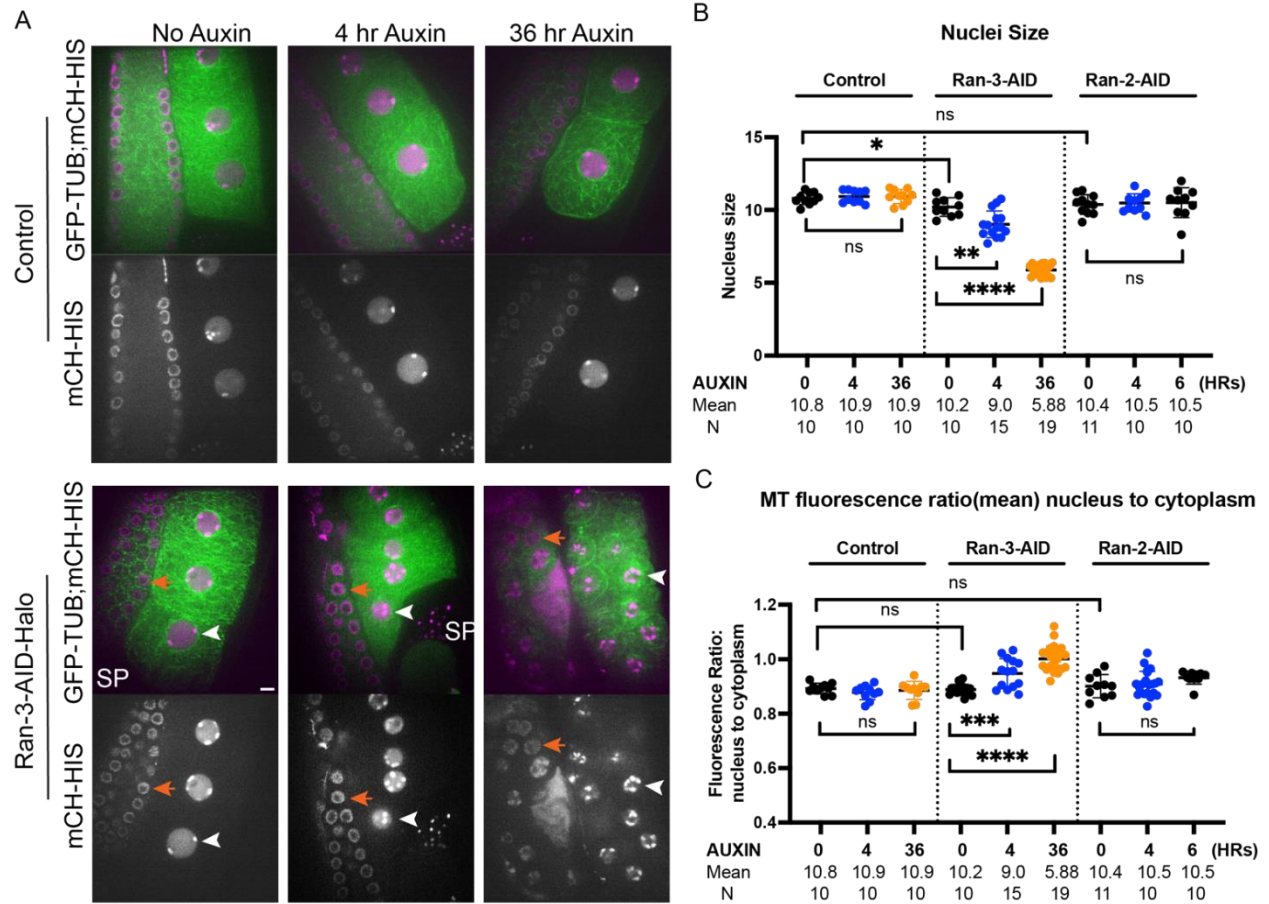


Fig S1. Halo-AID-RAN-3 oocytes treated with auxin for extended periods (36hrs) have even smaller nuclei and worse compartmentalization.

## Figure Legends

### **Fig 1. Ran-2 and Ran-3 are weakly associated with chromosomes during meiotic spindle assembly in *C. elegans* oocytes.**

(A) Diagram of Ran-GDP, Ran-GTP cycle in nucleoplasm transport.

(B) Embryonic viability of strains depleting RAN-2 or RAN-3 by Auxin-Induced Degradation.

(C) Time lapse images of meiotic embryo expressing Ran-3::AID::HALO, TIR1::mRuby, GFP::TUB and mCh::HIS.

(D) Time lapse images of meiotic embryo expressing Ran-2::AID::HALO, TIR1::mRuby, GFP::TUB and mCh::HIS. Graphs representing normalized fluorescence intensity along a 1-pixel-wide line scan (indicated by dashed line on the respective images) before GVBD, Ana I and Ana II are plotted on the bottom; position 0 corresponds to one end of the line scan. Scale bars, 5 $\mu$ m.

### **Fig 2. Ran-GEF and Ran-GAP are required for meiotic chromosome segregation but not for meiotic spindle formation.**

(A) Images of meiotic embryo expressing an-3::AID::HALO, TIR1::mRuby, GFP::TUB and mCh::HIS before Germinal Vesicle Breakdown(bGVBD) and after(aGVBD).

(B) Fluorescence intensity of Halo in embryos treated with 0, 4 or 6-hour Auxin. Control: strain not containing Degron. Ran-3::AID::Halo: strain expressing Ran-3::AID::HALO. Y axis (Left): fluorescence intensity ratio of Halo in nucleoplasm to background. Y axis (Right): fluorescence intensity ratio of Halo on chromosome to background.

(C) Images of meiotic embryo expressing Ran-2::AID::HALO, TIR1::mRuby, GFP::TUB and mCh::HIS before Germinal Vesicle Breakdown(bGVBD) and after(aGVBD).

(D) Fluorescence intensity of Halo in embryos treated with 0, 4 or 6-hour Auxin. Control: strain not expressing degron; Ran-2::AID::Halo: strain expressing Ran-2::AID::HALO. Y axis (Left): fluorescence intensity ratio of Halo in nucleoplasm to background. Y axis (Right): fluorescence intensity ratio of Halo on nuclear envelope to background.

(E) Time lapse images of meiotic embryo in control strain; Ran-3::AID::HALO or Ran-2::AID::HALO, all expressing TIR1::mRuby, GFP::TUB and mCh::HIS.

(F) Chromosome segregation defects in control strain, Ran-3::AID::halo or Ran-2::AID::Halo strain treated with 0 or 4-hour Auxin. Normal: chromosome segregated during MI (Metaphase I). Arrested: metaphase spindle was formed but chromosome did not segregate 30 min after MI and spindle microtubules disassembled. PB exclusion failure: half of the chromosomes were expelled into the first PB but then were re-absorbed.

**Fig 3. Free Tubulin concentrated in the nuclear volume at GVBD.**

(A) Diagram of chromosome and microtubule organization in *C. elegans* gonad. Chromosomal DNA or chromosomes(magenta); Microtubules (Green); Plasma Membrane (Black); Nuclear Envelope (Orange); -1 oocyte: most maturing oocyte; +1 oocyte: meiotic oocyte.

(B) Representative time-lapse images of the Germinal Vesicle in -1 oocyte expressing mNeonGreen::TBB-2 (green) and mCh::HIS (magenta). Tubulin concentrated in the nuclear volume at GVBD in worms treated with DMSO or

(C) Nocodazole. Non-chromosomal histone in the “nucleus” even out as the onset of GVBD. bGVBD, GVBD, aGVBD: before, at and after GVBD. Scale bars, 5  $\mu$ m.

(C) Plots of fluorescence intensity difference in nucleus and cytoplasm over time. Tubulin (green); Histone (Magenta). Y axis: mean fluorescence intensity in nucleus - mean

fluorescence intensity in cytoplasm. N: time lapse images analyzed. Average was shown in solid square [His] or solid circle [Tub].

(D) Ratio of mean fluorescence intensity of tubulin in nucleus over cytoplasm before GVBD and after GVBD. Tubulin were excluded from nucleus before GVBD (ratio < 1) and concentrated in nucleus after GVBD (ratio > 1). N: number of nuclei analyzed.

**Fig 4. Tubulin-sized molecules concentrated in the nuclear volume at GVBD.**

(A) Volume exclusion model of free tubulin rushing into nucleus (black circled region) where more space is available to tubulin-sized molecules (green dots) at GVBD.

(B) Representative time lapse images of meiotic embryo expressing tetrameric GFP (green) and mCh::His (magenta). Tetrameric GFP was expressed by inserting GFP::GCN4-*pli* onto ttTi5605(Chr. II) by RMCE method introduced in Monet. 2020. The ratio of fluorescence intensity of GFP (green) or non-chromosome histone (magenta) in nucleus to cytoplasm during GVBD over time are shown in the graph on the right. N: time lapse images analyzed. Average was shown in solid square [His] or solid circle [Tub].

(C) Representative time lapse images of meiotic embryo expressing un-polymerizable tubulin (green) and mCh::His (magenta). un-polymerizable tubulin was expressed by inserting *C. elegans* GFP::tba-2(T342E) onto ttTi5605(Chr. II) by RMCE method. The ratio of fluorescence intensity of GFP (green) or non-chromosome histone (magenta) in nucleus to cytoplasm during GVBD over time are shown in the graph on the right.

(D) Plots of fluorescence intensity ratio in nucleus to cytoplasm bGVBD, GVBD, aGVBD, MI, AI, MII and AII in (C) and (E). Blue: GFP::GCN4-*pli* or GFP::tba-2(T342E). Magenta: Histone. Y axis: mean fluorescence intensity[nucleus-background] ÷ mean fluorescence intensity[cytoplasm-background].



**Fig 5. The ER instead of the nuclear envelope delimits the concentration of free tubulin during meiosis and early mitosis.**

(A) Diagram of an intact nucleus before GVBD. ONM: Outer Nuclear Membrane. INN: Inner Nuclear Membrane. NPC: Nuclear Pore Complex. ER: Endoplasmic Reticulum.

(B) Time-lapse sequences of representative meiotic embryo expressing GFP::NPP-6 (green); mCh::HIS (red).

(C) or GFP::LMN-1 (green); mCh::HIS (magenta).

(D) or GFP::VIT-2 (green); mKate::TUB (red); Halo::ER (magenta).

(E) or GFP::COX-4 (cyan); mKate::TUB (red).

(F) or GFP::PLIN-1 (cyan); mCh::PH (red); mKate::TUB (red)

Scale Bar, 5 $\mu$ m. The cell cortex was drawn in white dash line in B, C and E. Arrows point to the spindle poles with dense ER cluster at metaphase I and metaphase II in D.

**Fig 6. ER sheets between the metaphase meiotic spindle and cytoplasm form a barrier to vesicles and mitochondria, but not to ribosomes.**

(A) Model of ER sheets on the partial exterior of a metaphase II meiotic spindle and spanning 1.2 mm in the z.

(B) Model of ER at one pole of a metaphase meiotic spindle and spanning 0.6 mm in the z.

(C) Model of ER in an outer 0.6mm z-section of a MI anaphase spindle. No large ER sheets were observed.

(D) Model of ER in a 0.6mm z-section of a late anaphase I spindle.

(E) Ribosomes were counted in 12mm sections of spindle and cytoplasm in metaphase I and metaphase II tomograms. Ribosomes were counted after setting the threshold value

to half of the peak value. Average ribosome areas in metaphase I spindles and cytoplasm, and metaphase II spindles and cytoplasm were: 30.9 +/- 2.0nm, 28.0 +/- 1.2nm, 26.3 +/- 1.0nm, and 26.8 +/- 1.7nm respectively.

(F) Time-lapse images of meiotic embryo expressing GFP::rpl-29(grayscale) and rpl-29 (tm3555). Scale Bar, 5um.

### **Fig 7. Molecule movement during GVBD is size dependent.**

(A) Molecular weight and net charge of molecules used in this study, expressed in the *C. elegans* germline: *pie-1p*::GFP; *mex-5p*::HALO; GFP::GCN4-*pli*; GFP::GCN4-*pli* (close to neutral); GFP::GCN4-*pli* (positive).

(B) Images of diakinesis oocytes expressing *pie-1p*::GFP (gray) before Germinal Vesicle Breakdown, and

(C) Diakinesis oocytes expressing GFP::TUB (green), mCh::HIS (magenta) and *mex-5p*::HALO (gray).

(D) Fluorescence intensity ratio of *pie-1p*::GFP or *mex-5p*::HALO in the nucleus to the cytoplasm in -1 or -2 oocytes.

(E) Time lapse images of meiotic embryo expressing GFP::TUB (green), mCh::HIS (magenta) and *mex-5p*::HALO (gray).

(F) Fluorescence intensity ratio of *mex-5p*::HALO (purple) and non-chromosome histone (magenta) in the nucleus to the cytoplasm before GVBD, at GVBD onset and after GVBD.

### **Fig 8. Molecule movement during GVBD is charge dependent.**

(A) Representative time lapse images of meiotic embryo expressing mCh::HIS and tetramerized GFP (green) with neutral charge or

(B) positive charge

(C) and (D) Plots of fluorescence intensity difference in nucleus to cytoplasm over time in (A) and (B), respectively. Y axis: mean fluorescence intensity [nucleus-background] ÷ mean fluorescence intensity [cytoplasm-background]. N: time lapse images analyzed. Average was shown in solid magenta square [His] or solid green circle [GFP].

**Fig S1. Halo-AID-RAN-3 oocytes treated with auxin for extended periods (36hrs) have even smaller nuclei and worse compartmentalization.**

(A) Representative Images of meiotic embryo expressing TIR1::mRuby, GFP::TUB and mCh::HIS or Ran-3::AID::HALO, TIR1::mRuby, GFP::TUB and mCh::HIS, treated with no auxin, 4hr auxin or 36hr auxin, respectively.

(B) Quantification of oocyte nuclei size of control strain, Ran-3::AID::halo or Ran-2::AID::Halo strain treated with 0, 4-hour, 6-hour, or 36-hour Auxin.

(C) Quantification of microtubule fluorescence ratio in nucleus to cytoplasm in same conditions shown in (B).

**Video 1. ER delimits the concentration of free tubulin GFP::GCn4 during meiosis.**

Time-lapse sequences of embryo expressing GFP::GCn4-pLI (green); mCh::HIS (red) and Halo::ER (magenta). Video started before GVBD and ended after Anaphase I. GFP fluorescence concentrated in the nuclear volume during GVBD, after GVBD and at metaphase I. The concentration is enclosed by ER.

**Video 2. ER delimits the concentration of free tubulin GFP::GCn4 during early mitosis.**

Time-lapse sequences of embryo expressing GFP::GCn4-pLI (green); mCh::HIS (red) and Halo::ER (magenta). The video started at the one-cell pronuclear meeting and ended at the four-cell stage. GFP fluorescence concentrated in the nuclear volume at metaphase

during the first mitosis and second mitosis. The concentration of GFP fluorescence is enclosed by ER.

**Video 3. ER sheets between metaphase II spindle and cytoplasm exclude vesicles and mitochondria.**

3D images of Fig 6A: Model of ER sheets on the partial exterior of a metaphase II meiotic spindle and spanning 1.2mm in the z.

**Video 4. ER between anaphase I spindle, and cytoplasm does not exclude vesicles and mitochondria.**

3D images of Fig 6D: Model of ER in a 0.6mm z-section of a late anaphase I spindle.

# Chapter 2

***Caenorhabditis elegans* spermatocytes can segregate achiasmate homologous chromosomes apart at higher than random frequency during meiosis I.**

Ting Gong, Francis J McNally

Gong T, McNally FJ. *Caenorhabditis elegans* spermatocytes can segregate achiasmate homologous chromosomes apart at higher than random frequency during meiosis I. *Genetics*. 2023 Apr 6;223(4):iyad021. doi: 10.1093/genetics/iyad021. PMID: 36792551; PMCID: PMC10319977.

I participated in designing and performing the experiments except examining chromosome segregation in *spo-11* oocytes (Figure 5B and 5C), which is done by Karen McNally. I participated in writing the paper and the revision process.

## Caenorhabditis elegans spermatocytes can segregate achiasmatic homologous chromosomes apart at higher than random frequency during meiosis I

Ting Gong, Francis J. McNally\*

Department of Molecular and Cellular Biology, University of California, Davis, Davis, CA 95616, USA

\*Corresponding author: Department of Molecular and Cellular Biology, University of California, Davis, One Shields Avenue Davis, CA 95616, USA. Email: fjmcnally@ucdavis.edu

### Abstract

Chromosome segregation errors during meiosis are the leading cause of aneuploidy. Faithful chromosome segregation during meiosis in most eukaryotes requires a crossover which provides a physical attachment holding homologs together in a "bivalent." Crossovers are critical for homologs to be properly aligned and partitioned in the first meiotic division. Without a crossover, individual homologs (univalents) might segregate randomly, resulting in aneuploid progeny. However, *Caenorhabditis elegans zim-2* mutants, which have crossover defects on chromosome V, have fewer dead embryos than that expected from random segregation. This deviation from random segregation is more pronounced in *zim-2* males than that in females. We found three phenomena that can explain this apparent discrepancy. First, we detected crossovers on chromosome V in both *zim-2(tm574)* oocytes and spermatocytes, suggesting a redundant mechanism to make up for the ZIM-2 loss. Second, after accounting for the background crossover frequency, spermatocytes produced significantly more euploid gametes than what would be expected from random segregation. Lastly, trisomy of chromosome V is viable and fertile. Together, these three phenomena allow *zim-2(tm574)* mutants with reduced crossovers on chromosome V to have more viable progeny. Furthermore, live imaging of meiosis in *spo-11(me44)* oocytes and spermatocytes, which exhibit crossover failure on all 6 chromosomes, showed 12 univalents segregating apart in roughly equal masses in a homology-independent manner, supporting the existence of a mechanism that segregates any 2 chromosomes apart.

**Keywords:** *Caenorhabditis elegans*, meiosis, chromosome segregation

### Introduction

Genetic recombination and random chromosome segregation during sexual reproduction reshuffle genetic variations, giving birth to diverse offspring to adapt to a varying environment. During meiotic prophase, homologs are tethered together as a "bivalent" by sister chromatid cohesion and crossovers between homologs (Fig. 1a) (Miller et al., 2013; Moore and Orr-Weaver, 1997). This bivalent configuration is essential for faithful chromosome segregation. At meiosis I, crossovers between homologs provide physical attachments for the homologs to be properly oriented toward opposite spindle poles and segregate normally. If homologs fail to pair and cohesion between sister chromatids is retained, the 2 univalents might segregate randomly at anaphase I resulting in gametes that have lost or retained both univalents (Fig. 1b) (Buonomo et al., 2000). Alternatively, if cohesion between sister chromatids is lost and they segregate apart at anaphase I, nonsisters would segregate randomly at anaphase II (Nicklas, 1977; LeMaire-Adkins and Hunt, 2000). Either case would result in a high percentage of progeny with monosomy or trisomy. The importance of crossover-based attachments between homologous chromosomes is supported by the high frequency of dead and aneuploid progeny (Dernburg et al., 1998; Blokhina et al., 2019) or a complete lack of functional gametes

(Romanienko and Camerini-Otero, 2000) produced by meiotic recombination mutants in a wide range of sexually reproducing organisms, including plants, yeast, worms, and mammals. In addition, aging causes spontaneous loss of inter-homolog attachments and production of aneuploid progeny in both *Caenorhabditis elegans* (Raices et al., 2021) and humans (Wartosch et al., 2021).

Parental aneuploidy and crossover failure are two situations where meiosis must proceed without a crossover. Whereas aneuploidy is often lethal, there are cases of viable and fertile aneuploids, which reveal backup mechanisms to restore euploidy. In XO mice, preferential retention of the univalent X at the first meiotic division is observed in 60% of oocytes rather than the 50% expected from random segregation (LeMaire-Adkins and Hunt, 2000). In trisomy IV or trisomy X in *C. elegans*, the extra univalents are preferentially eliminated during anaphase I of meiosis (Hodgkin et al., 1979; Cortes et al., 2015; Vargas et al., 2017). Keeping the univalent from monosomic parents or getting rid of the extra chromosome from trisomic parents both increase the frequency of euploid progeny.

Meiosis with 2 achiasmatic homologs is likely more common than meiosis with a single univalent due to monosomy or trisomy. Some species naturally do not undergo meiotic recombination but still accurately segregate pairs of homologous chromosomes. Recombination does not occur between homologs in oocytes of

Received: December 19, 2022. Accepted: February 7, 2023

© The Author(s) 2023. Published by Oxford University Press on behalf of the Genetics Society of America. All rights reserved. For permissions, please e-mail: journals.permissions@oup.com

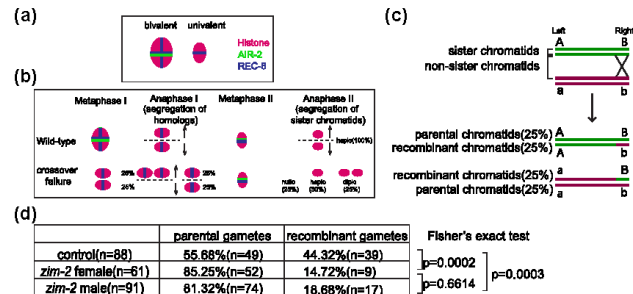


**Fig. 1.** Crossovers in *zim-2*(*tm574*) female oocytes and male spermatocytes. a) Diagram of bivalent, univalent, and associated AIR-2 and cohesin subunit REC-8 in *C. elegans*. b) Schematic of sequential cohesion loss and chromosome segregation during meiosis in wild type and in case of crossover failure with random segregation. c) Schematic of a crossover that gives rise to 50% recombinant gametes and 50% parental gametes. d) Percentage of parental gametes and recombinant gametes produced by *zim-2* females crossed with wild-type males or *zim-2* males crossed with *fog-2*(-) females. The P-values are shown on the right by 2 x 2 Fisher's exact test.

the silkworm *Bombyx mori*, but homologs remain attached at telomeres after breakdown of the synaptonemal complex to allow accurate segregation (Rosin et al., 2021). Likewise, in the plant species *Luzula elegans*, sister chromatid cohesion is lost during anaphase I of a "reverse meiosis" but homologous chromosomes remain tethered at telomeres at metaphase II to allow accurate segregation during anaphase II (Heckmann et al., 2014). During *Drosophila* male meiosis, homolog pairs are naturally held together by spermatocyte-specific protein complexes instead of crossovers (Thomas et al., 2005; Weber et al., 2020). During *Drosophila* female meiosis, the 4th chromosome naturally does not undergo recombination, but homologs of the 4th chromosome accurately segregate apart (Theurkauf and Hawley, 1992). This female-specific mechanism also functions when recombination is artificially blocked on the X chromosome and is promoted by heterochromatin bridges connecting the 2 homologs (Dernburg et al., 1996; Hughes et al., 2009).

The existence of backup mechanisms to promote accurate segregation of chromosomes lacking normal attachments has also been suggested in humans where loss of cohesion occurs as a spontaneous error. In the "reverse segregation" (RS) error, where sister chromatids segregate prematurely at meiosis I, nonsister chromatids would be expected to segregate randomly at anaphase II (50% euploid). Instead, 78% of the nonsisters remained correctly aligned at the spindle equator and segregated correctly at meiosis II. Similar to achiasmatic segregation in *Drosophila* oocytes, chromatid threads between nonsister chromatids were observed in 46% of RS MII eggs (Gruhn et al., 2019). Whether chromatin threads promote faithful chromosome segregation in the absence of normal attachments remains to be determined.

A nematode-specific family of Zn finger proteins provides a unique opportunity to study the response of the meiotic segregation machinery to crossover failure because loss of each family member results in crossover failure on specific chromosomes in *C. elegans*. There are 2 sexes in *C. elegans*, hermaphrodites and males, determined by the sex chromosome (X) to autosome ratio. Normally, hermaphrodites are XX and males are XO with a univalent at MI. HIM-8 mediates pairing and crossover formation on the X chromosome (Phillips et al., 2005). ZIM-1 mediates pairing of chromosomes II and III, ZIM-2 mediates pairing of chromosome V, and ZIM-3 mediates pairing of chromosomes I and IV (Phillips and Dernburg, 2006) by binding to chromosome-specific DNA

sequences (Phillips et al., 2009). Random meiotic segregation after crossover failure on the X in one parent due to loss of HIM-8 should result in 25% of progeny with monosomy (XO), 50% disomy (XX), and 25% trisomy (XXX). An early study first demonstrated that these 3 karyotypes have easily scorable phenotypes, then used these phenotypes to demonstrate sex-specific responses to crossover failure on the X (Hodgkin et al., 1979). *him-8*; XX males produced significantly more euploid haplo-X gametes than the 50% expected from random segregation (Supplementary Fig. 1; Hodgkin et al., 1979) suggesting that 2 unpaired sex chromosomes tend to be segregated apart during spermatogenesis. In contrast, *him-8* XX females produced an excess of nullo-X gametes (Supplementary Fig. 1) (Hodgkin et al., 1979) indicating that univalent chromosomes are preferentially deposited into polar bodies during oocyte meiosis (Cortes et al., 2015).

It is unclear whether these sex-specific responses to crossover failure are restricted to the X chromosome because unambiguous phenotypes have not been assigned to most autosomal aneuploidies in *C. elegans*. However, *zim-1* or *zim-2* females mated with WT males have less inviable progeny than what would be expected from random segregation if trisomies and monosomies of chromosomes II, III, or V are lethal. This deviation from random segregation was more substantial in *zim-1* or *zim-2* males mated with WT females (Jaramillo-Lambert et al., 2010; Fig. 2a, this study), suggesting a stronger sex-specific correction system in males to maximize the number of viable progeny in response to crossover failure.

In addition to accurate meiotic segregation of achiasmatic chromosomes, two other phenomena which could contribute to the results of Hodgkin et al. (1979) and Jaramillo-Lambert et al. (2010) are the potential for viable aneuploidy and mitotic correction. Whereas most aneuploidies in humans are lethal, viable trisomy of chromosome IV (Sigurdson et al., 1984) and X (Hodgkin et al., 1979; Vargas et al., 2017) in *C. elegans* have been reported in previous work.

An additional mechanism that could allow parents with crossover failure to have more viable progeny is correction of meiosis-derived aneuploidy by segregation errors during embryonic mitosis. Mosaicism and aneuploidy are very common in early human embryos, but significantly lower rates of aneuploidy or mosaicism are detected at birth (Nagaoka et al., 2012; Bielanska et al., 2002). The first mitotic divisions of human embryos are extremely error-prone (McCoy et al., 2015), which could result in

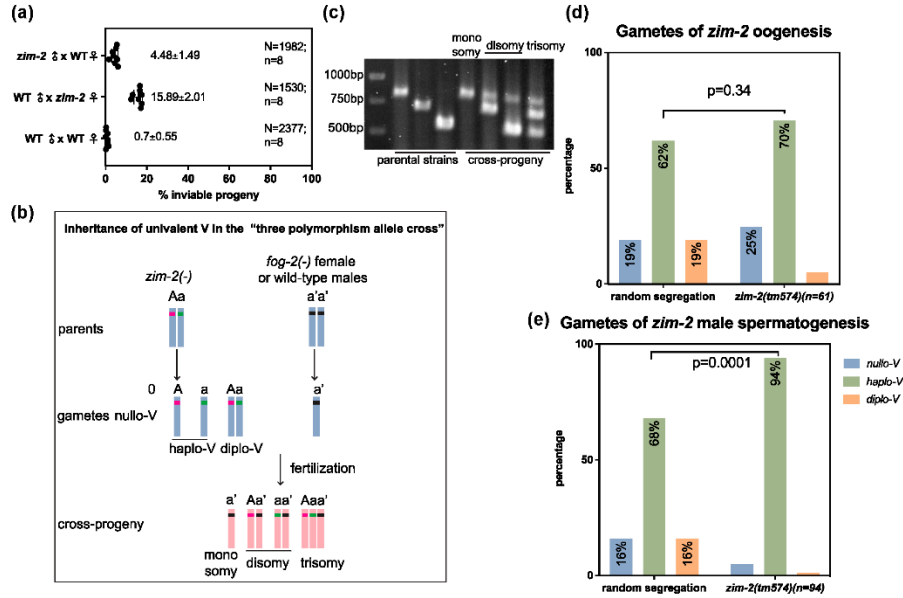


**Fig. 2.** *Zim-2(tm574)* males produce more euploid progeny than what would be expected from random segregation. a) Percentage of inviable progeny produced by *zim-2(tm574)* males mated with *fog-2(-)* females, *zim-2(tm574)* females mated with WT males, and WT males mated with WT females. Each dot represents progeny from one parent. N: total number of progeny counted; n: number of parents. The numbers shown next to the scatter plot are mean  $\pm$  SD. b) Diagram of the "three-polymorphism allele crosses" to detect nullo-V, haplo-V, and diplo-V gametes by *zim-2(tm574)* female oocytes and males. *Zim-2(tm574)* females or males with 2 different polymorphism alleles were mated/mated with males or *fog-2(-)* females with a third polymorphism allele on chromosome V. Their progeny was subject to PCRs for corresponding polymorphism alleles. Primers amplifying alleles are listed in [Supplemental Material](#). c) Agarose gel showing examples of parental strains with 3 distinguishable polymorphism alleles, and examples of monosomic V progeny (nullo-V gamete, 1 band); disomic V progeny (haplo-V gamete, 2 bands), and trisomic V progeny (diplo-V gamete, 3 bands). d) Percentage of nullo-V, haplo-V, and diplo-V gametes from *zim-2(tm574)* female oogenesis and e) *zim-2(tm574)* male spermatogenesis. Random segregation: percentage of 3 types of gametes expected from random segregation after correcting for pre-existing crossover rate. P-value by Fisher's exact test ( $2 \times 2$ , comparing aneuploidy and euploidy).

both mitotic aneuploidy as well as correction of meiotic aneuploidy. In addition, aneuploid cells are progressively eliminated during embryogenesis (Orvieto et al., 2020; Yang et al., 2021). This "mitotic correction" of meiotic aneuploidy likely explains uniparental disomy, the condition of having 2 chromosome copies from 1 parent and none from the other parent, in humans (Nakka et al., 2019).

Here, we conducted an investigation of a *C. elegans zim-2* mutant, which presents a unique opportunity to study the response of the meiotic machinery to a specific crossover defect of a specific autosome.

## Materials and methods

### C. elegans strains

Worms used in this study were maintained under standard laboratory conditions. Strains are listed in [Supplementary Table 1](#).

### Three-polymorphism allele crosses

The F2 progeny were obtained as follows:

For polymorphism allele crosses to identify chromosome V copy number of progeny from *zim-2(tm574)*, *zim-2(tm574)* hermaphrodites at the L4 stage were mated to *zim-2(tm574)* males

with JU258 polymorphisms on chromosome V to obtain F1 homozygous *zim-2(tm574)* worms with heterozygous polymorphisms (JU258/N2) on chromosome V. Only hermaphrodites with a mating plug and having more than 50% male progeny were considered to have mated. Males for crosses were generated by heat shocking L4 worms at 32° for 5 hr. To obtain F2 progeny from *zim-2(tm574)* male parents, F1 *zim-2(tm574)* males were mated to *fog-2(-)* CB4856 polymorphic hermaphrodites. To obtain F2 progeny from *zim-2(tm574)* female parents, F1 *zim-2(tm574)* females were mated to CB4856 Hawaiian males.

For polymorphism allele crosses to identify chromosome II and III copy number of progeny from *zim-1\**, *zim-1(tm1813)* hermaphrodites at the L4 stage were mated to a *zim-1(xoe6)* CB4856 polymorphic males to obtain F1 *zim-1\*(tm1813/xoe6)* worms with heterozygous polymorphisms (N2/CB4856). Only hermaphrodites with a mating plug and having 50% male progeny were considered to have mated. To obtain F2 progeny from *zim-1\** male parents, F1 *zim-1\** males were mated to JU258 polymorphic hermaphrodites. To obtain F2 progeny from *zim-1\** female parents, F1 *zim-1\** females were mated to JU258 Hawaiian males.

F2 eggs and hatched larvae (all progeny from the parents within 24 hr) from at least 3 individual mothers were subject to PCRs



within 0–24 hr after being laid. Strains, polymorphisms, and primers for PCRs are listed in [Supplementary Tables 1 and 2](#).

For PCRs, single progeny were sorted into PCR tubes and digested in 6 ml of lysis buffer and proteinase K. Lysis buffer was composed of the following: 1-M KCl, 1-M Tris pH 8.3, 1-M MgCl<sub>2</sub>, 0.45% IGEPAL, 0.45% Tween 20, and sterile water. The tubes were submerged in liquid nitrogen for 10 min and heated in a thermocycler at 60° for 60 min and 95° for 15 min. Each PCR reaction was 20 µl total. The following final concentrations of each reagent were used: 1x Standard Taq Reaction Buffer, 1-mM MgCl<sub>2</sub>, 300-µM dNTPs, 0.5-µM forward primer, 0.5-µM reverse primer, 1000-ng template DNA (1/6th of a worm/egg), 0.4 unit/20-µl PCR Hot Start Taq DNA Polymerase, and sterile water. Primers are listed in [Supplementary Table 2](#). All PCR reactions followed the standard Hot Start Taq Polymerase protocol with 38 cycles for denaturation, annealing, and extension. When doing PCR on adult animals, 32 cycles were utilized.

### Live imaging

*zim-2(tm574)*, *zim-1(tm1813)*, and *zim-3(tm2303)* strains expressing AIR-2::GFP, mCherry::histone H2B, and mKate::PH; *spo-11(me44)/nT1* strains expressing AIR-2::GFP and mCherry::histone; and *spo-11(me44)/nT1* strains expressing GFP::HIS and mKate::TUB were constructed. Worms were anesthetized with tricaine/tetramisole as described ([Kirby et al. 1990](#); [McCarter et al. 1999](#)) and gently mounted between a coverslip and a thin 2% agarose pad on a slide. Images in [Figs. 3–5](#) and [Supplementary Figs. 3–5](#) were captured with a Solamere Spinning Disk Confocal equipped with a Yokogawa CSU10, Hamamatsu Orca Flash 4.0 CMOS, and an Olympus 100x/1.35 oil objective. For counting chromosomes in female diakinesis oocytes and male spermatocytes, z-stack images were taken in a 0.5-µm step size to include all chromosomes. For time-lapse movies of male meiosis, 3 z-stacks in a 1-µm step size were captured every 20 s.

### Statistical analysis

Chi-square and Fisher's exact tests of 2x2 contingency tables were calculated with GraphPad Prism. Fisher's exact test of 2x3 contingency tables was calculated with <https://www.danielsoper.com/statcalc/calculator.aspx?id=58>.

## Results

### Crossovers in *zim-2(tm574)* male and female parents

*zim-2(tm574)* mutants have been reported to be defective in pairing and recombination of chromosome V ([Phillips and Dernburg, 2006](#)) but to have a higher than expected frequency of viable progeny ([Jaramillo-Lambert et al., 2010](#)). At diakinesis in *C. elegans*, when homolog pairing, recombination, and chromosome remodeling have completed, every pair of homologous chromosomes appears as 1 chromosome body called a "bivalent," consisting of 4 chromatids held together by a crossover and sister chromatid cohesion. In wild-type *C. elegans*, 6 chromosome bodies will be present, with 5 autosomal bivalents (autosomes I–V), and 1 X chromosome bivalent in oocytes (XX) or 1 unpaired X univalent in spermatocytes of males (XO). The majority of *zim-2(tm574)* diakinesis oocytes have 7 chromosome bodies, 5 bivalents, and 2 V univalents. However, a variable number of oocytes with 6 chromosome bodies have been reported, 28% ([Phillips and Dernburg, 2006](#)), 38% ([Cortes et al., 2015](#)), and 24% ([Supplementary Fig. 2a](#), [Supplementary Fig. 2c](#), this study). This is possibly due to chromosome V crossovers or noncrossover inter-homolog chromosome connections in the

absence of ZIM-2. To distinguish between these possibilities, we measured the crossover incidence in *zim-2(tm574)* oocytes by analyzing recombination between polymorphism alleles on the ends of chromosome V. *zim-2(tm574)* females heterozygous for polymorphism alleles on the 2 ends of V were crossed with wild-type males carrying a third set of polymorphism alleles on the 2 ends of chromosome V ([Fig. 1c](#), [Supplementary Fig. 3](#)). We found that 14.72% of cross progeny from *zim-2(tm574)* females were recombinant for chromosome V ([Fig. 1d](#)). Because there is exactly one crossover per *C. elegans* bivalent, equal numbers of recombinant and nonrecombinant progeny result from normal recombination. Thus *zim-2(tm574)* females have a crossover frequency of 2x 14.72% or 29.44% for chromosome V. The detected crossovers likely resulted from a redundant mechanism, instead of incomplete knockdown of *zim-2*, as no ZIM-2 was detected by antibody staining in *zim-2(tm574)* gonads ([Phillips and Dernburg, 2006](#)). This crossover frequency was also not significantly different than the 28% of *zim-2* oocytes with 6 DAPI-staining bodies observed by [Phillips and Dernburg \(2006\)](#) indicating that 29.44% of *zim-2* oocytes have a crossover rather than a noncrossover connection between homologous copies of chromosome V.

The higher frequency of viable progeny from *zim-2(tm574)* males in [Jaramillo-Lambert et al. \(2010\)](#) might be due to a higher frequency of background crossovers. To test this, we examined the progeny from *zim-2(tm574)* male parents. *zim-2(tm574)* males heterozygous for polymorphism alleles on the left end and right end of chromosome V were crossed with *fog-2(-)* females (unable to make their own sperm) with a third set of polymorphism alleles on the 2 ends of chromosome V. In addition, 18.68% of progeny from *zim-2(tm574)* male parents were recombinant ([Fig. 1d](#)). This is not significantly different from females ( $P=0.6614$ , 2x2 Fisher's exact test) and does not explain the higher progeny viability of *zim-2(tm574)* males.

### *zim-2(tm574)* males produce more euploid progeny than what would be expected from random segregation

To test whether *zim-2(tm574)* mutants have a higher percentage of euploid progeny than expected from random segregation, we analyzed the copy number of chromosome V among the progeny of *zim-2(tm574)* females carrying heterozygous polymorphism alleles on chromosome V mated with wild-type males with a third polymorphism allele on chromosome V. Euploid progeny will inherit only one chromosome V from the *zim-2(tm574)* female parent while trisomic progeny will inherit both maternal copies and monosomic progeny will inherit neither maternal copy of chromosome V ([Fig. 2b and c](#)). In addition, 30% of progeny were aneuploid ([Fig. 2d](#)), slightly less than what would be expected from random segregation (38%, after correcting for the crossover rate in females). In contrast, *zim-2(tm574)* males mated with *fog-2(-)* females had notably fewer aneuploid progeny (6%) than what would be expected from random segregation (32%, after correcting for the crossover rate in males) ([Fig. 2e](#)). This suggested that 2 univalent Vs in males were distributed to spermatids equally instead of randomly. Segregation of 2 achiasmate homologous chromosomes apart at higher than random frequency has been previously referred as distributive segregation ([Zhang and Hawley, 1990](#)).

To test the generality of the apparent distributive segregation of chromosome V univalents in *zim-2(tm574)* males, we performed a similar analysis of *zim-1(tm1813/xoe6)* worms which exhibit crossover failures on chromosomes II and III ([Phillips and Dernburg, 2006](#), alleles used are described in Materials and Methods). We observed 8 chromosome bodies in 100% of *zim-1*

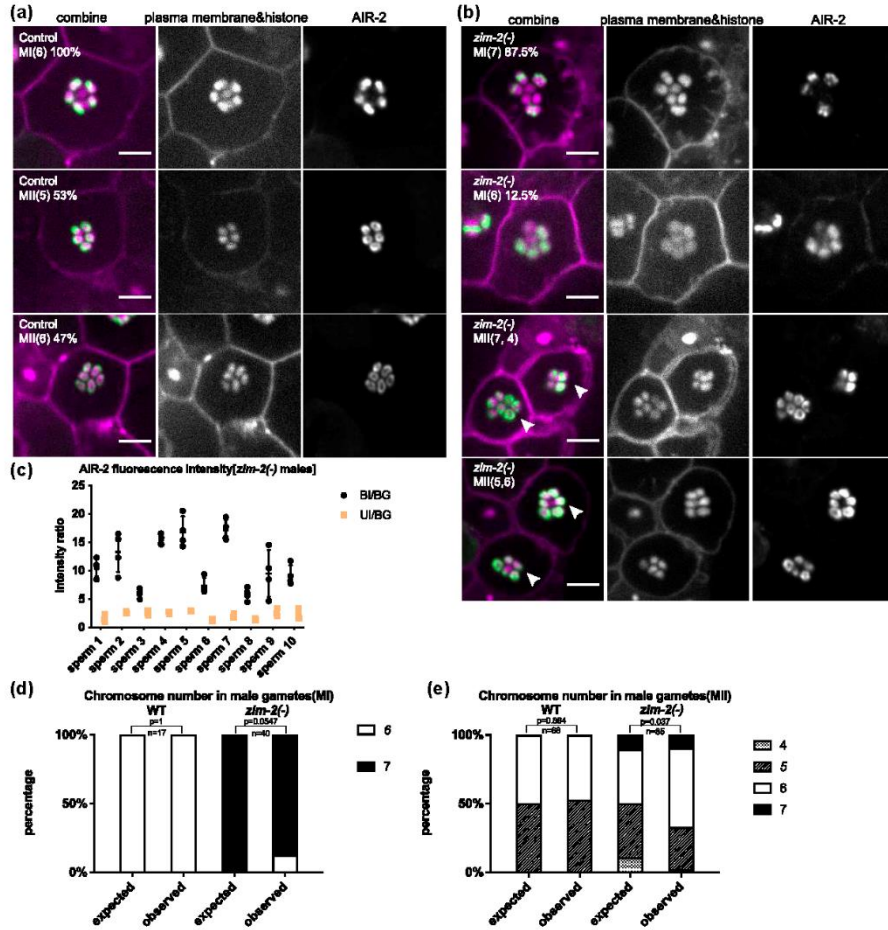


**Fig. 3.** *zim-2(tm574)* spermatocytes gave rise to more gametes with normal number of chromosomes. a) Representative images of live wild-type spermatocytes with 6 chromosome bodies at metaphase I and 5 or 6 chromosome bodies at metaphase II. AIR-2 in green; histone and plasma membrane in magenta. Scale bar: 2  $\mu$ m. b) Representative images of live *zim-2(tm574)* spermatocytes at metaphase I (with 7 or 6 chromosome bodies) and II (with 7, 4, 5, or 6 chromosome bodies). c) AIR-2::GFP fluorescence intensity ratio of 4 bivalent to background (BI/BG, black) and 3 univalent to background (UI/BG, yellow) in 10 individual *zim-2(tm574)* spermatocytes. d) Percentage of metaphase I spermatocytes with 6 or 7 chromosome bodies in control and *zim-2* males. e) Percentage of metaphase II spermatocytes with 4, 5, 6, or 7 chromosome bodies in control and *zim-2* males. Expected: expected from random segregation at metaphase II after correcting for existing chromosome alignment at metaphase I. 3.5% with 4 chromosome bodies, 32.5% with 5, 53.5% with 6, 10.5% comparing to 10.7%, 39.3%, 39.3%, and 10.7% expected from random segregation, respectively.

oocytes indicating a very low background crossover frequency on II and III (Supplementary Fig. 2b and c). *zim-1* males had more progeny that was euploid for chromosome II or III than what would be expected from random segregation and more euploid progeny than that of *zim-1* hermaphrodites (Supplementary Fig. 2e). Among *zim-3(tm2303)* diakinesis oocytes, 13.95% had 7 chromosome bodies and 78.05% had 8 chromosome bodies

(Supplementary Fig. 2b and c). The polymorphism assay to detect euploid progeny from *zim-3* mutant was not conducted due to unavailability of *zim-3* mutant carrying distinguishable polymorphisms. Interestingly, univalents loaded less Aurora B kinase AIR-2 than bivalents in *zim-1*, *zim-2*, and *zim-3* mutants (Supplementary Fig. 2d), consistent with a previous study (Muscat et al., 2015).

### Univalent V tends to be evenly distributed in *zim-2(tm574)* male spermatocytes

To examine whether the high incidence of euploid progeny from *zim-2(tm574)* males originates from meiosis (mitotic correction can also increase euploidy), we took images of spermatocytes at metaphase I and metaphase II. If distributive segregation occurs during anaphase I, then 2 univalents in metaphase I spermatocytes would segregate away from each other, resulting in more spermatocytes having a normal number of chromosomes at metaphase II than what would be expected from random segregation. Wild-type metaphase I spermatocytes had 6 chromosome bodies, of which 1 is the univalent X. If the sister chromatids of the univalent X remain intact at anaphase I, 50% of metaphase II spermatocytes will inherit the X and have 6 chromosome bodies, 1 X, and 5 autosomal chromosomes. In addition, 50% of metaphase II spermatocytes that do not inherit the X chromosome will have 5 autosomal chromosome bodies. If sister chromatids of the X split at anaphase I, then metaphase II spermatocytes will all have 6 chromosome bodies. Among wild-type metaphase II spermatocytes ( $n = 68$ ), 53% ( $n = 36$ ) had 5 chromosome bodies and 47% ( $n = 32$ ) had 6 chromosome bodies (Fig. 3a and d), indicating the X univalent remains intact at anaphase I, consistent with previous studies (Shakes et al., 2009).

12.5% ( $n = 5$ ) of *zim-2(tm574)* metaphase I spermatocytes ( $n = 40$  analyzed) had 6 chromosome bodies (Fig. 3b and d), indicating a chiasma between chromosome V homologs in those spermatocytes, and consistent with the crossovers detected by polymorphism analysis. This 12.5% of spermatocytes should behave like wild-type and at metaphase II should have 50% 5 autosomal bodies and 50% 6 chromosome bodies (5 autosomes and 1 X). In addition, 87.5% ( $n = 35$ ) of *zim-2* metaphase I spermatocytes had 7 chromosome bodies, comprised of 4 bivalents, 1 univalent X, and 2 univalent Vs (Fig. 3b and d). If 2 univalent Vs segregate randomly, 75% of their metaphase II spermatocytes will have 5 or 6 chromosome bodies. Therefore, 78% of total metaphase II spermatocytes will have 5 or 6 chromosome bodies ( $12.5\% \cdot 1 + 87.5\% \cdot 0.75$ ). In addition, 85% ( $n = 72$ ) of metaphase II spermatocytes ( $n = 85$  analyzed) had 5 or 6 chromosome bodies, significantly more than what would be expected from random segregation (78%, Fig. 3b and e,  $P = 0.037$  by Fisher's exact test  $2 \times 2$  after correcting for 12.5% nuclei with normal chromosome number). In conclusion, chromosome counting of the images of meiotic metaphase I and II in *zim-2(tm574)* males suggests 2 univalent Vs tend to be more equally distributed to the metaphase II spermatocytes than which would result from random segregation.

Faithful chromosome segregation relies on sequential cohesin release between homologs at anaphase I and sister chromatids at anaphase II as a result of phosphorylation of the cohesin subunit REC-8, which depends on the spatial and temporal activity of Aurora B kinase AIR-2 in *C. elegans* (Ferrandiz et al., 2018; De Carvalho et al., 2008; Tzur et al., 2012). We found that, like the univalent X in wild-type, V univalents in *zim-2(tm574)* metaphase I spermatocytes, in which 7 chromosome bodies were shown, loaded very little AIR-2 compared with bivalents (Fig. 3c). This suggests sister chromatids of univalents might remain intact at anaphase I due to insufficient AIR-2 loading. Moreover, AIR-2 appeared on all metaphase II chromosomes in both wild-type and *zim-2* mutants (Fig. 3a and b), suggesting that sister chromatids likely segregate at anaphase II.

### Time-lapse imaging of univalent V segregation in *zim-2(tm574)* males

To track univalent behavior more directly, we filmed meiotic chromosome segregation in wild-type and *zim-2(tm574)* males labeled with AIR-2::GFP, mCherry::histone, and mKate::PH (plasma membrane) (Fig. 4a and b, Supplementary Fig. 4). In *C. elegans* wild-type XO males, the univalent X frequently lags at meiosis I and sister chromatids of the X chromosome separate at meiosis II (Albertson and Thomson, 1993; Shakes et al., 2009). In all wild-type meiosis I spermatocytes ( $n = 21$ ), when segregation of autosomal homologs completed, the single X univalent still lagged at the midzone and the intensity of AIR-2::GFP on the lagging X was much lower than on metaphase bivalents. Meanwhile, separating autosomes had AIR-2 attached to their side at anaphase I (Fig. 4a). This is similar to what has been reported in a previous study by immunohistochemistry (Shakes et al., 2009) and is very different from oocytes, in which AIR-2 dissociates from chromosomes at anaphase I and relocates to the midzone (Rogers et al., 2002). Why the localization and dynamics of AIR-2 in males differ from female meiosis and whether this underlies different segregation mechanisms between sexes are not clear. Localization of AIR-2 in the middle of the univalent X indicated sister chromatids were oriented toward opposite spindle poles. If sister chromatids segregate precociously at anaphase I, the resulting single sister chromatids would be likely to lag at anaphase II. No lagging chromosomes were observed in anaphase II spermatocytes in both wild-type ( $n = 25$ , Fig. 4c) and *zim-2(tm574)* males ( $n = 20$ , Fig. 4c), suggesting univalents did not split at anaphase I.

Three out of 24 meiosis I spermatocytes in *zim-2(tm574)* males recapitulated wild-type male meiosis, in having a single lagging chromosome at anaphase I (Supplementary Fig. 4), consistent with 12.5% metaphase I spermatocytes having crossovers on V. In the remaining 21 spermatocytes, more than 1 univalent was observed lagging in the midzone when all other autosomes had segregated (Fig. 4b and c). In the spermatocytes ( $n = 20$ ) where 3 univalents (1 X and 2 V univalents) were present, the intensity of AIR-2::GFP on the lagging univalents was much lower than that on metaphase bivalents. In 1 spermatocyte, all 3 univalents moved to the same pole at anaphase I (4 aneuploid-V embryos will be made after fertilization) whereas in the other 19 spermatocytes, the 3 univalent segregated in a "two and one" manner to the opposite spindle pole during late anaphase (Fig. 4b). It is not possible to distinguish the X univalent from the 2 V univalents in these time-lapse sequences. However, the polymorphism assays demonstrated that *zim-2* males produce only 6% aneuploid-V gametes (4.8 out of 80 spermatids will be aneuploid). We therefore inferred that the other 19 spermatocytes with a "two and one" segregation pattern produced 76 euploid-V spermatids, suggesting that the 3 univalents segregating in the "two and one" manner were 1 X and 1 V univalents segregating away from the other V univalent. This is significantly higher than expected from random segregation (Fig. 4d). In conclusion, live imaging of *zim-2(tm574)* male meiosis suggests sister chromatids of univalents did not split at anaphase I and that 2 univalent Vs tend to segregate apart to opposite poles instead of segregating together to the same pole at anaphase I.

### Segregation of univalents in *spo-11(me44)* oocytes and spermatocytes

To eliminate the uncertainty generated by the univalent X in identifying autosomal univalents in *zim-2* males, we utilized a *spo-11*



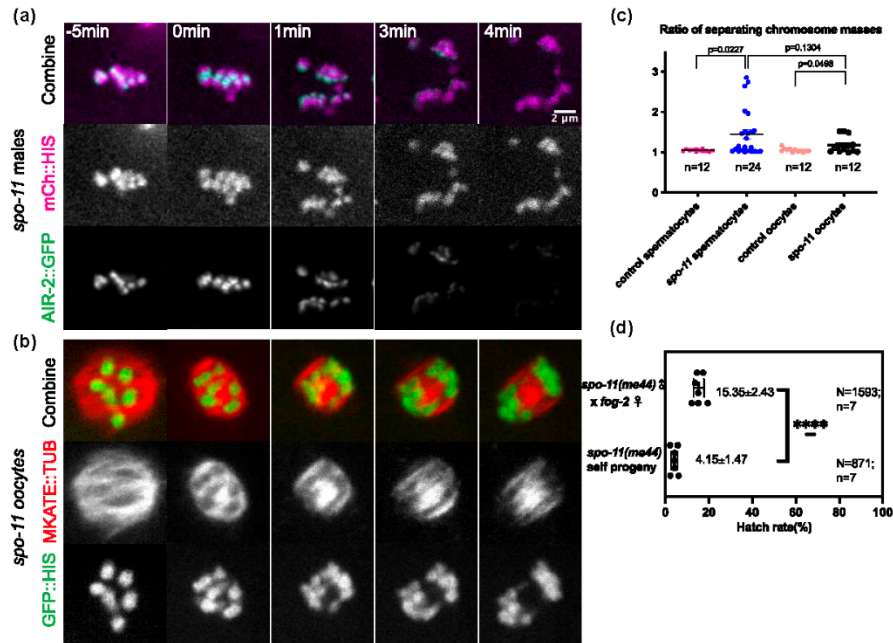


**Fig. 5.** A total of 12 univalents in *spo-11(me44)* segregated into 2 roughly equal masses at anaphase I. a) Single focal plane time-lapse images of *spo-11(me44)* male meiosis I spermatocytes labeled with AIR-2::GFP; mCherry::histone. A total of 7 AIR-2-labeled chromosomes are visible at metaphase in a single plane compared with 3 in control single planes (Supplementary Fig. 5). Chromosomes aligned at meiotic metaphase I plate and segregated roughly in half (12/16). Scale bar: 2  $\mu$ m. b) Single focal plane time-lapse images of *spo-11(me44)* meiosis I oocytes labeled with GFP::HIS; mKate::TUB. A total of 6 chromosomes are visible at metaphase in a single plane compared with 3 in control single planes (Supplementary Fig. 5). c) Fluorescence intensity ratio of separating chromosome masses in control male spermatocytes, *spo-11(me44)* male spermatocytes, control oocytes, and *spo-11(me44)* oocytes. Each dot represents the ratio of 2 separating chromosome masses in 1 cell by measuring the fluorescence intensity of maximum projection of separating masses from z-stack images of oocytes/spermatocytes at anaphase I. n, number of cells analyzed. d) The hatch rate of progeny from *spo-11(me44)* males crossed with *fog-2* females and *spo-11(me44)* hermaphrodites. N, total number of progeny counted; n, number of parents.  $P < 0.0001$ , unpaired t test.

*spo-11(me44)* hermaphrodites are viable but produce more than 90% dead self-progeny (Stamper et al., 2013). *Fog-2(-)* hermaphrodites crossed with *spo-11(me44)* males produce 84.65% dead eggs (Fig. 5d), significantly less than that of self-progeny from *spo-11(me44)* hermaphrodites ( $P < 0.0001$ , unpaired t test). This indicates that a high degree of aneuploidy is generated in both oocytes and spermatocytes, consistent with a previous study (Severson et al., 2009). The equal distribution of mCherry::histone-labeled chromatin in the majority of *spo-11(me44)* meiotic cells but high progeny lethality suggests that distributive segregation might separate any 2 univalents apart, instead of partitioning homologs specifically. This would result in gametes with a relatively normal number of chromosomes but high chromosomal aneuploidy (e.g. 1 gamete having 2 copies of chromosome I, II, and III, but no chromosome IV, V, and X).

### Trisomy I, II, and V are viable and fertile while monosomy is lethal

Our polymorphism-based karyotyping indicated that *zim-1* and *zim-2* females do not have significantly more euploid progeny than expected from random segregation, but progeny viability

was higher than expected if all aneuploidies are lethal. It might be that viable trisomy and monosomy could contribute to a higher-than-expected hatch rate. There are 6 possible trisomies and monosomies for *C. elegans*. Viable trisomy X and trisomy IV have been reported in previous studies (Sigurdson et al., 1984; Hodgkin et al., 1979; Vargas et al., 2017). The phenotypes of trisomy and monosomy of other chromosomes have not yet been reported. We examined the viability and fertility of trisomic, disomic, and monosomic female progeny from *zim-1* females crossed with WT males by a "three-polymorphism allele cross." *zim-1* hermaphrodites that were heterozygous for PCR polymorphism alleles on chromosome II and III were crossed with wild-type males homozygous for a third polymorphism allele. The F1 progeny (could be trisomic, disomic, or monosomic) was singled into individual plates, allowed to develop, and then scored as dead embryo, hatched larvae, or adults (Fig. 6a and b). If F1s hatched, DIC images of F1s were obtained to score for phenotypic characteristics (Fig. 6a), and hatch rates of F2 self-progeny were obtained after allowing F1's to lay eggs for 24 hr (Fig. 6c). Then F1s were subjected to the PCR analysis to determine the copy number of chromosomes II and III. Among all the trisomy II that we detected, the majority (83%)

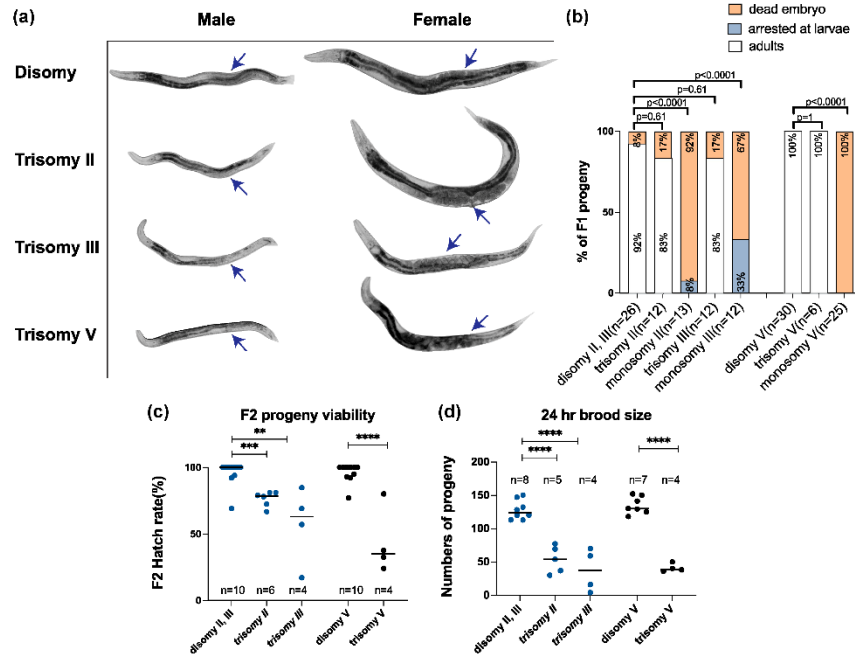


**Fig. 6.** Most trisomies are viable with reduced fertility whereas monosomies are lethal. a) Differential interference contrast (DIC) images of disomic/trisomic II, III, and V adults. The arrows point to gonads. b) Percentage of dead embryos, arrested larvae, and adults among disomic, trisomic, and monosomic F1 offspring from "zim-1 female x wild-type male polymorphism II and III cross" (left) and from "zim-2 female x wild-type male polymorphism V cross" (right) are presented. c) The F2 hatch rate and d) 24-hr brood size of disomy vs trisomy for chromosomes II, III, and V. For b, c, and d, disomies are F<sub>1</sub> siblings from the same cross used to generate the trisomies. For a, b, and d, all worms are zim-1<sup>-</sup> or zim-2<sup>+</sup>, and these mutations are recessive. For c, 25% of the F<sub>2</sub> progeny should be homozygous zim-1 or zim-2.

hatched and developed into adults with gonads, and 17% did not hatch, the viability of which is not significantly different from their disomic peers (Fig. 6b). Whereas for monosomy II, only 8% hatched and those all arrested at earlier larvae stages. Similarly, trisomy III had similar viability as disomy III: 83% trisomy III reached adulthood, and all monosomy III either did not hatch or were arrested before growing into adults (Fig. 6a and b). Similar crosses with zim-2 worms revealed that trisomy V progeny are viable whereas monosomy V progeny did not hatch (Fig. 6a and b).

In terms of phenotypic variations, monosomies II and III were extremely sick, small, and usually had motility issues. Trisomy II or III had variable length and width compared to disomy. Interestingly, trisomy II, III, or V hermaphrodites had significantly smaller brood sizes, and their progeny had lower hatch rates (Fig. 6c and d), suggesting that trisomy II or III was viable but had reduced fertility. Our results indicate that survival of trisomy II or trisomy III worms contributes to the high viability of progeny from zim-1 parents.

## Discussion

Our results indicate that spermatocytes in male *C. elegans* can compensate for spontaneous crossover failures by segregating

achiasmatic univalents apart at anaphase I. In addition, trisomic progeny from a male or female parent is viable, and fertile and previous studies have demonstrated that oocytes of trisomic worms can preferentially eliminate the extra chromosome during meiosis (Cortes et al., 2015; Vargas et al., 2017). Together these mechanisms constitute a robust system for ensuring that a high percentage of healthy euploid progeny can be produced after spontaneous crossover failures.

The different response of male spermatocytes and oocytes to achiasmatic univalents could be due to the presence of a third univalent (the X univalent) in males or to some other difference between oocyte and spermatocyte meiosis. Analysis of hermaphrodite spermatogenesis in a zim-2 mutant could distinguish between these possibilities because there is a bivalent X present. However, our polymorphism approach cannot be applied to hermaphrodite spermatogenesis. The "two and one" segregation pattern in most spermatocytes could be mechanically related to the "skew" phenomenon. *C. elegans* males that have an asymmetric bivalent, with one homolog larger than the other, preferentially segregate the larger homolog away from the univalent X (Wang et al., 2010; Le et al., 2017). It is possible that a crossover-independent mechanism equalizes the mass of chromatin moving toward each spindle pole and the univalent X affects this equalization only in XO males.

In *Drosophila* (Thomas et al., 2005; Weber et al., 2020), *Bombyx* (Rosin et al., 2021), *Luzula elegans* (Heckmann et al., 2014), and humans (Grühn et al., 2019), preferential segregation apart of homologs without a crossover is associated with a noncrossover tether between homologs. In *Arabidopsis*, crossover-defective mutants that assemble synaptonemal complex (SC) on univalents are able to segregate homologs apart, whereas mutants that fail to assemble (SC) segregate homologs randomly (Pradillo et al., 2007). Because an aberrant SC is a candidate for a tether that might promote segregation of achiasmatic homologs, it is pertinent to note that homologous chromosomes in *C. elegans spo-11* mutants pair and form a synaptonemal complex with transverse elements (Dernburg et al., 1998). However, these inter-homolog attachments are no longer detected in diakinesis oocytes. The univalents in *zim-1*, *zim-2*, and *zim-3* mutant oocytes load SC lateral element proteins, but do not pair or assemble SC transverse element proteins (Phillips and Dernburg, 2006). The naturally unpaired X of XO *C. elegans* males has been reported to form transient inter-sister pseudosynapsis that is part of a mechanism to prevent damage to and prevent checkpoint activation by the male-specific unpaired X (Checchi et al., 2014; Jaramillo-Lambert and Engebrecht, 2010). This male-specific pseudosynapsis mechanism might generate male-specific tethers between univalent autosomes in *zim-1* and *zim-2* mutants. We did not observe such tethers in *C. elegans zim-2* mutants, but they might be revealed with different fluorescent probes or imaging methods.

Alternatively, the sex-specific behavior of achiasmatic homolog pairs might be due to one of the several differences between oocyte and spermatocyte meiotic spindles. Unlike acentrosomal female meiotic spindles, male meiotic spindles assemble with centrosomes and robust astral microtubule arrays (Fabig et al., 2020). Plus ends of astral microtubules can interact with cortical dynein to generate pulling forces that contribute to anaphase spindle elongation. In addition, dynein/dynactin is not required for anaphase in oocytes (Laband et al., 2017; Danlasky et al., 2020) but is essential for anaphase in spermatocytes (Barbosa et al., 2021). Anaphase is described as two distinct processes, anaphase A in which chromosomes move closer to spindle poles and anaphase B in which spindle poles move apart. In *C. elegans* oocytes, anaphase A associated with kinetochore-dependent pulling forces (Danlasky et al., 2020) occurs before kinetochore-independent anaphase B (Dumont et al., 2010; McNally et al., 2016) that is associated with outward pushing from the spindle midzone (Laband et al., 2017). In *C. elegans* spermatocytes, anaphases A and B occur simultaneously (Fabig et al., 2020). In *C. elegans* spermatocytes, microtubules run continuously from spindle poles to chromosomes (Fabig et al., 2020) and make end-on attachments to the outside face of chromosomes (Wignall and Villeneuve, 2009; Fabig et al., 2020). End-on microtubule attachments to the outside face of chromosomes are a hallmark of kinetochore-dependent pulling forces generated by microtubule depolymerization coupled with NDC80 complexes (Joglekar et al., 2010). However, microtubules do not shorten during *C. elegans* spermatocyte anaphase A which is instead associated with changes in the shapes of the spindle and chromosomes (Fabig et al., 2020). In contrast, *C. elegans* oocyte microtubules form discontinuous, overlapping arrays of short microtubules (Laband et al., 2017; Redemann et al., 2018) that form only side-on contacts with chromosomes during metaphase (Wignall and Villeneuve, 2009; Redemann et al., 2018) or end-on contacts with the inside face of chromosomes during anaphase (Laband et al., 2017; Redemann et al., 2018). Univalent X chromosomes present during anaphase lag behind the main chromosome masses and are stretched, indicative of pulling forces, in both oocytes (Danlasky et al., 2020) and

spermatocytes (Fabig et al., 2020). In *C. elegans* oocytes, midzone microtubules can push chromosomes apart (Laband et al., 2017) and, in the absence of outer kinetochore function, can push intact bivalents apart in a homology-independent manner (Dumont et al., 2010; Danlasky et al., 2020). This midzone pushing mechanism might explain how univalents are separated into equal masses in *spo-11* oocytes. However, it has been reported that the midzone is composed of very few microtubules in *C. elegans* spermatocytes (Fabig et al., 2020), making it unclear if this pushing mechanism is present in spermatocytes.

### Data availability

Strains are available upon request. All polymorphisms and PCR primers used are listed in [Supplementary Table 2](#). Representative images are presented within the article, and complete imaging data sets are available upon request.

[Supplemental material](#) available at GENETICS online.

### Acknowledgments

We thank JoAnne Engebrecht and Leonid Kruglyak for strains and JoAnne Engebrecht for critical reading of the manuscript. Some strains were provided by the Caenorhabditis Genetics Center (CGC), which is funded by the NIH Office of Research Infrastructure Programs (P40 OD010440). We thank Karen McNally for her help with *spo-11* experiments and critical reading of the manuscript.

### Funding

This work was supported by the National Institute of General Medical Sciences grant R35GM136241 to FJM and by the US Department of Agriculture/National Institute of Food and Agriculture Hatch project (1009162 to FJM).

### Conflicts of interest

None declared.

### Literature cited

- Albertson DG, Thomson JN. Segregation of holocentric chromosomes at meiosis in the nematode, *Caenorhabditis elegans*. *Chromosom. Res.* 1993;1(1):15–26. doi:10.1007/BF00710603.
- Barbosa DJ, Teixeira V, Duro J, Carvalho AX, Gassmann R. Dynein-dynactin segregate meiotic chromosomes in *C. elegans* spermatocytes. *Dev.* 2021;148(3). doi:10.1242/DEV.197780/223267.
- Bielanska M, Tan SL, Ao A. Chromosomal mosaicism throughout human preimplantation development in vitro: incidence, type, and relevance to embryo outcome. *Hum Reprod.* 2002;17(2):413–419. doi:10.1093/HUMREP/17.2.413.
- Blokhina YP, Nguyen AD, Draper BW, Burgess SM. The telomere bouquet is a hub where meiotic double-strand breaks, synapsis, and stable homolog juxtaposition are coordinated in the zebrafish, *Danio rerio*. *PLoS Genet.* 2019;15(1):e1007730. doi:10.1371/JOURNAL.PGEN.1007730.
- Buonomo SBC, Clyne RK, Fuchs J, Loidl J, Uhlmann F, Nasmyth K. Disjunction of homologous chromosomes in meiosis I depends on proteolytic cleavage of the meiotic cohesin Rec8 by separin. *Cell.* 2000;103(3):387–398. doi:10.1016/S0092-8674(00)00131-8.
- Checchi PM, Lawrence KS, Van MV, Larson BJ, Engebrecht J. Pseudosynapsis and decreased stringency of meiotic repair

- pathway choice on the hemizygous sex chromosome of *Caenorhabditis elegans* males. *Genetics*. 2014;197(2):543–560. doi:10.1534/GENETICS.114.164152.
- Cortes D, McNally K, Mains PE, McNally FJ. The asymmetry of female meiosis reduces the frequency of inheritance of unpaired chromosomes. *Elife*. 2015;4:e06056. doi:10.7554/eLife.06056.
- Danlasky BM, Panzica MT, McNally KP, Vargas E, Bailey C, Li W, Gong T, Fishman ES, Jiang X, McNally FJ. Evidence for anaphase pulling forces during *C. elegans* meiosis. *J. Cell Biol.* 2020;219(12):e202005179. doi:10.1083/jcb.202005179.
- De Carvalho CE, Zaaier S, Smolikov S, Gu Y, Schumacher JM, Colaiácovo MP. LAB-1 antagonizes the Aurora B kinase in *C. elegans*. *Genes Dev.* 2008;22(20):2869–2885. doi:10.1101/gad.1691208.
- Dernburg AF, McDonald K, Moulder G, Barstead R, Dresser M, Villeneuve AM. Meiotic recombination in *C. elegans* initiates by a conserved mechanism and is dispensable for homologous chromosome synapsis. *Cell*. 1998;94(3):387–398. doi:10.1016/S0092-8674(00)81481-6.
- Dernburg AF, Sedat JW, Hawley RS. Direct evidence of a role for heterochromatin in meiotic chromosome segregation. *Cell*. 1996; 86(1):135–146. doi:10.1016/S0092-8674(00)80084-7.
- Dumont J, Oegema K, Desai A. A kinetochore-independent mechanism drives anaphase chromosome separation during acentrosomal meiosis. *Nat. Cell Biol.* 2010;12(9):894–901. doi:10.1038/ncb2093.
- Fabig G, Kiewisz R, Lindow N, Powers JA, Cota V, Quintanilla LJ, Brugués J, Prohaska S, Chu DS, Müller-Reichert T. Male meiotic spindle features that efficiently segregate paired and lagging chromosomes. *Elife*. 2020;9:e50988. doi:10.7554/eLife.50988.
- Ferrandiz N, Barroso C, Telecan O, Shao N, Kim HM, Testori S, Faull P, Cutillas P, Snijders AP, Colaiácovo MP, et al. Spatiotemporal regulation of Aurora B recruitment ensures release of cohesion during *C. elegans* oocyte meiosis. *Nat Commun.* 2018;9(1):834. doi:10.1038/s41467-018-03229-5.
- Gruhn JR, Zielinska AP, Shukla V, Blanshard R, Capalbo A, Cimadomo D, Nikiforov D, Chan ACH, Newnham LJ, Vogel I, et al. Chromosome errors in human eggs shape natural fertility over reproductive life span. *Science*. 2019;365(6460):1466–1469. doi:10.1126/SCIENCE.AAV7321.
- Heckmann S, Jankowska M, Schubert V, Kumke K, Ma W, Houben A. Alternative meiotic chromatid segregation in the holocentric plant *Luzula elegans*. *Nat Commun.* 2014;5(1):1–10. doi:10.1038/ncomms5979.
- Hodgkin J, Horvitz HR, Brenner S. Nondisjunction mutants of the nematode *Caenorhabditis elegans*. *Genetics*. 1979;91(1):67–94. doi:10.1093/genetics/91.1.67.
- Hughes SE, Gilliland WD, Cotitta JL, Takeo S, Collins KA, Hawley RS. Heterochromatic threads connect oscillating chromosomes during prometaphase I in drosophila oocytes. *PLOS Genet.* 2009;5(1):e1000348. doi:10.1371/JOURNAL.PGEN.1000348.
- Jaramillo-Lambert A, Engebrecht JA. A single unpaired and transcriptionally silenced X chromosome locally precludes checkpoint signaling in the *Caenorhabditis elegans* germ line. *Genetics*. 2010;184(3):613–628. doi:10.1534/GENETICS.109.110338.
- Jaramillo-Lambert A, Harigaya Y, Vitt J, Villeneuve A, Engebrecht J. Meiotic errors activate checkpoints that improve gamete quality without triggering apoptosis in male germ cells. *Curr Biol.* 2010; 20(23):2078–2089. doi:10.1016/j.cub.2010.10.008.
- Joglekar AP, Bloom KS, Salmon ED. Mechanisms of force generation by end-on kinetochore-microtubule attachments. *Curr. Opin. Cell Biol.* 2010;22(1):57–67. doi:10.1016/j.CEB.2009.12.010.
- Kirby C, Kusch M, Kemphues K. Mutations in the par genes of *Caenorhabditis elegans* affect cytoplasmic reorganization during the first cell cycle. *Dev Biol.* 1990;142:203–215. doi:10.1016/0012-1606(90)90164-E.
- Laband K, Le Borgne R, Edwards F, Stefanutti M, Canman JC, Verbavatz JM, Dumont J. Chromosome segregation occurs by microtubule pushing in oocytes. *Nat Commun.* 2017;8(1):1–11. doi:10.1038/s41467-017-01539-8.
- Le TS, Yang FJ, Lo YH, Chang TC, Hsu JC, Kao CY, Wang J. Non-Mendelian assortment of homologous autosomes of different sizes in males is the ancestral state in the *caenorhabditis* lineage. *Sci. Reports.* 2017;7(1):12819. doi:10.1038/s41598-017-13215-4.
- LeMaire-Adkins R, Hunt PA. Nonrandom segregation of the mouse univalent X chromosome: evidence of spindle-mediated meiotic drive. *Genetics*. 2000;156(2):775–783. doi:10.1093/genetics/156.2.775.
- McCarter J, Bartlett B, Dang T, Schedl T. On the control of oocyte meiotic maturation and ovulation in *Caenorhabditis elegans*. *Dev Biol.* 1999;205:111–128. doi:10.1006/DBIO.1998.9109.
- McCoy RC, Demko ZP, Ryan A, Banjevic M, Hill M, Sigurjonsson S, Rabinowitz M, Petrov DA. Evidence of selection against complex mitotic-origin aneuploidy during preimplantation development. *PLOS Genet.* 2015;11(10):e1005601. doi:10.1371/JOURNAL.PGEN.1005601.
- McNally KP, Panzica MT, Kim T, Cortes DB, McNally FJ. A novel chromosome segregation mechanism during female meiosis. *Mol Biol Cell.* 2016;27(16):2576–2589. doi:10.1091/mbc.E16-05-0331.
- Miller MP, Amon A, Ünal E. Meiosis I: when chromosomes undergo extreme makeover. *Curr. Opin. Cell Biol.* 2013;25(6):687–696. doi:10.1016/j.ceb.2013.07.009.
- Moore DF, Orr-Weaver TL. Chromosome segregation during meiosis: building an univalent bivalent. *Curr Top Dev Biol.* 1997;37: 263–299. doi:10.1016/S0070-2153(08)60177-5.
- Muscat CC, Torre-Santiago KM, Tran MV, Powers JA, Wignall SM. Kinetochore-independent chromosome segregation driven by lateral microtubule bundles. *Elife*. 2015;4:e06462. doi:10.7554/eLife.06462.
- Nagaoka SI, Hassold TJ, Hunt PA. Human aneuploidy: mechanisms and new insights into an age-old problem. *Nat Rev Genet.* 2012; 13(7):493. doi:10.1038/NRG3245.
- Nakka P, Pattillo Smith S, O'Donnell-Luria AH, McManus KF, Agee M, Auton A, Bell RK, Bryc K, Elson SL, Fontanillas P, et al. Characterization of prevalence and health consequences of uniparental disomy in four million individuals from the general population. *Am J Hum Genet.* 2019;105(5):921–932. doi:10.1016/j.AJHG.2019.09.016.
- Nicklas RB. Chromosome distribution: experiments on cell hybrids and in vitro. *Philos. Trans. R. Soc. London. B, Biol. Sci.* 1977;277-(955):267–276. doi:10.1098/rstb.1977.0017.
- Orvieto R, Shimon C, Rienstein S, Jonish-Grossman A, Shani H, Aizer A. Do human embryos have the ability of self-correction? *Reprod Biol Endocrinol.* 2020;18(1):1–6. doi:10.1186/S12958-020-00650-8.
- Phillips CM, Dernburg AF. A family of zinc-finger proteins is required for chromosome-specific pairing and synapsis during meiosis in *C. elegans*. *Dev Cell.* 2006;11(6):817–829. doi:10.1016/j.devcel.2006.09.020.
- Phillips CM, Meng X, Zhang L, Chretien JH, Urnov FD, Dernburg AF. Identification of chromosome sequence motifs that mediate meiotic pairing and synapsis in *C. elegans*. *Nat. Cell Biol.* 2009;11(8): 934–942. doi:10.1038/ncb1904.



- Phillips CM, Wong C, Bhalla N, Carlton PM, Weiser P, Meneely PM, Dernburg AF. HIM-8 binds to the X chromosome pairing center and mediates chromosome-specific meiotic synapsis. *Cell*. 2005; 123(6):1051–1063. doi:10.1016/j.cell.2005.09.035.
- Pradillo M, López E, Romero C, Sánchez-Morán E, Cuñado N, Santos JL. An analysis of univalent segregation in meiotic mutants of *Arabidopsis thaliana*: a possible role for synaptonemal complex. *Genetics*. 2007;175(2):505–511. doi:10.1534/GENETICS.106.067595.
- Raices M, Bowman R, Smolikove S, Yanowitz JL. Aging negatively impacts DNA repair and bivalent formation in the *C. elegans* germ line. *Front Cell Dev*. 2021;9:695333. doi:10.3389/FCELL.2021.695333.
- Redemann S, Lantsch I, Lindow N, Prohaska S, Srayko M, Müller-Reichert T. A switch in microtubule orientation during *C. elegans* meiosis. *Curr Biol*. 2018;28(18):2991–2997.e2. doi:10.1016/j.cub.2018.07.012.
- Rogers E, Bishop JD, Waddle JA, Schumacher JM, Lin R. The aurora kinase AIR-2 functions in the release of chromosome cohesion in *Caenorhabditis elegans* meiosis. *J Cell Biol*. 2002;157(2):219–229. doi:10.1083/jcb.200110045.
- Romanienko FJ, Camerini-Otero RD. The mouse Spo11 gene is required for meiotic chromosome synapsis. *Mol. Cell*. 2000;6(5): 975–987. doi:10.1016/S1097-2765(00)00097-6.
- Rosin LF, Gil J, Drinnenberg IA, Lei EP. Oligopaint DNA FISH reveals telomere-based meiotic pairing dynamics in the silkworm, *Bombyx mori*. *PLoS Genet*. 2021;17(7):e1009700. doi:10.1371/JOURNAL.PGEN.1009700.
- Severson AF, Ling L, Van Zuylen V, Meyer BJ. The axial element protein HTP-3 promotes cohesin loading and meiotic axis assembly in *C. elegans* to implement the meiotic program of chromosome segregation. *Genes Dev*. 2009;23(15):1763–1778. doi:10.1101/gad.1808809.
- Shakes DC, Wu JC, Sadler PL, LaPrade K, Moore LL, Noritake A, Chu DS. Spermatogenesis-specific features of the meiotic program in *Caenorhabditis elegans*. *PLoS Genet*. 2009;5(8):e1000611. doi:10.1371/JOURNAL.PGEN.1000611.
- Sigurdson DC, Spanier GJ, Herman RK. *Caenorhabditis elegans* deficiency mapping. *Genetics*. 1984;108(2):331–345. doi:10.1093/genetics/108.2.331.
- Stamper EL, Rodenbusch SE, Rosu S, Ahringer J, Villeneuve AM, Dernburg AF. Identification of DSB-1, a protein required for initiation of meiotic recombination in *Caenorhabditis elegans*, illuminates a crossover assurance checkpoint. *PLoS Genet*. 2013;9(8):e1003679. doi:10.1371/JOURNAL.PGEN.1003679.
- Theurkauf WE, Hawley RS. Meiotic spindle assembly in *Drosophila* females: behavior of nonexchange chromosomes and the effects of mutations in the nod kinesin-like protein. *J Cell Biol*. 1992; 116(5):1167–1180. doi:10.1083/JCB.116.5.1167.
- Thomas SE, Soltani-Bejnood M, Roth P, Dorn R, Logsdon JM, McKee BD. Identification of two proteins required for conjunction and regular segregation of achiasmata homologs in *Drosophila* male meiosis. *Cell*. 2005;123(4):555–568. doi:10.1016/j.cell.2005.08.043.
- Tzur YB, Egidio de Carvalho C, Nadarajan S, Van Bostelen I, Gu Y, Chu DS, Cheeseman IM, Colaiácovo MP. LAB-1 targets PP1 and restricts Aurora B kinase upon entrance into meiosis to promote sister chromatid cohesion. *PLoS Biol*. 2012;10(8):e1001378. doi:10.1371/journal.pbio.1001378.
- Vargas E, McNally K, Friedman JA, Cortes DB, Wang DY, Korf IF, McNally FJ. Autosomal trisomy and triploidy are corrected during female meiosis in *Caenorhabditis elegans*. *Genetics*. 2017;207(3): 911–922. doi:10.1534/genetics.117.300259.
- Wang J, Chen PJ, Wang GJ, Keller L. Chromosome size differences may affect meiosis and genome size. *Science*. 2010;329(5989): 293. doi:10.1126/SCIENCE.1190130.
- Wartosch L, Schindler K, Schuh M, Gruhn JR, Hoffmann ER, McCoy RC, Xing J. Origins and mechanisms leading to aneuploidy in human eggs. *Prenat Diagn*. 2021;41(5):620–630. doi:10.1002/PD.5927.
- Weber J, Kabacki Z, Chaurasia S, Brunner E, Lehner CF. Chromosome separation during *Drosophila* male meiosis I requires separase-mediated cleavage of the homolog conjunction protein UNO. *PLoS Genet*. 2020;16(10):e1008928. doi:10.1371/JOURNAL.PGEN.1008928.
- Wignall SM, Villeneuve AM. Lateral microtubule bundles promote chromosome alignment during acentrosomal oocyte meiosis. *Nat Cell Biol*. 2009;11(7):839–844. doi:10.1038/ncb1891.
- Yang M, Rito T, Metzger J, Naftaly J, Soman R, Hu J, Albertini DF, Barad DH, Brivanlou AH, Gleicher N. Depletion of aneuploid cells in human embryos and gastruloids. *Nat Cell Biol*. 2021;23(4): 314–321. doi:10.1038/s41556-021-00660-7.
- Zhang P, Hawley RS. The genetic analysis of distributive segregation in *Drosophila melanogaster*. II. Further genetic analysis of the nod locus. *Genetics*. 1990;125(1):115–127. doi:10.1093/genetics/125.1.115.

Editor: W. Gilliland

# Chapter 3

## **Evidence for anaphase pulling forces during *C. elegans* meiosis.**





Brennan M. Danlasky, Michelle T. Panzica, Karen P. McNally, Elizabeth Vargas, Cynthia Bailey, Wenzhe Li, Ting Gong, Elizabeth S. Fishman, Xueer Jiang, and Francis J. McNally

Danlasky BM, Panzica MT, McNally KP, Vargas E, Bailey C, Li W, Gong T, Fishman ES, Jiang X, McNally FJ. Evidence for anaphase pulling forces during *C. elegans* meiosis. *J Cell Biol.* 2020 Dec 7;219(12):e202005179. doi: 10.1083/jcb.202005179. PMID: 33064834; PMCID: PMC7577052.

In this project, I worked with Brennan and performed experiments examining the function of dynein during *C. elegans* meiosis. I participated in data analysis and preparing Fig 9 for this manuscript.

ARTICLE

# Evidence for anaphase pulling forces during *C. elegans* meiosis

Brennan M. Danlasky, Michelle T. Panzica\* , Karen P. McNally\*, Elizabeth Vargas, Cynthia Bailey, Wenzhe Li , Ting Gong, Elizabeth S. Fishman, Xueer Jiang , and Francis J. McNally 

**Anaphase chromosome movement is thought to be mediated by pulling forces generated by end-on attachment of microtubules to the outer face of kinetochores. However, it has been suggested that during *C. elegans* female meiosis, anaphase is mediated by a kinetochore-independent pushing mechanism with microtubules only attached to the inner face of segregating chromosomes. We found that the kinetochore proteins KNL-1 and KNL-3 are required for preanaphase chromosome stretching, suggesting a role in pulling forces. In the absence of KNL-1,3, pairs of homologous chromosomes did not separate and did not move toward a spindle pole. Instead, each homolog pair moved together with the same spindle pole during anaphase B spindle elongation. Two masses of chromatin thus ended up at opposite spindle poles, giving the appearance of successful anaphase.**

## Introduction

In eukaryotes, segregation of chromosomes during mitosis and meiosis is widely thought to require kinetochores, multiprotein structures that usually assemble at a single defined region of a chromosome called a centromere and that mediate binding to spindle microtubules. The outer kinetochore KMN network, composed of KNL-1, the MIS-12 complex, and the NDC-80 complex, is thought to directly mediate attachment of chromosomes to spindle microtubules (Cheeseman et al., 2006). End-on attachments of microtubule plus ends to NDC-80 complexes on the outer face of chromosome pairs is coupled with depolymerization of the plus ends to generate pulling forces that separate chromosomes from each other and move chromatids toward spindle poles. This results in a chromatid-to-pole movement called anaphase A (Inoué and Ritter, 1978; Vukušić et al., 2019). During anaphase B, the spindle lengthens and chromosomes move with the separating poles (Inoué and Ritter, 1978). Anaphase B is thought to be driven by outward pushing through a combination of anti-parallel sliding and microtubule polymerization between the separating chromosomes (Vukušić et al., 2019). Several observations have led to the idea that the outer faces of kinetochores are still attached to spindle microtubules during anaphase B. Bundles of microtubules called K-fibers extend from pole to kinetochore during anaphase B (Mastrorarde et al., 1993; McDonald et al., 1992), and chromosome arms trail behind kinetochores during anaphase B (Inoué and Ritter, 1978). Cutting the spindle between a kinetochore and

spindle pole sometimes caused the chromosome to transiently stop moving (Spurck et al., 1997). In addition, depletion of kinetochore proteins blocked anaphase B chromosome movement in the *Caenorhabditis elegans* embryonic mitotic spindle (Oegema et al., 2001).

Several observations in *C. elegans* oocyte meiotic spindles have suggested that different mechanisms are at work. (1) KNL-1, which is required for recruiting NDC-80 to the kinetochore, was reported to dissociate from chromosomes during anaphase and not be required for anaphase chromosome movement (Dumont et al., 2010). (2) Anaphase chromosome movement was not affected by laser ablation on the poleward side of chromosomes but was stopped by ablation between separating chromosomes, suggesting that microtubules push outward on the inner faces of separating chromosomes (Laband et al., 2017). (3) End-on microtubule attachments have not been observed on the poleward face of chromosomes. Only lateral microtubule attachments have been observed in metaphase and early anaphase, and end-on attachment to the inner face of chromosomes has been observed in late anaphase (Laband et al., 2017; McNally et al., 2006; Muscat et al., 2015; Redemann et al., 2018; Wignall and Villeneuve, 2009; Yu et al., 2019). (4) The kinetochore protein KNL-3 dissociated from chromosomes during anaphase, and KNL-3 depletion actually rescued anaphase in embryos depleted of the nuclear envelope and kinetochore protein MEL-28 (Hattersley et al., 2016). This latter result suggested

Department of Molecular and Cellular Biology, University of California, Davis, Davis, CA.

\*M.T. Panzica and K.P. McNally contributed equally to this paper; Correspondence to Francis J. McNally: [fjmcnally@ucdavis.edu](mailto:fjmcnally@ucdavis.edu).

© 2020 Danlasky et al. This article is distributed under the terms of an Attribution-Noncommercial-Share Alike-No Mirror Sites license for the first six months after the publication date (see <http://www.rupress.org/terms/>). After six months it is available under a Creative Commons License (Attribution-Noncommercial-Share Alike 4.0 International license, as described at <https://creativecommons.org/licenses/by-nc-sa/4.0/>).

Rockefeller University Press

J. Cell Biol. 2020 Vol. 219 No. 12 e202005179



<https://doi.org/10.1083/jcb.202005179>

1 of 18

Downloaded from [http://rupress.org/jcb/article-pdf/219/12/202005179/1831966/jcb\\_202005179.pdf](http://rupress.org/jcb/article-pdf/219/12/202005179/1831966/jcb_202005179.pdf) by guest on 06 December 2023

that MEL-28-dependent removal of the KMN network might be important for anaphase.

In organisms with localized centromeres, the cohesin that holds sister centromeres together is protected from separase during anaphase I, ensuring that homologs separate during anaphase I but sisters remain together until anaphase II (Watanabe, 2005). Because *C. elegans* chromosomes do not have localized centromeres, they cannot use this strategy for ensuring homolog segregation before sister separation during meiosis. Instead, a single crossover generates a bivalent with two long arms and two short arms. Cohesion is protected on the long arms during anaphase I (de Carvalho et al., 2008), and conserved kinetochore cups (Dumont et al., 2010; Kaitna et al., 2002; Rogers et al., 2002; Wignall and Villeneuve, 2009). Aurora B kinase mediates separase cleavage of short-arm cohesin and homolog separation at anaphase I (Ferrandiz et al., 2018a; Rogers et al., 2002). At anaphase onset, there is no apparent kinetochore protein on the inner face of separating homologs, raising the question of how microtubules might be attached to the inner face of chromosomes as suggested by Laband et al. (2017). To address this question, we first analyzed the localization of KNL-1 and the MIS-12 subunit KNL-3 during anaphase in *C. elegans* female meiosis.

## Results

### Endogenously GFP-tagged KNL-1 and KNL-3 transition from cups to rings at the start of anaphase B

Live imaging of a *C. elegans* strain bearing in-frame GFP insertions at the endogenous *knl-1* and *knl-3* loci revealed cup-shaped structures enveloping the poleward face of mCherry::histone H2b-labeled chromosomes during metaphase and early anaphase ( $n = 10/10$ ; Fig. 1 A, 0–2:05; Video 1). At the onset of anaphase B, defined as the switch from spindle shortening to spindle elongation, GFP-labeled KNL-1 and KNL-3 transitioned to enveloping all sides of each separating homolog so that they appeared as rings in optical sections ( $n = 10/10$ ; Fig. 1 A, 2:45–4:25). This transition was previously observed by antibody staining of un-tagged KNL-1 (Monen et al., 2005). The fluorescence intensity of chromosome-associated KNL-1::GFP + GFP::KNL-3, measured as a unitless ratio to background fluorescence, decreased significantly between metaphase,  $4.45 \pm 0.68$  min before initiation of spindle elongation, and the ring stage of anaphase B,  $0.63 \pm 0.11$  min after initiation of spindle elongation (metaphase: mean  $5.09 \pm 0.71$ ;  $n = 11$ ; anaphase B: mean  $1.96 \pm 0.15$ ;  $n = 11$ ;  $P = 0.0003$ ), whereas the fluorescence intensity of mCherry::H2b did not decrease significantly (metaphase: mean  $2.80 \pm 0.31$ ;  $n = 11$ ; anaphase B: mean  $3.00 \pm 0.36$ ;  $n = 11$ ;  $P = 0.70$ ). This decrease in intensity might explain why KNL-1 and KNL-3 were previously described as dissociating from chromosomes during anaphase (Davis-Roca et al., 2017; Dumont et al., 2010; Hattersley et al., 2016). These rings also appeared at the onset of anaphase B in strains with only KNL-1::GFP or only GFP::KNL-3

(Fig. 1 B). The localization of kinetochore proteins on the inner face of separating homologs could provide attachment points for midzone microtubules during anaphase B. Consistent with this idea, KNL-1::mCherry rings were surrounded by GFP::ASPM-1, a microtubule minus-end binding protein (Fig. 1 C).

Kinetochore proteins are found in at least three pools during oocyte meiosis. In addition to cups or rings around chromosomes, KNL-1 and 3 accumulated on spindle poles just before spindle rotation (Fig. 1 A; 0:00; 10/10 spindles), as previously reported for ZWL-1 (McNally et al., 2016), and were found in ROD-1-dependent linear elements on the spindle and embryo cortex during metaphase I (Fig. 1 D; 11/11 control embryos: cups and linear elements; 13/13 *rod-1(RNAi)* embryos: cups but no linear elements), as previously reported (Dumont et al., 2010). KNL-1 and 3 still localized in rings around late anaphase homologs after ROD-1 depletion (Fig. 1 E; 11/11 controls had rings, and 12/12 *rod-1(RNAi)* had rings), indicating they are not just caused by occlusion of linear elements that have accumulated at spindle poles. In control spindles, chromosomes are surrounded by the spindle pole protein ASPM-1 during anaphase and occlude GFP::ASPM-1 fluorescence (Fig. 1 F). Thus, the anaphase rings of KNL-1/3 could simply result from occlusion of spindle pole KNL-1,3 by chromosomes. However, in *mei-2(RNAi)* spindles, which have no discrete spindle poles (Fig. 1 F; Connolly et al., 2014; McNally and McNally, 2011), GFP-tagged KNL-1,3 still transitioned from cups to rings (Fig. 1 G; 3/3 time-lapse sequences). These results suggest that the KNL rings are not just an optical artifact of chromosomes occluding spindle pole KNL-1,3 and that the inner face of these rings could provide microtubule attachment points during anaphase B, as further suggested by time-lapse images of mKate2::tubulin and GFP-tagged KNL-1,3 (Fig. 2 A; 3:10–5:30) and by EM results (Laband et al., 2017; Redemann et al., 2018).

### Microtubules are in close proximity to the poleward face of kinetochore cups

It has been suggested that *C. elegans* oocyte bivalents lack end-on microtubule attachments on their poleward face for two reasons. First, mCherry::H2b-labeled chromatin (McNally et al., 2006, 2016; Wignall and Villeneuve, 2009) and DAPI-stained chromatin (Davis-Roca et al., 2017; Muscat et al., 2015) reside in microtubule-free channels during metaphase and early anaphase. Second, microtubule ends were not observed within 250 nm of the poleward chromatin surface at metaphase or anaphase by EM (Redemann et al., 2018). The 250-nm distance was chosen because of EM observations of a ribosome-free layer around *C. elegans* chromosomes that has been interpreted as the kinetochore (Howe et al., 2001; O'Toole et al., 2003). Endogenously GFP-tagged KNL-1 and 3, however, extended much farther poleward than mCherry::H2b (Fig. 1 A; 0:00). Indeed, simultaneous live imaging of mKate2::tubulin and GFP-tagged KNL-1,3 revealed that the KNL cups completely fill the microtubule-free channels (Fig. 2, B–D; and Video 1). In contrast, gaps are apparent between the poleward face of mCherry::H2b and spindle poles (Fig. 3 A). This observation raises the possibility that KNL-1,3 extend farther poleward than the ribosome-free zone. If microtubule plus ends are present in this farther-poleward

Danlasky et al.

Kinetochore pulling for meiotic homolog separation

Journal of Cell Biology

<https://doi.org/10.1083/jcb.202005179>

2 of 18

Downloaded from <http://ajph.org/> on July 21, 2020. For personal use only; all rights reserved.

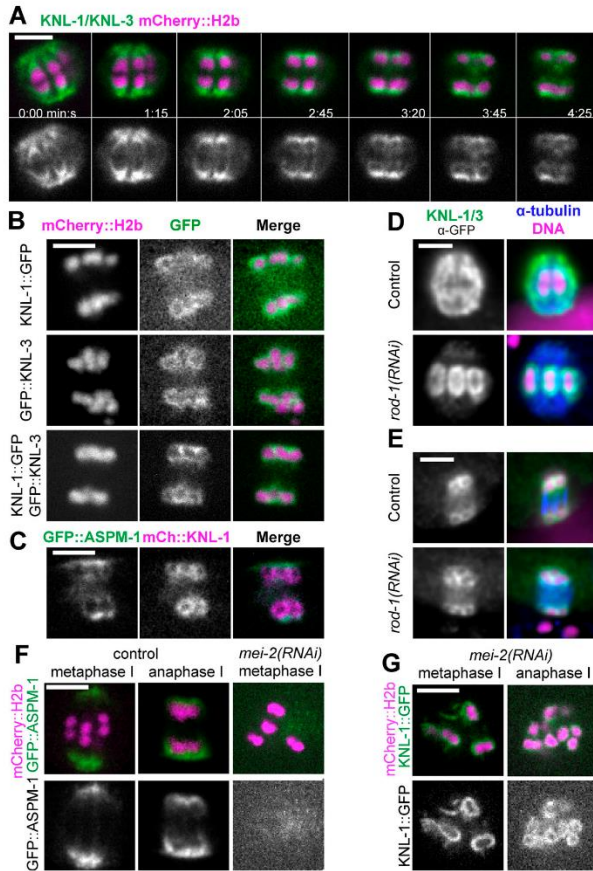


**Figure 1. Kinetochores transition from cups to rings at anaphase onset. (A–C)** Single-focal plane time-lapse imaging of meiosis I embryos expressing the indicated fusions. **(A)** 0 min is mid spindle rotation. 1:15 is the beginning of homolog separation. **(B)** Individual localization of KNL-1::GFP and GFP::KNL-3 in late anaphase, during spindle elongation. **(C)** KNL-1::mCherry is surrounded by GFP::ASPM-1 at anaphase. **(D and E)** Fixed immunofluorescence images show that metaphase kinetochore cups **(D)** and anaphase kinetochore rings **(E)** remain on chromosomes after depletion of linear elements. **(F and G)** Time-lapse images reveal that KNL-1/3 still transition from cups to rings in the absence of ASPM-1-labeled spindle poles. Bars = 3  $\mu$ m. mCh, mCherry.

volume, KNL-1-dependent NDC-80 (Dumont et al., 2010) might transiently engage with these plus ends as the spindle shortens. Alternatively, the microtubules on the poleward face of KNL-1,3 could generate pulling forces through lateral interactions with the KNL cups, as suggested by EM analysis (Redemann et al., 2018). The existence of pulling interactions is supported by the observation of points of GFP-tagged KNL-1,3 extending poleward from the tips of kinetochore cups (Fig. 2 B).

**KNL-1 and KNL-3 are required for metaphase chromosome congression and biorientation**

Because Dumont et al. (2010) found that GFP::KNL-3 remained in kinetochore cups after *knl-1(RNAi)*, we chose to double deplete KNL-1 and KNL-3 to more completely reduce kinetochore function during meiosis. Two previously described methods were used, auxin-induced degradation in strains with auxin-induced degrons (AIDs) appended to the endogenous *knl-1* and *knl-3* genes and *GFP(RNAi)* on strains with GFP appended to the endogenous *knl-1* and *knl-3* genes (Vargas et al., 2019). After 48-h RNAi, GFP fluorescence was not observed around chromosomes

in living embryos (Fig. 3 B); however, staining of fixed embryos with a polyclonal anti-GFP antibody revealed faint puncta associated with meiotic chromosomes (Fig. S1, A and B). The anti-GFP staining intensity of these residual puncta, measured as a unitless ratio to background, was sixfold lower than that of the cup structures around control RNAi chromosomes (control RNAi: mean  $12.6 \pm 1.2$ ;  $n = 44$  embryos; *GFP(RNAi)*: mean  $1.9 \pm 0.2$ ;  $n = 16$  embryos;  $P = 0.0001$ ). Both auxin-induced degradation (Fig. 3 A) and *GFP(RNAi)* depletion of KNL-1 and KNL-3 (Fig. 3 B) resulted in failure to position bivalents at the metaphase plate. Because no significant differences were found between the two depletion methods (Fig. S2), phenotypic data were pooled and are referred to as *knl-1,3(kd)* for “knockdown.” In addition to failure of bivalents to position at a metaphase plate (Fig. 3 C), bivalents frequently failed to orient down the pole-to-pole axis of the spindle (Fig. 3 D). These two defects were previously reported for *knl-1(RNAi)* (Dumont et al., 2010). In addition, 40% of double-depleted metaphase spindles had at least one bivalent on the outside edge of the spindle (Fig. 3, A, B, and E). *knl-1,3(kd)* spindles frequently had two or more bivalents

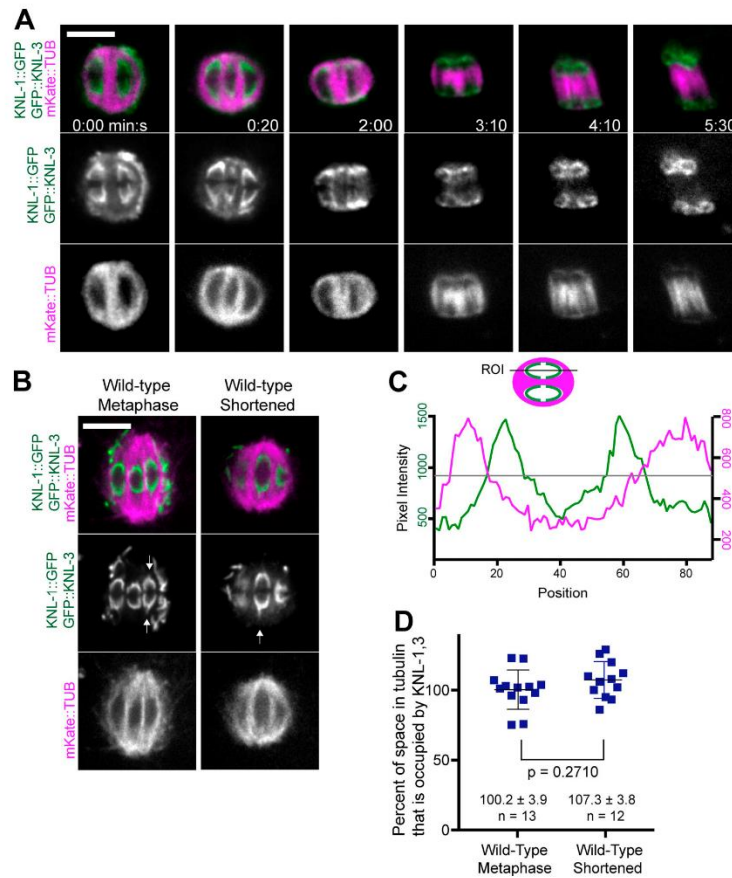


**Figure 2. Microtubule-free channels are filled with kinetochores. (A and B)** Single-focal plane time-lapse sequences of embryos expressing KNL-1::GFP, GFP::KNL-3, and mKate::tubulin. Arrows indicate points of KNL-1,3 extending poleward. **(C)** Fluorescence intensity profile down the length of a shortened spindle just before anaphase onset. Gray line indicates the half-maximal intensity of mKate::tubulin. The inside edge of the microtubule-free channel was defined as the position of the inner red half-maximal intensity, and the outside edge of KNL was defined as the position of the outer green half-maximal intensity. **(D)** The length of KNL signal divided by the length of its corresponding microtubule-free channel. Values and error bars indicate mean  $\pm$  SEM. Bars = 4  $\mu$ m. ROI, region of interest; TUB, tubulin.

stacked end to end along the pole-to-pole axis of the spindle (Fig. 3 A) as previously described (Vargas et al., 2019). Finally, *kn1-1,3(kd)* spindles did not have apparent microtubule-free channels oriented in the pole-to-pole axis (Fig. 3 A). This might indicate that intact kinetochore cups contribute to the organization of spindle microtubules. However, these congression defects were not due to a complete lack of spindle bipolarity as occurs in NDC-80-depleted mouse oocytes (Gui and Homer, 2013; Yoshida et al., 2020). Z-stacks of 16/18 *kn1-1,3(kd)* live metaphase spindles labeled with GFP::ASPM-1 exhibited two spindle poles (Video 2). 2/18 z-stacks exhibited a smaller third pole. Instead, these congression defects might be due to a lack of poleward pulling forces on chromosomes.

**KNL-1 and KNL-3 are required for bivalent stretching**

Poleward pulling forces on the two halves of a bivalent before cohesin cleavage should deform elastic chromatin, making bivalents longer and narrower. To specifically test for kinetochore-dependent chromosome stretching, we monitored bivalent length in control or *kn1-1,3(kd)* embryos expressing mCherry::H2b and GFP::NPP-6, which labels kinetochore cups independently of KNL-1 and 3 (Hattersley et al., 2016; Fig. 4 A). We previously found that ZWL-1-labeled kinetochore cups stretch dramatically just before homolog separation (McNally et al., 2016). Because homolog separation is defective in *kn1-1,3(kd)* embryos (see below), we measured the change in bivalent length between  $5.7 \pm 0.47$  min and  $2.2 \pm 0.15$  min before

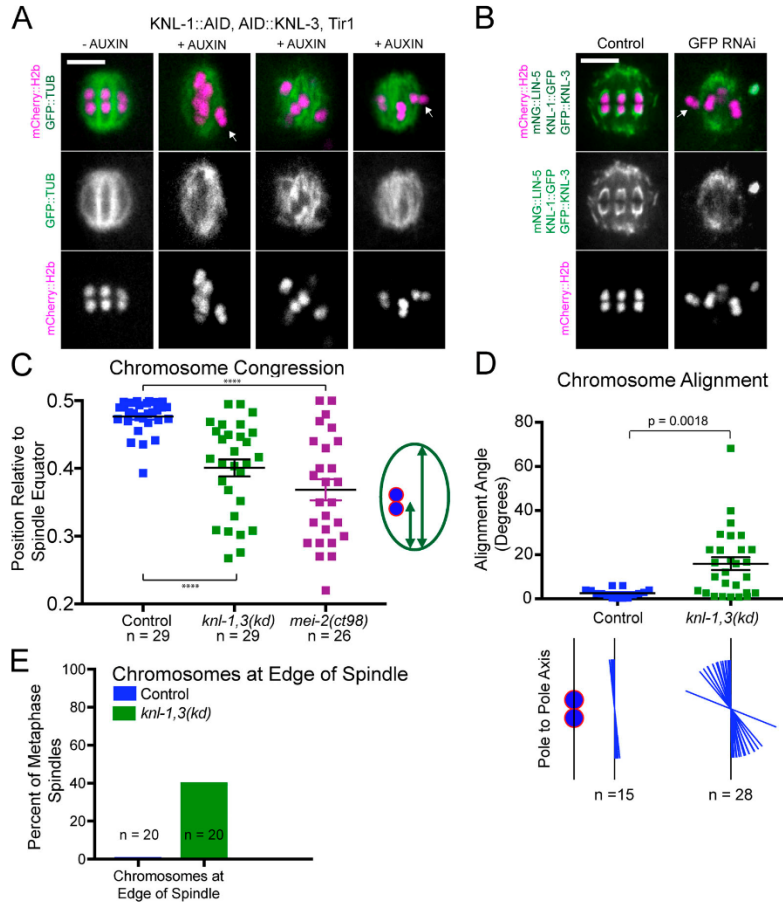


Figure 3. *knl-1,3(kd)* metaphase spindles have chromosome congression and alignment defects. (A and B) Single time points from time-lapse sequences of metaphase spindles depleted of KNL-1 and KNL-3 by auxin-induced degradation (A) or *GFP(RNAi)* (B). Arrows indicate chromosomes on periphery of spindle. The bright green body in the last image is that of a nearby sperm. (C) The relative position of each bivalent along the pole-to-pole axis of its spindle. A congressed bivalent has an expected ratio of 0.5. (D) The angle of individual chromosomes relative to the pole-to-pole axis was determined in five control and nine *knl-1,3(kd)* metaphase spindles. The alignment of each chromosome is illustrated below the graph. (E) The percentage of *knl-1,3(kd)* spindles with chromosomes on the outside edge of the spindle. Error bars indicate mean  $\pm$  SEM. Bars = 4  $\mu$ m. \*\*\*\*,  $P < 0.0001$ . mNG, mNeonGreen; TUB, tubulin.

Downloaded from [http://jcbpress.org/jcb/article-pdf/217/17/202005179/1831968/jcb\\_202005179.pdf](http://jcbpress.org/jcb/article-pdf/217/17/202005179/1831968/jcb_202005179.pdf) by guest on 06 December 2023

initiation of spindle elongation. Both inter-homolog (Fig. 4, B and C) and intra-homolog (Fig. 4 D) distances increased significantly between these time points (referred to as metaphase and preanaphase) in control embryos. In *knl-1,3(kd)* embryos, inter-homolog and intra-homolog distances did not increase between metaphase and preanaphase, and these distances were significantly smaller than in control embryos (Fig. 4, A-D; and Fig. S3, A-D). The increase in bivalent length between metaphase and preanaphase in control embryos might be due to ROD-1-dependent expansion of kinetochore volume (Pereira et al., 2018) or to stretching. However, the cross-sectional area of control bivalents did not change significantly at preanaphase when

length increased (Fig. S3 E), and bivalent length still increased after *rod-1(RNAi)* (distance between homolog centers, metaphase:  $1.15 \pm 0.05 \mu$ m and preanaphase:  $1.40 \pm 0.05 \mu$ m;  $P = 0.0013$ ). This result indicated that KNL-1 and 3 are required for stretching that would be indicative of preanaphase bipolar pulling forces on bivalents. Bivalent length (Fig. 4 B) and intra-homolog stretch (Fig. 4 D) were also significantly reduced in *knl-1,3(kd)* relative to controls at metaphase but to a lesser extent than at preanaphase. These results suggest that reduced pulling forces could contribute to the congression defect and that pulling forces increase just before homolog separation ( $2.2 \pm 0.15$  min before initiation of spindle elongation).

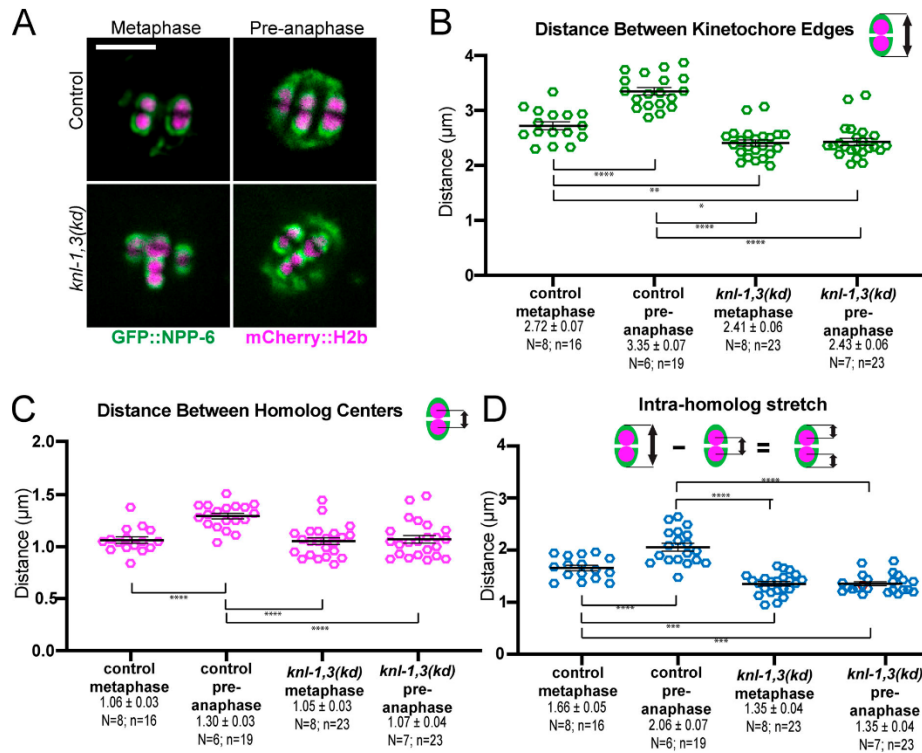


Figure 4. Depletion of KNL-1 and KNL-3 results in loss of bivalent stretching. (A) Single frames from time-lapse sequences showing the stages when measurements were made. Metaphase: 5.7 min and preanaphase: 2.2 min before initiation of spindle elongation. (B) Distances between GFP::NPP-6-labeled kinetochore edges. (C) Distances between mCherry::H2b-labeled homolog centers. (D) Distances between GFP::NPP-6-labeled kinetochore edges and mCherry::H2b homolog centers, as a metric for intra-homolog stretching. Error bars and values are mean  $\pm$  SEM. Bar = 4  $\mu$ m. \*,  $P < 0.05$ ; \*\*,  $P < 0.01$ ; \*\*\*,  $P < 0.001$ ; \*\*\*\*,  $P < 0.0001$ . N, number of embryos; n, number of bivalents.

**KNL-1 and KNL-3 are required for anaphase A and homolog separation**

In control time-lapse sequences, all bivalents split into two homologs that moved to opposite spindle poles before the initiation of spindle elongation (Fig. 5, A and E; and Video 3). In *knl-1,3(kd)* embryos, 60% of bivalents did not split into two homologs before the initiation of spindle elongation and instead moved intact with one spindle pole during spindle elongation (Fig. 5, B, C, and E; Video 4; and Video 5). 19 bivalents in 14 embryos that segregated intact with one spindle pole eventually separated at heterogeneous times during spindle elongation ( $1.12 \pm 0.91$  min; range, 0.5–3.2 min after initiation of spindle elongation; Video 6). Only five bivalents remained intact through the end of the time-lapse sequence. As judged by size, no bivalents were observed in 11/11 metaphase II spindles, and both sister chromatids of 14/23 metaphase II univalents ended up at the same end of the anaphase II spindle. The delay in bivalents splitting into two homologs is not entirely an indirect consequence of the preceding congression defect since bivalents separated into two

homologs in a *mei-2(ct98)* mutant that also had a severe congression defect (Fig. 3 C; and Fig. 5, D and E) but had intact kinetochore cups (Fig. 5 F). The congression defect could contribute, however, as most of the bivalents segregating intact were either stacked end to end at metaphase or were close to one pole at the onset of anaphase B. Separase localization on metaphase chromosomes and between anaphase chromosomes appeared normal in KNL-1,3-depleted spindles (Fig. S1), although a delay in relocalization might not be detected. AIR-2, which is required for cleavage of cohesin by separase (Ferrandiz et al., 2018b; Rogers et al., 2002), also localized normally between homologs at metaphase (Fig. S4, A and B). AIR-2 also dissociated from chromosomes and associated with midzone microtubules during anaphase in *knl-1,3(kd)* spindles as it did in controls (Fig. S4, A and B).

In control spindles, anaphase occurred in three phases. (1) Spindles first shortened in the pole-to-pole axis. (2) Chromosomes then separated a short distance as the spindle continued to shorten (anaphase A). (3) Spindles abruptly transitioned to lengthening (anaphase B), during which chromosomes moved at



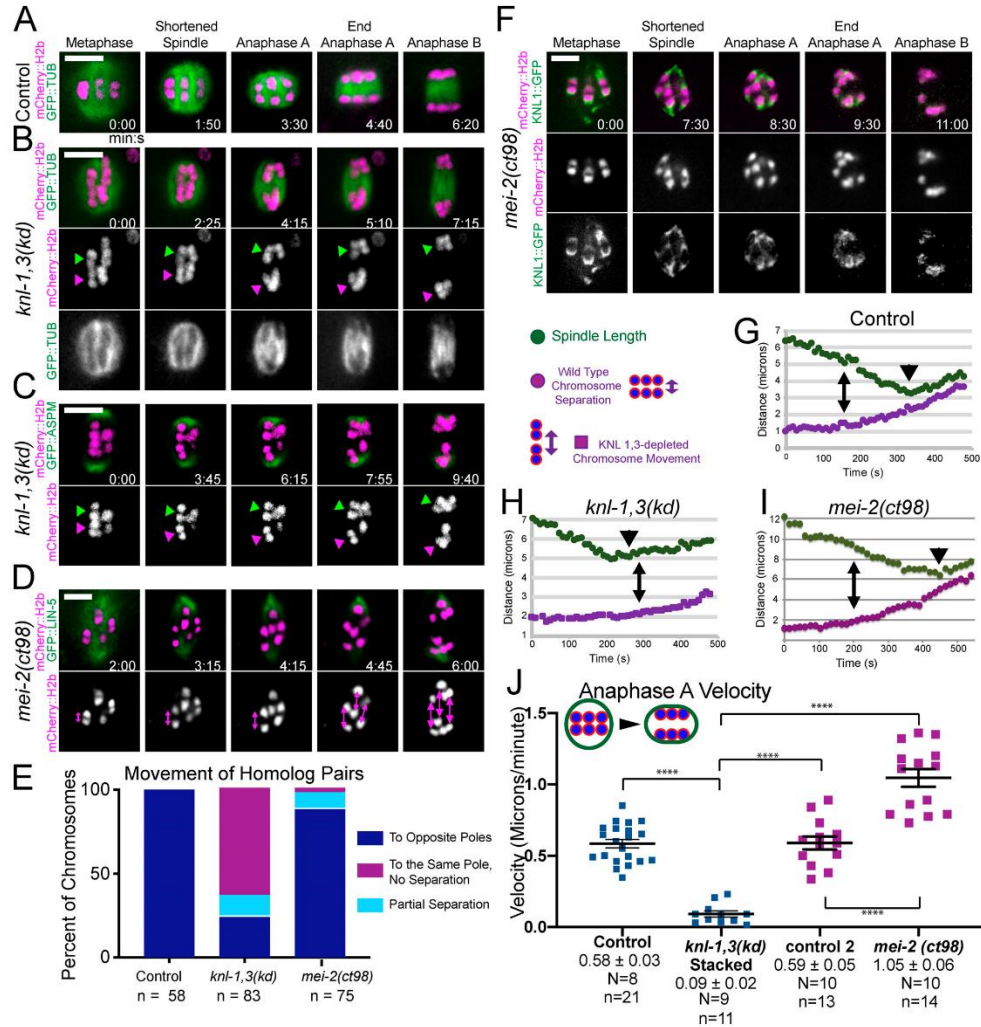


**Figure 5. KNL-1 and KNL-3 are required for anaphase A chromosome segregation.** (A–D) Representative time-lapse sequences of control (A), *knl-1,3(kd)* (B and C), and *mei-2(ct98)* (D) embryos. Arrowheads in B and C indicate intact bivalents segregating. Double arrows in D indicate homolog separation. (E) The fate of individual homolog pairs. (F) KNL-1 localizes properly to cups and rings in *mei-2(ct98)*. (G–I) Representative plots of spindle length and distance between homolog centers over time. For *knl-1,3(kd)* embryos, distance between separating intact bivalents is shown. Time 0 is initiation of spindle shortening. Double arrows indicate the initiation of homolog separation in G and I and initiation of bivalent separation in H. Arrowheads indicate initiation of spindle elongation. (J) Homolog separation velocities during the 90 s before initiation of spindle elongation. For *knl-1,3(kd)* embryos, velocities shown are between midbivalents of intact bivalents that later moved apart during anaphase B. Error bars and values are mean ± SEM. Bars = 4 μm. \*\*\*\*, P < 0.0001. N, number of embryos; n, number of chromosomes; TUB, tubulin.

the same speed as the separating spindle poles (Fig. 5, A and G; McNally et al., 2016). In *knl-1,3(kd)* spindles, spindle shortening occurred at wild-type velocities (control:  $-1.03 \pm 0.06 \mu\text{m}/\text{min}$ ;  $n = 22$ ; *knl-1,3(kd)*:  $-0.98 \pm 0.06 \mu\text{m}/\text{min}$ ;  $n = 18$ ), but chromosomes only began to move apart when spindle elongation started (Fig. 5, B, C, and H). This failure of anaphase A was not due only

to the preceding congression defect, as anaphase A occurred in *mei-2(ct98)* spindles, which also have a congression defect (Fig. 3 C; and Fig. 5, D and I).

To more carefully document anaphase A velocities, we measured the velocity of homolog separation during the 90 s before the initiation of spindle elongation because anaphase A

occurs during this period in control spindles (Fig. 5 G). Chromosome movement was greatly reduced during this period in *knl-1,3(kd)* spindles. These measurements included both distances between homologs that later segregated to opposite poles (Fig. S2 B) and distances between stacked bivalents that later separated from each other intact (Fig. 5 J). In contrast, anaphase A velocities were significantly faster in *mei-2(ct98)* spindles than in control spindles (Fig. 5 J). These results suggest that KNL-1 and 3 are required for pulling forces that drive anaphase A while the spindle is still shortening.

#### Anaphase B occurs in KNL-1,3-depleted spindles but is highly error prone

The majority of chromosomes in *knl-1,3(kd)* spindles moved at the same velocity as the separating spindle poles, and this anaphase B velocity was significantly faster than controls (Fig. 6 A and Fig. S2 D). GFP::tubulin fluorescence appeared between separating chromosomes in both control (Fig. 6 B) and *knl-1,3(kd)* spindles (Fig. 6 C, arrowhead), consistent with fibers pushing chromosomes apart. However, anaphase B was highly error prone in *knl-1,3(kd)* spindles. One chromosome frequently moved in a direction nearly perpendicular to the two major separating masses of chromosomes, with bundles of microtubules lengthening between each major mass and the errant chromosome (Fig. 6 C, 10:10–12:10; Fig. 6, D and E; and Fig. S2 C). The observations of intact bivalents moving apart (Fig. 5, C–E) and microtubule bundles lengthening in three-way anaphases (Fig. 6 C) suggested that microtubule bundles push any two chromosome masses apart in *knl-1,3(kd)* spindles. The result of this promiscuous pushing between intact bivalents was that the total mass of chromatin in the two separated masses of chromosomes, measured as the 3D sum of mCherry::H2b pixel values, was unequal in *knl-1,3(kd)* spindles at the end of anaphase B (Fig. 6 F).

#### KNL-1,3 surround late-lagging univalents as they are stretched

Univalent X chromosomes, resulting from crossover failure in a *him-8* mutant, do not lose cohesion, frequently lag during late anaphase, and appear to be stretched as they are captured by the ingressing polar body membrane (Cortes et al., 2015; Fig. 7 A). The explanation for stretching has been unclear because chromosome stretching is associated with bipolar pulling forces and because laser cutting experiments suggested that pushing forces predominate in late anaphase (Laband et al., 2017). In 9/9 *him-8* anaphase I spindles with a late-lagging univalent, GFP-tagged KNL-1,3 enveloped the univalent as it stretched (Fig. 7 A and Video 7). Because KNL-1,3 are required for metaphase chromosome stretching (Fig. 4), this result suggested that KNL-1,3 could still be exerting pulling forces during late anaphase. The naturally univalent X chromosome in spermatocytes is also stretched during anaphase and is associated with both end-on and lateral microtubule attachments to kinetochores (Fabig et al., 2020). Davis-Roca et al. (2017) reported that a variety of conditions causing meiotic errors result in a delay in the dissociation of KNL-3 from anaphase chromosomes. However, we observed no difference between control and *him-8* embryos in the decrease of KNL-1::GFP + GFP::KNL-3 between metaphase and anaphase (Fig. 7 B).

#### NDC-80 is required for KNL-1,3-dependent anaphase A homolog separation but not anaphase A chromosome-to-pole movement

NDC-80 and RZZ-dependent dynein are the most obvious candidates for KNL-1,3-dependent poleward force generators at kinetochores because of their *in vitro* activities and because both NDC-80 and the RZZ component ZWL-1 require KNL-1 for association with kinetochore cups (Dumont et al., 2010). To test whether the phenotypes of *knl-1,3(kd)* spindles could be caused only by loss of NDC-80, we constructed a strain with a GFP tag at the endogenous *ndc-80* gene that also expressed mNeonGreen-tagged tubulin and mCherry::H2b and that also contained the KNL-1 and KNL-3 degrons. Auxin treatment indicated that association of endogenously GFP-tagged NDC-80 is dependent on KNL-1,3 (Fig. 8, A and B;  $n = 6/6 -1$  oocytes). We then subjected the *ndc-80(GFP)* worms to GFP(RNAi). This treatment resulted in a complete loss of NDC-80 from kinetochore cups (Fig. 8 C;  $n = 14/15 -1$  oocytes). Metaphase congression defects were observed in a significantly lower fraction of NDC-80-depleted embryos than in *knl-1,3(kd)* embryos (Fig. 8 D vs. Fig. 3 C; 21/24 spindles in *knl-1,3(kd)* versus 4/10 *ndc-80* spindles; Fisher's exact test;  $P = 0.008$ ). Bivalent stretching in NDC-80-depleted embryos was intermediate between that of control and *knl-1,3(kd)* embryos (Fig. S3, F–I). Similar to *knl-1,3(kd)* embryos (Fig. 5 E), intact bivalents were observed moving apart from each other at high frequency in NDC-80-depleted embryos (Fig. 8, D–F; Video 8; and Video 9). In contrast with intact bivalents in *knl-1,3(kd)* embryos, which exhibited no anaphase A-like chromosome movement (Fig. 5, H and J), intact bivalents in NDC-80-depleted spindles moved toward one pole at wild-type velocities (Fig. 8 F, arrows; and Fig. 8 G). Anaphase B velocity was the same between control, NDC-80-depleted (Fig. 8 H), and *knl-1,3(kd)* embryos (Fig. 6). The weaker phenotypes of NDC-80 depletion suggested that either KNL-1,3 have some NDC-80-independent function or that residual amounts of NDC-80, which were not detectable by GFP fluorescence (Fig. 8 C), remain after GFP(RNAi) but not after *knl-1,3(kd)*.

#### Cytoplasmic dynein is not associated with anaphase chromosomes, is not required for anaphase A, and restrains anaphase B

Using endogenously GFP-tagged dynein heavy chain, we first found that dynein was associated with metaphase I kinetochore cups in time-lapse sequences of 8/10 control embryos (Fig. 9 A). Previous studies of *C. elegans* mitosis (Gassmann et al., 2008) or meiosis (Muscat et al., 2015) found kinetochore dynein only in experimentally induced monopolar spindles. Our robust detection in control embryos allowed us to demonstrate that association of dynein with metaphase kinetochore cups was dependent on KNL-1,3 (Fig. 9, A and B) and on ROD-1 (Fig. 9 C; mean background subtracted pixel values at bivalents: control,  $135 \pm 24$ ;  $n = 10$ ; *knl-1,3(kd)*,  $32 \pm 11$ ;  $n = 10$ ; *rod-1(RNAi)*,  $16 \pm 8$ ;  $n = 8$ ). During anaphase A, kinetochore dynein merges with spindle pole dynein (Fig. 9 A), and spindle pole dynein is ASPM-1 dependent (van der Voet et al., 2009). To test whether DHC-1 is associated with chromosomes during anaphase B, we imaged endogenously tagged DHC-1 in *aspm-1(RNAi)* spindles.

Danlasky et al.

Kinetochore pulling for meiotic homolog separation

Journal of Cell Biology

<https://doi.org/10.1083/jcb.202005179>

8 of 18

Downloaded from <http://jcbpress.org/> on October 19, 2020. For personal use only; all rights reserved.

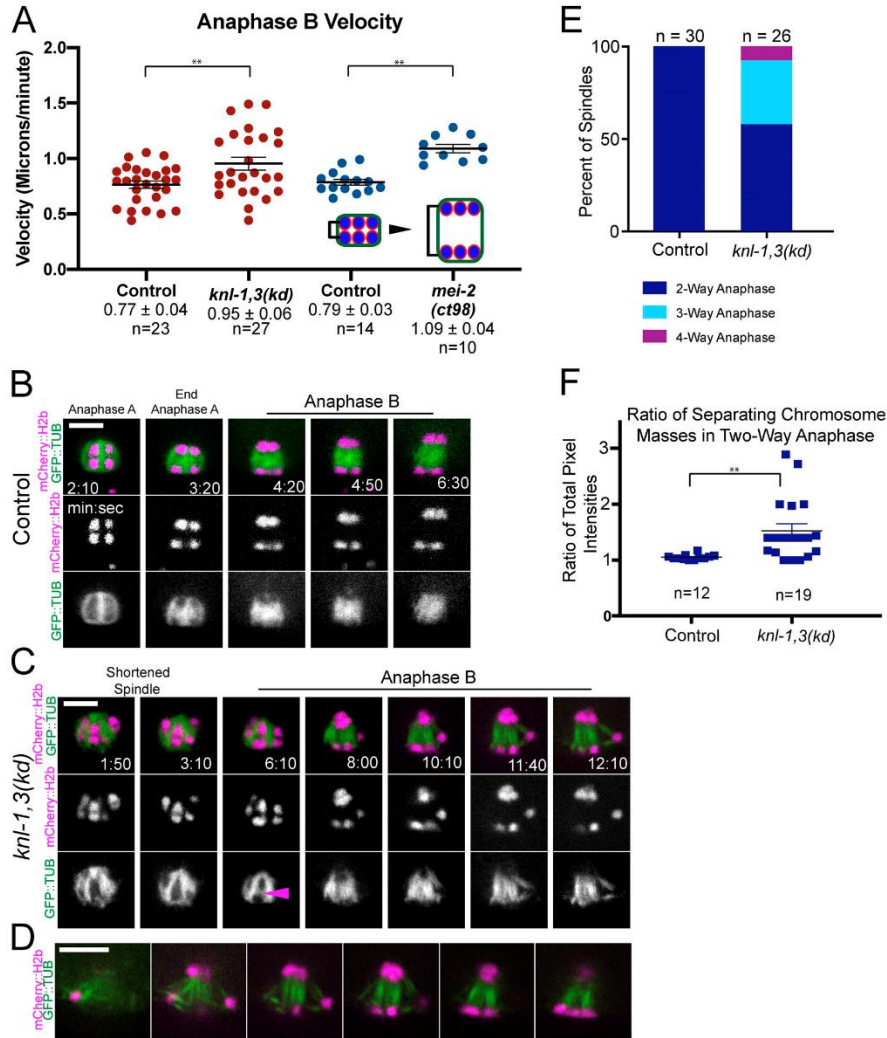


Figure 6. **Aberrant anaphase B occurs in *knl-1,3(kd)* embryos.** (A) Velocities of chromosome separation during spindle elongation. (B and C) Representative time-lapse sequences of anaphase B. Arrowhead in C indicates tubulin appearing between separating chromosomes. 8:00–12:10 min:sec in C shows an example of “three-way anaphase” in which a chromosome moved perpendicular to the spindle axis while attached to the spindle by two microtubule bundles. Arrowhead indicates microtubules between separating chromosomes. (D) z-Stack of a single time point in a *knl-1,3(kd)* embryo shows a “four-way anaphase.” (E) Frequencies of aberrant anaphases. (F) Fluorescence intensity of separated chromosome masses at the end of anaphase B. Error bars and values are mean  $\pm$  SEM. \*\*,  $P < 0.01$ . Bars = 4  $\mu$ m. TUB, tubulin.

In *aspm-1(RNAi)* embryos, DHC-1 localized in kinetochore cups during metaphase (8/10 embryos) but completely dissociated from chromosomes before anaphase A (Fig. 9 D;  $n = 5/5$  embryos, mean background subtracted pixel values at *aspm-1(RNAi)* chromosomes: metaphase,  $152 \pm 34$ ;  $n = 10$ ; anaphase,  $30 \pm 11$ ;  $n = 5$ ). These results indicated that KNL-1,3 and ROD-1 target dynein to kinetochore cups during metaphase but that dynein near

chromosomes during anaphase A is not directly associated with chromosomes and is instead associated with ASPM-1 and microtubules that surround the chromosomes.

To address the role of dynein in anaphase chromosome movement, we monitored anaphase A velocities after 1 h of auxin-induced degradation of DHC-1 (Zhang et al., 2015) and after *rod-1(RNAi)*. DHC-1::degron + auxin spindles failed to rotate

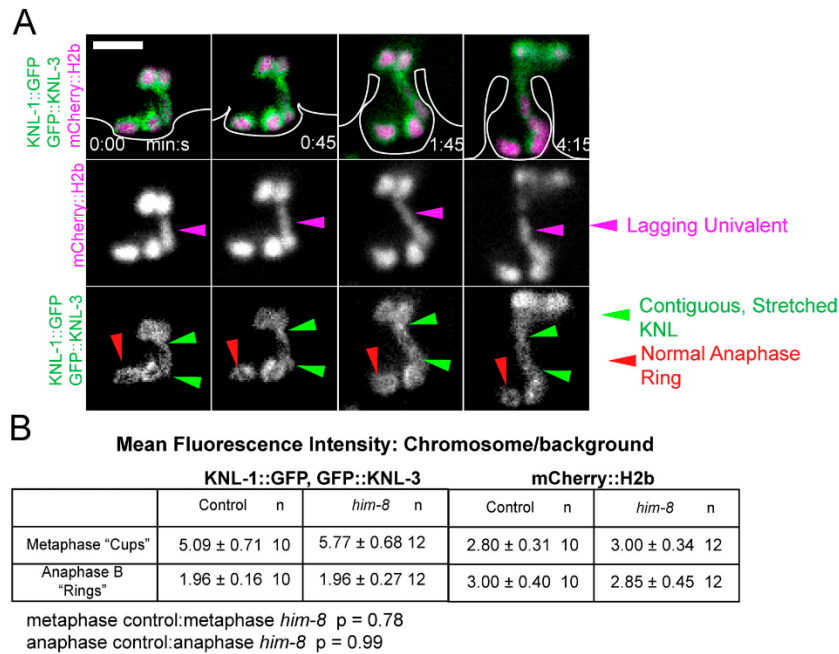


Figure 7. **Univalent X chromosomes in a *him-8* mutant are coated in KNL-1,3 as they are stretched during late anaphase.** (A) Representative time-lapse sequence of late anaphase in a *him-8* mutant. Polar body ingress, which is only visible with enhanced contrast, has been drawn for clarity. (B) The decrease in fluorescence intensity of KNL-1::GFP, GFP::KNL-3 between metaphase and anaphase is not significantly different between control and *him-8*. Values are mean ± SEM. Bar = 3 μm.

and were long with pointed poles as previously reported for partial RNAi depletion (Crowder et al., 2015; Ellefson and McNally, 2009), but anaphase A velocities were not significantly slower than controls in DHC-1::AID + auxin or in *rod-1*(RNAi) spindles (Fig. 9 E). Anaphase B velocities were significantly faster in DHC-1::AID + auxin but not in *rod-1*(RNAi) (Fig. 9 F). These results are consistent with previously reported wild-type or faster than wild-type anaphase velocities in *dhc-1*(RNAi) (McNally et al., 2016), *dhc-1*(ts), *dnc-6*(null), *zwl-1*(RNAi), and *spd-1*(RNAi) (Laband et al., 2017). These results indicate that chromosomal dynein does not play a role in anaphase A or B but that nonchromosomal dynein slows spindle elongation during anaphase B. We were unable to test for redundancy between NDC-80 and dynein because endogenously tagged NDC-80::GFP was not completely depleted in worms treated with both *GFP*(RNAi) and *rod-1*(RNAi). However, because DHC-1 is not associated with chromosomes during anaphase, it is not likely to be an anaphase force generator at chromosomes.

**Robust mechanisms mediate attachment of chromosomes to microtubules**

Kinetochores are widely thought to mediate attachment of chromosomes to microtubules, but chromosomes were never observed to completely dissociate from spindle microtubules in *kn1-1,3(kd)* spindles. This attachment might be mediated by a

small residual number of molecules of KMN network proteins or by KNL-1,3-independent microtubule-binding proteins. Microtubule-binding proteins known to associate with chromosomes in the absence of KNL-1 during metaphase include the midbivalent ring components KLP-19, HCP-1,2, and CLS-2 (Dumont et al., 2010). The SUMO ligase, GEI-17, and SUMO are required for recruitment of KLP-19 and BUB-1 to the midbivalent ring (Pelisch et al., 2019, 2017). Midbivalent rings elongate in microtubule-free channels between separating homologs during early anaphase, and then some components transfer to microtubules in late anaphase (Fig. S4, A and C; Davis-Roca et al., 2018; Dumont et al., 2010; Laband et al., 2017; Muscat et al., 2015; Pelisch et al., 2019). Meiosis in auxin-treated *kn1-1*, *kn1-3*, *k1p-19*, and *kn1-1*, *kn1-3*, *gei-17* triple-degron strains proceeded essentially identically to *kn1-1,3(kd)* meiosis (Fig. S4, D-G; and Video 10). No chromosomes completely detached from the spindle in 21 *GEI-17* triple-depleted meioses and in only 2/14 *KLP-19* triple-depleted meioses, a chromosome that moved perpendicular to the long axis of the spindle completely detached during late anaphase I and was not incorporated into the metaphase II spindle (Fig. S4 H).

The kinesin 13, KLP-7, is also a microtubule-binding protein that is associated with chromosomes during meiosis and thus might provide redundant attachments between chromosomes

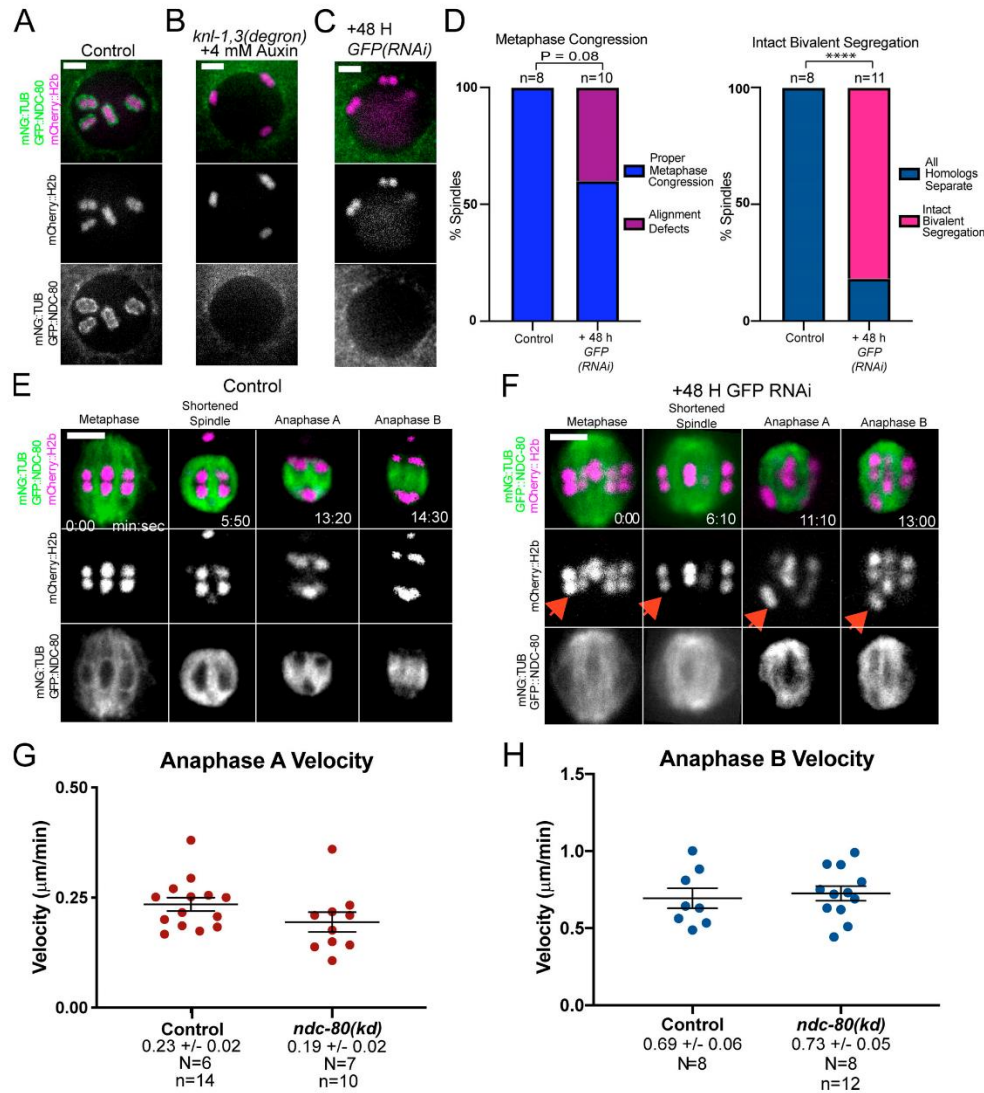


Figure 8. NDC-80 depletion results in intact bivalents moving poleward at wild-type anaphase A velocity. (A–C) Maximum intensity projections of –1 oocytes. GFP::NDC-80 was not detected on bivalents in *knl-1,3(kd)* (B) or *GFP(RNAi)* oocytes (C). (D) Frequency of congression and anaphase defects in control and NDC-80-depleted embryos from time-lapse sequences. \*\*\*\*,  $P < 0.0001$ . (E and F) Representative time-lapse sequences of control (E) and NDC-80-depleted (F) embryos. Arrows indicate an intact bivalent moving poleward. (G) Chromatid-to-pole velocities in control and NDC-80-depleted embryos. Note these control velocities are one half the homolog separation velocities reported in Fig. 5. (H) Anaphase B velocities of control and NDC-80-depleted embryos. Error bars and values are mean  $\pm$  SEM. Bars = 3  $\mu\text{m}$ . N, number of embryos; n, number of chromosomes. mNG, mNeonGreen; TUB, tubulin.

and microtubules. KLP-7 endogenously tagged at the C-terminus with mNeonGreen (Heppert et al., 2018) and, observed live, was most concentrated on meiotic chromosomes in a bi-lobed pattern similar to histone H2b-labeled chromatin throughout metaphase and anaphase, with lower amounts in the

midbivalent ring during metaphase (Fig. 10 A, 0 and 2:30; Fig. S5 A; 11/11 control embryos). This pattern was similar to that previously observed (Connolly et al., 2015; Gigant et al., 2017; Han et al., 2015). KLP-7::mNeonGreen was lost from midbivalent rings in 6/7 *knl-1,3(kd)* embryos but remained associated with

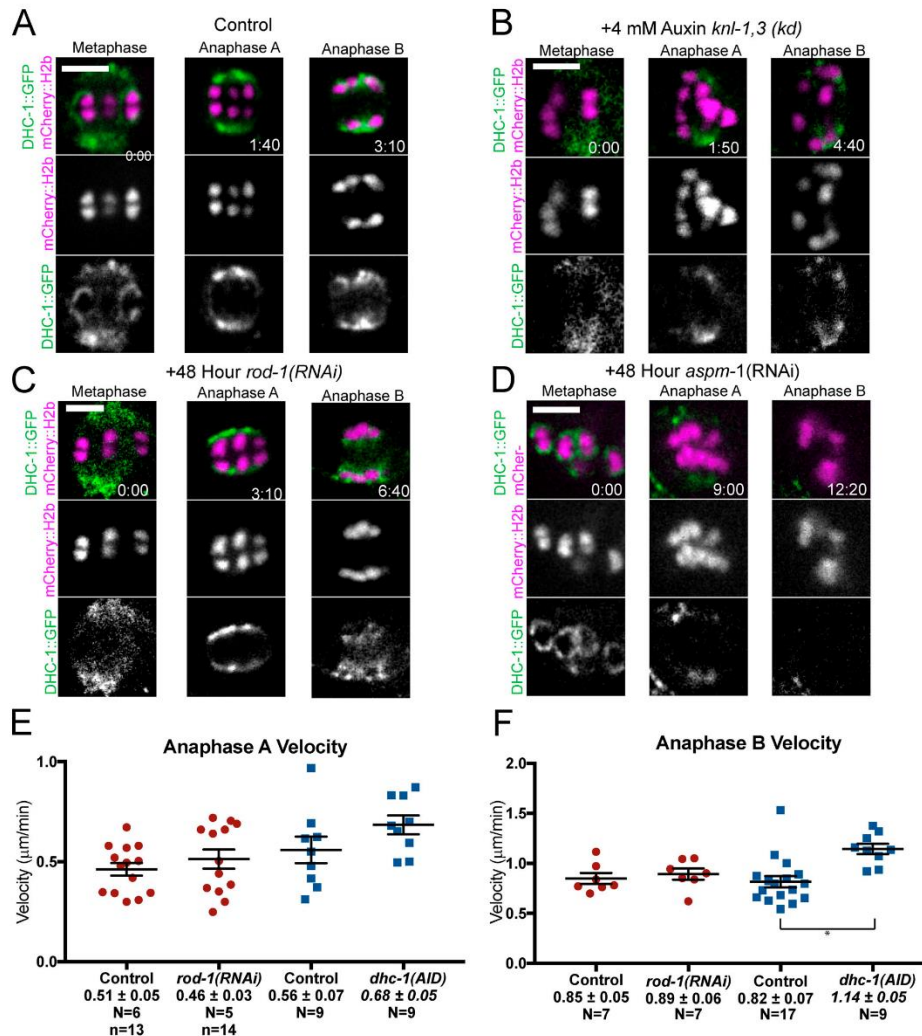


Figure 9. Dynein is not present on anaphase chromosomes, and auxin-induced degradation of dynein does not slow anaphase. (A–D) Representative time-lapse images of endogenously GFP-tagged DHC-1. (A) In control embryos, DHC-1 is in kinetochore cups at metaphase and spindle poles during anaphase A and overlaps with poles and chromosomes during anaphase B. (B and C) Neither *knl-1,3(kd)* bivalents (B) nor *rod-1(RNAi)* bivalents (C) exhibit DHC-1 on kinetochore cups at metaphase. (D) *aspm-1(RNAi)* embryos retain DHC-1 on kinetochore cups at metaphase but have no DHC-1 on poles or anaphase chromosomes. (E and F) Auxin-induced degradation of DHC-1 does not slow anaphase A or B. \*,  $P < 0.05$ . Error bars and values are mean  $\pm$  SEM. Bars = 3  $\mu$ m. N, number of embryos; n, number of chromosomes.

chromatin throughout metaphase and anaphase in 7/7 *knl-1,3(kd)* embryos (Fig. 10 B; and Fig. S5, A and B). In agreement with previous studies (Connolly et al., 2015; Gigant et al., 2017; Han et al., 2015), KLP-7 accumulated on spindle poles during spindle shortening in control embryos (Fig. 10 A, 2:30). In contrast, KLP-7 did not accumulate on spindle poles in 6/7 *knl-1,3(kd)* embryos (Fig. 10 B). In control but not *knl-1,3(kd)* embryos, the mean

fluorescence intensity of KLP-7::mNeonGreen increased between metaphase and anaphase (Fig. 10 C). These results indicate that KNL-1,3 recruited KLP-7 to spindle poles but not to chromatin and that the increase in apparent chromosomal intensity during anaphase in control embryos was due to merging of pole and chromosomal pools. These results also suggest that KLP-7 could mediate chromosome–microtubule attachments in

the absence of KNL-1,3 during error-prone anaphase B. We were unable to directly test this because *knl-1,3(degron) klp-7(RNAi)* oocytes would not ovulate.

The *C. elegans* katanin, MEI-1/MEI-2, binds microtubules (Joly et al., 2016; McNally et al., 2014; McNally and McNally, 2011) and colocalizes with DAPI or mCherry::H2b inside the kinetochore cups (McNally et al., 2006; Srayko et al., 2000). *mei-1(null)* mutants assemble apolar meiotic spindles (Connolly et al., 2014; McNally and McNally, 2011). *mei-1(RNAi)* also results in an increased velocity of cytoplasmic streaming during meiosis (Kimura et al., 2017), which should scatter any chromosomes not attached to the apolar spindle. Anti-GFP staining of fixed embryos from a strain with endogenously GFP-tagged *knl-1*, *knl-3*, and *mei-1* genes after *GFP(RNAi)* did not reveal any GFP remaining on chromosomes. In 14/16 of these embryos, all maternal chromosomes were associated with the apolar spindle (Fig. S5, C and D). In only two triple-depleted embryos (Fig. S5 E), chromosomes were observed far from the apolar spindle. Attachment of chromosomes to microtubules in *knl-1,3(kd)* thus may be mediated by KLP-7, by very low amounts of MEI-1/2 or KLP-19, or by unknown factors.

## Discussion

The results presented here extend the findings of Dumont et al. (2010) by showing that KNL-1,3 are required for homolog separation and anaphase A chromosome-to-pole movement. Our results are consistent with their study in that anaphase B velocities are not affected by depletion of the KMN network and this kinetochore-independent anaphase is highly error prone. Dumont et al. (2010) reported that the number of chromosomes on the metaphase II plate of *knl-1(RNAi)* embryos was altered to 5.6 from the wild-type number of 6. This number was reported as a mean, and since error-prone anaphase I segregation can result in loss or gain of chromosomes, the only clue to the severity of this phenotype was the reported standard error of 1.1.

The finding that depletion of KNL-1,3 or NDC-80 diminishes the bivalent stretching that occurs between metaphase and preanaphase strongly supports the existence of poleward pulling forces that may be established during spindle shortening. Purified NDC-80 complexes generate force at the plus end of depolymerizing microtubules (Powers et al., 2009), but only the sides of microtubules have been observed in close proximity to the ribosome-free layer of *C. elegans* chromosomes during late metaphase by EM (Redemann et al., 2018). Possible explanations for this discrepancy include the following: (1) Plus-end attachments may have been missed in EM analysis because the kinetochore extends much farther poleward than the ribosome-free zone, as suggested in Fig. 2. (2) Plus-end attachments may occur only transiently just before homolog separation, a stage not yet captured by EM. (3) The lateral contacts observed by EM are converted to a transient plus-end attachment when each microtubule depolymerizes from its plus end. By analogy, the plus-end contacts with the embryo cortex that mediate spindle positioning have an average lifetime of 1.4 s (Kozłowski et al., 2007). Photobleaching experiments indicate that meiotic spindle microtubules turn over extremely rapidly (Yu et al., 2019). (4)

NDC-80 and KNL-1 (Espeut et al., 2012) might bind the side of a microtubule, while the minus end of that microtubule is transported toward the minus end of another microtubule by ROD-1-independent dynein (Eking et al., 2014; Sikirzhyski et al., 2014; Tan et al., 2018). (5) Pulling on the lateral surface of microtubules is generated either by an unknown KMN-dependent protein or by an unknown mechanism of the known KMN components. Whatever the mechanism, pulling is likely achieved by arrays of very short overlapping microtubules rather than microtubules running contiguously from chromosome to pole (Laband et al., 2017; Redemann et al., 2018; Srayko et al., 2006).

The observation that both homologs that later separate during anaphase B and bivalents that remain intact during anaphase B undergo attenuated anaphase A movement toward spindle poles in *knl-1,3(kd)* suggests a lack of poleward pulling forces that persist during normal anaphase A. In addition, the presence of GFP::KNL rings around *him-8* univalent X chromosomes that are stretched during late anaphase also supports the persistence of pulling forces into late anaphase B. The homolog separation failure after depletion of KNL-1,3 or NDC-80 thus could indicate that homologs must be pulled apart even after cohesin cleavage. Pulling might help resolve remaining topological entanglements (Hong et al., 2018a, 2018b), or molecular crowding might slow the separation of chromosome-sized objects by Brownian motion (Delarue et al., 2018) in the absence of pulling. Alternatively, KMN might act as a positive regulator of separase through an unknown mechanism. In *Drosophila melanogaster* oocyte meiosis, the KNL-1 homolog SPC105R is a negative regulator of separase (Wang et al., 2019). The end-to-end stacking of bivalents at metaphase of *knl-1,3(kd)* spindles may also inhibit homolog separation. Anaphase A homolog separation may be important to generate a sufficient distance to allow the microtubule polymerization between homologs that drives anaphase B (Dumont et al., 2010; Laband et al., 2017).

Prior observations that spindle cutting on the poleward face of *C. elegans* female meiotic spindles did not alter anaphase velocity (Laband et al., 2017) and that cutting between separating chromosomes immediately stopped chromosome movement (Laband et al., 2017; Yu et al., 2019) are consistent with a long history of spindle cutting experiments in mitotic and meiotic spindles of a variety of species (Spurck et al., 1997, 1990). Elting et al. (2014) and Sikirzhyski et al. (2014) found that poleward chromosome movement after cutting on the poleward side was caused by dynein-mediated transport of the minus end of a kinetochore fiber on other spindle microtubules. Thus, cutting on the poleward face of a chromosome does not necessarily block pulling forces on that chromosome. Cutting between homologs in meiosis I or between sister chromatids in meiosis II or mitosis is not possible until after proper chromosome separation has started. Thus, midzone cutting experiments cannot show that poleward pulling is dispensable for proper chromosome separation. In some studies (Nicklas, 1989), neither cutting in front of nor behind an anaphase chromosome was able to stop anaphase motion.

The idea that anti-parallel microtubule bundles push on the inner faces of separating chromosomes must be resolved with

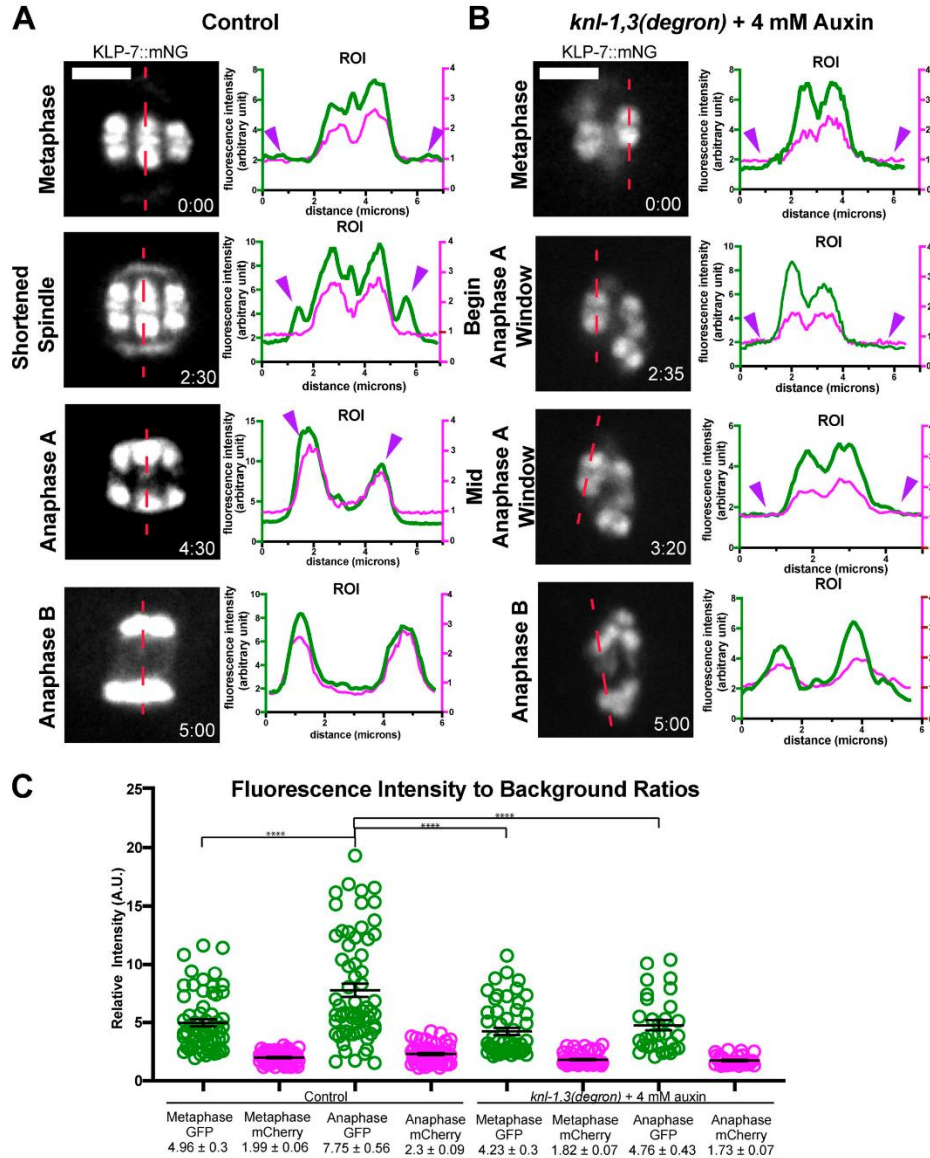


Figure 10. **The kinesin-13 KLP-7 is retained on bivalent chromatin in KNL-1,3-depleted embryos.** (A and B) Representative time-lapse sequences of endogenously tagged KLP-7::mNeonGreen in control and *knl-1,3(kd)* embryos. Fluorescence intensity plots along the dotted red lines are shown for KLP-7::mNeonGreen in green and mCherry::H2b in red. Purple arrowheads indicate spindle poles. (C) KLP-7::mNeonGreen fluorescence associated with chromosomes. Error bars and values are mean ± SEM. Bars = 3 μm. \*\*\*\*, P < 0.0001. mNG, mNeonGreen; ROI, region of interest.

the observation that chromosome arms lag behind kinetochores during anaphase B in species with localized centromeres (Inoué and Ritter, 1978) and that chromosomes move in unison without tumbling or dissociating from the spindle even in the presence

of cytoplasmic streaming, as occurs in the *C. elegans* meiotic embryo (McNally et al., 2010; Yang et al., 2003). Our finding that KNL-1, KNL-3, and NDC-80, representatives of the three components of the KMN network, all transition into rings that cover



the inner face of anaphase B chromosomes suggests a possible attachment point for pushing fibers.

## Materials and methods

*C. elegans* strains were generated by standard genetic crosses, and genotypes were confirmed by PCR. Genotypes of all strains are listed in Table S1.

### Live in utero imaging

L4 larvae were incubated at 20°C overnight on MYOB plates seeded with OP50, except for auxin treatments in which L4 larvae were incubated at 16°C overnight, and FGP7 L4 larvae were treated at 25°C overnight. Worms were anesthetized by picking 20 adult hermaphrodites with a platinum wire into a solution of 0.1% tricaine, 0.01% tetramisole in PBS in a watch glass for 30 min as described in Kirby et al. (1990) and McCarter et al. (1999). Worms were then transferred in a small volume (@ 20  $\mu$ l) to the center of a thin agarose pad (2% in water) on a slide. Additional PBS was pipetted around the edges of the agarose pad, and a 22- $\times$ -30-mm cover glass was placed on top. The slide was then inverted and placed on the stage of an inverted microscope. Meiotic embryos adjacent to the spermatheca were then identified by bright-field microscopy before initiating time-lapse fluorescence. For all live imaging, the stage and immersion oil temperature was 22°C–24°C. For all live imaging data other than Video 2 and Fig. 8, A–C, single-focal plane time-lapse images were acquired with a Solamere spinning disk confocal microscope equipped with an Olympus IX-70 stand, Yokogawa CSU10, Hamamatsu ORCA FLASH 4.0 CMOS (complementary metal oxide semiconductor) detector, Olympus 100 $\times$ /1.35 objective, 100-mW Coherent Obis lasers set at 30% power, and MicroManager software control. Pixel size was 65 nm. Exposures were 100 ms. Time interval between image pairs was 10 s with the following exceptions. Fig. 1, A–C; Fig. 3, A and B; Fig. 5, A–C; and Fig. 6, B and C were acquired at 5-s intervals. Fig. 5, D and F was captured at 15-s intervals. Focus was adjusted manually during time-lapse imaging. Only images in which both spindle poles and/or both bivalent halves were in focus were used for quantitative analysis. Both poles or both half-bivalents were considered to be in focus when both exhibited equal brightness and sharpness.

For scoring spindle bipolarity by imaging GFP::ASPM-1 (Video 2 and data in text), nine images were acquired at 1- $\mu$ m z-steps for the first time point. Subsequently, single-plane images were acquired at 5-s intervals.

For documenting NDC-80 depletion from bivalents in Fig. 8, A–C, z-stacks were acquired at 1- $\mu$ m steps and 100-ms exposures through the entire nucleus of the -1 oocyte, the most mature oocyte before nuclear envelope breakdown. -1 oocytes were used because mNeonGreen::tubulin, which is required for documenting anaphase A versus B, is excluded from the nucleus, allowing documentation of GFP::NDC-80 depletion. Only two or three focal planes were subjected to maximum intensity projection for the figure because of cytoplasmic mNeonGreen::tubulin fluorescence in the focal planes above and below.

Danlasky et al.

Kinetochores pulling for meiotic homolog separation

### Timing

Control spindles maintain a steady-state length of 8  $\mu$ m for 7 min before initiating APC-dependent spindle shortening, followed by spindle rotation, followed by homolog separation as the spindle continues to shorten (anaphase A), and followed by a transition to spindle elongation (anaphase B; McNally et al., 2016; Yang et al., 2005). Because *knl-1,3(kd)* affects spindle dimensions, spindle rotation (Vargas et al., 2019), chromosome congression, and anaphase movement, we used time relative to the initiation of spindle elongation to compare parameters between control and *knl-1,3(kd)*.

### Auxin

*C. elegans* strains with *knl-1* and *knl-3* endogenously tagged with auxin-inducible degrons and aTIR1 transgene were treated with 4 mM auxin overnight on seeded plates. *dhc-1(AID)* (Zhang et al., 2015) strains were treated with 4 mM auxin for 1 h on seeded plates.

### RNAi

L4 larvae were placed on IPTG-induced lawns of HT115 bacteria bearing L4440-based plasmids. After 48 h, worms were fixed or imaged live. RNAi clones for *aspm-1*, *rod-1*, and *mei-2* were from the genomic RNAi feeding library (Medical Research Council Gene Services, Source BioScience, Nottingham, UK; Kamath et al., 2003). *C. elegans* optimized GFP was cloned into L4440 for the GFP(RNAi) experiments.

### Fixed immunofluorescence

*C. elegans* meiotic embryos were extruded from hermaphrodites in 0.8 $\times$  egg buffer by gently compressing worms between coverslip and slide, flash frozen in liquid N<sub>2</sub>, permeabilized by removing the coverslip, and then fixed in ice-cold methanol before staining with antibodies and DAPI. The primary antibodies used in this work were mouse monoclonal anti-tubulin (DM1 $\alpha$ ; Sigma-Aldrich; 1:200), rabbit anti-SEP-1 (Bembenek et al., 2007; 1:350), and rabbit anti-GFP (NB600-308SS; Novus Biologicals; 1:600). The secondary antibodies used were Alexa Fluor 488 anti-mouse (A-11001; Thermo Fisher Scientific; 1:200) and Alexa Fluor 594 anti-rabbit (A11037; Thermo Fisher Scientific; 1:200). z-stacks were captured at 1- $\mu$ m steps for each meiotic embryo. Images in Fig. 1, D and E; Fig. S1, C–F; and Fig. S5, C and E were captured with an inverted microscope (Olympus IX-81) equipped with a 60 $\times$  PlanApo 1.42 objective, a disk-scanning unit (Olympus), and an ORCA Flash 4.0 CMOS detector and controlled with MicroManager software. Exposure time for anti-GFP, DAPI, and anti-tubulin was 250 ms. Exposure time for anti-SEP-1 was 500 ms. Pixel size is 130 nm. The images shown are maximum intensity projections of five focal planes. Images in Fig. S1, A and B were captured with the Solamere system described under live imaging. Pixel size is 65 nm. Images in Fig. S1, A and B were deconvolved with Huygens Essentials, and the images shown are maximum intensity projections of four focal planes.

### Fluorescence intensity measurements

Fluorescence intensity line profiles in Fig. 2 and Fig. 10 are from single-focal plane images. Quantification of fluorescence

intensity change in KNL-1::GFP/GFP::KNL-3 when transitioning from cups to rings was done on single focal plane images using the segmentation function in Ivision software (BioVision Technologies). Mean pixel intensities of kinetochores as metaphase cups and anaphase rings were divided by mean background fluorescence intensity to generate a ratio for comparison between embryos. mCherry::H2b values were also measured at these time points as a control for photobleaching. All other quantifications were done through ImageJ software. Fluorescence intensity of KLP-7::mNeogreen was measured by drawing ellipses around individual homologs. Mean pixel values were then divided by background mean pixel values to generate a ratio for comparison. mCherry::H2b values were also measured at these time points as a control for photobleaching. A region of interest line was drawn through spindles progressing through meiosis in Fig. 10, A and B to show a change in KLP-7 localization over time relative to mCherry::H2b as a control.

#### Bivalent stretching measurements

For Fig. 4, Fig. S3, and Fig. S5, spindles were filmed in utero at 10-s intervals. Metaphase values were measured  $5.7 \pm 0.47$  min before initiation of spindle elongation. "Preanaphase" values were measured  $2.2 \pm 0.15$  min before initiation of spindle elongation because this corresponds to the time just before homolog separation in controls. In the first method, a fluorescence intensity profile was generated along a 1-pixel-wide line drawn from a point halfway between one spindle pole and the proximal half-bivalent to a point halfway between the opposite half-bivalent and the opposite spindle pole. The peaks of mCherry fluorescence were used as the centers of mCherry histone half-bivalents. The outer edges of GFP::NPP-6 or mCherry histone were determined as the points of half-maximal GFP or mCherry fluorescence intensity. In the second method, a rectangular region of interest was drawn around each half-bivalent, and the auto contrast function in FIJI was used to set the dimmest pixel to black and the brightest pixel to white. Homolog centers were determined by zooming, such that the cross-shaped cursor was the same size as the homolog, and manually centering the cursor over the homolog. The outer edges of GFP::NPP-6 were then determined by visual inspection. Comparison of these two methods on 10 bivalents by one-way ANOVA yielded P values of 0.88 for NPP-6 outer edges and 0.98 for homolog centers. To ensure that homologs had not yet separated at the time of each preanaphase measurement, the ratio between peak mCherry pixel values and the pixel values of the trough between homologs was made for each bivalent. No significant difference in this ratio was found between metaphase and preanaphase or between control and *knl-1,3(kd)*. Intrahomolog stretch in Figs. 4, D and E, was determined by subtracting the distance between mCherry::H2b homolog centers from the distance between the outside edges of NPP-6::GFP-labeled outer edges of bivalents. Cross-sectional areas of chromosomes in Fig. S3 D and Fig. S5 D were calculated by treating bivalents as ellipses, using the equation  $1/2(\text{width}) \cdot 1/2(\text{length}) \cdot \pi$ .

#### Anaphase velocity assays

For anaphase chromosome separation velocities in control embryos for Fig. 5, Fig. 6, Fig. 8, Fig. 9, Fig. S2, and Fig. S4, the

change in distance between homolog centers was divided by time elapsed in minutes. For intact bivalent movement measurements of auxin-depleted *knl-1,3(kd)* embryos in Fig. 5 J, the change in distance was measured between the midbivalent regions of each intact bivalent. Anaphase B velocities in Fig. 6 A and Fig. S2 C included only chromosomes separating parallel with the main spindle axis. Chromosomes segregating oblique to the main spindle axis in three- or four-way anaphases were not included in these figures; however, the velocities of these oblique anaphase B movements were not significantly different from the displayed values. For Fig. 8 anaphase A measurements, one half of the pole-to-pole spindle shortening velocity was subtracted from the rate of decrease in chromosome-to-pole distance. For wild-type-appearing anaphase B, only the number of embryos, N, is shown, since at this stage chromosomes grouped together and were treated as one moving mass.

#### Statistics

P values were calculated in GraphPad Prism using Student's t test for comparing means of only two groups (e.g., Fig. 2 D), one-way ANOVA for comparing means of three or more groups, and Fisher's exact test when comparing frequencies of contingent data.

#### Online supplemental material

Fig. S1 shows anti-GFP staining relevant to Fig. 3 and anti-SEP-1 staining relevant to Fig. 5. Fig. S2 compares depletion methods relevant to Fig. 3. Fig. S3 shows bivalent stretching data relevant to Fig. 4 and Fig. 8. Fig. S4 shows AIR-2 localization relevant to Fig. 5 and triple-depletion results. Fig. S5 shows KLP-7 localization relevant to Fig. 10 and triple-depletion results. Table S1 presents the *C. elegans* strain list. Video 1 is relevant to Fig. 1 and Fig. 2. Video 2 is relevant to Fig. 3. Video 3, Video 4, Video 5, and Video 6 are relevant to Fig. 5. Video 7 is relevant to Fig. 7. Video 8 and Video 9 are relevant to Fig. 8. Video 10 is relevant to Fig. S4 and triple-depletion results.

#### Acknowledgments

We thank Jordan Ward (University of California, Santa Cruz, Santa Cruz, CA), Abby Dernburg (University of California, Berkeley, Berkeley, CA), Bruce Bowerman (University of Oregon, Eugene, OR), Fede Pelisch (University of Dundee, Dundee, UK), Sander van den Heuvel (Utrecht University, Utrecht, Netherlands), Akatsuki Kimura (National Institute of Genetics, Mishima, Japan), Bob Goldstein (University of North Carolina, Chapel Hill, NC), and Arshad Desai (University of California, San Diego, San Diego, CA) for strains. Some strains were provided by the Caenorhabditis Genetics Center, which is funded by the National Institutes of Health, Office of Research Infrastructure Programs (P40 OD010440). We thank Lesilee Rose for critical reading of the manuscript.

This work was supported by National Institute of General Medical Sciences grants 1R01GM079421 and 1R35GM124889 and by the U.S. Department of Agriculture/National Institute of Food and Agriculture Hatch project (1009162 to F.J. McNally).

The authors declare no competing financial interests.

Danlasky et al.

Kinetochores pulling for meiotic homolog separation

Journal of Cell Biology

<https://doi.org/10.1083/jcb.202005179>

16 of 18

Author contributions: B.M. Danlasky, M.T. Panzica, K.P. McNally, E. Vargas, C. Bailey, W. Li, T. Gong, E.S. Fishman, and X. Jiang performed experiments, analyzed data, and prepared figures. F.J. McNally wrote the manuscript with contributions from all authors.

Submitted: 24 May 2020

Revised: 20 July 2020

Accepted: 16 September 2020

## References

- Bembenek, J.N., C.T. Richie, J.M. Squirell, J.M. Campbell, K.W. Eliceiri, D. Poteryaev, A. Spang, A. Golden, and J.G. White. 2007. Cortical granule exocytosis in *C. elegans* is regulated by cell cycle components including separase. *Development*. 134:3837–3848. <https://doi.org/10.1242/dev.011361>
- Cheeseman, I.M., J.S. Chappie, E.M. Wilson-Kubalek, and A. Desai. 2006. The conserved KMN network constitutes the core microtubule-binding site of the kinetochore. *Cell*. 127:983–997. <https://doi.org/10.1016/j.cell.2006.09.039>
- Connolly, A.A., V. Osterberg, S. Christensen, M. Price, C. Lu, K. Chicas-Cruz, S. Lockery, P.E. Mains, and B. Bowerman. 2014. Caenorhabditis elegans oocyte meiotic spindle pole assembly requires microtubule severing and the calponin homology domain protein ASPM-1. *Mol. Biol. Cell*. 25:1298–1311. <https://doi.org/10.1091/mbc.e13-11-0687>
- Connolly, A.A., K. Sugioka, C.H. Chuang, J.B. Lowry, and B. Bowerman. 2015. KLP-7 acts through the Ndc80 complex to limit pole number in *C. elegans* oocyte meiotic spindle assembly. *J. Cell Biol.* 210:917–932. <https://doi.org/10.1083/jcb.201412010>
- Cortes, D.B., K.L. McNally, P.E. Mains, and F.J. McNally. 2015. The asymmetry of female meiosis reduces the frequency of inheritance of unpaired chromosomes. *eLife*. 4:e06056. <https://doi.org/10.7554/eLife.06056>
- Crowder, M.E., J.R. Flynn, K.P. McNally, D.B. Cortes, K.L. Price, P.A. Kuehnert, M.T. Panzica, A. Andaya, J.A. Leary, and F.J. McNally. 2015. Dynactin-dependent cortical dynein and spherical spindle shape correlate temporally with meiotic spindle rotation in *Caenorhabditis elegans*. *Mol. Biol. Cell*. 26:3030–3046. <https://doi.org/10.1091/mbc.E15-05-0290>
- Davis-Roca, A.C., C.C. Muscat, and S.M. Wignall. 2017. *Caenorhabditis elegans* oocytes detect meiotic errors in the absence of canonical end-on kinetochore attachments. *J. Cell Biol.* 216:1243–1253. <https://doi.org/10.1083/jcb.201608042>
- Davis-Roca, A.C., N.S. Divekar, R.K. Ng, and S.M. Wignall. 2018. Dynamic SUMO remodeling drives a series of critical events during the meiotic divisions in *Caenorhabditis elegans*. *PLoS Genet*. 14:e1007626. <https://doi.org/10.1371/journal.pgen.1007626>
- de Carvalho, C.E., S. Zaaijer, S. Smolikov, Y. Gu, J.M. Schumacher, and M.P. Colaiacovo. 2008. LAB-1 antagonizes the Aurora B kinase in *C. elegans*. *Genes Dev*. 22:2869–2885. <https://doi.org/10.1101/gad.1691208>
- Delarue, M., G.P. Brittingham, S. Pfeffer, I.V. Surovtsev, S. Pinglay, K.J. Kennedy, M. Schaffer, J.I. Gutierrez, D. Sang, G. Poterewicz, et al. 2018. mTORC1 Controls Phase Separation and the Biophysical Properties of the Cytoplasm by Tuning Crowding. *Cell*. 174:338–349.E20. <https://doi.org/10.1016/j.cell.2018.05.042>
- Dumont, J., K. Oegema, and A. Desai. 2010. A kinetochore-independent mechanism drives anaphase chromosome separation during centrosomal meiosis. *Nat. Cell Biol.* 12:894–901. <https://doi.org/10.1038/ncb2093>
- Ellefson, M.L., and F.J. McNally. 2009. Kinesin-1 and cytoplasmic dynein act sequentially to move the meiotic spindle to the oocyte cortex in *Caenorhabditis elegans*. *Mol. Biol. Cell*. 20:2722–2730. <https://doi.org/10.1091/mbc.e08-12-1253>
- Eltling, M.W., C.L. Hueschen, D.B. Udy, and S. Dumont. 2014. Force on spindle microtubule minus ends moves chromosomes. *J. Cell Biol.* 206:245–256. <https://doi.org/10.1083/jcb.201401091>
- Espeut, J., D.K. Cheerambathur, L. Krenning, K. Oegema, and A. Desai. 2012. Microtubule binding by KNL-1 contributes to spindle checkpoint silencing at the kinetochore. *J. Cell Biol.* 196:469–482. <https://doi.org/10.1083/jcb.20111107>
- Fabig, G., R. Kiewisz, N. Lindow, J.A. Powers, V. Cota, L.J. Quintanilla, J. Brugués, S. Prohaska, D.S. Chu, and T. Müller-Reichert. 2020. Male meiotic spindle features that efficiently segregate paired and lagging chromosomes. *eLife*. 9:e50988.
- Ferrandiz, N., C. Barroso, O. Telecan, N. Shao, H.M. Kim, S. Testori, P. Faull, P. Cutillas, A.P. Snijders, M.P. Colaiacovo, et al. 2018a. Author Correction: Spatiotemporal regulation of Aurora B recruitment ensures release of cohesion during *C. elegans* oocyte meiosis. *Nat. Commun.* 9:3558. <https://doi.org/10.1038/s41467-018-05848-4>
- Ferrandiz, N., C. Barroso, O. Telecan, N. Shao, H.M. Kim, S. Testori, P. Faull, P. Cutillas, A.P. Snijders, M.P. Colaiacovo, et al. 2018b. Spatiotemporal regulation of Aurora B recruitment ensures release of cohesion during *C. elegans* oocyte meiosis. *Nat. Commun.* 9:3544. <https://doi.org/10.1038/s41467-018-03229-5>
- Gassmann, R., A. Essex, J.S. Hu, P.S. Maddox, F. Motegi, A. Sugimoto, S.M. O'Rourke, B. Bowerman, I. McLeod, J.R. Yates III, et al. 2008. A new mechanism controlling kinetochore-microtubule interactions revealed by comparison of two dynein-targeting components: SPD-1 and the Rod/Zw10/Zw10 complex. *Genes Dev*. 22:2385–2399. <https://doi.org/10.1101/gad.1687508>
- Gigant, E., M. Stefanutti, K. Laband, A. Gluszek-Kustusz, F. Edwards, B. Lacroix, G. Maton, J.C. Canman, J.P.I. Welburn, and J. Dumont. 2017. Inhibition of ectopic microtubule assembly by the kinesin-13 KLP-7 prevents chromosome segregation and cytokinesis defects in oocytes. *Development*. 144:1674–1686. <https://doi.org/10.1242/dev.147504>
- Gui, L., and H. Homer. 2013. Hecl1-dependent cyclin B2 stabilization regulates the G2-M transition and early prometaphase in mouse oocytes. *Dev. Cell*. 25:43–54. <https://doi.org/10.1016/j.devcel.2013.02.008>
- Han, X., K. Adames, E.M. Sykes, and M. Strayko. 2015. The KLP-7 Residue S546 Is a Putative Aurora Kinase Site Required for Microtubule Regulation at the Centrosome in *C. elegans*. *PLoS One*. 10:e0132593. <https://doi.org/10.1371/journal.pone.0132593>
- Hattersley, N., D. Cheerambathur, M. Moyle, M. Stefanutti, A. Richardson, K.Y. Lee, J. Dumont, K. Oegema, and A. Desai. 2016. A Nucleoporin Dock Protein Phosphatase 1 to Direct Meiotic Chromosome Segregation and Nuclear Assembly. *Dev. Cell*. 38:463–477. <https://doi.org/10.1016/j.devcel.2016.08.006>
- Heppert, J.K., A.M. Pani, A.M. Roberts, D.J. Dickinson, and B. Goldstein. 2018. A CRISPR Tagging-Based Screen Reveals Localized Players in Wnt-Directed Asymmetric Cell Division. *Genetics*. 208:1147–1164. <https://doi.org/10.1534/genetics.117.300487>
- Hong, Y., R. Sonnevill, B. Wang, V. Scheidt, B. Meier, A. Woglar, S. Demetriou, K. Labib, V. Jantsch, and A. Gartner. 2018a. LEM-3 is a midbody-tethered DNA nuclease that resolves chromatin bridges during late mitosis. *Nat. Commun.* 9:728. <https://doi.org/10.1038/s41467-018-03135-w>
- Hong, Y., M. Velkova, N. Silva, M. Jagut, V. Scheidt, K. Labib, V. Jantsch, and A. Gartner. 2018b. The conserved LEM-3/Anklel nuclease is involved in the combinatorial regulation of meiotic recombination repair and chromosome segregation in *Caenorhabditis elegans*. *PLoS Genet*. 14:e1007453. <https://doi.org/10.1371/journal.pgen.1007453>
- Howe, M., K.L. McDonald, D.G. Albertson, and B.J. Meyer. 2001. HIM-10 is required for kinetochore structure and function on *Caenorhabditis elegans* holocentric chromosomes. *J. Cell Biol.* 153:1227–1238. <https://doi.org/10.1083/jcb.153.6.1227>
- Inoué, S., and H. Ritter Jr. 1978. Mitosis in *Barbulanympha*. II. Dynamics of a two-stage anaphase, nuclear morphogenesis, and cytokinesis. *J. Cell Biol.* 77:655–684. <https://doi.org/10.1083/jcb.77.3.655>
- Joly, N., L. Martino, E. Gigant, J. Dumont, and L. Pintard. 2016. Microtubule-severing activity of the AAA+ ATPase Katanin is essential for female meiotic spindle assembly. *Development*. 143:3604–3614. <https://doi.org/10.1242/dev.140830>
- Kaitna, S., P. Pasierbek, M. Jantsch, J. Loidl, and M. Glotzer. 2002. The aurora B kinase AIR-2 regulates kinetochores during mitosis and is required for separation of homologous chromosomes during meiosis. *Curr. Biol.* 12:798–812. [https://doi.org/10.1016/S0960-9822\(02\)00820-5](https://doi.org/10.1016/S0960-9822(02)00820-5)
- Kamath, R.S., A.G. Fraser, Y. Dong, G. Poulin, R. Durbin, M. Gotta, A. Kanapin, N. Le Bot, S. Moreno, M. Sohrmann, et al. 2003. Systematic functional analysis of the *Caenorhabditis elegans* genome using RNAi. *Nature*. 421:231–237. <https://doi.org/10.1038/nature01278>
- Kimura, K., A. Mamane, T. Sasaki, K. Sato, J. Takagi, R. Niwayama, L. Hufnagel, Y. Shimamoto, J.F. Joanny, S. Uchida, et al. 2017. Endoplasmic reticulum-mediated microtubule alignment governs cytoplasmic streaming. *Nat. Cell Biol.* 19:399–406. <https://doi.org/10.1038/ncb3490>
- Kirby, C., M. Kusch, and K. Kempfues. 1990. Mutations in the par genes of *Caenorhabditis elegans* affect cytoplasmic reorganization during the first cell cycle. *Dev. Biol.* 142:203–215. [https://doi.org/10.1016/0012-1606\(90\)90164-E](https://doi.org/10.1016/0012-1606(90)90164-E)

Danlasky et al.

Kinetochore pulling for meiotic homolog separation

Journal of Cell Biology

17 of 18

<https://doi.org/10.1083/jcb.202005179>

- Kozłowski, C., M. Srayko, and F. Nédélec. 2007. Cortical microtubule contacts position the spindle in *C. elegans* embryos. *Cell*. 129:499-510. <https://doi.org/10.1016/j.cell.2007.03.027>
- Laband, K., R. Le Borgne, F. Edwards, M. Stefanutti, J.C. Canman, J.M. Verbavatz, and J. Dumont. 2017. Chromosome segregation occurs by microtubule pushing in oocytes. *Nat. Commun.* 8:1499. <https://doi.org/10.1038/s41467-017-01539-8>
- Mastronarde, D.N., K.L. McDonald, R. Ding, and J.R. McIntosh. 1993. Interpolar spindle microtubules in PTK cells. *J. Cell Biol.* 123:1475-1489. <https://doi.org/10.1083/jcb.123.6.1475>
- McCarter, J., B. Bartlett, T. Dang, and T. Schedl. 1999. On the control of oocyte meiotic maturation and ovulation in *Caenorhabditis elegans*. *Dev. Biol.* 205:111-128. <https://doi.org/10.1006/dbio.1998.9109>
- McDonald, K.L., E.T. O'Toole, D.N. Mastronarde, and J.R. McIntosh. 1992. Kinetochores microtubules in PTK cells. *J. Cell Biol.* 118:369-383. <https://doi.org/10.1083/jcb.118.2.369>
- McNally, K.P., and F.J. McNally. 2011. The spindle assembly function of *Caenorhabditis elegans* katanin does not require microtubule-severing activity. *Mol. Biol. Cell.* 22:1550-1560. <https://doi.org/10.1091/mbc.e10-12-0951>
- McNally, K., A. Audhya, K. Oegema, and F.J. McNally. 2006. Katanin controls mitotic and meiotic spindle length. *J. Cell Biol.* 175:881-891. <https://doi.org/10.1083/jcb.200608117>
- McNally, K.L., J.L. Martin, M. Ellefson, and F.J. McNally. 2010. Kinesin-dependent transport results in polarized migration of the nucleus in oocytes and inward movement of yolk granules in meiotic embryos. *Dev. Biol.* 339:126-140. <https://doi.org/10.1016/j.ydbio.2009.12.021>
- McNally, K., E. Berg, D.B. Cortes, V. Hernandez, P.E. Mains, and F.J. McNally. 2014. Katanin maintains meiotic metaphase chromosome alignment and spindle structure in vivo and has multiple effects on microtubules in vitro. *Mol. Biol. Cell.* 25:1037-1049. <https://doi.org/10.1091/mbc.e13-12-0764>
- McNally, K.P., M.T. Panzica, T. Kim, D.B. Cortes, and F.J. McNally. 2016. A novel chromosome segregation mechanism during female meiosis. *Mol. Biol. Cell.* 27:2576-2589. <https://doi.org/10.1091/mbc.e16-05-0331>
- Monen, J., P.S. Macdox, F. Hyndman, K. Oegema, and A. Desai. 2005. Differential role of CENP-A in the segregation of holocentric *C. elegans* chromosomes during meiosis and mitosis. *Nat. Cell Biol.* 7:1248-1255. <https://doi.org/10.1038/ncb1331>
- Muscat, C.C., K.M. Torre-Santiago, M.V. Tran, J.A. Powers, and S.M. Wignall. 2015. Kinetochores-independent chromosome segregation driven by lateral microtubule bundles. *eLife*. 4:e06462. <https://doi.org/10.7554/eLife.06462>
- Nicklas, R.B. 1989. The motor for poleward chromosome movement in anaphase is in or near the kinetochore. *J. Cell Biol.* 109:2245-2255. <https://doi.org/10.1083/jcb.109.5.2245>
- Oegema, K., A. Desai, S. Rybina, M. Kirkham, and A.A. Hyman. 2001. Functional analysis of kinetochore assembly in *Caenorhabditis elegans*. *J. Cell Biol.* 153:1209-1226. <https://doi.org/10.1083/jcb.153.6.1209>
- O'Toole, E.T., K.L. McDonald, J. Mäntler, J.R. McIntosh, A.A. Hyman, and T. Müller-Reichert. 2003. Morphologically distinct microtubule ends in the mitotic centrosome of *Caenorhabditis elegans*. *J. Cell Biol.* 163:451-456. <https://doi.org/10.1083/jcb.200304035>
- Pelisch, F., T. Tammsalu, B. Wang, E.G. Jaffray, A. Gartner, and R.T. Hay. 2017. A SUMO-Dependent Protein Network Regulates Chromosome Congression during Oocyte Meiosis. *Mol. Cell.* 65:66-77. <https://doi.org/10.1016/j.molcel.2016.11.001>
- Pelisch, F., L. Bel Borja, E.G. Jaffray, and R.T. Hay. 2019. Sumoylation regulates protein dynamics during meiotic chromosome segregation in *C. elegans* oocytes. *J. Cell Sci.* 132:jcs232330.
- Pereira, C., R.M. Reis, J.B. Gama, R. Celestino, D.K. Cheerambathur, A.X. Carvalho, and R. Gassmann. 2018. Self-Assembly of the RZZ Complex into Filaments Drives Kinetochore Expansion in the Absence of Microtubule Attachment. *Curr. Biol.* 28:3408-3421.e8.
- Powers, A.F., A.D. Franck, D.R. Gestaut, J. Cooper, B. Graczyk, R.R. Wei, L. Wordeman, T.N. Davis, and C.L. Asbury. 2009. The Ndc80 kinetochore complex forms load-bearing attachments to dynamic microtubule tips via biased diffusion. *Cell.* 136:865-875. <https://doi.org/10.1016/j.cell.2008.12.045>
- Redemann, S., I. Lantzsch, N. Lindow, S. Prohaska, M. Srayko, and T. Müller-Reichert. 2018. A Switch in Microtubule Orientation during *C. elegans* Meiosis. *Curr. Biol.* 28:2991-2997.e2.
- Rogers, E., J.D. Bishop, J.A. Waddle, J.M. Schumacher, and R. Lin. 2002. The aurora kinase AIR-2 functions in the release of chromosome cohesion in *Caenorhabditis elegans* meiosis. *J. Cell Biol.* 157:219-229. <https://doi.org/10.1083/jcb.200110045>
- Sikirzhitski, V., V. Magidson, J.B. Steinman, J. He, M. Le Berre, I. Tikhonenko, J.G. Ault, B.F. McEwen, J.K. Chen, H. Sui, et al. 2014. Direct kinetochore-spindle pole connections are not required for chromosome segregation. *J. Cell Biol.* 206:231-243. <https://doi.org/10.1083/jcb.201401090>
- Spurck, T.P., O.G. Stonington, J.A. Snyder, J.D. Pickett-Heaps, A. Bajer, and J. Mole-Bajer. 1990. UV microbeam irradiations of the mitotic spindle. II. Spindle fiber dynamics and force production. *J. Cell Biol.* 111:1505-1518. <https://doi.org/10.1083/jcb.111.4.1505>
- Spurck, T., A. Forer, and J. Pickett-Heaps. 1997. Ultraviolet microbeam irradiations of epithelial and spermatocyte spindles suggest that forces act on the kinetochore fibre and are not generated by its disassembly. *Cell Motil. Cytoskeleton.* 36:136-148. [https://doi.org/10.1002/\(SICI\)1097-0169\(1997\)36:2<136::AID-CM4>3.0.CO;2-7](https://doi.org/10.1002/(SICI)1097-0169(1997)36:2<136::AID-CM4>3.0.CO;2-7)
- Srayko, M., D.W. Buster, O.A. Bazirgan, F.J. McNally, and P.E. Mains. 2000. MEI-1/MEI-2 katanin-like microtubule severing activity is required for *Caenorhabditis elegans* meiosis. *Genes Dev.* 14:1072-1084.
- Srayko, M., E.T. O'toole, A.A. Hyman, and T. Müller-Reichert. 2006. Katanin disrupts the microtubule lattice and increases polymer number in *C. elegans* meiosis. *Curr. Biol.* 16:1944-1949. <https://doi.org/10.1016/j.cub.2006.08.029>
- Tan, R., P.J. Foster, D.J. Needleman, and R.J. McKenney. 2018. Cooperative Accumulation of Dynein-Dynactin at Microtubule Minus-Ends Drives Microtubule Network Reorganization. *Dev. Cell.* 44:233-247.E4. <https://doi.org/10.1016/j.devcel.2017.12.023>
- van der Voet, M., C.W. Berends, A. Perreault, T. Nguyen-Ngoc, P. Gonczyk, M. Vidal, M. Boxem, and S. van den Heuvel. 2009. NuMA-related LIN-5, ASPM-1, calmodulin and dynein promote meiotic spindle rotation independently of cortical LIN-5/GPR/Galpa. *Nat. Cell Biol.* 11:269-277. <https://doi.org/10.1038/ncb1834>
- Vargas, E., K.P. McNally, D.B. Cortes, M.T. Panzica, B.M. Danlasky, Q. Li, A.S. Macdox, and F.J. McNally. 2019. Spherical spindle shape promotes perpendicular cortical orientation by preventing isometric cortical pulling on both spindle poles during *C. elegans* female meiosis. *Development.* 146:dev178863.
- Vukušić, K., R. Buda, and I.M. Tolic. 2019. Force-generating mechanisms of anaphase in human cells. *J. Cell Sci.* 132:jcs231985.
- Wang, L.L., A. Das, and K.S. McKim. 2019. Sister centromere fusion during meiosis I depends on maintaining cohesins and destabilizing microtubule attachments. *PLoS Genet.* 15:e1008072. <https://doi.org/10.1371/journal.pgen.1008072>
- Watanabe, Y. 2005. Sister chromatid cohesion along arms and at centromeres. *Trends Genet.* 21:405-412. <https://doi.org/10.1016/j.tig.2005.05.009>
- Wignall, S.M., and A.M. Villeneuve. 2009. Lateral microtubule bundles promote chromosome alignment during acentrosomal oocyte meiosis. *Nat. Cell Biol.* 11:839-844. <https://doi.org/10.1038/ncb1891>
- Yang, H.Y., K. McNally, and F.J. McNally. 2003. MEI-1/katanin is required for translocation of the meiosis I spindle to the oocyte cortex in *C. elegans*. *Dev. Biol.* 260:245-259. [https://doi.org/10.1016/S0012-1606\(03\)00216-1](https://doi.org/10.1016/S0012-1606(03)00216-1)
- Yang, H.Y., P.E. Mains, and F.J. McNally. 2005. Kinesin-I mediates translocation of the meiotic spindle to the oocyte cortex through KCA-1, a novel cargo adapter. *J. Cell Biol.* 169:447-457. <https://doi.org/10.1083/jcb.200411132>
- Yoshida, S., S. Nishiyama, L. Lister, S. Hashimoto, T. Mishina, A. Courtois, H. Kyogoku, T. Abe, A. Shiraishi, M. Choudhary, et al. 2020. Prcl-rich kinetochores are required for error-free acentrosomal spindle bipolarization during meiosis I in mouse oocytes. *Nat. Commun.* 11:2652. <https://doi.org/10.1038/s41467-020-16488-y>
- Yu, C.H., S. Redemann, H.Y. Wu, R. Kiewisz, T.Y. Yoo, W. Conway, R. Farhadifar, T. Müller-Reichert, and D. Needleman. 2019. Central-spindle microtubules are strongly coupled to chromosomes during both anaphase A and anaphase B. *Mol. Biol. Cell.* 30:2503-2514. <https://doi.org/10.1091/mbc.e19-01-0074>
- Zhang, L., J.D. Ward, Z. Cheng, and A.F. Dernburg. 2015. The auxin-inducible degradation (AID) system enables versatile conditional protein depletion in *C. elegans*. *Development.* 142:4374-4384. <https://doi.org/10.1242/dev.129635>

Supplemental material

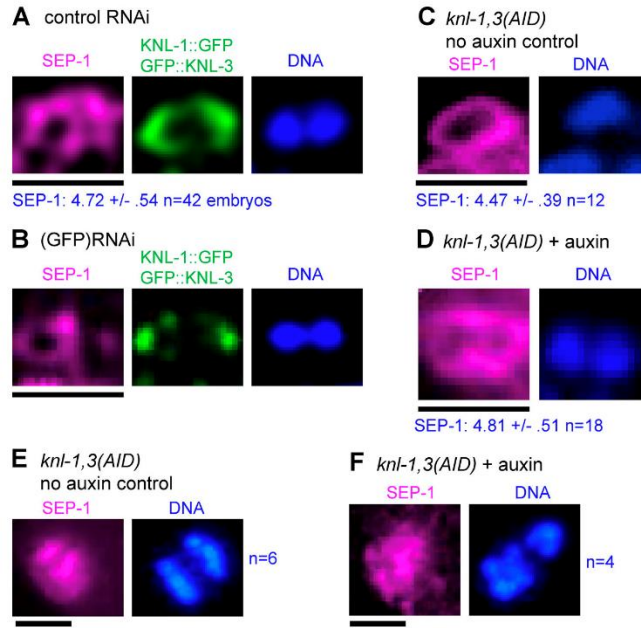


Figure S1. **Separase localizes normally after KNL-1,3 depletion.** Meiotic embryos were fixed and stained with anti-separase (SEP-1), anti-GFP, and DAPI. **(A-D)** Single bivalents in metaphase I embryos of the indicated genotype. Values for SEP-1 are the mean pixel value of the brightest region around a bivalent  $\pm$  SEM. Results of Student's *t* test: control RNAi versus *GFP(RNAi)*,  $P = 0.037$ ; and *AID* no auxin control versus *AID* + auxin,  $P = 0.71$ . **(E and F)** Early anaphase spindles with separase localized in between separating chromosomes. Bars = 2.6  $\mu$ m.

Downloaded from [http://jcb.org/jcb/article-pdf/219/12/202005179/1831968/jcb\\_202005179.pdf](http://jcb.org/jcb/article-pdf/219/12/202005179/1831968/jcb_202005179.pdf) by guest on 06 December 2023

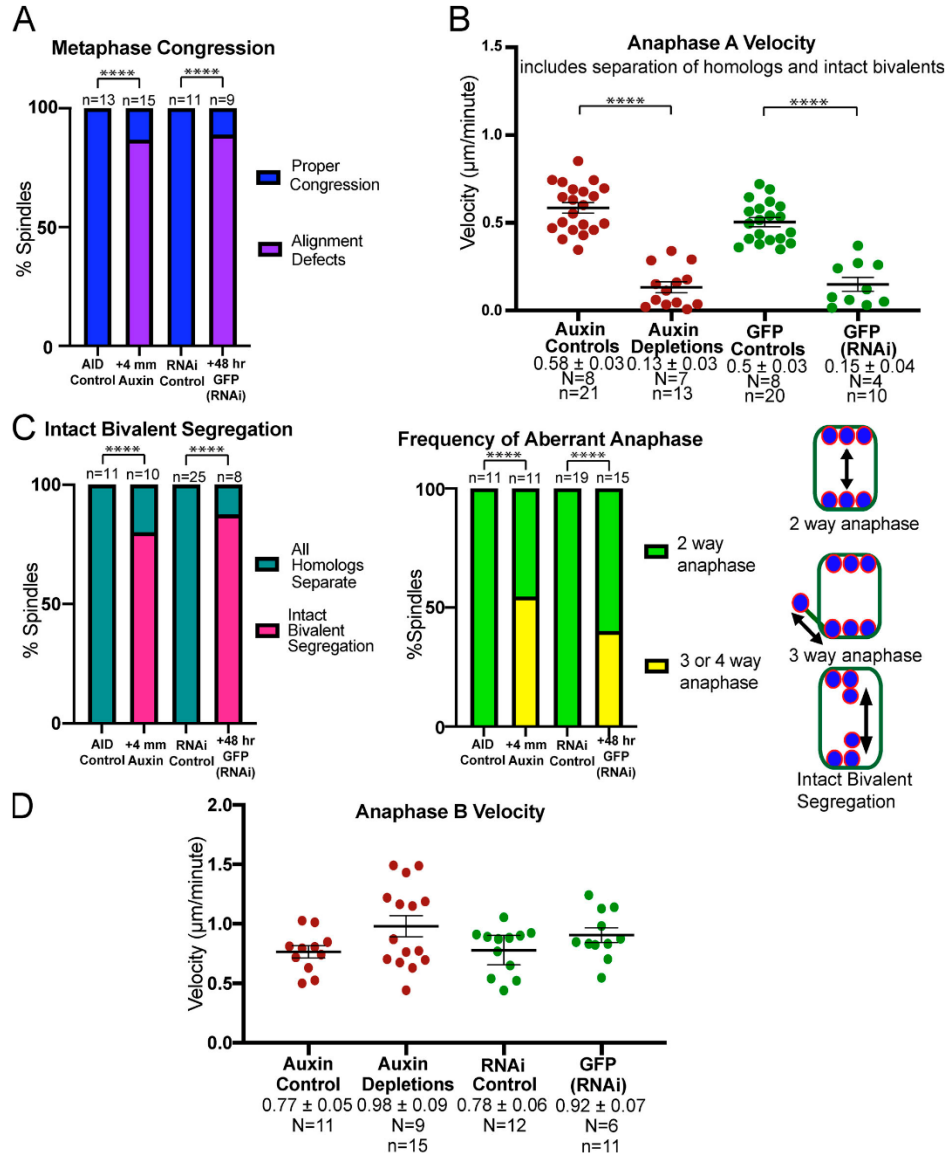


Figure S2. Comparison between auxin-inducible degron and *GFP(RNAi)* double depletions of endogenously tagged KNL-1 and KNL-3. (A) Frequency of congression defects observed in time-lapse sequences. Auxin versus *GFP(RNAi)*,  $P = 1$ ; Fisher's exact test. (B) Rates of anaphase A chromosome separation during the time interval that anaphase A occurred in controls ( $-90$  s from anaphase B onset). Auxin versus *GFP(RNAi)*,  $P = 0.99$ ; ANOVA. (C) Frequency of the anaphase defects depicted in the cartoon, determined from time-lapse sequences. Auxin versus *GFP(RNAi)* three- or four-way anaphase,  $P = 0.69$ ; intact bivalent segregation,  $P = 1$ ; Fisher's exact test. (D) Anaphase B velocities determined from time-lapse sequences. Auxin versus *GFP(RNAi)*,  $P = 0.87$ ; ANOVA. Error bars and values are mean  $\pm$  SEM. \*\*\*\*,  $P < 0.0001$ . N, number of embryos; n, number of chromosomes.

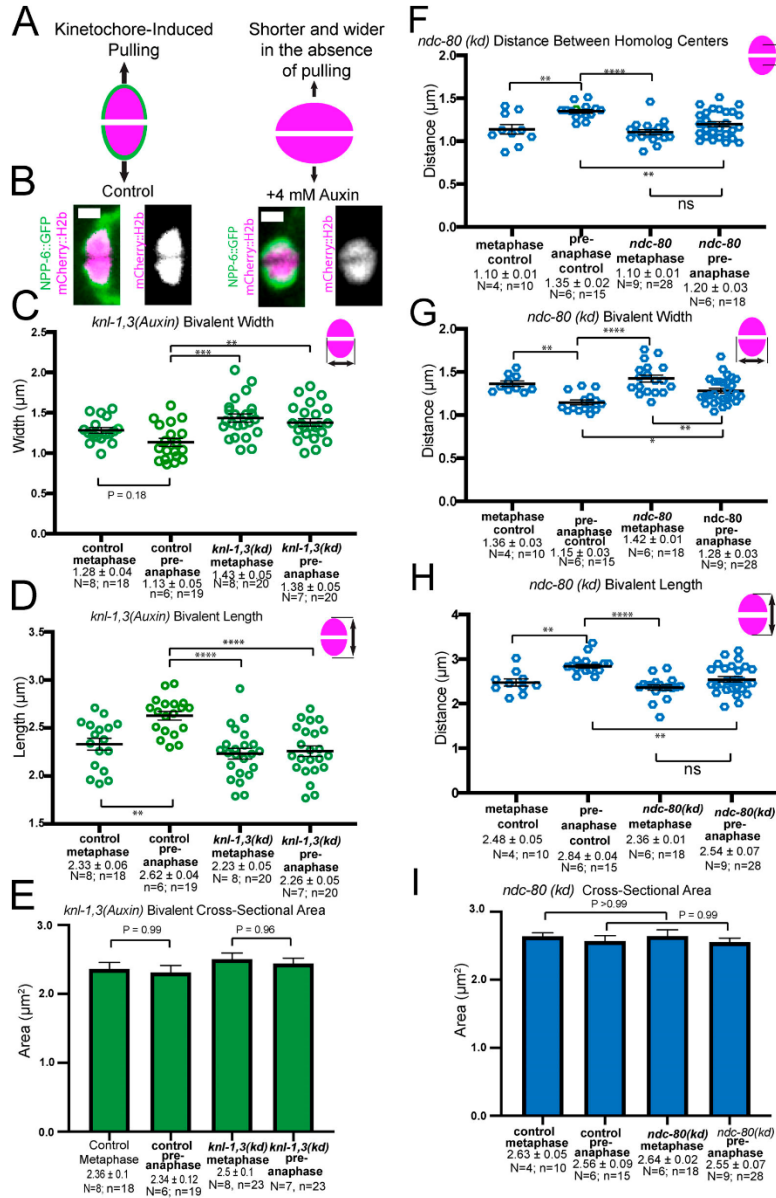


Figure S3. **Bivalent stretching in KNL-1,3-depleted embryos and NDC-80-depleted embryos measured from mCherry::histone live images.** (A) Diagram depicting increased length and decreased width expected from pulling. (B) Images of single bivalents taken from time-lapse sequences. (C) KNL-1,3-depleted bivalents are wider than controls due to decreased end-on pulling forces. (D) KNL-1,3-depleted bivalents are shorter than controls. (E) No significant difference in cross-sectional area between control and *knl-1,3(kd)* bivalents. (F) Distances between homolog centers in GFP::NDC-80 embryos treated with control or *GFP(RNAi)* indicate reduced stretching between metaphase and preanaphase. (G) Bivalent width decreases in NDC-80-depleted embryos, indicating residual stretching. (H) End-to-end bivalent length measurements indicate reduced stretching after NDC-80 depletion. (I) Cross-sectional area does not change in control or NDC-80 depletion. Bar = 1  $\mu\text{m}$ . Error bars and values are mean  $\pm$  SEM. \*,  $P < 0.05$ ; \*\*,  $P < 0.01$ ; \*\*\*,  $P < 0.001$ ; \*\*\*\*,  $P < 0.0001$ ; ANOVA. N, number of embryos; n, number of bivalents.

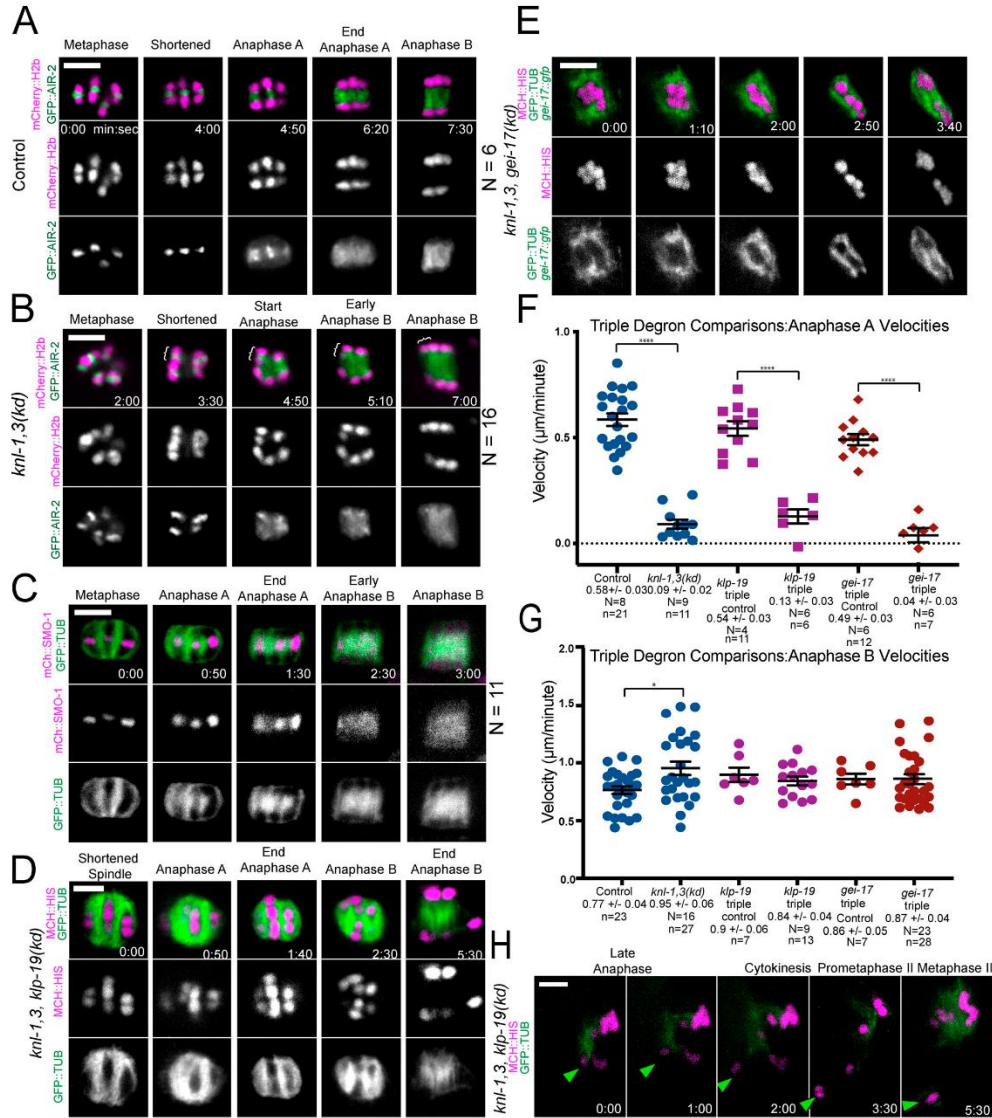


Figure S4. **AIR-2 localizes normally in *knl-1,3(kd)* bivalents.** AID triple depletions of KNL-1,3 and chromokinesin KLP-19 or SUMO E3 ligase GEI-17. (A-C) Representative time-lapse sequences of GFP-tagged AIR-2 (A and B) or mCherry-tagged SUMO (SMO-1; C) in control (A and C) or *knl-3(kd)* (B) embryos. Brackets in B indicate an intact bivalent segregating. (D) Time-lapse images of a spindle following overnight auxin-induced degradation of KNL-1,3, and KLP-19. (E) Time-lapse images of a spindle following overnight auxin-induced degradation of KNL-1,3, and GEI-17 displaying an abnormal disorganized structure. (F and G) No significant difference is observed in anaphase A or B velocities for KNL-1,3 double depletion or either triple depletion. (H) In 2/14 live time-lapse sequences, an intact bivalent (arrowhead) escaped the spindle in KNL-1,3 and KLP-19-depleted spindles during late anaphase I. It did not reincorporate into the MII spindle. Error bars and values are mean ± SEM. \*, P < 0.05; \*\*\*\*, P < 0.0001. Bars = 3 µm. N, number of embryos; n, number of chromosomes. mCh MCh, mCherry; TUB, tubulin.



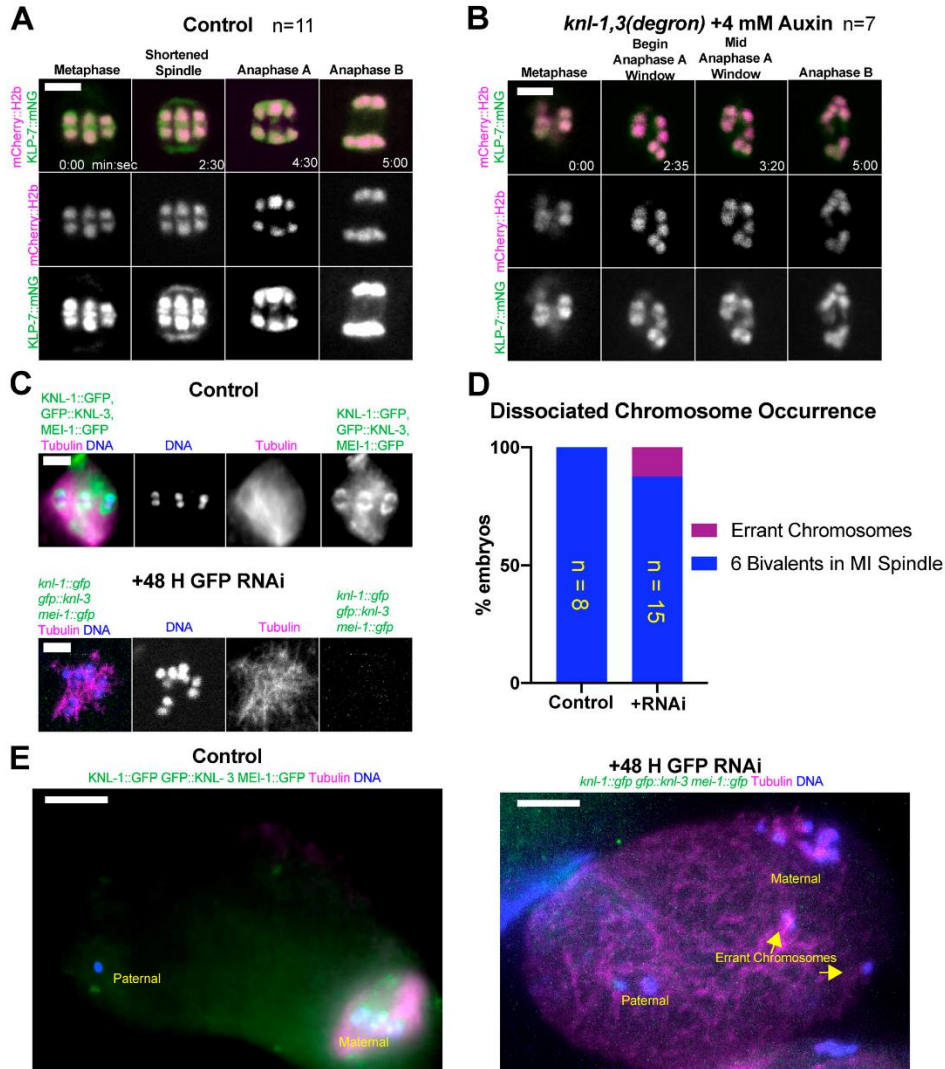


Figure S5. **The kinesin-13 KLP-7 is retained on bivalents following KNL-1,3 depletion.** (A and B) Representative time-lapse sequences. (A) In control spindles, endogenously tagged KLP-7::mNG localizes to meiotic spindle poles, the main chromatin masses, and in midbivalent rings. (B) Following KNL-1,3 depletion, KLP-7::mNG is retained on the main chromatin masses but is no longer present at spindle poles or midbivalent rings. (C-E) Results of fixed immunofluorescence. (C and D) Following triple GFP(RNAi) depletion of endogenously GFP-tagged KNL-1,3 and MEI-1, all bivalents were associated with apolar meiotic spindles in the majority of embryos. (E) Example of a rare occurrence of errant maternal chromosomes that appear to have left the meiotic spindle. Bars (A-C) = 3  $\mu$ m. Bars (E) = 7  $\mu$ m. MI, meiosis one; mNG, mNeonGreen.

Video 1. Control meiosis I filmed in utero in a strain with endogenously GFP-tagged *knl-1* and *knl-3* genes and a transposon insertion expressing *mKate::tubulin*. Playback speed is six frames per second.

Video 2. **Demonstration of spindle bipolarity after KNL-1,3 double depletion.** z-Stack of images taken at 1- $\mu$ m steps through a KNL-1, KNL-3 double-depleted, 4 mM auxin, metaphase I spindle filmed in utero in a strain with auxin-induced degrons appended to the endogenous *knl-1* and *knl-3* genes and GFP appended to the endogenous *aspm-1* gene and expressing TIR1, GFP::tubulin, and mCherry::histone H2b from transgenes.

Video 3. **Control, no auxin, meiosis I filmed in utero in a strain with auxin-induced degrons appended to the endogenous *knl-1* and *knl-3* genes and expressing TIR1, GFP::tubulin, and mCherry::histone H2b from transgenes.** Playback speed is six frames per second.

Video 4. **KNL-1, KNL-3 double depletion, 4 mM auxin, meiosis I filmed in utero in a strain with auxin-induced degrons appended to the endogenous *knl-1* and *knl-3* genes and expressing TIR1, GFP::tubulin, and mCherry::histone H2b from transgenes.** Playback speed is six frames per second.

Video 5. **KNL-1, KNL-3 double depletion, 4 mM auxin, meiosis I filmed in utero in a strain with auxin-induced degrons appended to the endogenous *knl-1* and *knl-3* genes, endogenously GFP-tagged *aspm-1* gene, and expressing TIR1 and mCherry::histone H2b from transgenes.** Playback speed is six frames per second.

Video 6. **Delayed separation of homologs after KNL-1, KNL-3 double depletion.** Meiosis I filmed in utero in a 4-mM auxin-treated strain with auxin-induced degrons appended to the endogenous *knl-1* and *knl-3* genes and expressing TIR1, GFP::tubulin, and mCherry::histone H2b from transgenes. Left arrow: bivalent splits and the two homologs segregate to opposite poles. Upper right arrow: bivalent splits after segregating intact to one pole. Lower right arrow: bivalent segregates intact to one pole and remains intact at the end of the time-lapse sequence. Playback speed is six frames per second.

Video 7. **Lagging univalent X chromosome segregation during meiosis I filmed in utero in a *him-8* strain with endogenously GFP-tagged *knl-1* and *knl-3* genes and a transposon insertion expressing mCherry::histone H2b.** Playback speed is six frames per second. mNG, mNeonGreen.

Video 8. **RNAi control meiosis I filmed in utero in a strain with endogenously GFP-tagged *ndc-80* gene and a transposon insertion expressing mNeonGreen::tubulin and mCherry::histone H2b.** Playback speed is six frames per second. mNG, mNeonGreen.

Video 9. **NDC-80 depletion, via *GFP(RNAi)*, meiosis I filmed in utero in a strain with endogenously GFP-tagged *ndc-80* gene and a transposon insertion expressing mNeonGreen::tubulin and mCherry::histone H2b.** Playback speed is six frames per second.

Video 10. **KNL-1, KNL-3, GEI-17 triple depletion, 4 mM auxin, meiosis I filmed in utero in a strain with auxin-induced degrons appended to the endogenous *knl-1*, *knl-3*, and *gei-17* genes and expressing TIR1, GFP::tubulin, and mCherry::histone H2b from transgenes.** Playback speed is six frames per second.

**Table S1, which is provided online, presents the *C. elegans* strain list.**

# Chapter 4

**Paternal mitochondria from an *rmd-2*, *rmd-3*, *rmd-6* triple mutant are properly positioned in the *C. elegans* zygote.**

Iris Y Juanico, Christina M Meyer, John E McCarthy, Ting Gong, and Francis J McNally

Juanico IY, Meyer CM, McCarthy JE, Gong T, McNally FJ. Paternal mitochondria from an *rmd-2*, *rmd-3*, *rmd-6* triple mutant are properly positioned in the *C. elegans* zygote. MicroPubl Biol. 2021 Jul 19;2021:10.17912/micropub.biology.000422. doi: 10.17912/micropub.biology.000422. PMID: 34296068; PMCID: PMC8290264.

In this project, I helped IRIS with generating *rmd-2*, *rmd-3*, and *rmd-6* single mutant. I used CRISPR-CAS9 to knockout *rmd-2*, *rmd-3* and *rmd-6*.

## Paternal mitochondria from an *rmd-2, rmd-3, rmd-6* triple mutant are properly positioned in the *C. elegans* zygote

Iris Y Juanico<sup>1</sup>, Christina M Meyer<sup>1</sup>, John E McCarthy<sup>1</sup>, Ting Gong<sup>1</sup> and Francis J McNally<sup>1§</sup>

<sup>1</sup>Dept. of Molecular and Cellular Biology, University of California, Davis, Davis, CA USA

<sup>§</sup>To whom correspondence should be addressed: fjmcnally@ucdavis.edu

### Abstract

RMD-1,2,3,6 (regulator of microtubule dynamics) is a family of homologous proteins conserved between humans and *C. elegans*. Human RMD-3/PTPIP51 is a mitochondrial protein that tethers mitochondria to the endoplasmic reticulum. *C. elegans* RMD-2, 3, and 6 are expressed in sperm. To test whether paternal RMD-2, 3, 6 might redundantly tether paternal mitochondria to maternal ER at fertilization, we generated an *rmd-2, rmd-3, rmd-6* triple mutant. Paternal mitochondria derived from control or triple mutant worms were concentrated in a cloud around the paternal DNA at the future posterior end of zygotes during meiosis. No significant difference was detected in the position of paternal mitochondria within the zygote nor in the position of paternal mitochondria relative to paternal DNA within the zygote. There was also no reduction in progeny viability between control and triple mutant worms.

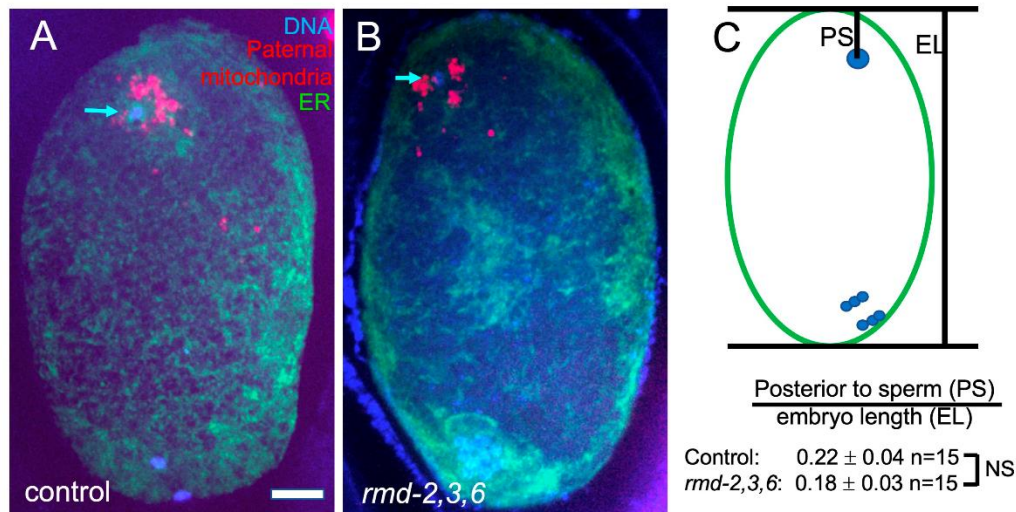


**Figure 1.** Position of paternal DNA within meiotic embryos. Hermaphrodites expressing GFP::SPCS-1, which labels the endoplasmic reticulum, were mated with control or *rmd-2, 3, 6* triple mutant males expressing MEV-1::mCherry, which labels mitochondria. (A, B) Representative *z* projections of methanol-fixed meiotic embryos stained with DAPI and anti-GFP antibodies. Blue indicates DAPI-stained DNA. Red indicates mCherry-labeled paternal mitochondria from the sperm. Green indicates maternal endoplasmic reticulum labeled with anti-GFP, which labels GFP::SPCS-1. Arrows indicate paternal DNA. Control and *rmd-2,3,6* indicate paternal genotypes. The control embryo shown is in anaphase I. The triple mutant embryo shown is in metaphase I. Bar = 5  $\mu$ m. (C) Diagram indicates how sperm DNA position relative to the future posterior tip was measured. PS indicates the distance from the future posterior tip of the ellipsoid embryo to the sperm DNA. EL indicates embryo length from the future posterior tip to the future anterior tip of the ellipsoid embryo. PS was divided by EL and the mean and SEM for the resulting ratios are shown. n indicates the number of embryos analyzed. Results of Student's unpaired t test indicated no significant difference (NS) between control and *rmd-2,3,6* ( $p=0.42$ ).

### Description

RMD-1 was discovered as a cytoplasmic regulator of microtubule dynamics in *C. elegans* and several highly homologous proteins were inferred from the *C. elegans* and human genome sequences (Oishi *et al.*, 2007). One of the human homologs, RMD-3/PTPIP51, has an N-terminal extension relative to other RMDs that targets it to the mitochondrial outer membrane and which binds the endoplasmic reticulum (ER) protein VAPB (De Vos *et al.*, 2012). This interaction mediates tethering of mitochondria to the ER in human cells (Stoica *et al.*, 2014). None of the *C. elegans* RMDs have sequence homology with the N-terminal extension found on human RMD-3/PTPIP51, however, *C. elegans* RMD-2 has an N-terminal extension relative to the other RMDs and this extension has potential to form a transmembrane helix as determined by IMPred release 25 ([https://embnet.vital-it.ch/software/IMPRED\\_form.html](https://embnet.vital-it.ch/software/IMPRED_form.html)). RMD-2 is present in sperm whereas RMD-3 and RMD-6 are highly enriched in sperm (Ma *et al.*, 2014). Paternal mitochondria are eventually degraded in the embryo (Sato and Sato, 2011). However, they are maintained, along with other sperm contents, at the opposite end of the zygote from the female meiotic spindle during meiosis (Fig. 1). We hypothesized that RMD-2, 3 and 6 on paternal mitochondria bind to the VAPB homolog, VPR-1, on maternal ER at fertilization to tether the sperm contents at the future posterior end of the zygote.

To test this hypothesis, we mated *rmd-2, rmd-3, rmd-6* triple mutant males bearing a transgene labeling mitochondria, *mCherry::mev-1* also called *mCherry::sdhc-1* (Trewin *et al.*, 2019), to hermaphrodites expressing a fluorescent marker of the ER. Resulting meiotic zygotes were fixed, stained with DAPI, and imaged (Fig. 1A-B). The position of the sperm DNA within the zygote was quantified (Fig. 1C) and no significant difference from control matings was observed. No qualitative difference was observed in distance of paternal mitochondria from the sperm DNA (Fig. 1A, B). Self progeny of triple mutant worms had a hatch rate that was not significantly less than progeny from control worms at 20°C (control KWN724: 94.9% hatching n=6 mothers, 731 progeny; triple deletion FM697: 97.6% hatching n=6 mothers 937 progeny).

Possible explanations are that RMD-1 carries out all the essential functions of this gene family, or that the triple mutant strain has a phenotype that was not assayed.

## Methods

### [Request a detailed protocol](#)

*rmd-2(du8)* was generated by co-injecting KWN724 with two Cas9 RNPs (Upstream Guide Sequence + PAM (rev):

tcagatgaaaggggacat cgg

Downstream Guide Sequence + PAM (for):

GCCACCAACTGCCACTGTTCG AGG

and the plasmid repair template:

aaatcagatgataagataaaaatctccaatcataaataatgaaaagataagatgctctataaataatgacgtcaactcttgcAATatgctcatc

GCCACTGTGCAATAGGCTATCGCCGACTTCCAAGCAGCTCATGAAATCAATCCAGACTGGATTGAAAACACGGTTTACCTCGGAAAAGCTCTTCA

using the *dpy-10* co-CRISPR method (Paix *et al.*, 2015). An *rmd-2* deletion was identified by PCR screening non-Dpy siblings of Dpy progeny. *rmd-2(du8)*

removes exons 4, 5 and half of exon 6 of *rmd-2* isoform b. *rmd-6(du9)* was generated by co-injecting *rmd-2(du8)* worms with two Cas9 RNPs (Upstream

Guide Sequence + PAM (rev):

ATCGCGGTTCTTGGTTCCGA AGG

Downstream Guide Sequence + PAM (rev):

CGATGTCACACTTCGGTA AGG

and the ultramer repair template:

taatcagtagcaccaccaccAI GgtaagttaactccgatcttcaaatgttaagctcttttcagAGI'IT'GAI'GAAAI'GACAAGAAAI'CGGAAGCAAGIA

taggtaactgaTGTGTGACATCGAACCCTATTCCGACGCTGAACAAGAGTTTCCGATGATGCGAAGCAGATGTTGTCTAAGCTTTAAgttt

using *dpy-10* co-CRISPR. PCR screening yielded an *rmd-6* deletion in a *dpy-10* worm. *rmd-6(du9)* removes all of exon 3 and half of exons 2 and 4. *rmd-*

*3(tm2635)* was obtained from Shohei Mitani (National Bioresource Project for the Experimental Animal "Nematode *C. elegans*"). To make the triple mutant

strain, *rmd-3(tm2635)* males were mated to *rmd-2(du8)*; *rmd-6(du9)*; *dpy-10*; *him-5*; *mev-1(jbm1 [mev-1::mCherry])* hermaphrodites. F2 self progeny of the

F1 heterozygotes were allowed to lay eggs before being subjected to PCR screening for all three deletions. Some genotyping PCRs for *tm2635* yielded an

apparent wild-type product, however, sequencing of this PCR product revealed it to be from *rmd-4*, which is annotated as a pseudogene.

Hatch rates were determined by singling L4 hermaphrodites, moving the worm to a fresh plate at 24 hr intervals, then counting eggs and larvae 48 hrs after removing adults from a plate.

### Reagents

strain	genotype	available from
KWN724	<i>mev-1(jbm1 [mev-1::mCherry]) III him-5(e1490) V</i>	McNally lab
WH327	<i>unc-119(ed3) III; ojs23 [pie-1p::GFP::spcs-1]</i> .	CGC
FM697	<i>rmd-2(du8); rmd-3(tm2635); rmd-6(du9); mev-1(jbm1 [mev-1::mCherry]) III him-5(e1490) V</i>	McNally lab

**Acknowledgments:** We thank Shohei Mitani and the National Bioresource Project for the Experimental Animal "Nematode *C. elegans*" for *tm2635*, the CGC for WH327, and Keith Nehrke for KWN724.

### References

De Vos KJ, Mórocz GM, Stoica R, Tudor EL, Lau KF, Ackerley S, Warley A, Shaw CE, Miller CC. 2012. VAPB interacts with the mitochondrial protein PTP1P51 to regulate calcium homeostasis. *Hum Mol Genet* 21: 1299-311. PMID: 22131369.

Ma X, Zhu Y, Li C, Xue P, Zhao Y, Chen S, Yang F, Miao L. 2014. Characterisation of *Caenorhabditis elegans* sperm transcriptome and proteome. *BMC Genomics* 15: 168. PMID: 24581041.

Oishi K, Okano H, Sawa H. 2007. RMD-1, a novel microtubule-associated protein, functions in chromosome segregation in *Caenorhabditis elegans*. *J Cell Biol* 179: 1149-62. PMID: 18070910.

Paix A, Folkmann A, Rasoloson D, Seydoux G. 2015. High Efficiency, Homology-Directed Genome Editing in *Caenorhabditis elegans* Using CRISPR-Cas9 Ribonucleoprotein Complexes. *Genetics* 201: 47-54. PMID: 26187122.

Sato M, Sato K. 2011. Degradation of paternal mitochondria by fertilization-triggered autophagy in *C. elegans* embryos. *Science* 334: 1141-4. PMID: 21998252.

Stoica R, De Vos KJ, Paillusson S, Mueller S, Sancho RM, Lau KF, Vizcay-Barrena G, Lin WL, Xu YF, Lewis J, Dickson DW, Petrucelli L, Mitchell JC, Shaw CE, Miller CC. 2014. ER-mitochondria associations are regulated by the VAPB-PTP1P51 interaction and are disrupted by ALS/FTD-associated TDP-43. *Nat Commun* 5: 3996. PMID: 24893131.

Trewin AJ, Bahr LL, Almast A, Berry BJ, Wei AY, Foster TH, Wojtovich AP. 2019. Mitochondrial Reactive Oxygen Species Generated at the Complex-II Matrix or Intermembrane Space Microdomain Have Distinct Effects on Redox Signaling and Stress Sensitivity in *Caenorhabditis elegans*. *Antioxid Redox Signal* 31: 594-607. PMID: 30887829.

**Funding:** This work was supported by National Institute of General Medical Sciences grant R35GM136241 and by the U.S. Department of Agriculture/National Institute of Food and Agriculture Hatch project (1009162 to F.J. McNally).

**Author Contributions:** Iris Y Juanico: Writing - review and editing, Conceptualization, Formal analysis, Investigation, Methodology. Christina M Meyer: Investigation. John E McCarthy: Formal analysis, Investigation. Ting Gong: Investigation, Methodology. Francis J McNally: Conceptualization, Project administration, Supervision, Writing - original draft.

**Reviewed By:** Paul E. Mains

**History:** Received June 25, 2021 Revision received July 9, 2021 Accepted July 12, 2021 Published July 19, 2021

**Copyright:** © 2021 by the authors. This is an open-access article distributed under the terms of the Creative Commons Attribution 4.0 International (CC BY 4.0) License, which permits unrestricted use, distribution, and reproduction in any medium, provided the original author and source are credited.

**Citation:** Juanico, IY; Meyer, CM; McCarthy, JE; Gong, T; McNally, FJ (2021). Paternal mitochondria from an *rmd-2*, *rmd-3*, *rmd-6* triple mutant are properly positioned in the *C. elegans* zygote. *microPublication Biology*. <https://doi.org/10.17912/micropub.biology.000422>

# Chapter 5

**Cohesin is required for meiotic spindle assembly independent of its role in cohesion in *C. elegans*.**

Karen P. McNally, Elizabeth A. Beath, Brennan M. Danlasky, Consuelo Barroso, Ting Gong, Wenzhe Li, Enrique Martinez-Perez, Francis J. McNally

McNally KP, Beath EA, Danlasky BM, Barroso C, Gong T, Li W, Martinez-Perez E, McNally FJ. Cohesin is required for meiotic spindle assembly independent of its role in cohesion in *C. elegans*. PLoS Genet. 2022 Oct 24;18(10):e1010136. doi: 10.1371/journal.pgen.1010136. PMID: 36279281; PMCID: PMC9632809.

I obtained the live imaging data and quantification of microtubules in control; *spo-11 rec-8* double mutant; *spo-11 rec-8 coh-3 coh-4* quadruple mutant and *bir-1* mutant (Figure S6).

## RESEARCH ARTICLE

Cohesin is required for meiotic spindle assembly independent of its role in cohesion in *C. elegans*Karen P. McNally<sup>1</sup>, Elizabeth A. Beath<sup>1</sup>, Brennan M. Danlasky<sup>1</sup>, Consuelo Barroso<sup>2</sup>, Ting Gong<sup>1</sup>, Wenzhe Li<sup>1</sup>, Enrique Martinez-Perez<sup>2,3</sup>, Francis J. McNally<sup>1\*</sup><sup>1</sup> Department of Molecular and Cellular Biology University of California, Davis, California, United States of America, <sup>2</sup> MRC London Institute of Medical Sciences London, United Kingdom, <sup>3</sup> Imperial College Faculty of Medicine London, United Kingdom\* [fjmcnally@ucdavis.edu](mailto:fjmcnally@ucdavis.edu)

## OPEN ACCESS

**Citation:** McNally KP, Beath EA, Danlasky BM, Barroso C, Gong T, Li W, et al. (2022) Cohesin is required for meiotic spindle assembly independent of its role in cohesion in *C. elegans*. PLoS Genet 18(10): e1010136. <https://doi.org/10.1371/journal.pgen.1010136>

**Editor:** Sarit Smolnikova, University of Iowa, UNITED STATES

**Received:** March 9, 2022

**Accepted:** October 10, 2022

**Published:** October 24, 2022

**Peer Review History:** PLOS recognizes the benefits of transparency in the peer review process; therefore, we enable the publication of all of the content of peer review and author responses alongside final, published articles. The editorial history of this article is available here: <https://doi.org/10.1371/journal.pgen.1010136>

**Copyright:** © 2022 McNally et al. This is an open access article distributed under the terms of the [Creative Commons Attribution License](https://creativecommons.org/licenses/by/4.0/), which permits unrestricted use, distribution, and reproduction in any medium, provided the original author and source are credited.

**Data Availability Statement:** All relevant data are within the paper and its [Supporting Information files](#).

## Abstract

Accurate chromosome segregation requires a cohesin-mediated physical attachment between chromosomes that are to be segregated apart, and a bipolar spindle with microtubule plus ends emanating from exactly two poles toward the paired chromosomes. We asked whether the striking bipolar structure of *C. elegans* meiotic chromosomes is required for bipolarity of acentrilolar female meiotic spindles by time-lapse imaging of mutants that lack cohesion between chromosomes. Both a *spo-11 rec-8 coh-4 coh-3* quadruple mutant and a *spo-11 rec-8* double mutant entered M phase with separated sister chromatids lacking any cohesion. However, the quadruple mutant formed an apolar spindle whereas the double mutant formed a bipolar spindle that segregated chromatids into two roughly equal masses. Residual non-cohesive COH-3/4-dependent cohesin on separated sister chromatids of the double mutant was sufficient to recruit haspin-dependent Aurora B kinase, which mediated bipolar spindle assembly in the apparent absence of chromosomal bipolarity. We hypothesized that cohesin-dependent Aurora B might activate or inhibit spindle assembly factors in a manner that would affect their localization on chromosomes and found that the chromosomal localization patterns of KLP-7 and CLS-2 correlated with Aurora B loading on chromosomes. These results demonstrate that cohesin is essential for spindle assembly and chromosome segregation independent of its role in sister chromatid cohesion.

## Author summary

Meiosis is the process that reduces the number of chromosomes from four to one during the formation of eggs and sperm so that a fertilized egg has exactly two copies of each chromosome. Meiotic errors result in offspring with an incorrect number of chromosomes which results in prenatal death or birth defects. Accurate meiosis requires that the four chromosomes at the beginning of meiosis are attached to each other by a protein called cohesin and a structure called a spindle that pulls individual chromosomes in two directions. Here we show that in the roundworm, *C. elegans*, cohesin is required for

**Funding:** This work was funded by National Institute of General Medical Sciences grant R35GM136241 to F.J.M., U.S. Department of Agriculture/National Institute of Food and Agriculture Hatch project 1009162 to F.J.M. and Medical Research Council core-funded grant MC-A652-5PY60 to E.M.P. The funders had no role in study design, data collection and analysis, decision to publish, or preparation of the manuscript.

**Competing Interests:** The authors have declared that no competing interests exist.

building a spindle that can pull in two directions independently of its role in attaching chromosome copies to each other. Because cohesin is gradually lost in aging women, these results may clarify why aging women have an increasing incidence of babies with birth defects caused by an incorrect number of chromosomes.

## Introduction

The accurate segregation of chromosomes during meiosis and mitosis requires sister chromatid cohesion (SCC) provided by the cohesin complex and a bipolar spindle with microtubule minus ends oriented toward the two poles and microtubule plus ends extending from the two poles toward the chromosomes [1]. During mitosis in most animal cells, spindle formation is initiated when organelles known as centrosomes are duplicated and move to opposite sides of the cell. There they anchor, nucleate and stabilize microtubules with their plus ends polymerizing away from the poles [2]. Microtubule plus ends puncture the nuclear membrane and capture the kinetochores of chromosomes, thus establishing a symmetric spindle axis.

In contrast to the pathway of mitotic spindle formation, the female meiotic cells of many animals lack centrosomes and spindle formation initiates when microtubules organize around chromatin during the two consecutive meiotic divisions. In *Xenopus* egg extracts and mouse oocytes, DNA-coated beads are sufficient to induce bipolar spindle assembly [3,4]. The mechanisms of acentrosomal spindle assembly are being elucidated in several species and two alternate pathways have been implicated. The first molecular activity to be identified in the assembly of microtubules around meiotic chromatin is the GTPase Ran. In the Ran pathway, spindle assembly factors (SAFs) contain nuclear localization sequences and are imported into the nucleus during interphase by binding to importins. GTP-Ran, which is maintained at a high concentration in the nucleus by the chromatin-bound GEF RCC1, causes dissociation of the SAFs from importins inside the nucleus, thus driving the directionality of import. Upon nuclear envelope breakdown, tubulin enters the region adjacent to chromatin and the locally activated SAFs initiate MT nucleation and stabilization [5]. Inhibition of the Ran pathway prevents or affects the assembly of acentrosomal spindles in *Xenopus* egg extracts [6] and in mouse [7], *Drosophila* [8] and *C. elegans* oocytes [9]. In *Xenopus* egg extracts, spindle assembly is induced by beads coated with the Ran GEF, RCC1, even without DNA [10].

The second pathway which has been implicated in acentrosomal spindle assembly requires the Chromosomal Passenger Complex (CPC), which includes the chromatin-targeting proteins Survivin and Borealin, the scaffold subunit INCENP, and Aurora B kinase [11]. The CPC is recruited to distinct regions on mitotic chromosomes by at least three different pathways [12]. Depletion of CPC components resulted in a lack of spindle microtubules in *Drosophila* oocytes [13] and in *Xenopus* egg extracts to which sperm nuclei or DNA-coated beads are added [14–16]. In *C. elegans* oocytes, the CPC subunits, BIR-1/survivin [17], INCENP [18], and the Aurora B-homolog AIR-2 [19,20] contribute to meiotic spindle assembly.

While the GTP Ran and CPC pathways are known to be involved in the initiation of acentrosomal spindle assembly, the mechanism by which the microtubules are captured into two poles is unclear. Spindles with one or more poles form when chromatin-coated beads are added to *Xenopus* egg extracts, suggesting that pole formation is an intrinsic activity of microtubules assembling around chromatin [10]. However, the results also suggest that the reproducible production of bipolar spindles requires that the process includes some bidirectionality. In *C. elegans*, meiotic bivalents, which promote assembly of a bipolar metaphase I spindle, are composed of 4 chromatids held together by chiasmata, physical attachments provided by



cohesin and a single crossover formed between homologous chromosomes. These bivalents have a discrete bipolar symmetry with a mid-bivalent ring containing the CPC, and they are capped at their two ends by cup-shaped kinetochores. Metaphase II univalents, which promote assembly of a bipolar metaphase II spindle, are composed of 2 chromatids held together by cohesin. These univalents also have a discrete bipolar symmetry with a CPC ring between sister chromatids that are each capped by cup-shaped kinetochores [18,19,21].

To test whether this chromosomal bipolar symmetry is required for spindle bipolarity, we analyzed cohesin mutants that start meiotic spindle assembly with separated sister chromatids rather than the bivalents present in wild-type meiosis I or the univalents present in wild-type meiosis II. During meiosis, cohesin is composed of SMC-1, SMC-3, and one of 3 meiosis-specific kleisin subunits: REC-8 and the functionally redundant COH-3 and COH-4 [22–24]. Both REC-8 and COH-3/4 cohesin promote pairing and recombination between homologous chromosomes during early meiosis, thus ensuring chiasma formation. However, SCC appears to be provided by REC-8 complexes, while COH-3/4 complexes associate with individual chromatids [25,26]. Previous work indicated that *rec-8* single mutants have 12 univalents at meiosis I, with each pair of sister chromatids held together by recombination events dependent on COH-3/COH-4 cohesin [25,27]. Sister chromatids segregated equationally at anaphase I of *rec-8* mutants with half the chromatids going into a single polar body [23]. This suggests that *rec-8* embryos enter metaphase II with 12 separated sister chromatids. Although it was reported that *rec-8* embryos do not extrude a second polar body, the structure of the metaphase II spindle was not described in detail. To address the question of whether chromosomal bipolarity is required for spindle bipolarity, we first monitored metaphase II spindle assembly in a *rec-8* mutant by time-lapse imaging of living embryos *in utero*.

## Results

### Apolar spindles assemble around separated sister chromatids of metaphase II *rec-8* embryos

Time-lapse *in utero* imaging of control embryos with microtubules labeled with mNeonGreen::tubulin and chromosomes labeled with mCherry::histone H2b revealed bipolar spindles that shorten, then rotate, then segregate chromosomes in both meiosis I and meiosis II (Fig 1A and S1 Video). Wild-type embryos enter metaphase I with 6 bivalents and enter metaphase II with 6 univalents whereas *rec-8* embryos enter metaphase I with 12 univalents (Fig 1B and S1A Fig) and enter metaphase II with approximately 12 separated sister chromatids (Fig 1B) [23]. Time-lapse imaging of *rec-8* embryos revealed bipolar metaphase I spindles that shortened, rotated, and segregated chromosomes (Fig 1C, -1:45–5:15; and S2 Video). Metaphase II *rec-8* embryos, however, assembled an amorphous cloud of microtubules around separated sister chromatids which did not segregate into two masses. The apolar spindle shrank with timing similar to spindle shortening that occurs during wild-type meiosis (Fig 1C, 9:15–18:00). Because spindle shortening is caused by APC-dependent inactivation of CDK1 [28], this suggests that the failure in metaphase II spindle assembly is not due to a lack of cell cycle progression. The bipolar nature of metaphase I *rec-8* spindles and the apolar nature of *rec-8* metaphase II spindles was confirmed by time-lapse imaging of GFP::ASPM-1 (Fig 1D). ASPM-1 binds at microtubule minus ends [29] so the dispersed appearance of GFP::ASPM-1 on *rec-8* metaphase II spindles suggests that microtubules are randomly oriented in the spindle.

Time-lapse imaging of the kinetochore protein GFP::MEL-28 in *rec-8* embryos revealed metaphase I univalents with discrete bipolar structure similar to wild-type metaphase II

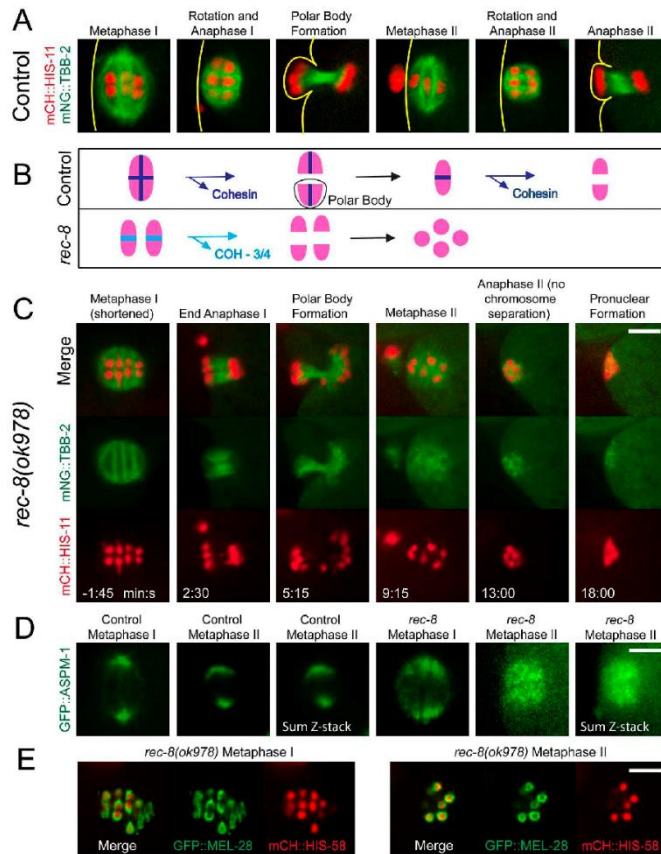


**Fig 1. Metaphase II spindles are apolar in *rec-8(ok978)*.** (A) In 8/8 control embryos, bipolar MI spindles shorten and rotate, chromosomes segregate, and a polar body forms. The cycle repeats with a bipolar MII spindle. Lines indicate the position of the cortex. (B) In metaphase I, both sister chromatids and homologs are bound by cohesin containing both REC-8 and COH-3/4 (dark blue); homologs are released and separate in Anaphase I; sister chromatids are released and separate in Anaphase II. In *rec-8(ok978)*, COH-3/4 cohesin (light blue) is present in an expanded region between sister chromatids in MI and no cohesin is present in MII. (C) Time-lapse imaging of *rec-8(ok978)* expressing mNG::TBB-2 and mCH::HIS-11. The metaphase II spindle appears disorganized and no anaphase chromosome separation occurs in 8/8 embryos. 0 minutes is the end of MI spindle rotation. (D) Control and *rec-8(ok978)* embryos expressing GFP::ASPM-1. Single-focal plane imaging was ended at metaphase II and z-stacks were acquired. 7/7 control MI spindles, 7/7 *rec-8* MI spindles, and 7/7 control MII spindles were bipolar. 8/8 *rec-8* MII spindles were apolar. (E) Imaging of *rec-8* embryos expressing GFP::MEL-28 revealed kinetochore cups in 4/4 MI spindles and chromatids enclosed by GFP::MEL-28 in 7/7 MII spindles. All bars = 4 $\mu$ m.

<https://doi.org/10.1371/journal.pgen.1010136.g001>

univalents, whereas metaphase II separated sister chromatids were enveloped by a continuous shell of GFP::MEL-28 with no bipolar symmetry (Fig 1E).

### Apolar spindles assemble around separated sister chromatids of metaphase I *rec-8 coh-4 coh-3* embryos and *spo-11 rec-8 coh-4 coh-3* embryos

To test whether the apparent inability of separated sister chromatids to drive bipolar spindle assembly is specific for meiosis II, we compared control embryos (Fig 2A and 2B) with embryos of a *rec-8 coh-4 coh-3* triple mutant which lack meiotic cohesin and therefore enter metaphase I with 24 separated sister chromatids [23] (Fig 2A and S1C Fig). In the majority of these embryos, an amorphous cloud of microtubules assembled around the separated sister chromatids (Fig 2C) at the same time after ovulation that a bipolar spindle assembled in control embryos (Fig 2B). This amorphous cloud shrank in diameter (Fig 2C, -0:20) at a similar time as control spindles, which shortened prior to anaphase chromosome separation (Fig 2B, -1:10). The mutant spindles did not undergo anaphase like control spindles. In a minority of *rec-8 coh-4 coh-3* triple mutant embryos, a bipolar metaphase I spindle started to form (Fig 2D, -6:50 and -6:10) but then quickly collapsed into an amorphous cloud of microtubules (Fig 2D, -4:20). These spindles also shrank with timing similar to wild-type spindle shortening and did not undergo anaphase (Fig 2D, 5:00). Triple mutant embryos assembled a second amorphous mass of microtubules at the time of normal metaphase II spindle assembly (Fig 2D, 13:20) and this meiosis II spindle also shrank without segregating chromosomes (Fig 2D, 16:10). Similar results were obtained by fixed immunofluorescence (Fig 2E).

We also examined meiotic embryos within a *spo-11 rec-8 coh-4 coh-3* quadruple mutant (Fig 3A), which lack meiotic cohesin and the double strand breaks that initiate meiotic recombination (*spo-11* mutation) and also enter metaphase I with 24 separated sister chromatids [23] (Fig 3B). In all of these embryos, an amorphous mass of microtubules formed around the 24 chromatids (Fig 3A, -2:30; and S3 Video). This cloud of microtubules shrank with similar timing to wild-type spindle shortening and was not followed by any separation of chromosomes (Fig 3A, -2:30–2:30). A second large mass of microtubules formed at the time that a metaphase II spindle normally forms (Fig 3A, 12:15). This metaphase II mass also shrank with similar timing to normal spindle shortening (Fig 3A, 12:15–16) and chromatids did not separate into two masses and polar bodies did not form in 10/10 time-lapse sequences. Possible reasons for the stronger defect in the quadruple mutant than the triple mutant are discussed below. These results indicated that bipolar spindle assembly around separated sister chromatids that lack both cohesin and cohesion, is severely defective at both metaphase I and metaphase II.

### Bipolar spindles assemble around separated sister chromatids of metaphase I *spo-11 rec-8* embryos

To distinguish whether cohesin vs cohesion is required for bipolar spindle assembly, we analyzed *spo-11 rec-8* double mutants (Fig 3C) which enter metaphase I with 24 separated sister chromatids [24] (Fig 3D and S1B Fig) but have been reported to retain COH-3/4 cohesin on pachytene chromosomes [24,26]. Bipolar metaphase I spindles assembled in *spo-11 rec-8* double mutants and these spindles shortened, rotated, and then segregated the chromatids into two masses (Fig 3C, -6:50–5:20; and S4 Video). During meiosis II, an amorphous mass of microtubules assembled around the chromatids and this mass shrank but did not separate chromatids into two masses (Fig 3C, 16:10–18:40), similar to meiosis I in the triple and quadruple mutant, and meiosis II in the triple mutant, the quadruple mutant and the *rec-8* single mutant. The spindle pole protein, GFP::MEL-1, clearly labelled two poles of metaphase I and

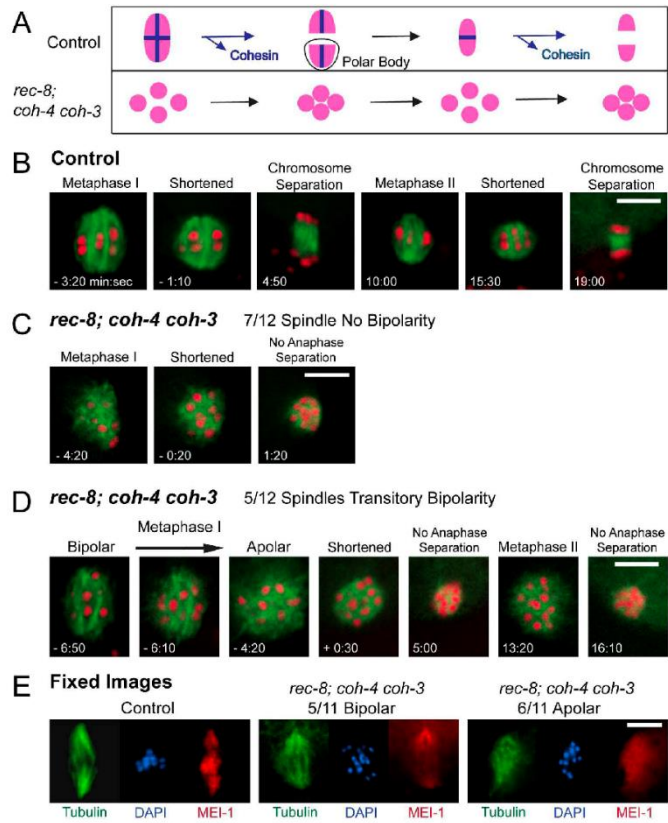


**Fig 2. Bipolar spindles can form in *rec-8; coh-4 coh-3* embryos, but they are unstable and become apolar.** (A) In metaphase I of control embryos, both sister chromatids and homologs are bound by cohesin; homologs are released and separate in Anaphase I; sister chromatids are released and separate in anaphase II. In *rec-8; coh-4 coh-3* embryos, no cohesin is present in either MI or MII and chromatids do not separate. (B) Time-lapse images of a control embryo expressing mNG::TBB-2 and mCH::HIS-11 show bipolar meiosis I and meiosis II spindles which shorten and undergo anaphase chromosome separation. Time 0:00 for B, C, and D is the time of full contact between the spindle and the cortex. (C) Time-lapse images captured with 7/12 *rec-8; coh-4 coh-3* embryos expressing mNG::TBB-2 and mCH::HIS-11 show MI spindles which were apolar at ovulation, then shortened and chromosome separation did not occur. MII (not shown) was similar to MI. (D) In 5/12 embryos, MI spindles initially appeared to be bipolar, but were unstable and became apolar. The MI spindles shortened and no anaphase chromosome separation occurred. MII was similar to MI. (E) Control and *rec-8; coh-4 coh-3* embryos were fixed and stained with both tubulin and MEI-1 antibodies and with DAPI. 10/10 Control and 5/11 mutant embryos had spindles with MEI-1 concentrated on chromosomes and at two poles. 6/11 mutant spindles were apolar. All bars = 5 $\mu$ m.

<https://doi.org/10.1371/journal.pgen.1010136.g002>

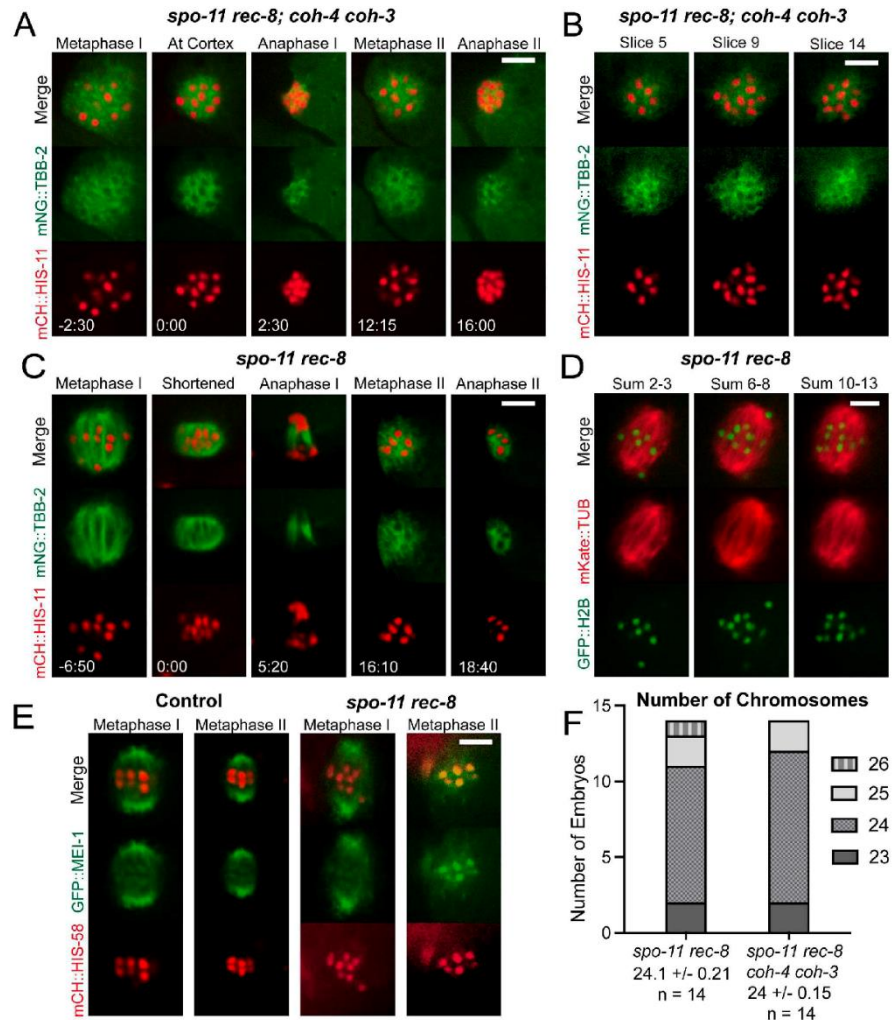


**Fig 3. *spo-11 rec-8; coh-4 coh-3* embryos have disorganized meiotic spindles whereas *spo-11 rec-8* embryos have bipolar spindles in meiosis I. (A)** Single-focal plane time-lapse imaging of a *spo-11 rec-8; coh-4 coh-3* mutant expressing mNeonGreen::TBB-2 and mCherry::HIS. Disorganized spindles were observed in both MI and MII in 10/10 embryos. 0 minutes is the time when the MI spindle contacts the cortex. (B) Z-stack slices of a *spo-11 rec-8; coh-4 coh-3* MI spindle show 24 chromatids with one chromatid visible in both slices 9 and 14. (C) Single-focal plane time-lapse imaging of 13/13 *spo-11 rec-8* embryos show bipolar MI spindles which undergo anaphase chromosome separation and MII spindles which are disorganized and do not undergo anaphase chromosome separation. 0 minutes is the completion of MI spindle rotation. (D) Combined z-stack slices of a *spo-11 rec-8* MI spindle show 24 chromatids. (E) Time-lapse imaging of *spo-11 rec-8* embryos expressing GFP::MEI-1. 10/10 Control MI spindles, 5/5 Control MII spindles and 9/9 *spo-11 rec-8* MI spindles were bipolar. 8/8 *spo-11 rec-8* MII spindles were apolar. (F) Graph showing chromosome numbers during MI in both *spo-11 rec-8*, and *spo-11 rec-8; coh-4 coh-3* mutant embryos. All bars = 4 $\mu$ m.

<https://doi.org/10.1371/journal.pgen.1010136.g003>

metaphase II control spindles but only labelled spindle poles of metaphase I *spo-11 rec-8* mutants (Fig 3E). GFP::MEI-1 was dispersed on metaphase II spindles, confirming the apolar structure of these spindles. GFP::MEI-1 also associated with chromosomes and this chromosome association was much more apparent in metaphase II *spo-11 rec-8* spindles (Fig 3E). However, the background subtracted ratio of mean GFP::MEI-1 pixel intensity on chromosomes divided by mean cytoplasmic intensity was not significantly increased between metaphase I and metaphase II for either *spo-11 rec-8* (MI:  $7.01 \pm 0.89$ , N = 5 embryos, n = 15 chromosomes; MII:  $5.62 \pm 0.76$ , N = 5, n = 15; p = 0.23) or control spindles (MI:  $5.62 \pm 0.33$ , N = 6, n = 18; MII:  $5.47 \pm 0.35$ , N = 6, n = 18; p = 0.74). This result indicated that the enhanced contrast of chromosomal GFP::MEI-1 in *spo-11 rec-8* embryos was due to the decrease in microtubule-associated GFP::MEI-1.

The ability of *spo-11 rec-8* embryos to form bipolar metaphase I spindles might be due to one or two univalents held together by residual COH-3/COH-4 cohesin. However, 24 chromosome bodies could be counted in Z-stacks of the majority of metaphase I spindles (Fig 3F) and all metaphase I spindles were bipolar (13/13 mNeonGreen tubulin, 9/9 GFP::MEI-1). The ability of *spo-11 rec-8* embryos to undergo anaphase I but inability to undergo anaphase II is consistent with the single polar body previously described for this double mutant [23].

#### Cohesin rather than cohesion is required for bipolar spindle assembly

The ability of *spo-11 rec-8* mutants to build bipolar metaphase I spindles but not metaphase II spindles might be because metaphase I chromatids retain cohesin, as high levels of COH-3/4 associate with pachytene chromosomes of *rec-8* mutants [24,26]. This non-cohesive COH-3/4 cohesin might be removed at anaphase I, leaving the metaphase II chromatids with no cohesin. This hypothesis was validated by time-lapse imaging of the cohesin subunit, SMC-1::AID::GFP, which would be a component of both REC-8 cohesin and COH-3/4 cohesin. SMC-1::AID::GFP was found on control metaphase I and metaphase II chromosomes and on most metaphase I chromosomes of *spo-11 rec-8* mutants but was absent from the metaphase II chromatids of *spo-11 rec-8* mutants (Fig 4A–4C). The absence of SMC-1 from a subset of metaphase I *spo-11 rec-8* chromatids may be due to WAPL-1-dependent and WAPL-1-independent pre-anaphase removal pathways [25]. To more directly test the requirement for cohesin, we monitored metaphase I spindle assembly in embryos depleted of SMC-1 with an auxin-induced degron [30]. For this experiment we monitored endogenously tagged GFP::LIN-5 as a spindle pole marker instead of GFP::ASPM-1 because the *aspm-1* gene is linked to *smc-1*. The majority of SMC-1-depleted embryos formed apolar metaphase I spindles (Fig 4D). The small number of multipolar spindles likely resulted from an incomplete depletion of SMC-1 as a subset of oocyte nuclei exhibited residual SMC-1::AID::GFP fluorescence after auxin treatment (S2A and S2B Fig) and auxin treatment only caused a reduced brood size (S1 Table) whereas null mutants have been reported to be completely sterile [31]. These results support the idea that cohesin on chromosomes rather than cohesion between chromosomes is required for bipolar spindle assembly during both meiosis I and meiosis II.

#### A specific subclass of chromosome-associated Aurora B kinase correlates with competence for bipolar spindle assembly

We then asked why cohesin might be required for bipolar spindle assembly. During mitosis in cultured human cells [32] and fission yeast [33], cohesin-associated PDS5 recruits haspin kinase to chromosomes [32] and the recruited haspin phosphorylates histone H3 threonine 3. Although PDS5 has important functions during meiotic prophase in several species [34–37], a role in recruiting haspin during meiosis has not been reported to our knowledge. The survivin

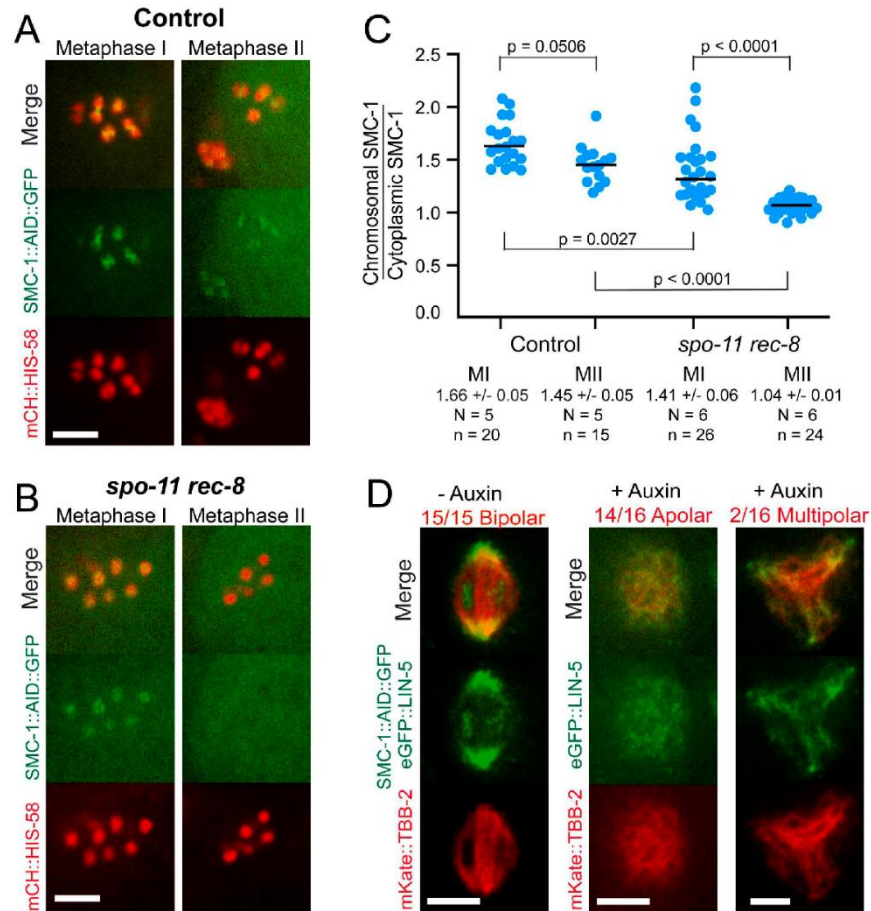


**Fig 4. Non-cohesive cohesin is sufficient for bipolar spindle formation.** Single-plane time-lapse images from control (A) and *spo-11 rec-8* (B) embryos expressing SMC-1::AID::GFP and mCH::HIS-58. (C) SMC-1::AID::GFP pixel intensities on individual chromosomes were determined relative to cytoplasmic background. N, number of embryos. n, number of chromosomes. (D) *C. elegans* expressing SMC-1::AID::GFP, eGFP::LIN-5 and mKate::TBB-2 were incubated overnight in the presence or absence of auxin. Single slices of z-stack MI images are shown. All bars = 4 $\mu$ m.

<https://doi.org/10.1371/journal.pgen.1010136.g004>

(BIR-1 in *C. elegans*) subunit of the CPC binds to the phosphorylated histone thereby recruiting Aurora B to chromosomes [32,38,39]. In *C. elegans*, haspin (HASP-1) is required to promote recruitment of Aurora B (AIR-2) to the midbivalent region in diakinesis oocytes [40] and AIR-2 is essential for bipolar meiotic spindle assembly in *C. elegans* [19,20]. Therefore we hypothesized that chromatids that lack cohesin-recruited AIR-2 would be unable to form

bipolar meiotic spindles. Time-lapse imaging of control embryos with endogenously tagged AIR-2::GFP (Fig 5A) revealed bright rings between homologs at metaphase I, microtubule association during anaphase I, bright rings between sister chromatids at metaphase II, and microtubule association during anaphase II as previously described [19]. In *rec-8* embryos, AIR-2 formed bright structures between sister chromatids at metaphase I and filled spaces between chromosomes at anaphase I, consistent with transfer to microtubules. However, at metaphase II in *rec-8* embryos, AIR-2::GFP was dim and diffuse on bipolar-spindle-incompetent separated sister chromatids, then became bright in regions between chromosomes, consistent with transfer to microtubules at anaphase II (Fig 5B). In *rec-8* embryos, AIR-2::GFP was significantly dimmer on chromosomes at metaphase II relative to metaphase I whereas no such decrease was observed in control embryos (Fig 5C).

In control -1 diakinesis oocytes, which will initiate meiosis I spindle assembly within 1–23 min [41], AIR-2::GFP brightly labeled the space between the homologous chromosomes in 6 bivalents. In contrast, GFP::AIR-2 was dim and diffuse on all of the bipolar-spindle-incompetent separated sister chromatids of *spo-11 rec-8 coh-4 coh-3* quadruple mutants (Fig 5D and 5E, S3 Fig). Unlike the quadruple mutant, a fraction of chromatids in the triple mutant had AIR-2::GFP intensities that overlapped with those of controls (Fig 5E) providing a possible explanation for the stronger spindle assembly defect in the quadruple mutant. Diakinesis oocytes of bipolar-spindle-competent *spo-11 rec-8* double mutants contained a mixture of separated sister chromatids with either dim diffuse AIR-2::GFP or bright patterned AIR-2::GFP (Fig 5D and 5E, S3 Fig). The bright patterned AIR-2::GFP on a subset of separated sister chromatids could also be observed in bipolar metaphase I spindles of *spo-11 rec-8* mutants (Fig 5F). The subset of metaphase I chromatids in *spo-11 rec-8* mutants with bright patterned AIR-2 was the same subset that retained COH-3/4 cohesin (S4 Fig). In bipolar-spindle-incompetent metaphase II embryos of *spo-11 rec-8* embryos, AIR-2::GFP was again dim and diffuse on all separated sister chromatids (Fig 5F). These results indicated that a specific subclass of AIR-2::GFP, that which is cohesin-dependent and forms a bright pattern on chromosomes, can promote bipolar spindle assembly. The subclasses of AIR-2::GFP that are cohesin-independent label chromatin dimly and diffusely, and label anaphase microtubules, but cannot efficiently promote bipolar spindle assembly.

To further test this idea, we analyzed sperm-derived chromatin in meiotic embryos. Whereas demembrated sperm [42] or DNA-coated beads [3] added to *Xenopus* egg extracts induce bipolar spindle assembly, the sperm-derived chromatin in *C. elegans* meiotic embryos does not induce spindle assembly [43]. Endogenously tagged GFP::SMC-1 was not detected on sperm-derived DNA in meiotic embryos (S5A Fig). When male worms with unlabelled AIR-2 were mated to hermaphrodites expressing endogenously tagged AIR-2::GFP, maternal AIR-2::GFP was recruited to the sperm DNA (S5B Fig) but this cohesin-independent AIR-2 did not induce bipolar spindle assembly. The cohesin-dependent subclass of AIR-2 might have a unique substrate specificity or it might be needed to reach a threshold of activity in combination with cohesin-independent AIR-2.

The reason for the heterogeneity of AIR-2 loading on separated sister chromatids of *spo-11 rec-8* mutants is not known, although it correlates with the heterogeneity of residual COH-3/4 cohesin (S4 Fig). The heterogeneity of AIR-2 loading on the 12 univalents of a *spo-11* single mutant correlates with heterogeneity in retention of LAB-1 and protein phosphatase 1, which remove haspin-dependent histone H3 T3 phosphorylation [40,44,45]. Our results suggest that bright patterned AIR-2 on only a subset of chromatids is sufficient to promote bipolar spindle assembly.



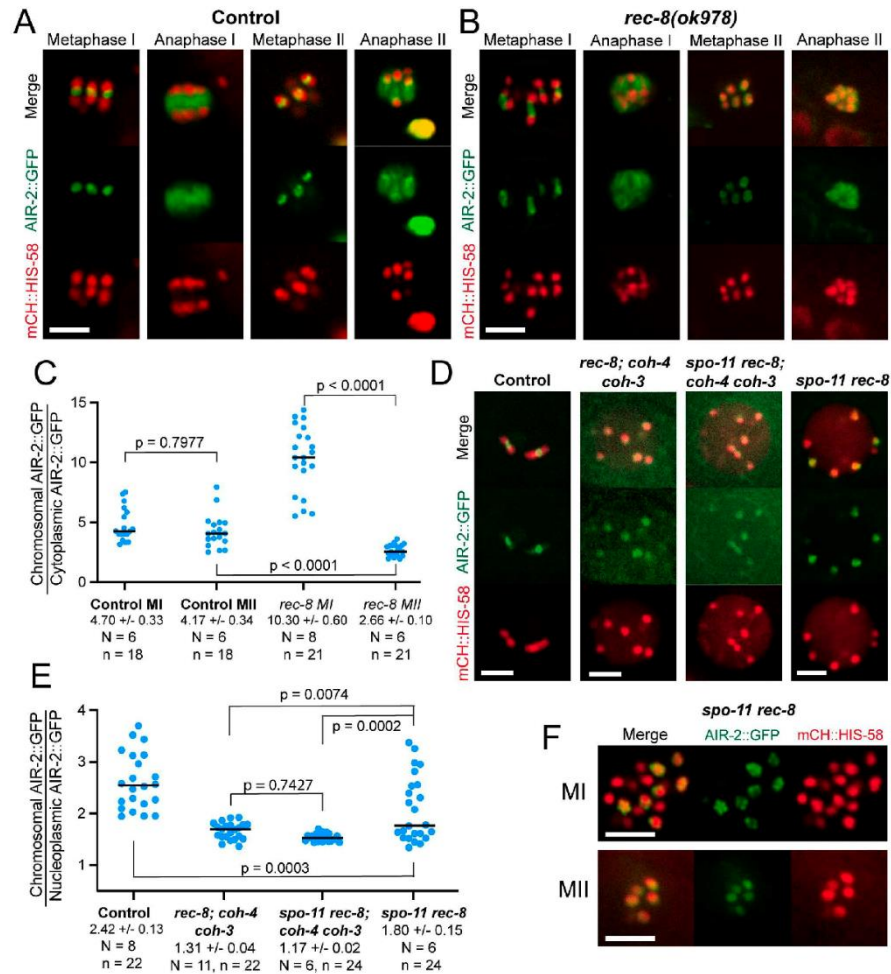


**Fig 5. AIR-2::GFP levels are diminished and diffuse in the absence of cohesin.** (A) In time-lapse images of control embryos, AIR-2::GFP is in the midvalvular ring structure during metaphase I and II and on MTs during anaphase I and II. (B) In *rec-8(ok978)*, AIR-2::GFP is an expanded ring structure during MI, diffuse on chromatids in MII and extends into a broader area during both anaphase I and II, consistent with transfer to microtubules. (C) Quantification of AIR-2::GFP intensities on chromosomes relative to the cytoplasm in control and *rec-8(ok978)*. Ratios varied depending on the distance of the chromosomes from the coverslip. N, number of embryos. n, number of chromosomes. The higher than control intensities in *rec-8* MI might be due to the previously reported [23] expanded ring structure between chromatids which might involve unresolved synaptonemal complex intermediates [25,27]. (D) -1 oocyte nuclei in living control and mutant worms expressing AIR-2::GFP and mCH::HIS-58. (E) Quantification of AIR-2::GFP intensities on chromosomes relative to the nucleoplasm in control and mutant oocytes. N, number of oocytes. n, number of chromosomes. (F) MI and MII metaphase chromosomes in living *spo-11(met4) rec-8(ok978)* embryos. All bars = 4µm.

<https://doi.org/10.1371/journal.pgen.1010136.g005>

### Haspin-dependent Aurora B kinase is required for bipolar meiotic spindle assembly

To more specifically identify the subclass of Aurora B that is required for bipolar spindle assembly, we analyzed a *bir-1(E69A, D70A)* mutant. This double mutation is equivalent to the D70A, D71A mutation in human survivin that prevents binding to T3-phosphorylated histone H3 and prevents recruitment of Aurora B to mitotic centromeres in HeLa cells [39]. Time-lapse imaging of mNeonGreen::tubulin in *bir-1(E69A, D70A)* mutants revealed apolar metaphase spindles that shrank without chromosome separation during both meiosis I and meiosis II (Fig 6A). The *bir-1(E69A, D70A)* embryos were unlike the cohesin mutants in that they entered meiosis I with 6 bivalents (11/11 z-stacks of -1 oocytes), suggesting successful formation of chiasmata between homologous chromosomes during meiotic prophase and intact SCC (Fig 6A). Endogenously-tagged AIR-2::GFP diffusely labeled both lobes of metaphase I (Fig 6B) and diakinesis (Fig 6C) bivalents in *bir-1(E69A, D70A)*. This was in contrast to the bright ring of AIR-2::GFP that is observed between the lobes in controls. AIR-2::GFP localized in a broader pattern consistent with transfer to microtubules during anaphase I and anaphase II (Fig 6B) as was observed in cohesin mutants. Apolar metaphase I spindles (Fig 6D, center) also formed after depletion of haspin kinase with an auxin-induced degron. Like *bir-1(E69A, D70A)* embryos, haspin-depleted embryos entered meiosis I with 6 bivalents (10/10 z-stacks of metaphase I), indicating the presence of chiasmata and SCC. As with cohesin mutants that were bipolar-spindle-incompetent, the fluorescence intensity of AIR-2::GFP on chromosomes was strongly reduced in both *bir-1(E69A, D70A)* and *hasp-1(degron)* embryos (Fig 6E). Whereas all *bir-1(E69A, D70A)* spindles were apolar, a minority of *hasp-1(degron)* spindles were multipolar (Fig 6D right, and 6F). Apolar spindles had undetectable phosphor H3 T3 staining whereas multipolar spindles had reduced phosphor H3 T3 staining relative to no auxin controls (S2C–S2E Fig). In addition, a low frequency of hatching was observed among the progeny of *hasp-1(AID)* worms on auxin plates (S1 Table). Because a *hasp-1(null)* mutant is completely sterile [46], the low hatch rate suggested that the low frequency of bipolar spindles in HASP-1-depleted worms was due to incomplete depletion by the degron. Because haspin is recruited to chromosomes by cohesin-associated PDS5 [32], these results indicated that the subclass of Aurora B that is recruited to chromosomes by cohesin and haspin-dependent phosphorylation of histone H3 is required for bipolar spindle assembly and that cohesin-independent and haspin-independent Aurora B on chromosome lobes and anaphase microtubules are not sufficient to drive bipolar spindle assembly.

### Cohesin is required for coalescence of microtubule bundles into spindle poles

*C. elegans* meiotic spindle assembly begins at germinal vesicle breakdown in the -1 oocyte that is still in the gonad. Microtubule bundles assemble within the volume of the nucleus as the nuclear envelope breaks down. Oocytes are then fertilized as they ovulate into the spermatheca and meiosis is completed in fertilized embryos that have moved out of the spermatheca into the uterus. Microtubule bundles can coalesce into poles either before, during, or shortly after ovulation [47–50]. The meiosis I spindle assembly defect in *spo-11 rec-8 coh-4 coh-3* mutants shown in Fig 3A was determined from time-lapse imaging of fertilized embryos in the uterus. To more precisely define the spindle assembly step that is defective in cohesin mutants, we conducted time-lapse imaging starting at nuclear envelope breakdown in -1 oocytes. In bipolar-spindle-competent control (Fig 7A and 7B) and *spo-11 rec-8* (Fig 7C and 7D) -1 oocytes, as well as bipolar-spindle-incompetent *spo-11 rec-8 coh-4 coh-3* (Fig 7E and 7F) -1 oocytes, microtubule bundles initially filled the entire volume of the germinal vesicle as it broke down.

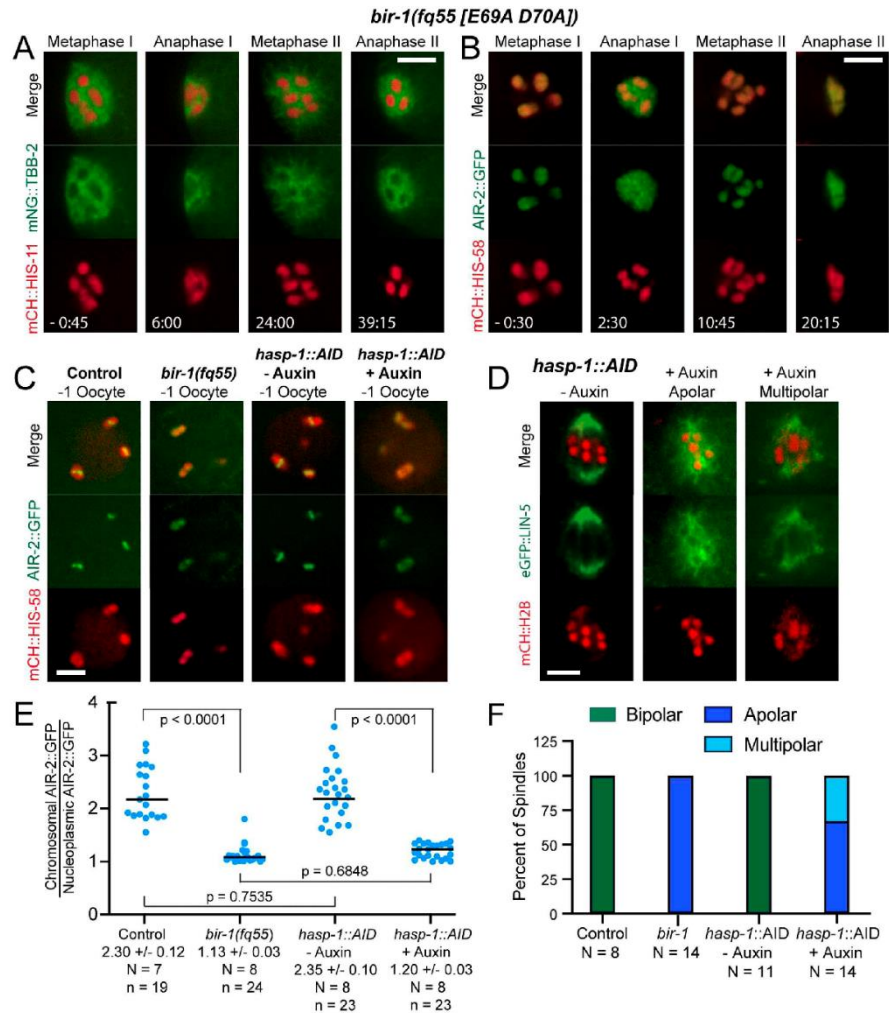


**Fig 6. AIR-2 is recruited by Survivin and Haspin for bipolar spindle formation.** (A) Time-lapse images of 14/14 *bir-1(fq55)* embryos expressing mNG::TBB-2 and mCH::HIS-11 show disorganized MI spindles and no MI anaphase chromosome separation. An example of a *bir-1(+)/bir-1(+)* control with the same transgenes is shown in Fig 1A. (B) Similar results were obtained in 4/4 *bir-1(fq55)* embryos expressing AIR-2::GFP, which is diffuse on both MI and MII metaphase chromosomes and present in a broader pattern consistent with microtubules during anaphase. An example of a *bir-1(+)/bir-1(+)* control with the same transgenes is shown in Fig 5A. (C) Single slices from z-stack images of -1 oocytes in *C. elegans* expressing AIR-2::GFP and mCH::HIS-58. 11/11 -1 oocytes in *bir-1(fq55)* embryos had 6 mCH::HIS-58 labelled bodies. (D) Single-plane images of *hasp-1::AID* embryos expressing eGFP::LIN-5 and mCH::H2B. Left: Bipolar spindle without auxin (- auxin). Center: An apolar spindle with auxin (+ auxin). Right: A multipolar spindle with auxin (+ auxin). 10/10 MI spindles in Auxin-treated *hasp-1::AID* embryos had 6 mCH::HIS-58 labelled bodies. (E) AIR-2::GFP pixel intensities on individual chromosomes were determined relative to nucleoplasmic background. N, number of oocytes. n, number of

chromosomes. (F) Graph showing percent of apolar, multipolar, and bipolar spindles in *bir-1* and auxin-treated *hasp-1::AID* embryos. N, number of embryos. All bars = 4  $\mu$ m.

<https://doi.org/10.1371/journal.pgen.1010136.g006>

The microtubule bundles of control (Fig 7B) and *spo-11 rec-8* (Fig 7D) coalesced first into multiple poles, then into two poles as the oocytes squeezed into, then out of, the spermatheca. In contrast, the microtubule bundles of *spo-11 rec-8 coh-4 coh-3* (Fig 7F) did not coalesce even after ovulation into the uterus. This phenotype is consistent with that previously observed by fixed immunofluorescence of *air-2(degron)* embryos [20] and is distinct from the pole-stability phenotype reported for *zyg-9(RNAi)* where poles form but then fall apart [9]. In addition, the

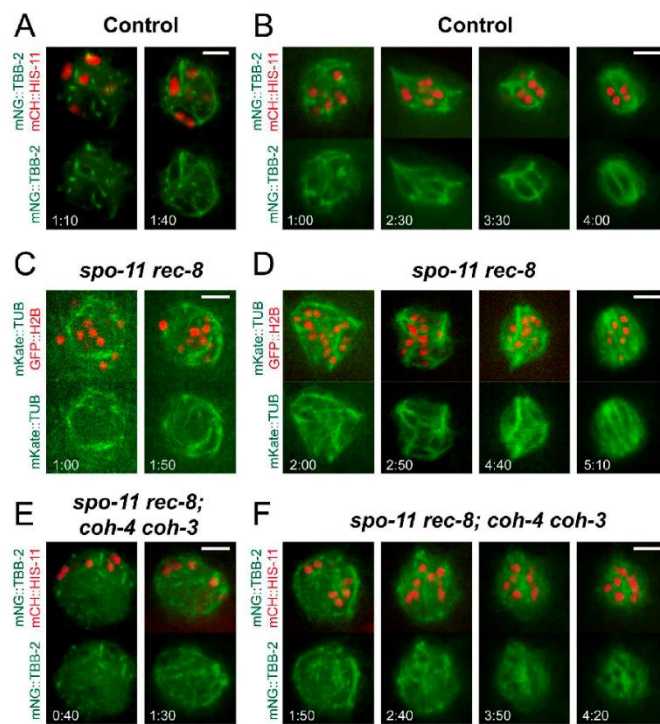


**Fig 7. Cohesin is necessary to direct the formation of spindle poles.** Time-lapse images in A, C, and E were captured in the gonad prior to ovulation; images in B, D, and F were captured post-ovulation in the uterus. (A, B) Time-lapse images of 7/7 control embryos show MT fibers organizing rapidly around chromosomes. Spindles become multipolar, then bipolar as poles coalesce. Times are from the initial observation of spindle MTs. (C, D) Time-lapse images of 13/13 *spo-11 rec-8* embryos show spindle fibers coalescing into multiple poles, then two poles. (E, F) Time-lapse images of 7/7 *spo-11 rec-8 coh-4 coh-3* embryos show that spindle fibers begin to form, but do not become organized into poles. All bars = 4  $\mu$ m.

<https://doi.org/10.1371/journal.pgen.1010136.g007>

mean fluorescence intensity of mNeonGreen::tubulin, indicative of microtubule density, was significantly reduced in apolar metaphase I spindles of *bir-1(E69A, D70A)* and *spo-11 rec-8 coh-4 coh-3* embryos relative to the bipolar spindles in control and *spo-11 rec-8* metaphase I spindles (S6 Fig). These results suggested that cohesin-dependent AIR-2 might regulate proteins that promote coalescence of microtubule bundles and promote microtubule polymerization, although other models are possible.

### Cohesin-dependent Aurora B kinase correlates with altered localization of spindle assembly factors on meiotic chromosomes

We hypothesized that cohesin-dependent Aurora B on chromosomes might activate microtubule-binding proteins that are required for coalescence of microtubule bundles and microtubule polymerization, or inhibit proteins that antagonize bundle coalescence and microtubule polymerization. Meiotic chromosome-associated spindle assembly factors include the katanin homolog, MEI-1 [51], the kinesin-13, KLP-7 [50,52], and the CLASP2 homolog, CLS-2 [19,53]. Loss of MEI-1 function results in apolar spindles with dispersed ASPM-1 [54] and reduced microtubule density [48,55] similar to those observed in cohesin mutants. However, apolar spindles in *mei-1* mutants are far from the cortex at metaphase I [47] whereas cohesin-mutant apolar spindles were cortical at metaphase I (Figs 1C, 1D, 2C, 3A and 3B). In addition, endogenously tagged GFP::MEI-1 was retained on chromosomes of apolar metaphase II *spo-11 rec-8* mutants (Fig 3E). These results suggest that MEI-1 is active in embryos that are deficient in cohesin-recruited AIR-2.

Endogenously tagged KLP-7::mNeonGreen localized to the midbivalent ring and to the two lobes of control bivalents (Fig 8A) but localized only to the two lobes in *bir-1(E69A, D70A)* mutants (Fig 8B). KLP-7 is also lost from the midbivalent ring after *air-2(degron)* depletion [20]. In living *spo-11 rec-8* double mutants, KLP-7::mNeonGreen localized in a bright pattern with a larger area on a subset of separated sister chromatids in bipolar-spindle-competent metaphase I embryos but labeled separated sister chromatids with a more uniform smaller area in bipolar-spindle-incompetent metaphase II embryos (Fig 8C and 8D). In fixed *spo-11 rec-8* embryos stained with antibodies and imaged with Airyscan, the pattern of KLP-7 on single chromatids was clearly distinct from that of AIR-2 (Fig 8E). In living *spo-11 rec-8* metaphase I embryos there was a positive correlation between the fluorescence intensity of endogenously tagged mScarlet::AIR-2 and the area of endogenously tagged KLP-7::mNeonGreen (Fig 8F). This result indicated that a subclass of bright patterned AIR-2 that is cohesin-dependent, and that correlates with bipolar spindle assembly, also correlates with a subclass of KLP-7 on chromosomes.

CLS-2::GFP labeled the kinetochore cups enveloping the two lobes of metaphase I bivalents but was not detected in the midbivalent region in control embryos (Fig 9A and S5 Video) in agreement with a previous study [56]. In contrast, CLS-2::GFP labeled kinetochore cups and the midbivalent region in *bir-1(E69A, D70A)* mutants (Fig 9A and S6 Video). In *spo-11 rec-8* double mutants, CLS-2::GFP localized in hollow spheres with a larger diameter on a subset of separated sister chromatids in bipolar-spindle-competent metaphase I embryos but labeled separated sister chromatids with more uniform, smaller diameter hollow spheres in bipolar-spindle-incompetent metaphase II embryos (Fig 9B and 9C). In *spo-11 rec-8* metaphase I embryos there was a weak positive correlation between the diameter of histone H2b and the diameter of CLS-2::GFP (correlation coefficient 0.37; Fig 9D) and a strong positive correlation (correlation coefficient 0.79) between the fluorescence intensity of endogenously tagged mScarlet::AIR-2 and the diameter of CLS-2::GFP spheres (Fig 9E and 9F). These results indicate that cohesin-dependent AIR-2 both excludes CLS-2 from the midbivalent region and

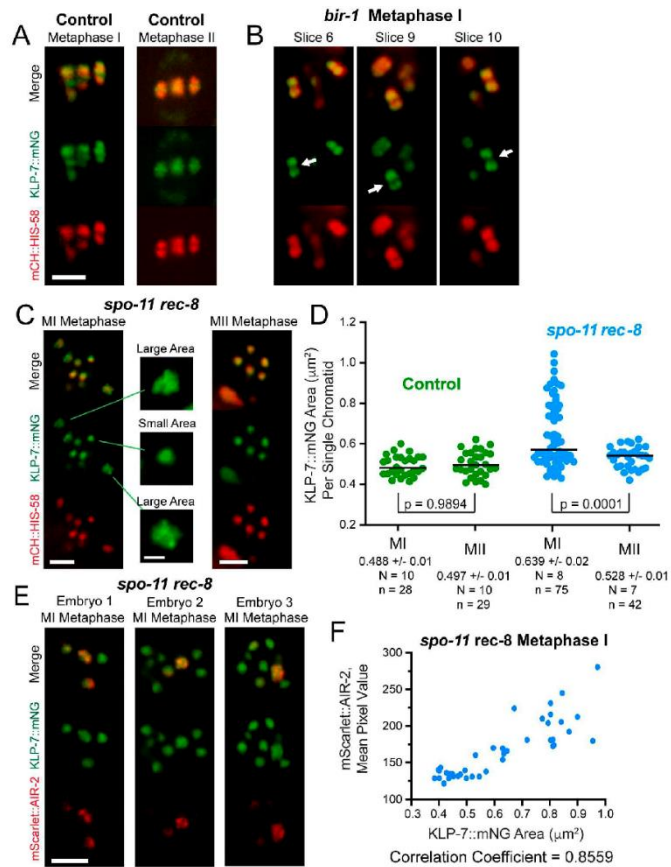


**Fig 8. Survivin-dependent AIR-2 is required for KLP-7 recruitment to the midbivalent ring.** (A) KLP-7::mNG localized to the two lobes and the ring complex (indicated by an arrowhead) of bivalents in 7/7 living control metaphase I embryos, but localized only to the two lobes in (B) 8/8 *bir-1(jg55) [E69A D70A]* embryos. (Arrows indicate bivalents which clearly lack a ring complex). Bar = 3  $\mu\text{m}$ . (C) In living *spo-11 rec-8* MI metaphase spindles, one subset of chromosomes had a small area of KLP-7::mNG and a second subset had a larger area of KLP-7::mNG that was unevenly dispersed around the DNA. Bar, spindle images = 3  $\mu\text{m}$ . Bar, single chromosome images = 1  $\mu\text{m}$ . (D) KLP-7::mNG areas were determined in *spo-11 rec-8* MI metaphase and MII metaphase spindles. N, number of embryos. n, number of chromosomes. (E) Single plane Airyscan images from z-stacks of 14/14 fixed *spo-11 rec-8* embryos showed expanded KLP-7::mNG on chromosomes with the highest mScarlet::AIR-2 fluorescence intensity. Bar = 3  $\mu\text{m}$ . (F) Graph of mScarlet::AIR-2 mean pixel value relative to KLP-7::mNG area from live images. The Pearson  $r$  correlation coefficient is 0.8559. N = 8, n = 40,  $p < 0.0001$ .

<https://doi.org/10.1371/journal.pgen.1010136.g008>

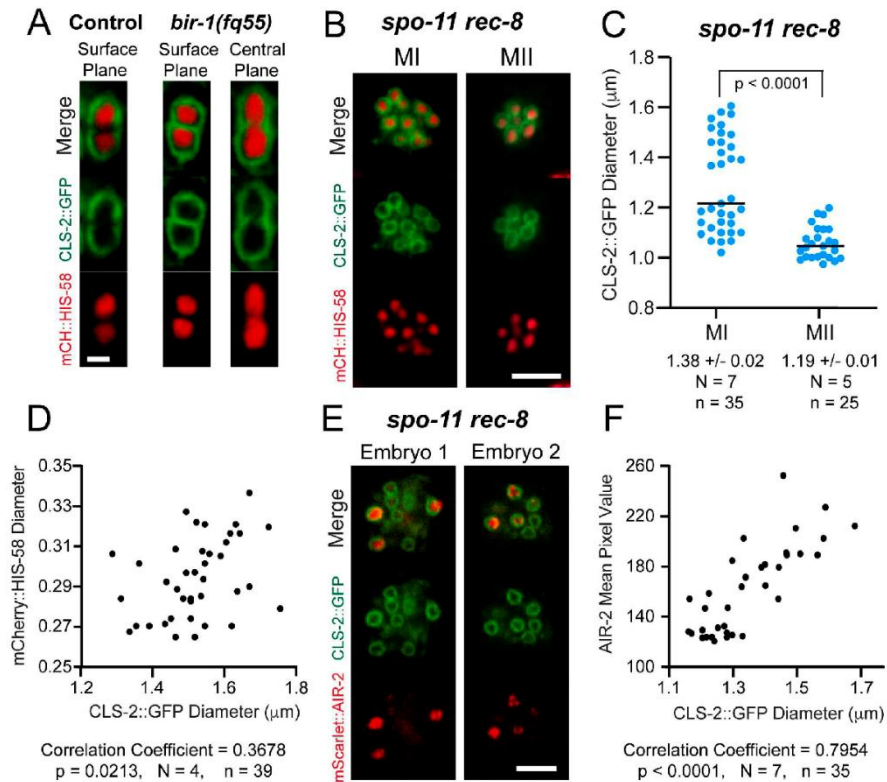


**Fig 9. BIR-1-recruited AIR-2 excludes CLS-2 from the midbivalent region.** (A) Individual chromosomes in living embryos expressing CLS-2::GFP show that CLS-2 is excluded from the midbivalent region in 9/9 control embryos and present in the midbivalent region in 16/16 *bir-1(fq55)* embryos. Bar = 1  $\mu\text{m}$ . (B) CLS-2::GFP encircles both MI and MII metaphase chromosomes in *spo-11 rec-8* embryos. (C) The diameter of CLS-2::GFP spheres on MI and MII metaphase chromosomes was determined. N, number of embryos, n, number of chromosomes. (D) Graph showing mCherry::HIS-58 diameter versus CLS-2::GFP diameter on *rec-8 spo-11* chromosomes. (E) Single plane images taken from z-stacks of two *spo-11 rec-8* embryos expressing CLS-2::GFP and mScarlet::AIR-2. (F) Graph showing mean pixel value of mScarlet::AIR-2 versus CLS-2::GFP diameter on *rec-8 spo-11* chromosomes. Bars, B and E = 4  $\mu\text{m}$ . N, number of embryos, n, number of chromosomes.

<https://doi.org/10.1371/journal.pgen.1010136.g009>

either recruits CLS-2 into larger spheres around separated sister chromatids or increases the diameter of separated sister chromatids.

### Most *C. elegans* meiotic SAFs are cytoplasmic

Vertebrate Ran-dependent SAFs bind importins through a nuclear localization signal (NLS) and are nuclear during interphase [5]. This arrangement places SAFs close to chromosomes at nuclear envelope breakdown when tubulin enters the nuclear space. In contrast, endogenously

GFP-tagged MEI-1, LIN-5, CLS-2, and AIR-1, which all contribute to bipolar spindle assembly in *C. elegans* [19,57–59], were all cytoplasmic before nuclear envelope breakdown (S7 Fig). In addition, KLP-15/16, which are required for spindle assembly, have been reported to be cytoplasmic in -1 oocytes [60]. The cytoplasmic location of these SAFs may sequester them from cohesin-associated CPC and thus prevent premature coalescence of microtubule bundles. These results also make it unlikely that most of the known SAFs during *C. elegans* meiosis are activated by the canonical Ran pathway, which involves release of an NLS from an importin by GTP-Ran [5].

## Discussion

Our results indicate that cohesin is required for efficient acentrosomal spindle assembly independent of its role in SCC because it is required for recruitment of a specific pool of Aurora B kinase to chromatin. The requirement for cohesin is independent of SCC because separated sister chromatids bearing COH-3/4 cohesin in *spo-11 rec-8* double mutants support the assembly of bipolar spindles. In contrast, separated sister chromatids in mutants lacking any cohesin assembled amorphous masses of microtubules with no discrete foci of spindle pole proteins. The cohesin-dependent pool of Aurora B kinase is then required for microtubule bundles to coalesce to form spindle poles during *C. elegans* oocyte meiotic spindle assembly. In the absence of either cohesin, haspin kinase, or phosphorylated histone H3-bound survivin, Aurora B remains dispersed on metaphase chromatin and localizes on anaphase microtubules but is insufficient to promote spindle pole formation. This could be due to a need for a threshold concentration of Aurora B on chromatin or a need for a specific activity unique to cohesin-dependent Aurora B.

The mechanism by which a specific pool of Aurora B kinase promotes spindle pole formation is not clear. In *Drosophila* oocytes, Aurora B phosphorylates the microtubule-binding tail of the kinesin-14, *ncd*, releasing it from inhibition by 14-3-3 [61]. Aurora B is thus activating *ncd*'s ability to bind microtubules and its loss should have a similar phenotype to loss of *ncd*. In *C. elegans*, depletion of the kinesin-14's, KLP-15/16, results in apolar meiotic spindles [60], a phenotype similar to that reported for loss of Aurora B [20] or cohesin (this study). Thus KLP-15/16 are potential targets of activation by Aurora B in *C. elegans*. Completely apolar meiotic spindles have also been observed in *C. elegans* upon depletion of MEI-1/2 katanin [54] and AIR-1 [59]. Thus MEI-1/2 and AIR-1 are potential targets of activation in *C. elegans*.

In contrast with activation of kinesin-14, Aurora B promotes bipolar spindle assembly by phosphorylating and inhibiting the microtubule-disassembly activity of the *Xenopus* kinesin-13, XMCAK [62]. If Aurora B inhibits kinesin-13, then depletion of Aurora B or kinesin-13 should have opposite phenotypes. Indeed, depletion of kinesin-13 suppresses the spindle assembly defect of Aurora B inhibition in both *Xenopus* extracts [16] and *Drosophila* oocytes [63]. Loss of the *C. elegans* kinesin-13, KLP-7 [50,52] results in multi-polar meiotic spindles which might be viewed as the opposite phenotype of the apolar spindles resulting from depletion of AIR-2 [20] or cohesin (this study). Katanin is also inhibited in *Xenopus laevis* egg extracts by phosphorylation of an Aurora consensus site [64]. Whereas this exact site is not conserved in *C. elegans* MEI-1, the activity of MEI-1 is inhibited by phosphorylation at several sites [65]. If Aurora B acts by inhibiting one SAF, then over-expression of that SAF or expression of a non-phosphorylatable SAF should phenocopy loss of Aurora B. However, technical limitations of *C. elegans* transgene technology have limited over-expression of meiotic SAFs or expression of hyperactive mutant SAFs. If Aurora B acts by inhibiting or activating multiple SAFs, then reproducing the Aurora B depletion phenotype with phosphorylation site mutants of SAFs will be challenging.



Loss of haspin-dependent CPC in this study caused a change in the localization pattern of KLP-7 and CLS-2 on chromosomes. The CPC also regulates the chromosomal localization of the KLP-7 homolog, MCAK, on mammalian mitotic chromosomes [66]. Thus Aurora B may promote bipolar spindle assembly by regulating chromosomal targeting of SAFs in addition to regulating the activity of SAFs.

Depletion of SMC3, which should remove all cohesin from chromatin, has been reported in mouse oocytes [67] and *Drosophila* oocytes [68]. Metaphase I spindle defects were not reported in either case. In both cases, cohesin depletion may have been incomplete. Mouse oocyte spindle assembly is dependent on haspin [69], independent of Aurora B because AuroraA can substitute for B in the CPC [70], and dependent on Aurora A [71]. In *Drosophila*, bipolar spindle assembly is CPC-dependent [13] but the relevant CPC recruitment depends on borealin binding to HP1 [72] rather than survivin binding to haspin-phosphorylated histone H3. *Drosophila sunn* null mutants lack SCC and also form bipolar metaphase I spindles [68]. Thus it remains unclear how widely the cohesin-dependence of centrosomal spindle assembly applies in phyla other than Nematoda. In addition, future analysis of centrosome-based *C. elegans* male meiosis in cohesin mutants should reveal whether the cohesin-dependence of spindle bipolarity is specific to centrosomal spindle assembly.

Our time-lapse imaging revealed separated sister chromatids separating into two masses during anaphase I in *spo-11 rec-8* embryos. This result is consistent with the previously published observation of a single polar body and equational segregation interpreted from polymorphism analysis [23,24]. Similarly, *Drosophila sunn* mutants are able to carry out anaphase I [68]. HeLa cells induced to enter mitosis with unreplicated genomes likely have G1 non-cohesive cohesin on their individual unreplicated chromatids. These cells assemble bipolar spindles but do not separate the unreplicated chromatids into two masses. Instead, all of the chromatids end up in one daughter cell at cytokinesis [73]. In *C. elegans* meiosis, anaphase B occurs by CLS-2-dependent microtubule pushing on the inner faces of separating chromosomes [74]. During normal meiosis, the pushing microtubules assemble between homologous chromosomes in a manner that depends on the CPC which is localized between homologous chromosomes, thus driving correct chromosome segregation [19,20]. In a *spo-11 rec-8* double mutant, bright patterned AIR-2 is only on a subset of chromatids but microtubules still appeared to push all of the chromatids apart. Presumably, microtubules are pushing between any two chromatids. This *faux* anaphase likely occurs by the same mechanism as anaphase B in embryos depleted of outer kinetochore proteins [19,75].

The bipolar-spindle-competent separated sister chromatids of *C. elegans spo-11 rec-8* mutants had a severe congression defect (Fig 3C and 3D). In contrast, unreplicated chromatids in HeLa cells congress normally to the metaphase plate [73]. It is likely that antagonism between dynein in kinetochore cups and KLP-19 in the midbivalent ring is important for chromosome congression in *C. elegans* oocytes [76], thus the striking bipolar structure of *C. elegans* metaphase I bivalents and metaphase II univalents is essential for congression while dispensable for bipolar spindle assembly or anaphase.

## Materials and methods

CRISPR-mediated genome editing to create the *bir-1(fq55[E69A D70A])* allele was performed by microinjecting preassembled Cas9sgRNA complexes, single-stranded DNA oligos as repair templates, and *dpy-10* as a co-injection marker into the *C. elegans* germline as described in Paix et al [77]. The TCGTACCACGGATCGTCTTC sequence was used for the guide RNA and the single-stranded DNA oligo repair template had the following sequence: `tgtagcattttgcaacaaggaacttgattttgaccccgctgctgaccggtgtacgagcacacgaaacgtgatgaaccgtg`.

*C. elegans* strains were generated by standard genetic crosses, and genotypes were confirmed by PCR. Genotypes of all strains are listed in [S2 Table](#).

### Live *in utero* imaging

L4 larvae were incubated at 20°C overnight on MYOB plates seeded with OP50. Worms were anesthetized by picking adult hermaphrodites into a solution of 0.1% tricaine, 0.01% tetramisole in PBS in a watch glass for 30 min as described in Kirby et al. [78] and McCarter et al [41]. Worms were then transferred in a small volume to a thin agarose pad (2% in water) on a slide. Additional PBS was pipetted around the edges of the agarose pad, and a 22-x-30-mm cover glass was placed on top. The slide was inverted and placed on the stage of an inverted microscope. Meiotic embryos or -1 diakinesis oocytes were identified by bright-field microscopy before initiating time-lapse fluorescence. For all live imaging, the stage and immersion oil temperature was 22°C–24°C. For all time-lapse data, single-focal plane images were acquired with a Solamere spinning disk confocal microscope equipped with an Olympus IX-70 stand, Yokogawa CSU10, Hamamatsu ORCA FLASH 4.0 CMOS (complementary metal oxide semiconductor) detector, Olympus 100×/1.35 objective, 100-mW Coherent Obis lasers set at 30% power, and MicroManager software control. Pixel size was 65 nm. Exposures were 300 ms. Time interval between image pairs was 15 s with the exception of [Fig 6](#) images, which were captured at 10 s intervals. Focus was adjusted manually during time-lapse imaging. Control and experimental time-lapse data sets always included sequences acquired on multiple different days. For chromosome counting in oocyte nuclei, z-stacks were captured at 0.4 μm intervals. For chromosome counting in metaphase spindles, z-stacks were captured at 0.2 μm intervals. Chromosomes were counted in z-stacks, not in z projections.

### Timing

Control spindles maintain a steady-state length of 8 μm for 7 min before initiating APC-dependent spindle shortening, followed by spindle rotation and movement to the cortex [79]. Because the majority of our videos began after MI metaphase onset, we measured time relative to the arrival of the spindle at the cortex in [Figs 1, 2, 3 and 6](#); for control embryos, this corresponded to the completion of rotation. For [Fig 7](#), time was measured relative to the initial appearance of MT fibers.

### Fixed immunofluorescence and Airyscan imaging

*C. elegans* meiotic embryos were extruded from hermaphrodites in 0.8× egg buffer by gently compressing worms between coverslip and slide, flash frozen in liquid N<sub>2</sub>, permeabilized by removing the coverslip, and then fixed in ice-cold methanol before staining with antibodies and DAPI. The primary antibodies used in this work were mouse monoclonal anti-tubulin (DM1α; Sigma-Aldrich; 1:200), GFP Booster Alexa 488 (gb2AF488; Chromotek; 1:200), rabbit anti-GFP (NB600-308SS; Novus Biologicals; 1:600), rabbit anti-KLP-7 ([20]; 1:300), rabbit anti-MEL-1 ([80]; 1:200), rabbit anti-H3 pT3 (07–424; Merck Millipore; 1:700) and rabbit anti-COH-3 ([24]; 1:500). The secondary antibodies used were Alexa Fluor 488 anti-mouse (A-11001; Thermo Fisher Scientific; 1:200), Alexa Fluor 594 anti-rabbit (A11037; Thermo Fisher Scientific; 1:200) and Alexa Fluor Plus 647 anti-rabbit (A32733; Thermo Fisher). z-stacks were captured at 1-μm steps for each meiotic embryo using the same microscope described above for live imaging. Super resolution images shown in [Fig 8E](#) were acquired on a ZEISS LSM 980 with Airyscan 2.

### Auxin

*C. elegans* strains endogenously tagged with auxin-inducible degrons and a TIR1 transgene were treated with auxin overnight on seeded plates. Auxin (indole acetic acid) was added to molten agar from a 400 mM stock solution in ethanol to a final concentration of 4 mM auxin before pouring plates, which were subsequently seeded with OP50 bacteria. Depletion of SMC-1::AID::GFP is shown in S2A and S2B Fig. Depletion of HASP-1 was indicated by reduced phosphor h3T3 staining (S2C–S2E Fig). Bipolar spindle assembly occurs in *knl-1(AID)* *knl-3(AID)* *tir1* worms [75] and in *dhc-1(AID)* worms (S8 Fig) treated with auxin using the same protocol. Bipolar spindle assembly also occurred in *smc-1::AID::GFP* worms with no auxin (Fig 4D) and *hasp-1(AID)* worms with no auxin (Fig 6D). Embryonic lethality was dependent on auxin for both degrons and auxin did not induce embryonic lethality in a strain carrying only endogenously tagged *lin-5* (S1 Table). Thus the spindle assembly defects observed for *smc-1::AID::GFP* and *hasp-1(AID)* likely do not result from non-specific effects.

### Fluorescence intensity measurements

Fluorescence intensity measurements are from single focal plane images chosen from z-stacks. Single focal plane images were chosen that had similar nucleoplasmic or cytoplasmic pixel values and in which the majority of a chromosome was in focus. A chromosome was judged to be in focus in the focal plane with the highest pixel intensity, largest diameter, and sharpest edges. Choosing focal planes with similar cytoplasmic or nucleoplasmic pixel values was used to partially eliminate the problem of spherical aberration due to different distances from the coverslip. For counting the number of bright vs dim AIR-2::GFP-labeled chromosomes in entire nuclei in S3 Fig, chromatids were subjectively scored as bright vs dim by comparing chromosomes within the same focal plane to compensate for the loss of intensity due to distance from the coverslip. In Figs 4B, 4C, 4E and 6E, total pixel values of chromosomal SMC-1::AID::GFP or AIR-2::GFP were obtained using the Freehand Tool (ImageJ) software to outline individual chromosomes. For each chromosome, the ROI was dragged to the adjacent nucleoplasm or cytoplasm and the total pixel value obtained. A background value was determined by dragging the ROI to a region of the image outside the worm. The values were background-subtracted, then divided in order to generate a ratio for comparison. This method was also used to determine the intensity of GFP::MEI-1 on chromosomes reported in the text of the results corresponding to Fig 3E. MEI-1 looks brighter on the chromosomes in the *spo-11 rec-8* metaphase II image because the original 16 bit image (65,000 grey levels) has been scaled to display the brightest pixel as 256 in the 8 bit (256 grey levels) figure panel. The chromosomes are not actually brighter as explained in the Results. In Fig 8D and 8F, areas of KLP-7::mNG on individual chromosomes was measured using the Freehand Tool (ImageJ). The diameter of CLS-2::GFP spheres in Fig 9 was calculated from the area using the equation  $D = 2\sqrt{\frac{A}{\pi}}$  where D is diameter and A is area. Area was obtained by hand drawing a circular ROI over each sphere. Focal planes in which each sphere had the largest diameter were used. Mean mScarlet::AIR-2 pixel values in Figs 8 and 9 were determined after outlining individual chromosomes with the Freehand Tool (ImageJ). In S1 Fig, single-plane images were captured at the midsection of -1 oocytes. For each image, regions of nucleoplasm and cytoplasm were outlined and the mean pixel values determined. In S6 Fig, single-plane images were captured at the midsection of metaphase I spindles. For each image, mean pixel values of the spindle and a region of cytoplasm were determined. For both figures, the mean values were background-subtracted and divided to generate ratios for comparison.

### Statistics

P values were calculated in GraphPad Prism using one-way ANOVA for comparing means of three or more groups. Pearson correlation coefficients were calculated using GraphPad Prism.

### Supporting information

**S1 Fig. DNA body counts in -1 oocytes of mutant *C. elegans*.** (A) Single and Z-stack sum slices of a living *rec-8* oocyte nucleus expressing mCherry::HIS-11. *rec-8* oocyte nuclei contained 12.33 +/- 0.37 DNA bodies (n = 9), which included univalents and an occasional chromatid. (B) Single and Z-stack sum slices of a living *spo-11 rec-8* oocyte nucleus expressing GFP::H2B show 22 of the 24 total chromatids. *spo-11 rec-8* oocyte nuclei contained 23.8 +/- 0.01 DNA bodies (n = 10). (C) Single and Z-stack sum slices of a living *rec-8; coh-4 coh-3* oocyte nucleus expressing mCH::HIS-11. *rec-8; coh-4 coh-3* nuclei contained 24.5 +/- 0.43 DNA bodies (n = 14). 4/14 oocytes contained one or two small DNA bodies which may indicate chromosomes fragmented by SPO-11 activity. All bars = 5  $\mu$ m. (TIF)

**S2 Fig. Auxin depletion of SMC-1::AID::GFP and HASP-1::AID is incomplete in some embryos.** (A) Single-plane images of SMC-1::AID::GFP in the gonad of living worms incubated overnight in either the presence or absence of auxin. (B) The ratio of SMC-1::AID::GFP mean pixel intensity to mCH::HIS-58 mean pixel intensity in gonad nuclei was determined in worms incubated as described in (A). Several of the ratios in auxin-treated worms approach the values obtained in untreated worms. N, number of worms. n, number of nuclei. (C) Embryos from worms expressing HASP-1::AID and incubated in either the presence or absence of auxin were fixed and stained with tubulin and phosphor H3(T3) antibodies, and with DAPI. (D) Ratios of chromosomal to cytoplasmic H3(T3) antibody staining were determined in worms incubated as described in (C). N, number of spindles. n, number of chromosomes. (E) The values for worms incubated in the presence of auxin were separated into those obtained from chromosomes in apolar spindles and those obtained from chromosomes in multipolar spindles. N, number of spindles. n, number of chromosomes. All bars equal 4 $\mu$ m. (TIF)

**S3 Fig. Some chromatids are bound by bright patterned AIR-2::GFP in *spo-11 rec-8* oocytes.** (A) Single chromosomes from z-stack images of living control and mutant *C. elegans* oocytes expressing mCherry::HIS-58 and AIR-2::GFP. Two examples are shown of a *spo-11 rec-8* chromosome, one bound by bright patterned AIR-2::GFP and one with dim diffuse AIR-2::GFP. All bars = 1 $\mu$ m. (B) Graph showing the percent of chromosomes bound by bright AIR-2::GFP in living -1 oocytes of control and mutant *C. elegans*. Z-stacks of entire nuclei were analyzed. For *spo-11 rec-8*, bright vs dim AIR-2::GFP was scored by only comparing chromatids within the same focal plane. Bright AIR-2::GFP was observed on 100 percent of control chromosomes, 0 percent of *spo-11 rec-8; coh-4 coh-3* chromatids and 39.5 +/- 4.0 percent of *spo-11 rec-8* chromatids. N, number of oocytes. n, number of chromosomes. (TIF)

**S4 Fig. Colocalization of AIR-2 and COH-3 in *spo-11 rec-8* metaphase I embryos.** (A) Meiotic embryos within control and *spo-11 rec-8* worms expressing AIR-2::GFP were fixed and stained with DAPI, COH-3/4 antibodies, and GFP antibodies. The control spindle displays consistent intensities of AIR-2 and COH-3/4 on each chromosome while the *spo-11 rec-8* spindle displays varying intensities. Bars = 3  $\mu$ m. (B) High magnification view of single chromatids from (A). The control chromosome shows bright COH-3/4 and bright AIR-2. Two

chromosomes from the same *spo-11 rec-8* embryo are shown, one with bright COH-3/4 and AIR-2 and one with dim COH-3/4 and AIR-2. Bars = 1  $\mu$ m. (C) Graph showing mean pixel value of COH-3/4 versus mean pixel value of AIR-2 on *rec-8 spo-11* chromosomes. Mean pixel values were taken by using a circle ROI with a 22 pixel diameter (covering the entire univalent's area). N, number of embryos. n, number of chromosomes.

(TIF)

**S5 Fig. Maternal AIR-2, but not SMC-1, is recruited to the sperm DNA.** (A) Time-lapse images of 15/15 embryos from worms expressing SMC-1::GFP and mCH::HIS-58 in both oocytes and spermatocytes show no SMC-1::GFP on sperm-derived paternal DNA within the zygote during meiosis. SMC-1::GFP was observed in the sperm-derived paternal pronucleus in 7/7 embryos. Bar = 3  $\mu$ m. (B) Male worms were soaked in mitotracker before mating to hermaphrodites. The sperm-derived paternal DNA is found at the center of the cloud of paternal mitochondria within meiotic embryos (far right). In 5/5 mated hermaphrodites, paternal AIR-2::GFP was present on spermatids, but was not detected post-fertilization within the cloud of paternal mitochondria in meiotic embryos identified by their position in the uterus adjacent to the spermatheca (+1 embryo). 13/13 unmated hermaphrodites expressing AIR-2::GFP, and 11/11 AIR-2::GFP expressing hermaphrodites mated with non-expressing males had AIR-2::GFP on the sperm DNA in +1 embryos. Bar = 4  $\mu$ m.

(TIF)

**S6 Fig. MT density is decreased in *spo-11 rec-8; coh-3 coh-4* and *bir-1(fq55)* spindles.** (A) Single slices from z-stack images of embryos expressing mNG::TBB-2 and mCH::HIS-11. Bar = 4  $\mu$ m. (B) Ratios of mean, background-subtracted mNG::TBB-2 pixel values in spindles vs. nearby cytoplasm of control and mutant embryos. N = number of embryos.

(TIF)

**S7 Fig. Spindle assembly factors are cytoplasmic prior to nuclear envelope breakdown.** (A) Single plane images of -1 oocytes in *C. elegans* expressing GFP::H2B, SMC-1::AID::GFP, and spindle assembly factors. Bar = 10  $\mu$ m. (B) Nucleoplasmic to cytoplasmic ratios were determined for mean, background-subtracted pixel values in -1 oocytes.

(TIF)

**S8 Fig. Bipolar spindles form in the presence of Auxin.** *C. elegans* expressing DHC-1::AID::GFP, eGFP::LIN-5, mCH::H2B and mKate2::PH were incubated for 2–4 hours in the presence or absence of auxin. (A) Images of metaphase I spindles show that 9/9 spindles were bipolar in the absence of auxin and 10/10 metaphase I spindles were bipolar in the presence of auxin. (B) Quantification of spindle bipolarity. (C) Time-lapse images of *C. elegans* incubated in the absence of auxin show bipolar spindles shorten and rotate prior to chromosome separation (n = 5). (D) Time-lapse images of *C. elegans* incubated in the presence of auxin show bipolar spindles shorten and remain parallel to the cortex due to the depletion of DHC-1::AID::GFP (n = 7).

(TIF)

**S1 Table. Hatch rate data for auxin-induced degron experiments.**

(DOCX)

**S2 Table. *C. elegans* Strain List.** List of genotypes of all strains used in this paper.

(DOCX)

**S1 Data. Numerical values for all graphs shown in this paper.**

(XLSX)

**S1 Video. Metaphase I through anaphase II filmed in utero in a control strain.** Green is mNeonGreen::tubulin. Red is mCherry::histone H2b.  
(MP4)

**S2 Video. Metaphase I through anaphase II filmed in utero in a *rec-8* strain.** Green is mNeonGreen::tubulin. Red is mCherry::histone H2b.  
(MP4)

**S3 Video. Metaphase I through anaphase II filmed in utero in a *spo-11 rec-8 coh-4 coh-3* strain.** Green is mNeonGreen::tubulin. Red is mCherry::histone H2b.  
(MP4)

**S4 Video. Metaphase I through anaphase II filmed in utero in a *spo-11 rec-8* strain.** Green is GFP::histone H2b. Red is mKate::tubulin.  
(MP4)

**S5 Video. z-stack showing the pattern of CLS-2::GFP on control bivalents.**  
(MP4)

**S6 Video. z-stack showing the pattern of CLS-2::GFP on *bir-1(fq55)* bivalents.**  
(MP4)

### Acknowledgments

We thank Fede Pelisch, Arshad Desai, and the CGC, which is funded by NIH Office of Research Infrastructure Programs (P40 OD010440), for strains. We thank Sadie Wignall and Aaron Severson for antibodies. We thank Thomas Wilkop for assistance with Airyscan imaging.

### Author Contributions

**Conceptualization:** Karen P. McNally, Francis J. McNally.

**Data curation:** Karen P. McNally, Brennan M. Danlasky, Wenzhe Li, Francis J. McNally.

**Formal analysis:** Karen P. McNally, Elizabeth A. Beath, Brennan M. Danlasky, Ting Gong, Wenzhe Li, Francis J. McNally.

**Funding acquisition:** Enrique Martinez-Perez, Francis J. McNally.

**Investigation:** Karen P. McNally, Elizabeth A. Beath, Brennan M. Danlasky, Consuelo Barroso, Ting Gong, Wenzhe Li, Francis J. McNally.

**Methodology:** Karen P. McNally.

**Project administration:** Francis J. McNally.

**Resources:** Consuelo Barroso, Enrique Martinez-Perez.

**Supervision:** Enrique Martinez-Perez, Francis J. McNally.

**Validation:** Karen P. McNally.

**Visualization:** Karen P. McNally.

**Writing – original draft:** Karen P. McNally, Francis J. McNally.

**Writing – review & editing:** Karen P. McNally, Enrique Martinez-Perez, Francis J. McNally.

## References

1. Nasmyth K. Segregating sister genomes: the molecular biology of chromosome separation. *Science*. 2002; 297(5581):559–65. <https://doi.org/10.1126/science.1074757> PMID: 12142528
2. Blanco-Arneja J, Lozano-Fernandez P, Marti E. Centrosome maturation—in tune with the cell cycle. *J Cell Sci*. 2022; 135(2). <https://doi.org/10.1242/jcs.259395> PMID: 35088834
3. Heald R, Tournebise R, Blank T, Sandaltzopoulos R, Becker P, Hyman A, et al. Self-organization of microtubules into bipolar spindles around artificial chromosomes in *Xenopus* egg extracts. *Nature*. 1996; 382(6590):420–5. <https://doi.org/10.1038/382420a0> PMID: 8684481
4. Deng M, Suraneni P, Schultz RM, Li R. The Ran GTPase mediates chromatin signaling to control cortical polarity during polar body extrusion in mouse oocytes. *Dev Cell*. 2007; 12(2):301–8. <https://doi.org/10.1016/j.devcel.2006.11.008> PMID: 17276346
5. Cavazza T, Vernos I. The RanGTP Pathway: From Nucleo-Cytoplasmic Transport to Spindle Assembly and Beyond. *Front Cell Dev Biol*. 2015; 3:82. <https://doi.org/10.3389/fcell.2015.00082> PMID: 26793706
6. Carazo-Salas RE, Guarguaglini G, Gruss OJ, Segref A, Karsenti E, Mattaj JW. Generation of GTP-bound Ran by RCC1 is required for chromatin-induced mitotic spindle formation. *Nature*. 1999; 400(6740):178–81. <https://doi.org/10.1038/22133> PMID: 10408446
7. Dumont J, Petri S, Pellegrin F, Terret ME, Bohnsack MT, Rassinier P, et al. A centriole- and RanGTP-independent spindle assembly pathway in meiosis I of vertebrate oocytes. *J Cell Biol*. 2007; 176(3):295–305. <https://doi.org/10.1083/jcb.200605199> PMID: 17261848
8. Cesario J, McKim KS. RanGTP is required for meiotic spindle organization and the initiation of embryonic development in *Drosophila*. *J Cell Sci*. 2011; 124(Pt 22):3797–810. <https://doi.org/10.1242/jcs.084855> PMID: 22100918
9. Chuang CH, Schlientz AJ, Yang J, Bowerman B. Microtubule assembly and pole coalescence: early steps in *C. elegans* oocyte meiosis I spindle assembly. *Biol Open*. 2020; 9(6).
10. Halpin D, Kalab P, Wang J, Weis K, Heald R. Mitotic spindle assembly around RCC1-coated beads in *Xenopus* egg extracts. *PLoS Biol*. 2011; 9(12):e1001225. <https://doi.org/10.1371/journal.pbio.1001225> PMID: 22215983
11. Willems E, Dedobbeleer M, Digregorio M, Lombard A, Lumapat PN, Rogister B. The functional diversity of Aurora kinases: a comprehensive review. *Cell Div*. 2018; 13:7. <https://doi.org/10.1186/s13008-018-0040-6> PMID: 30250494
12. Broad AJ, DeLuca KF, DeLuca JG. Aurora B kinase is recruited to multiple discrete kinetochore and centromere regions in human cells. *J Cell Biol*. 2020; 219(3). <https://doi.org/10.1083/jcb.201905144> PMID: 32028528
13. Radford SJ, Jang JK, McKim KS. The chromosomal passenger complex is required for meiotic acentrosomal spindle assembly and chromosome biorientation. *Genetics*. 2012; 192(2):417–29. <https://doi.org/10.1534/genetics.112.143495> PMID: 22865736
14. Kelly AE, Sampath SC, Maniar TA, Woo EM, Chait BT, Funabiki H. Chromosomal enrichment and activation of the aurora B pathway are coupled to spatially regulate spindle assembly. *Dev Cell*. 2007; 12(1):31–43. <https://doi.org/10.1016/j.devcel.2006.11.001> PMID: 17189039
15. Maresca TJ, Groen AC, Gatlin JC, Ohi R, Mitchison TJ, Salmon ED. Spindle assembly in the absence of a RanGTP gradient requires localized CPC activity. *Curr Biol*. 2009; 19(14):1210–5. <https://doi.org/10.1016/j.cub.2009.05.061> PMID: 19540121
16. Sampath SC, Ohi R, Leisemann O, Salic A, Pozniakovski A, Funabiki H. The chromosomal passenger complex is required for chromatin-induced microtubule stabilization and spindle assembly. *Cell*. 2004; 118(2):187–202. <https://doi.org/10.1016/j.cell.2004.06.026> PMID: 15260989
17. Speliotis EK, Uren A, Vaux D, Horvitz HR. The survivin-like *C. elegans* BIR-1 protein acts with the Aurora-like kinase AIR-2 to affect chromosomes and the spindle midzone. *Mol Cell*. 2000; 6(2):211–23. [https://doi.org/10.1016/s1097-2765\(00\)00023-x](https://doi.org/10.1016/s1097-2765(00)00023-x) PMID: 10883970
18. Wignall SM, Villeneuve AM. Lateral microtubule bundles promote chromosome alignment during acentrosomal oocyte meiosis. *Nat Cell Biol*. 2009; 11(7):839–44. <https://doi.org/10.1038/ncb1891> PMID: 19525937
19. Dumont J, Oegema K, Desai A. A kinetochore-independent mechanism drives anaphase chromosome separation during acentrosomal meiosis. *Nat Cell Biol*. 2010; 12(9):894–901. <https://doi.org/10.1038/ncb2093> PMID: 20729837
20. Divekar NS, Davis-Roca AC, Zhang L, Demburg AF, Wignall SM. A degron-based strategy reveals new insights into Aurora B function in *C. elegans*. *PLoS Genet*. 2021; 17(5):e1009567. <https://doi.org/10.1371/journal.pgen.1009567> PMID: 34014923

21. Monen J, Maddox PS, Hyndman F, Oegema K, Desai A. Differential role of CENP-A in the segregation of holocentric *C. elegans* chromosomes during meiosis and mitosis. *Nat Cell Biol.* 2005; 7(12):1248–55. <https://doi.org/10.1038/ncb1331> PMID: 16273096
22. Pasierbek P, Jantsch M, Melcher M, Schleiffer A, Schweizer D, Loidl J. A *Caenorhabditis elegans* cohesin protein with functions in meiotic chromosome pairing and disjunction. *Genes Dev.* 2001; 15(11):1349–60. <https://doi.org/10.1101/gad.192701> PMID: 11390355
23. Severson AF, Ling L, van Zuylen V, Meyer BJ. The axial element protein HTP-3 promotes cohesin loading and meiotic axis assembly in *C. elegans* to implement the meiotic program of chromosome segregation. *Genes Dev.* 2009; 23(15):1763–78. <https://doi.org/10.1101/gad.1808809> PMID: 19574299
24. Severson AF, Meyer BJ. Divergent kleisin subunits of cohesin specify mechanisms to tether and release meiotic chromosomes. *Elife.* 2014; 3:e03467. <https://doi.org/10.7554/eLife.03467> PMID: 25171895
25. Crawley O, Barroso C, Testori S, Ferrandiz N, Silva N, Castellano-Pozo M, et al. Cohesin-interacting protein WAPL-1 regulates meiotic chromosome structure and cohesion by antagonizing specific cohesin complexes. *Elife.* 2016; 5:e10851. <https://doi.org/10.7554/eLife.10851> PMID: 26841696
26. Woglar A, Yamaya K, Roelens B, Boettiger A, Kohler S, Villeneuve AM. Quantitative cytogenetics reveals molecular stoichiometry and longitudinal organization of meiotic chromosome axes and loops. *PLoS Biol.* 2020; 18(8):e3000817. <https://doi.org/10.1371/journal.pbio.3000817> PMID: 32813728
27. Cahoon CK, Helm JM, Libuda DE. Synaptonemal Complex Central Region Proteins Promote Localization of Pro-crossover Factors to Recombination Events During *Caenorhabditis elegans* Meiosis. *Genetics.* 2019; 213(2):395–409. <https://doi.org/10.1534/genetics.119.302625> PMID: 31431470
28. Ellefson ML, McNally FJ. CDK-1 inhibits meiotic spindle shortening and dynein-dependent spindle rotation in *C. elegans*. *J Cell Biol.* 2011; 193(7):1229–44. <https://doi.org/10.1083/jcb.201104008> PMID: 21690306
29. Jiang K, Rezakova L, Hua S, Liu Q, Capitani G, Altelaar AFM, et al. Microtubule minus-end regulation at spindle poles by an ASPM-katanin complex. *Nat Cell Biol.* 2017; 19(5):480–92. <https://doi.org/10.1038/ncb3511> PMID: 28436967
30. Castellano-Pozo M, Pacheco S, Sioutas G, Jaso-Tamame AL, Dore MH, Karim MM, et al. Surveillance of cohesin-supported chromosome structure controls meiotic progression. *Nat Commun.* 2020; 11(1):4345. <https://doi.org/10.1038/s41467-020-18219-9> PMID: 32859945
31. Chan RC, Chan A, Jeon M, Wu TF, Pasqualone D, Rougvié AE, et al. Chromosome cohesion is regulated by a clock gene paralogue TIM-1. *Nature.* 2003; 423(6943):1002–9. <https://doi.org/10.1038/nature01697> PMID: 12827206
32. Yamagishi Y, Honda T, Tanno Y, Watanabe Y. Two histone marks establish the inner centromere and chromosome bi-orientation. *Science.* 2010; 330(6001):239–43. <https://doi.org/10.1126/science.1194498> PMID: 20929775
33. Goto Y, Yamagishi Y, Shintomi-Kawamura M, Abe M, Tanno Y, Watanabe Y. Pds5 Regulates Sister-Chromatid Cohesion and Chromosome Bi-orientation through a Conserved Protein Interaction Module. *Curr Biol.* 2017; 27(7):1005–12. <https://doi.org/10.1016/j.cub.2017.02.066> PMID: 28343969
34. Joo JH, Kang HA, Kim KP, Hong S. Meiotic prophase roles of Pds5 in recombination and chromosome condensation in budding yeast. *J Microbiol.* 2022; 60(2):177–86. <https://doi.org/10.1007/s12275-022-1635-9> PMID: 35102525
35. Pradillo M, Knoll A, Oliver C, Varas J, Corredor E, Puchta H, et al. Involvement of the Cohesin Cofactor PDS5 (SPC76) During Meiosis and DNA Repair in *Arabidopsis thaliana*. *Front Plant Sci.* 2015; 6:1034. <https://doi.org/10.3389/fpls.2015.01034> PMID: 26648949
36. Ding DQ, Matsuda A, Okamasa K, Nagahama Y, Haraguchi T, Hiraoka Y. Meiotic cohesin-based chromosome structure is essential for homologous chromosome pairing in *Schizosaccharomyces pombe*. *Chromosoma.* 2016; 125(2):205–14. <https://doi.org/10.1007/s00412-015-0551-8> PMID: 26511279
37. Kusch T. Brca2-Pds5 complexes mobilize persistent meiotic recombination sites to the nuclear envelope. *J Cell Sci.* 2015; 128(4):717–27. <https://doi.org/10.1242/jcs.159988> PMID: 25588834
38. Kelly AE, Ghenoiu C, Xue JZ, Zierhut C, Kimura H, Funabiki H. Survivin reads phosphorylated histone H3 threonine 3 to activate the mitotic kinase Aurora B. *Science.* 2010; 330(6001):235–9. <https://doi.org/10.1126/science.1189505> PMID: 20705815
39. Wang F, Dai J, Daum JR, Niedzialkowska E, Banerjee B, Stukenberg PT, et al. Histone H3 Thr-3 phosphorylation by Haspin positions Aurora B at centromeres in mitosis. *Science.* 2010; 330(6001):231–5. <https://doi.org/10.1126/science.1189435> PMID: 20705812
40. Ferrandiz N, Barroso C, Telecan O, Shao N, Kim HM, Testori S, et al. Spatiotemporal regulation of Aurora B recruitment ensures release of cohesion during *C. elegans* oocyte meiosis. *Nat Commun.* 2018; 9(1):834. <https://doi.org/10.1038/s41467-018-03229-5> PMID: 29483514



41. McCarter J, Bartlett B, Dang T, Schedl T. On the control of oocyte meiotic maturation and ovulation in *Caenorhabditis elegans*. *Dev Biol*. 1999; 205(1):111–28. <https://doi.org/10.1006/dbio.1998.9109> PMID: 9882501
42. Sawin K, Mitchison T. Cell biology. Motoring in the spindle. *Nature*. 1990; 345(6270):22–3. <https://doi.org/10.1038/345022a0> PMID: 2139498
43. McNally KL, Fabritius AS, Ellefson ML, Flynn JR, Milan JA, McNally FJ. Kinesin-1 prevents capture of the oocyte meiotic spindle by the sperm aster. *Dev Cell*. 2012; 22(4):788–98. <https://doi.org/10.1016/j.devcel.2012.01.010> PMID: 22465668
44. de Carvalho CE, Zaalijer S, Smolnikov S, Gu Y, Schumacher JM, Colaiácovo MP. LAB-1 antagonizes the Aurora B kinase in *C. elegans*. *Genes Dev*. 2008; 22(20):2869–86. <https://doi.org/10.1101/gad.1694108> PMID: 18923084
45. Martínez-Pérez E, Schwarzstein M, Barroso C, Lightfoot J, Demburg AF, Villeneuve AM. Crossovers trigger a remodeling of meiotic chromosome axis composition that is linked to two-step loss of sister chromatid cohesion. *Genes Dev*. 2008; 22(20):2886–901. <https://doi.org/10.1101/gad.1694108> PMID: 18923085
46. Macaraeg J, Reinhard I, Ward M, Carmeci D, Stanaway M, Moore A, et al. Genetic analysis of *Caenorhabditis elegans* Haspin-like genes shows that hasp-1 plays multiple roles in the germline. *Biol Open*. 2022; 11(7). <https://doi.org/10.1242/bio.059277> PMID: 35678140
47. Yang HY, McNally K, McNally FJ. MEI-1/katanin is required for translocation of the meiosis I spindle to the oocyte cortex in *C. elegans*. *Dev Biol*. 2003; 260(1):245–59. [https://doi.org/10.1016/S0012-1606\(03\)00216-1](https://doi.org/10.1016/S0012-1606(03)00216-1) PMID: 12885567
48. McNally K, Audhya A, Oegema K, McNally FJ. Katanin controls mitotic and meiotic spindle length. *J Cell Biol*. 2006; 175(6):881–91. <https://doi.org/10.1083/jcb.200608117> PMID: 17176907
49. Wolff ID, Tran MV, Mullen TJ, Villeneuve AM, Wignall SM. Assembly of *Caenorhabditis elegans* acerosomal spindles occurs without evident microtubule-organizing centers and requires microtubule sorting by KLP-18/kinesin-12 and MESP-1. *Mol Biol Cell*. 2016; 27(20):3122–31. <https://doi.org/10.1091/mbc.E16-05-0291> PMID: 27559133
50. Gigant E, Stefanutti M, Laband K, Gluszek-Kustusz A, Edwards F, Lacroix B, et al. Inhibition of ectopic microtubule assembly by the kinesin-13 KLP-7 prevents chromosome segregation and cytokinesis defects in oocytes. *Development*. 2017; 144(9):1674–86. <https://doi.org/10.1242/dev.147504> PMID: 28289130
51. Srayko M, Buster DW, Bazirgan OA, McNally FJ, Mains PE. MEI-1/MEI-2 katanin-like microtubule severing activity is required for *Caenorhabditis elegans* meiosis. *Genes Dev*. 2000; 14(9):1072–84. PMID: 10809666
52. Connolly AA, Sugioka K, Chuang CH, Lowry JB, Bowerman B. KLP-7 acts through the Ndc80 complex to limit pole number in *C. elegans* oocyte meiotic spindle assembly. *J Cell Biol*. 2015; 210(6):917–32. <https://doi.org/10.1083/jcb.201412010> PMID: 26370499
53. Schlientz AJ, Bowerman B. *C. elegans* CLASP/CLS-2 negatively regulates membrane ingression throughout the oocyte cortex and is required for polar body extrusion. *PLoS Genet*. 2020; 16(10): e1008751. <https://doi.org/10.1371/journal.pgen.1008751> PMID: 33027250
54. McNally KP, McNally FJ. The spindle assembly function of *Caenorhabditis elegans* katanin does not require microtubule-severing activity. *Mol Biol Cell*. 2011; 22(9):1550–60. <https://doi.org/10.1091/mbc.E10-12-0951> PMID: 21372175
55. Srayko M, ET, Hyman AA, Müller-Reichert T. Katanin disrupts the microtubule lattice and increases polymer number in *C. elegans* meiosis. *Curr Biol*. 2006; 16(19):1944–9. <https://doi.org/10.1016/j.cub.2006.08.029> PMID: 17027492
56. Pellich F, Bel Borja L, Jaffray EG, Hay RT. Sumoylation regulates protein dynamics during meiotic chromosome segregation in *C. elegans* oocytes. *J Cell Sci*. 2019; 132(14). <https://doi.org/10.1242/jcs.292330> PMID: 31243051
57. Mains PE, Kempthues KJ, Sprunger SA, Sulston IA, Wood WB. Mutations affecting the meiotic and mitotic divisions of the early *Caenorhabditis elegans* embryo. *Genetics*. 1990; 126(3):593–605. <https://doi.org/10.1093/genetics/126.3.593> PMID: 2249759
58. van der Voet M, Berends CW, Perreault A, Nguyen-Ngoc T, Gonczyk P, Vidal M, et al. NuMA-related LIN-5, ASPM-1, calmodulin and dynein promote meiotic spindle rotation independently of cortical LIN-5/GPR/Galpha. *Nat Cell Biol*. 2009; 11(3):269–77. <https://doi.org/10.1038/ncb1834> PMID: 19219036
59. Sumiyoshi E, Fukata Y, Namai S, Sugimoto A. *Caenorhabditis elegans* Aurora A kinase is required for the formation of spindle microtubules in female meiosis. *Mol Biol Cell*. 2015; 26(23):4187–96. <https://doi.org/10.1091/mbc.E15-05-0258> PMID: 26378257

60. Mullen TJ, Wignall SM. Interplay between microtubule bundling and sorting factors ensures acentrilolar spindle stability during *C. elegans* oocyte meiosis. *PLoS Genet.* 2017; 13(9):e1006986. <https://doi.org/10.1371/journal.pgen.1006986> PMID: 28910277
61. Beever R, Bastos RN, Spanos C, Romé P, Cullen CF, Rappalber J, et al. 14-3-3 regulation of Ncd reveals a new mechanism for targeting proteins to the spindle in oocytes. *J Cell Biol.* 2017; 216(10):3029–39. <https://doi.org/10.1083/jcb.201704120> PMID: 28860275
62. Ohl R, Sapra T, Howard J, Mitchison TJ. Differentiation of cytoplasmic and meiotic spindle assembly MCAK functions by Aurora B-dependent phosphorylation. *Mol Biol Cell.* 2004; 15(6):2895–906. <https://doi.org/10.1091/mbc.e04-02-0082> PMID: 15064354
63. Jang JK, Gladstein AC, Das A, Shapiro JG, Sisco ZL, McKim KS. Multiple pools of PP2A regulate spindle assembly, kinetochore attachments and cohesion in *Drosophila* oocytes. *J Cell Sci.* 2021; 134(14). <https://doi.org/10.1242/jcs.254037> PMID: 34297127
64. Loughlin R, Wilbur JD, McNally FJ, Nedelec FJ, Heald R. Katanin contributes to interspecies spindle length scaling in *Xenopus*. *Cell.* 2011; 147(6):1397–407. <https://doi.org/10.1016/j.cell.2011.11.014> PMID: 22153081
65. Joly N, Beaumale E, Van Hove L, Martino L, Pintard L. Phosphorylation of the microtubule-severing AAA+ enzyme Katanin regulates *C. elegans* embryo development. *J Cell Biol.* 2020; 219(6). <https://doi.org/10.1083/jcb.201912037> PMID: 32412594
66. Tanno Y, Khtajima TS, Honda T, Ando Y, Ishiguro K, Watanabe Y. Phosphorylation of mammalian Sgo2 by Aurora B recruits PP2A and MCAK to centromeres. *Genes Dev.* 2010; 24(19):2169–79. <https://doi.org/10.1101/gad.1945310> PMID: 20889715
67. Yuesh WT, Singh VP, Gerton JL. Maternal Smc3 protects the integrity of the zygotic genome through DNA replication and mitosis. *Development.* 2021; 148(24). <https://doi.org/10.1242/dev.199800> PMID: 34935904
68. Gyuricza MR, Manhelmer KB, Apte V, Krishnan B, Joyce EF, McKee BD, et al. Dynamic and Stable Cohesins Regulate Synaptonemal Complex Assembly and Chromosome Segregation. *Curr Biol.* 2016; 26(13):1688–98. <https://doi.org/10.1016/j.cub.2016.05.008> PMID: 27291057
69. Balboula AZ, Nguyen AL, Gentilello AS, Quartuccio SM, Drutovic D, Solc P, et al. Haspin kinase regulates microtubule-organizing center clustering and stability through Aurora kinase C in mouse oocytes. *J Cell Sci.* 2018; 129(19):3648–60. <https://doi.org/10.1242/jcs.189340> PMID: 27582071
70. Nguyen AL, Drutovic D, Vazquez BN, El Yakoubi W, Gentilello AS, Malumbres M, et al. Genetic Interactions between the Aurora Kinases Reveal New Requirements for AURKB and AURKC during Oocyte Meiosis. *Curr Biol.* 2018; 28(21):3458–68.e5. <https://doi.org/10.1016/j.cub.2018.08.052> PMID: 30415701
71. Blengini CS, Ibrahimian P, Vaskovicova M, Drutovic D, Solc P, Schindler K. Aurora kinase A is essential for meiosis in mouse oocytes. *PLoS Genet.* 2021; 17(4):e1009327. <https://doi.org/10.1371/journal.pgen.1009327> PMID: 33901174
72. Wang LI, DeFosse T, Jang JK, Battaglia RA, Wagner VF, McKim KS. Borealin directs recruitment of the CPC to oocyte chromosomes and movement to the microtubules. *J Cell Biol.* 2021; 220(6).
73. O'Connell CB, Loncarek J, Hergert P, Kourtidis A, Conklin DS, Khodjakov A. The spindle assembly checkpoint is satisfied in the absence of interkinetochore tension during mitosis with unreplicated genomes. *J Cell Biol.* 2008; 183(1):29–36. <https://doi.org/10.1083/jcb.200801038> PMID: 18824563
74. Laband K, Le Borgne R, Edwards F, Stefanutti M, Canman JC, Verbavatz JM, et al. Chromosome segregation occurs by microtubule pushing in oocytes. *Nat Commun.* 2017; 8(1):1499. <https://doi.org/10.1038/s41467-017-01539-8> PMID: 29133801
75. Danilasky BM, Panzica MT, McNally KP, Vargas E, Bailey C, Li W, et al. Evidence for anaphase pulling forces during *C. elegans* meiosis. *J Cell Biol.* 2020; 219(12). <https://doi.org/10.1083/jcb.202005179> PMID: 33064834
76. Muscal CC, Torre-Santiago KM, Tran MV, Powers JA, Wignall SM. Kinetochore-independent chromosome segregation driven by lateral microtubule bundles. *Elife.* 2015; 4:e06462. <https://doi.org/10.7554/eLife.06462> PMID: 26026148
77. Paix A, Folkmann A, Seydoux G. Precision genome editing using CRISPR-Cas9 and linear repair templates in *C. elegans*. *Methods.* 2017; 121–122:86–93. <https://doi.org/10.1016/j.ymeth.2017.03.023> PMID: 28392283
78. Kirby C, Kusch M, Kempthues K. Mutations in the par genes of *Caenorhabditis elegans* affect cytoplasmic reorganization during the first cell cycle. *Dev Biol.* 1990; 142(1):203–15. [https://doi.org/10.1016/0012-1606\(90\)90164-e](https://doi.org/10.1016/0012-1606(90)90164-e) PMID: 2227096

79. Yang HY, Mains PE, McNally FJ. Kinesin-1 mediates translocation of the meiotic spindle to the oocyte cortex through KCA-1, a novel cargo adapter. *J Cell Biol.* 2005; 169(3):447–57. <https://doi.org/10.1083/jcb.200411132> PMID: 15883196
80. McNally K, Berg E, Cortes DB, Hernandez V, Mains PE, McNally FJ. Katanin maintains meiotic metaphase chromosome alignment and spindle structure in vivo and has multiple effects on microtubules in vitro. *Mol Biol Cell.* 2014; 25(7):1037–49. <https://doi.org/10.1091/mbc.E13-12-0764> PMID: 24501424